Università Politecnica delle Marche

Scuola di Dottorato di Ricerca in Scienze dell'Ingegneria

Corso di Dottorato in Ingegneria Industriale, Curriculum Materiali

Sustainable materials for improving Indoor Air Quality

Ph.D. Dissertation of:

Natalia Czerwinska

Supervisor:

Dr. Maria Letizia Ruello

Co-supervisor:
Dr. Chiara Giosuè

Ph.D. Course coordinator:

Prof. Giovanni Di Nicola

XXXVI cycle

Università Politecnica delle Marche

Scuola di Dottorato di Ricerca in Scienze dell'Ingegneria

Corso di Dottorato in Ingegneria Industriale, Curriculum Materiali

Sustainable materials for improving Indoor Air Quality

Ph.D. Dissertation of:

Natalia Czerwinska

Supervisor:

Dr. Maria Letizia Ruello

Co-supervisor:

Dr. Chiara Giosuè

Ph.D. Course coordinator:

Prof. Giovanni Di Nicola

XXXVI cycle

Acknowledgments

I believe that the last three years have been very intense and developmental not only on the academic level, but also on the personal level. Thanks to the doctoral course, I had the opportunity to meet many interesting people from various corners of the world, engage in numerous discussions in the scientific field and beyond, and form new friendships. I could not have undertaken this journey without my supervisor Dr. Maria Letizia Ruello. Our paths crossed for the first time when I participated in the international internship in 2019 and began my adventure with materials engineering in the SIMAU department. Dr. Maria Letizia Ruello was always very available and, with a lot of patience, was always able to find a solution to every problem or question I came to her with. Her expertise and encouragement have been invaluable in shaping my research and academic growth. I would like also to express my deepest gratitude to my co-supervisor, Dr. Chiara Giosue', for the unwavering support, guidance, and mentorship throughout my doctoral journey, but also for a very empathetic approach.

I would like also to acknowledge the Greenering Cost Action, which financially supported my international mobility and allowed me to spend a month in University of Nova in Portugal, where I gained new skills and met experts in the field of activated carbon. I would also like to thank my committee members, Dr. David B. DeVallance and Dr. Jolanda Palmisani - for their insightful feedback and constructive criticism that helped shape this thesis into its final form.

Furthermore, I am incredibly grateful to my mum and all my family for the unwavering love and encouragement. I would also like to thank my friends for their patience and understanding during the ups and downs of this journey. I am thankful also to my colleague with whom I have shared an office for the last two years, Rida Jbr, for a great collaboration together.

Finally, I would like to thank the person who has a special place in my heart. Thank you for never doubting me, thank you for every conversation, thanks to which I gained strength and courage during different stages of my life. Thank you for your never-ending motivation and for your patience, but also for your sense of humor, which can relieve any tension. Thank you for showing me that with determination and self-belief, we can succeed and achieve our goals. Grazie di cuore per essere sempre al mio fianco, amore mio.

Abstract

In recent years, the control of airborne contaminants has been of great interest in improving Indoor Air Quality (IAQ), especially because the concentrations often exceed the limits established by different organizations. This requires the adoption of a series of precautionary measures.

Particulate Matter (PM) and gaseous pollutants like Volatile Organic Compounds (VOCs) or Nitrogen Oxides (NO_X) represent a considerable problem both for the environment and for humans. In light of this, it becomes imperative to act at the root of the problem by reducing the origin of indoor air pollutants (especially anthropogenic) as much as possible, but also by identifying purifying systems that improve IAQ.

It is precisely in this last context that the aim of the following study fits the material science and engineering purposes, where developing the **next generation of materials and systems improves existing solutions and drives innovations**. Currently, due to the increased environmental awareness reducing greenhouse gas emissions, addressing resource depletion and environmental pollution, and optimizing waste management have become global hot topics and the challenge is to design green and sustainable systems that reduce air pollutants.

This thesis deals with different approaches for indoor air pollutants capture and degradation. In particular, **highly efficient air filters** that can be used for PM removal have been fabricated via electrospinning technique where biodegradable polymers and solvents with reduced toxicity were used. The samples produced were then tested in order to determine their particulate filtration efficiency and compared with the commercially available filters.

The second part of the study instead, is focused on the **adsorbents**, in particular, on activated carbon and biochar preparation. Activated carbon is one of the most used adsorbents, with a very high specific surface area and a well-developed pore structure, which make it suitable for use as an adsorbent for the removal of gaseous pollutants. However, the main issue present throughout the entire process of producing these materials is the use of nonrenewable precursors, such as petroleum residues, coal, peat, and lignite, which are associated with high costs and extensive energy consumption. This thesis presents alternative precursors, like wasted coffee grounds and olive stones, for the production of the adsorbents. Obtained carbon materials and commercially available activated carbon, were characterized and examined for VOCs removal applications.

Furthermore, two commercial TiO$_2$ **photocatalytic agents** have been selected and tested in terms of depolluting properties. Moreover, possible application of novel potassium vanadate photocatalytic agent for indoor air pollutants abatement have been considered. The selection of the best performing photocatalytic agent on a lab-scale was the first part of the project related to development of multifunctional finishing.

Combined systems were also investigated as a way to enhance pollutant removal. In particular, activated carbon-electrospun filters were designed and tested in terms of PM and VOCs removal. Whereas potassium vanadate's specific surface area was improved by mixing with zeolite. Obtained composite's properties were evaluated by means of VOCs and NO$_x$ removal. Moreover, innovative finish with photocatalytic and adsorptive properties has been tested in a lab and pilot-scale conditions. Additionally, commercially available single filters or multi-layer systems for air purification were evaluated in terms of filtration/adsorption/ photocatalytic degradation in lab-scale and pilot-scale.

Abbreviations

ANSES	Agency for Food, Environmental and Occupational Health & Safety
XRD	X-ray diffraction
AC	Activated Carbon
ACFC	Activated Carbon Fiber Cloth
AC	Alternating Current
ASHRAE	American Society of Heating, Refrigeration, and Air Conditioning Engineers
ASTM	American Society for Testing and Materials
ATR	Attenuated Total Reflection
BJH	Barrett-Joyner-Halenda method
B	Biochar
BET	Brunauer–Emmett–Teller method
CA	Carbon Aerogels
CO2	Carbon Dioxide
CMC	Carboxymethyl Cellulose
CA	Cellulose Acetate
CN	Cellulose Nitrate
CS	Cellulose Sulfate
CG	Coffee Grounds
CB	Conduction Band
DFT	Density Functional Theory
DTG	Derivative Thermogravimetry
DC	Direct Current
EDX	Energy Dispersive X-Ray
EPA	Environmental Protection Agency
EC	Ethyl Cellulose
EAC	Extruded Activated Carbon
FFP	Filtering Face Piece
FID	Photoionization Detector
FTIR	Fourier-Transform Infrared Spectroscopy
GAC	Granular Activated Carbon
HEPA	High Efficiency Particulate Air filter
HEC	Hydroxyethyl Cellulose
HPMC	Hydroxypropyl Cellulose
HPMC	Hydroxypropyl methyl cellulose
IAQ	Indoor Air Quality
IAQGs	Indoor Air Quality Guidelines
IR	Infrared radiation
IUPAC	International Union of Pure and Applied Chemistry
LA	Lactic Acid
Dmax	Maximum diameter
V_{meso}	Mesopore volume

MOFs	Metal Organic Frameworks
CM	Methyl Cellulose
MEK	Methyl Ethyl Ketone
MCC	Microcrystalline cellulose
MCC	Microcrystalline Cellulose
V_{micro}	Micropore volume
MPPS	Most Penetrating Particle Size
NCC	Nanocrystalline Cellulose
NFC	Nanofibrillated Cellulose
NAAQS	National Ambient Air Quality Standards
NIOSH	National Institute for Occupational Safety and Health
NHL	Natural Hydraulic Limes
NO2	Nitrogen dioxide
NO	Nitrogen Oxide
NOx	Nitrogen Oxides
NLDFT	Non-Local Density Functional Theory
OSHA	Occupational Safety and Health Administration
OMSW	Olive Mill Solid Wastes
OMW	Olive Mill Wastewater
OS	Olive Stones
PSD	Particle Size Distribution
PM	Particulate Matter
PM	Particulate Matter
PFE	Particulate Filtration Efficiency
ppb	parts per billion
ppm	parts per million
ppmv	parts per million by volume
PEL	Permissible Exposure Limits
PCO	Photocatalytic Oxidation
PID	Photoionization Detector
pHpzc	point of zero charge
PLA	Polylactic Acid
PMMA	Polymethylmethacrylate
PVC	Polyvinyl Chloride
KVO	Potassium vanadate
KVO	Potassium vanadate
PAC	Powdered Activated Carbon
PFE	Particulate Filtration Efficiency
∆P	Pressure Drop
P-MCC	Pure Microcrystalline cellulose
QF	Quality Factor
RH	Relative Humidity
SEM	Scanning Electron Microscope
SRA	Shrinkage Reducing Admixtures

SBS	Sick Building Syndrome
SSA	Specific Surface Area
SDGs	Sustainable Development Goals
T	Temperature
TGA	Thermal Gravimetric Analysis
TLV	Threshold Limit Values
TWA	Time-Weighted Average
V_{total}	Total pore volume
TVOCs	Total Volatile Organic Compounds
UV and VIS	Ultraviolet and Visible
VB	Valance Band
VOCs	Volatile Organic Compounds
V	Volume
W-MCC	Waste-derived microcrystalline cellulose
WGBC	World Green Building Council
WHO	World Health Organization
XPS	X-ray photoelectron spectroscopy
ZEO	Zeolite

Contents

Overview of the thesis

Motivation and research aims

In the pursuit of creating healthier built environments for occupants, indoor air quality has emerged as a crucial factor. With the majority of people spending a significant amount of time indoors (homes, schools, workplaces, or any public and private building) concerns over indoor air quality have been on the rise, as it poses a substantial threat to the well-being and comfort of individuals inhabiting buildings. Indoor air quality can be influenced by several factors, encompassing microbiological agents, physical parameters, indoor and outdoor ventilations.

To underline the impact of air pollution in general on human health, the World Health Organization (WHO) data [1] show that in the World, 9 people out of 10 regularly breathe air containing high levels of pollutants and the death toll related to the adverse effects of air pollution is estimated to be of 7 million deaths worldwide every year, 3.2 million of which due to the air pollution of indoor environments.

Despite several solutions available on the market that capture and/or degrade air pollutants, not all of them are considered as sustainable and fit in the circular economy approach. In the circular economy concept, waste remediation and valorization aim to lower the amount of waste disposed in landfills through recycling and the efficient use of renewable resources and therefore contributing to pollution reduction.

The aim of this thesis is to study, design, and test eco sustainable materials which can improve Indoor Air Quality, and consequently humans' comfort and health, while reducing the negative impact on the environment.

Summary

The thesis is structured in six chapters; each one subdivided into different sections in order to help the reader to better follow the argument of the research project. A summary of this thesis is shown in the following list, where a brief description of each chapter is given:

Chapter 1 – Introduction

This chapter introduces the current problems concerning indoor air quality and waste management.

Chapter 2 - Materials and methods of characterization

This chapter presents the materials used for indoor air pollutants' abatement. Materials have been classified according to the pollutant removal mechanism. In particular, precursors from different waste sources, mechanical filters, adsorbents, photocatalytic agents and combined systems have been described. Moreover, methods of materials characterization have been presented, including a description of laboratory-built reactors and pipe for pollutant removal tests.

Chapter 3 - Mechanical filters

In this chapter commercial filters (polypropylene, glass fiber, surgical and FFP masks) and fabricated electrospun membranes have been characterized and Particulate Filtration Efficiency (PFE) was determined.

Chapter 4 – Adsorbents

In this chapter, commercial and synthesized activated carbons and biochar from organic wastes have been characterized and tested in terms of VOCs adsorption.

Chapter 5 - Photocatalytic agents

In this chapter, two types of commercial TiO_2 photocatalytic agents have been tested for NO_x and VOCs remediation. Different test methodologies have been evaluated. Moreover, in collaboration with another research group, possible application of novel potassium vanadate for indoor air pollutants abatement have been considered.

The results provided in this section constitute the first phase of experimentation for the project focused on innovative multifunctional finishing development.

Chapter 6 - Combined systems

In this chapter electrospun filters with additives (activated carbon and TiO$_2$), potassium vanadate-zeolite composites, commercial air purificator, innovative multifunctional finishing have been tested in terms of different pollutants capture through synergistic effect (filtration/adsorption/photodegradation). Tests have been performed both in lab and pilot scale.

Chapter 1   Introduction

1.1. Indoor air pollutants classification and guidelines

Different types of pollutants are present in indoor environments, including gaseous pollutants (inorganic chemicals, Volatile Organic Compounds and radon), particulate matter (PM_2, PM_{10}) and biological contaminants (allergens, viruses, bacteria, mold). Indoor air pollutants can be generated inside homes or buildings through occupants' activities, such as cooking, smoking, use of electronic machines, use of consumer products, or emission from building materials.
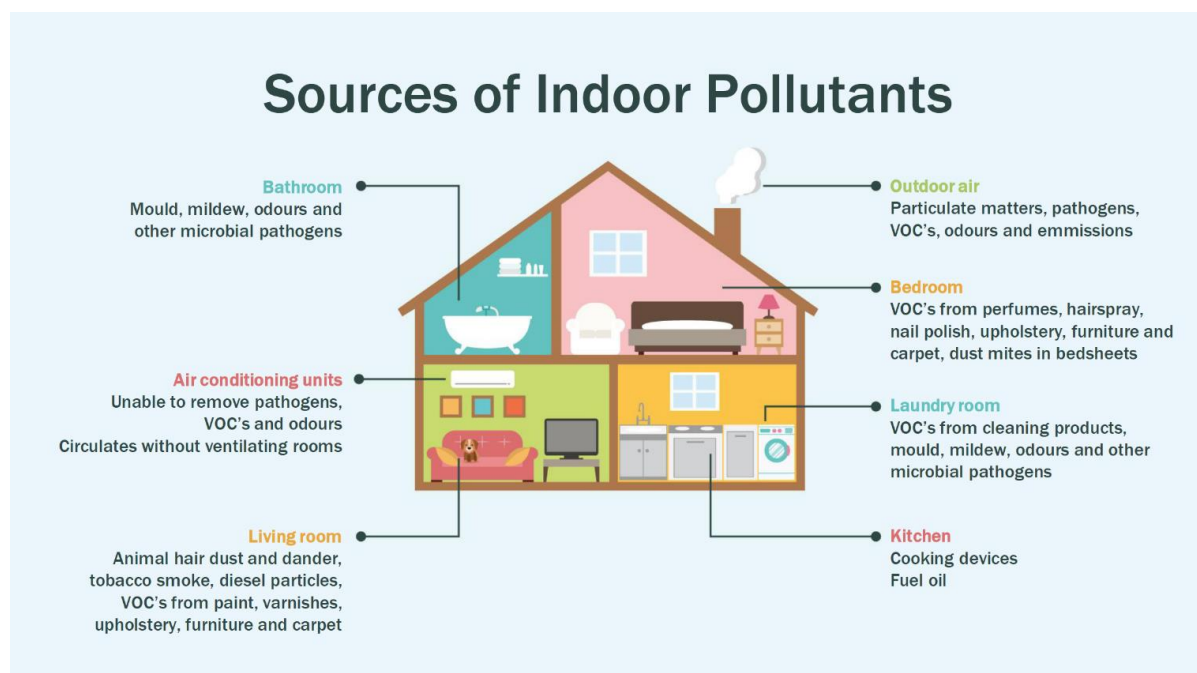
Figure 1. Sources of indoor (residential) pollutants (source: https://minettcapital.ca/improving-indoor-air-quality/).

Prolonged exposure to indoor air pollution can induce headaches, fatigue, and impaired cognitive function. Additionally, indoor air pollutants are associated with cardiovascular problems and long-term health effects such as cancer and even premature death. IAQ guidelines (presented in Table 1.) set the bar for acceptable concentrations of indoor pollutants that may be harmful to people's health and welfare. These regulations are created by numerous organizations and regulatory bodies and are disseminated worldwide. However, there is no consensus globally about indoor air quality standards, or health-based guidelines, but regulations from some individual countries and from health organizations. For example, the World Health Organization's (WHO) indoor air quality regulations and guidelines [2], [3] list

a number of potentially dangerous organic and non-organic compounds like PM, CO, formaldehyde, Radon, and VOCs that can have negative health effects in homes in large quantities or after prolonged exposure. According to the World Health Organization's definition of air quality guidelines, these guideline values correspond to safe levels of indoor pollutant concentrations below which adverse health effects are not expected to occur in the general population, including sensitive groups (children, elderly people). The WHO's guidelines are currently regarded as the primary source in Europe, upon which the air quality (ambient) directive of the European Commission is based.

Guidelines for indoor air quality (IAQGs) have been developed by the French Agency for Food, Environmental and Occupational Health & Safety (ANSES) since 2005. Up to now, 11 indoor air pollutants of interest have been assessed by ANSES's experts: formaldehyde, carbon monoxide, benzene, naphthalene, trichloroethylene, tetrachloroethylene, particulate matter, cyanhydric acid, nitrogen dioxide, acrolein and acetaldehyde [4].

The Environmental Protection Agency (EPA) is an autonomous agency of the United States government in charge of environmental protection concerns, as well as research, development, and enforcement of environmental legislation. EPA does not regulate indoor air, but IAQ Tools for Schools Action Kit gives institutions access to tools, best practices, and best practices policies designed to enhance IAQ [5]. The Building Air Quality (BAQ), developed by the EPA and the National Institute for Occupational Safety and Health, provides practical suggestions on preventing, identifying and resolving indoor air quality (IAQ) problems in public and commercial buildings. Moreover, Clean Air Act, which is the comprehensive federal law that regulates air emissions from stationary and mobile sources and was last amended in 1990, requires EPA to set National Ambient Air Quality Standards (NAAQS) for six principal air pollutants which can be harmful to public health and the environment. These include carbon monoxide, lead, nitrogen dioxide, ozone, particulate matter and sulfur dioxide.

There are also guidelines for occupational exposure that apply to healthy persons who are exposed to various chemicals over time in their workplaces, which are typically industrial settings. These are disseminated by entities like the UK Health and Safety Executive (HSE), the National Institute for Occupational Safety and Health (NIOSH), and the Occupational Safety and Health Administration (OSHA).

It is worth noting that at European level, there are directives concerning the emissions of Volatile Organic Compounds (VOCs) from commercial products (Directive 1999/13/EC, The Industrial Emission Directive 2010/75/EU, Italian Directive 11/01/2017), but no specific

regulatory standards regarding a specific concentration limit of Total Volatile Organic Compounds (TVOCs) in indoor environments. This is because odor and irritation responses to organic compounds are highly variable. Moreover, there is no single method currently in use that measures all organic compounds that may be of interest. For this, setting target concentrations for TVOCs is not recommended, just for specific VOCs of concern is preferred.

Table 1. Exposure limits for the main air pollutants.

Indoor air contaminants	Indoor WHO		Indoor ANSES		Outdoor EPA	
	Short-term Exposures	Long-term Exposures	Short-term Exposures	Long-term Exposures	Short-term Exposures	Long-term Exposures
TVOCs	-	-	-	-	-	-
Toluene	-	-	6 ppm (24h-mean)	5 ppm (annual-mean)	-	-
Formaldehyde	0.08 ppm (30min-mean)	-	0.4 ppm (2h-mean)	0.08 ppm (annual-mean)	-	-
Benzene	No safe level of exposure can be recommended		9 ppb (2week-mean)	3 ppb (annual-mean)	-	-
NO_2	25 µg/m³ (1h-mean)	10 µg/m³ (annual-mean)	200 µg/m³ (1h-mean)	20 µg/m³ (annual-mean)	188 µg/m³ (1h-mean)	100 µg/m³ (annual-mean)
CO_2	-	-	-	-	-	-
CO	35 ppm					
$PM_{2.5}$	15 µg/m³ (24h-mean)	5 µg/m³ (annual-mean)	-	-	35 µg/m³ (24h-mean)	15 µg/m³ (annual-mean)
PM_{10}	45 µg/m³ (24h-mean)	15 µg/m³ (annual-mean)	-	-	150 µg/m³ (24h-mean)	-
Radon	-	-	-	-	-	-

1.1.1. Gaseous pollutants

1.1.1.1. Volatile Organic Compounds

According to a World Health Organization classification system, Volatile Organic Compounds are defined by a boiling point range with a lower limit between 50 and 100 °C and an upper limit between 240 and 260 °C [6]. The ASTM International standard D3960-05 (2018) refers to a VOC as any organic compound that can participate in atmospheric photochemical reactions.

VOCs originate from a wide range of sources, both natural and anthropogenic. They are emitted from building materials, furnishings, cleaning products, and can also enter indoor environments from outdoor pollution sources like traffic. VOCs are responsible for the odor of scents and perfumes, and some of them, like formaldehyde, emit strong odors that can cause physical irritation and may have long-term chronic health effects. Common physical and chemical properties of VOCs are:

- Their relative vapor density is heavier than air.
- Most of them are insoluble or sparingly soluble in water, but easily soluble in organic solvents.
- Low melting point, easy to decompose, and volatile.
- There are millions of species, most of which are flammable and explosive, and some are toxic or even highly toxic - such as benzene, toluene, acetone, dimethylamine, and thiohydrocarbons. When the emission concentration of these substances is high, and they encounter static sparks or other sources of ignition, they may easily cause fires.
- Most of them are colorless, with many having pungent or special odors - causing people's sensory discomfort and seriously reducing people's quality of life. Benzene, toluene, xylene, and formaldehyde have toxic, irritating, teratogenic, and carcinogenic effects. In addition, VOCs can also cause diseases of the respiratory tract, kidneys, lungs, liver, nervous system, digestive system, and hematopoietic system. As the concentration of VOCs increases, the human body will experience symptoms such as nausea, headache, convulsions, and coma.
- Photochemically reactive - under sunlight, VOCs will chemically react with NO_x in the atmosphere to form secondary pollutants (such as ozone, etc.) or strong chemically active intermediate products (such as free radicals, etc.).

Recently, various research has found reliable links between exposure to Volatile Organic Compounds and negative effects on human health and well-being in both the short and long term. Some of the most frequently researched VOCs found in indoor spaces include benzene, toluene, ethylbenzene, known as xylenes (BTEX), as well as styrene, n-hexane, 2-ethylexanol, 2-butoxyethanol, aldehydes (e.g., formaldehyde, acetaldehyde, benzaldehyde, acrolein), and certain terpenes (primarily α-pinene and d-limonene). In the study of Rovelli [7] nine different residential buildings in Como (Northern Italy) were randomly selected and investigated to assess the indoor concentrations of the target VOCs during the dishwasher washing cycle. D-limonene was the most common VOC found in every household, with concentration levels frequently exceeding 100 μg/m^3, averaging 231 μg/m^3, and reaching a maximum of 611 μg/m^3. This outcome was anticipated because d-limonene is a common fragrance ingredient in dishwasher tablets, liquid detergents, and other cleaning products. Along with limonene, toluene (3.2–63.1 μg/m^3), m-xylene (1.7–38.6 μg/m^3), α-Pinene (1.2–33.1 μg/m^3), benzene (1.8–9.3 μg/m^3), and other VOCs were also identified. In the another study, performed in the hair studio, more than 50 VOCs were identified (occurrence ≥60%) and 14 of them were quantified. Among the main compounds detected there were benzene (88 ppb), toluene (941 ppb), ethylbenzene (98 ppb), diethyl phthalate (21 ppb), 1,4-dioxane (147 ppb), etc. Colors, hair cosmetics, sprays can be mentioned as common sources of these compounds.

1.1.1.2. Nitrogen oxides

Nitrogen oxides (NO$_x$) are the class of pollutants present in both outdoor and indoor, which have significant impacts on human health, most notably when it comes to respiratory and cardiovascular health. Nitrogen dioxide (NO$_2$) and nitrogen oxide (NO) are subclasses of NO$_x$ and are highly reactive gases, which are formed during combustion. Indoor concentrations are a function of both indoor and outdoor sources: the first are influenced by the latter, and the levels of pollutants are often higher in the confined spaces. Building's proximity to roads or the presence of an attached garage, shown to be the largest factor influencing indoor concentrations [8]. The primary indoor sources of NO$_x$ are building heating, cooking with fossil fuels, and tobacco smoke. Increased levels of nitrogen oxides can occur in homes with gas cookers, paraffin heaters and certain portable bottled gas heaters, as well as with badly maintained central heating boilers or gas fires [9]. A.Dedele and A.Miskinyte [10] analyzed the differences of nitrogen dioxide concentrations between kitchens with gas and electric stoves and the outdoor air during different seasons. Their results demonstrated that the WHO daily

NO$_2$ guideline value of 25 μg/m^3 was regularly exceeded in nearly all gas cooking scenarios. The highest median concentration of NO$_2$ in kitchens with gas stoves was measured during the winter period, and it was 28.4 μg/m^3 which was 2.5 times higher in kitchen with gas stoves than with electric stoves.

1.1.2. Particulate Matter

Particulate matters (PMs) represent a diverse group of solid or liquid particles suspended in the air, encompassing a complex mixture of organic compounds, metals, and soil or dust particles. Their size spectrum spans a wide range, from a few tens of Ångstroms to several hundred micrometers. The classification of PMs is varied, encompassing their size range, source of origin, chemical composition, and associated effects.

Regarding the classification based on the size range, PMs are typically categorized into two main size fractions, considering their aerodynamic diameter. The aerodynamic diameter is defined as the diameter of a sphere with unit density that exhibits the same aerodynamic characteristics, i.e., terminal settling velocity, as the particle in question. It's used to express the aerodynamic behavior of particles with irregular shapes as a length measure to be able to compare them more effectively. The two main categories are:

- **PM$_{2.5}$ (Fine Particles)**: particles with an aerodynamic diameter of less than 2.5 μm [11], approximately one-twentieth the width of a human hair. They possess a high potential for penetration deep into the respiratory system, posing significant health risks.
- **PM$_{10}$ (Coarse Particles)**: particles with an aerodynamic diameter between 2.5 and 10 μm; larger than PM$_{2.5}$ but still have the ability to enter the respiratory tract.

PM$_{10}$ and PM$_{2.5}$ are the main measured and regulated categories, but a further categorization of the finer fraction is possible:

- **UFP (Ultrafine Particles)**: are particulate matter of nanoscale size, specifically with an aerodynamic diameter of less than 0.1 μm. They are far smaller than the regulated PM$_{10}$ and PM$_{2.5}$ particle classes and are believed to have several more aggressive health implications.
- **Nanoparticles:** particles with an aerodynamic diameter of less than 0.05 μm.
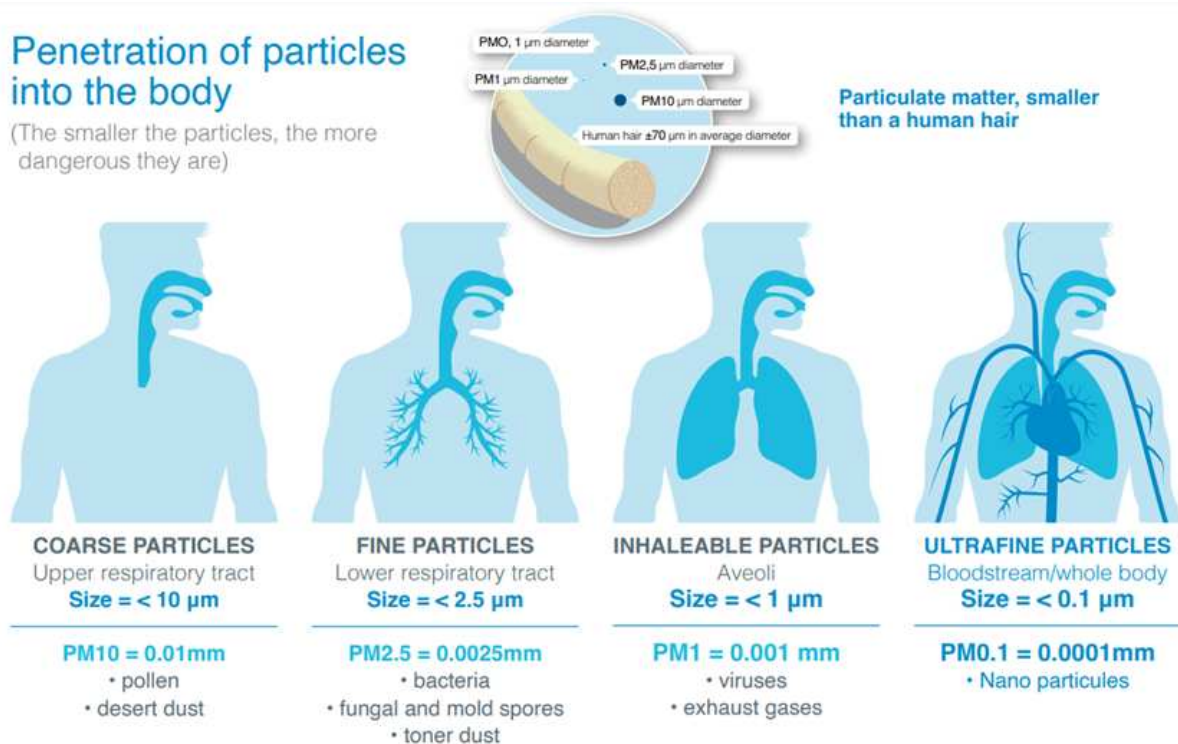
Figure 2. PM classification and penetration of PM into the body (source: www.afprofilters.com).

Indoors PM are generated by cooking, cleaning activities, combustion activities (burning candles or incenses, use of fireplaces, smoking), biological contaminants, printers. WHO air quality guidelines (2020) [3] set limits for ambient air $PM_{2.5}$ and PM_{10} concentrations at 15 $\mu g/m^3$ and 45 $\mu g/m^3$ for 24-hour and 5 $\mu g/m^3$ and 15 $\mu g/m^3$ for 1-year averages, respectively. As there is no convincing evidence of a difference in the hazardous nature of particulate matter from indoor sources as compared with those from outdoors and the indoor levels of PM_{10} and $PM_{2.5}$, in the presence of indoor sources of PM, are usually higher than the outdoor PM levels, the air quality guidelines for particulate matter recommended by the 2005 global update [3] are also applicable to indoor spaces and a new review of the evidence is not necessary at present. Cooking emissions have been identified as a major source of indoor particulate matter. Different cooking methods emit different quantities of particles. Emission rates of PM from cooking are impacted by the type of appliance used, the condition of cooking, temperatures and the fat content of the ingredients. For example, frying can produce peak particle levels of 745 $\mu g/m^3$ (2.22×10^3 $\mu g/min$) [12], exceeding WHO 24-h 15 $\mu g/m^3$ exposure threshold almost 50 times. In another study [13], the highest emission rates of both PM_{10} and $PM_{2.5}$ at a single time point were found to be generated by deep-frying with values of 7586 $\mu g/min$ and 1229 $\mu g/min$, respectively. The results showed also that deep-frying and stir-frying had much higher

emission rates than boiling and steaming, in line with several previous studies; larger particle production is caused by cooking with oil as opposed to water. See and Balasubramanian [14] conducted experiments by steaming, boiling, stir-frying, pan-frying, and deep-frying 150 grams of tofu. Deep-frying, stir-frying, boiling and steaming generated the largest mass of PM2.5, with average concentrations of PM2.5 at 190, 120, 81 and 66 g $\mu g \ m^{-3}$, respectively. In another study of the Alamaddine et al. [15] researchers examined the potential impacts of the school's locality and its administration on IAQ by quantifying the indoor and outdoor $PM_{2.5}$ exposure at 40 urban and rural school. They demonstrated that concentrations of indoor $PM_{2.5}$ (20–180 $\mu g/m^3$, and a mean of 62 $\mu g/m^3$) showed differences between urban and rural as well as between private and public schools. Some rural schools exhibited greater exposure than urban schools, depending on their immediate surrounding environment and their internal $PM_{2.5}$ sources.

1.1.3. Biological contaminants

Biological contaminants contain a complex mixture of bacteria, molds, mildew, viruses, animal dander and cat saliva, house dust, mites, cockroaches, and pollen. They are originated by pets, plants (pollen, odors, allergens), building materials, and their effects can be aggravated by the heating modes (temperature, humidity), the degree of ventilation, carpets, and tissues (mites) [16]. By controlling the relative humidity at home, which according to the Environmental Protection Agency [17] optimal level should range between 30 and 50%, the growth of some sources of biologicals can be minimized.

1.2. The impact of indoor carbon dioxide

Carbon dioxide (CO_2) is a colorless and odorless gas. It is a natural component of ambient air, at a concentration of around 400 ppm (parts per million) and can be generated both by human activities and human respiration. The latter has no impact on global warming, unlike human activities. Because humans produce and exhale carbon dioxide, concentrations of CO_2 in occupied indoor spaces are often higher than concentrations outdoors.
Using ventilation rates of CO_2 as an indicator for IAQ, ASHRAE (Standard 62.1-2016) recommends that indoor CO_2 concentrations must be maintained not greater than 700 ppm above the ambient level. Elevated levels of CO_2 may serve as an indicator of insufficient number of air changes in that environment.

In the workplace environments, the United States Occupational Safety and Health Administration (OSHA) and National Institute for Occupational Safety and Health (NIOSH) have established a time weighted average limit value of 5000 ppmv for airborne exposure in any 8-hour work shift during a 40-hour workweek and 30,000 ppmv as a short-term exposure limit (15-minute time weighted average) that should not be exceeded at any time during a workday.

Normally carbon dioxide is non-toxic, however, in crowded and poorly ventilated rooms, it could weaken IAQ, and it has been associated with Sick Building Syndrome (SBS) which is related to the reduced work efficiency. In the literature there are evidences that CO_2 levels in two schools located in Italy reached up to 5136 ppm in classrooms where the windows were closed during lessons [18]. In a study of 10 classrooms in Australia, the average CO_2 levels ranged between 657 ppm and 2235 ppm, and the maximum values for CO_2 concentrations ranged from 3799 ppm to 5000 ppm; these values were recorded in three classes during school hours [19].

1.3. Strategies to improve indoor air quality

The most effective strategy to improve IAQ is prevention: elimination individual sources of pollution or reduction their emissions. For instance, some initiatives have been carried out to reduce exposure to one of the most prominent particulate pollutant, asbestos, which has been used in the past in a variety of building materials and currently is considered a carcinogen. In this context, the European Directive 99/77/EC restricted harmful construction materials and products containing hazardous components.

Ventilation (natural, mechanical or hybrid)- the second strategy to control indoor air contaminants involves diluting contaminants with outdoor air or isolating or removing contaminants by controlling air pressure relationships. Natural ventilation, the most cost-effective and eco-friendly way, is intended to dilute indoor air contaminants without using mechanical equipment. While mechanical ventilation is driven by fans. Fans can either be installed directly in windows or walls, or installed in air ducts for supplying air into, or exhausting air from, a room. Mechanical ventilation can be expensive to install and maintain and requires a reliable power source. It can also be noisy, which may be a concern in certain settings, however, provides greater control in contrast to the natural ventilation. Hybrid

ventilation (two mode system) is controlled to minimize energy consumption while maintaining acceptable indoor air quality and thermal comfort. The two modes refer to natural and mechanical driving forces.

Air cleaning equipment and materials are another effective strategy to provide better indoor air quality for occupants, and must be properly selected and designed for the particular pollutants of interest. For example, VOCs can be removed typically through two principles: adsorption by porous materials or catalytic degradation.

1.4. Circular economy and sustainability

The circular economy concept has become the driving force for sustainable development, based on maximizing resources efficiency and by minimizing environmental impacts with the aim of achieving a vision of **zero waste** and **friendly environment**. The conversion of renewable resources and biomass into sustainable materials is a crucial step to reduce the dependence on depleting fossil resources.

The 2030 Agenda for Sustainable Development, adopted by all United Nations Member States in 2015 provides 17 Sustainable Development Goals (SDGs), with the 169 targets, form the core of the 2030 Agenda. They balance the economic, social, and ecological dimensions of sustainable development, and place the fight against poverty and sustainable development. Policies and actions aimed at addressing air pollution have a direct and positive impact on population health (**SDG 3**), which subsequently leads to increased labor productivity and economic growth (**SDG 8**: Decent Work and Economic Growth) and improved education (**SDG 4**). The development of sustainable cities and communities (**SDG 11**) depends on maintaining safe levels of particulate matter pollution, while achieving universal access to sustainable energy (**SDG 7**) requires a shift away from polluting fuels that cause both outdoor and indoor (household) air pollution. Ozone, a significant air pollutant, considerably reduces crop yield, hence, clean air supports food security and better nutrition (**SDG 2**). It is typically the most vulnerable individuals and communities, including children, women, and the elderly, who suffer the most from air pollution. As a result, policies and actions aimed at improving air quality can also contribute to reducing inequalities (**SDG 10**: Reduced Inequalities; **SDG 5**: Gender Equality).

Since both air pollution and climate change are mainly caused by burning fossil fuels, actions aimed at improving air quality often also address climate change (**SDG 13**). Solutions to improving air quality, such as switching to affordable and cleaner energy, reducing emissions from cooking and transportation, can also help address the climate emergency. Reducing air pollution associated with responsible production and consumption is crucial for achieving **SDG 12**, which includes reducing emissions from transportation, waste burning, and industrial activities. Clean air can also support **SDG 15**, as air pollution can harm ecosystems and biodiversity, including plants, animals, and microorganisms. Maintaining clean air will help protect these species and preserve healthy ecosystems.

Figure 3. Sustainable development goals (source: https://sdgs.un.org/goals).

Environmental Protection Agency (EPA) and World Green Building Council (WGBC), provide a strong foundation for improving air quality in sustainable design by:

- Raising awareness of how other structural aspects of buildings contribute to and amplify air quality;
- Educating how retrofitting and using quality construction materials help green buildings have cleaner air;
- Encouraging greener solutions to fight air pollutants and minimizing the threats from existing contaminants;
- Protecting building occupants by regulating humidity and purifying particulates for optimal safety and decreasing the spread of disease;

- Ensuring buildings can filter outside air entering the structure.

1.5. Waste valorization

In contrast to the conventional linear economy model's "take-make-consume-dispose" policy, the circular economy model's "made-to-be-made-again" policy presents immense opportunities to significantly reduce the demand for virgin resources and reconsider the entire process of managing resources and waste. This approach involves redesigning products to make them more cost-effective, environmentally friendly, and efficient, and it can create new jobs and foster innovative technologies. The goal of the circular economy is to achieve sustainable resource management by reusing, sharing, repairing, refurbishing, remanufacturing, and recycling materials to form a closed-loop system, while also minimizing the use of natural resources. The circular economy model emphasizes bringing waste back into the production process so that it can be used as a resource for the next production cycle or transformed into an independent product.

Agricultural byproducts, food waste, and industrial byproducts necessitate an environmentally friendly way of reducing issues related to their disposal; it is also necessary to recover as much as new raw material from these resources as possible, especially when we consider their potential usage as a precursor to preparing depolluting materials. Waste valorization is a key solution and refers to any industrial processing activities aimed at reusing, recycling, or composting from wastes, useful products. In this thesis three types of waste (textiles, food and after combustion-delivered) were used as alternative precursors to obtain new valuable materials.

1.5.1. Food waste

Estimates show that, in 2021 in the EU, **over 58 million tons** of food waste (131 kg/inhabitant) – around 20% of all food produced are generated annually, with an associated market value estimated at **132 billion euros**. Figure 4 shows food waste generated by different sectors. The highest amount of food waste, 54% is generated by households (70 kg per inhabitant). The remaining 46% of waste is generated upwards in the food supply chain. Household food waste is nearly twice the amount of food waste arising from the sectors of primary production and manufacture of food products and beverages (11 kg and 28 kg per

inhabitant; 9% and 21%, respectively), sectors in which strategies exist for reducing food waste, for instance with the use of discarded parts as by-products. Restaurants and food services accounted for 12 kg of food waste per person (9%), while retail and other distribution of food was the sector with the least amount of food waste (9 kg; 7%) [20], [21].
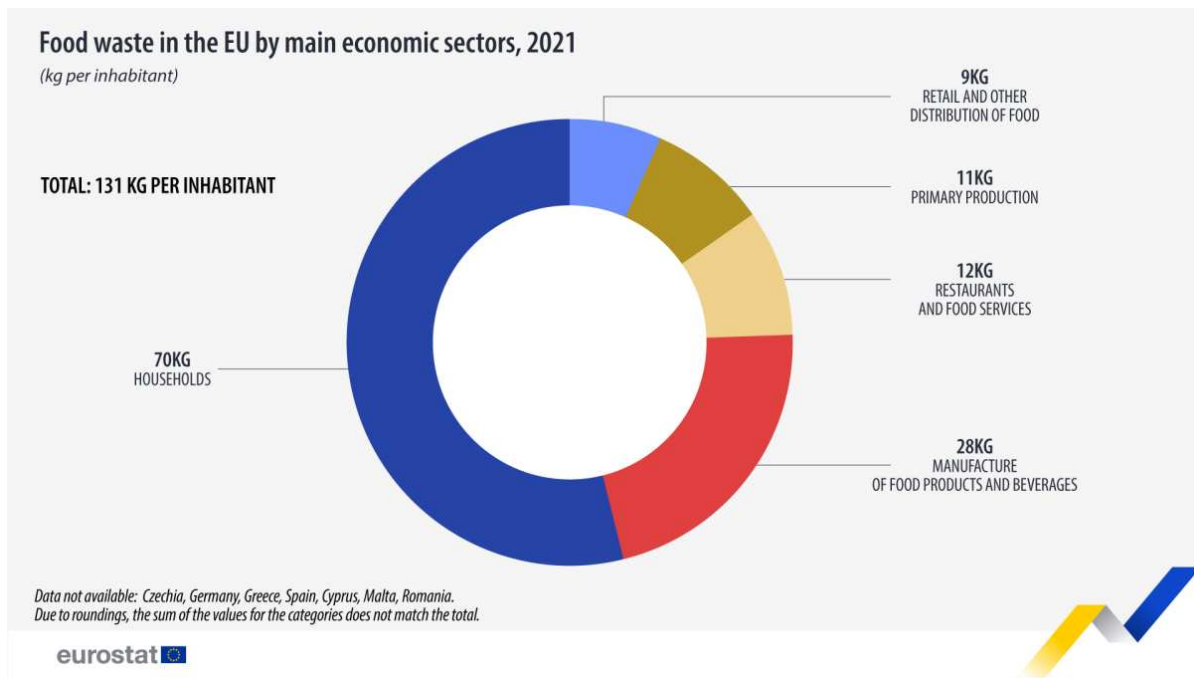
Figure 4. Food waste generated by different sectors (kg per inhabitant) (source: https://ec.europa.eu/eurostat/statistics-explained/index.php?title=Food_waste_and_food_waste_prevention_-_estimates).

Preventing food waste can make an important contribution also to other Sustainable Development Goals: tackling climate change (SDG 13); saving nutritious food to give to those in need (SDG 2 – zero hunger); and bringing cost-savings for farmers, companies and households (SDG 8).

In this thesis, coffee grounds and olive stones were used as a precursor for activated carbon and biochar preparation.

Coffee is one of the most widely consumed beverages worldwide. Each year the coffee industry generates over 10 million tons of coffee waste worldwide [14]. Typically, coffee grounds and other organic waste are composted, burned, or, in the worst-case scenario, end up in the landfill. Alternative ways of using waste coffee grounds on an industrial scale include, for example, transforming them into biofuel, biodiesel, bioethanol, or biomaterials.

In 2022–2023, around 1.5 million tons of olive oil was produced by the leading producers of olive oil in Europe (Spain, Italy, Greece, and Portugal) [22]. Due to its range of different valuable properties, it is used in gastronomy, cosmetics, and pharmaceuticals. However, the process of manufacturing olive oil is also related to the generation of large amounts of waste and byproducts such as leaves, olive mill wastewater (OMW), and olive mill solid wastes (OMSW), i.e., olive stones, olive mill husks, olive cakes, and pomace.

1.5.2. Textile waste

On average, each European consumes 26 kg of textiles, of which 11 kg are discarded after being worn only 7–8 times. Currently, only 22% of post-consumer textile waste is collected separately for re-use or recycling, while the remainder is often incinerated or landfilled.

The textile industry is in the top five most polluting sectors, together with housing, transport, and food. This is caused by the strong impact it has on land use and water pollution. The production and consumption of textiles also generates greenhouse gas emissions, in particular from resource extraction, production, washing and drying, and waste incineration. As shown in Figure 5 in 2020, producing textile generated greenhouse gas emissions of 121 million tons carbon dioxide equivalent (CO_2e) in total, or 270 kg CO_2e per person. This makes textiles the household consumption domain responsible for the fifth-largest impact on climate change, after housing, food, transport and mobility, and recreation and culture [23].

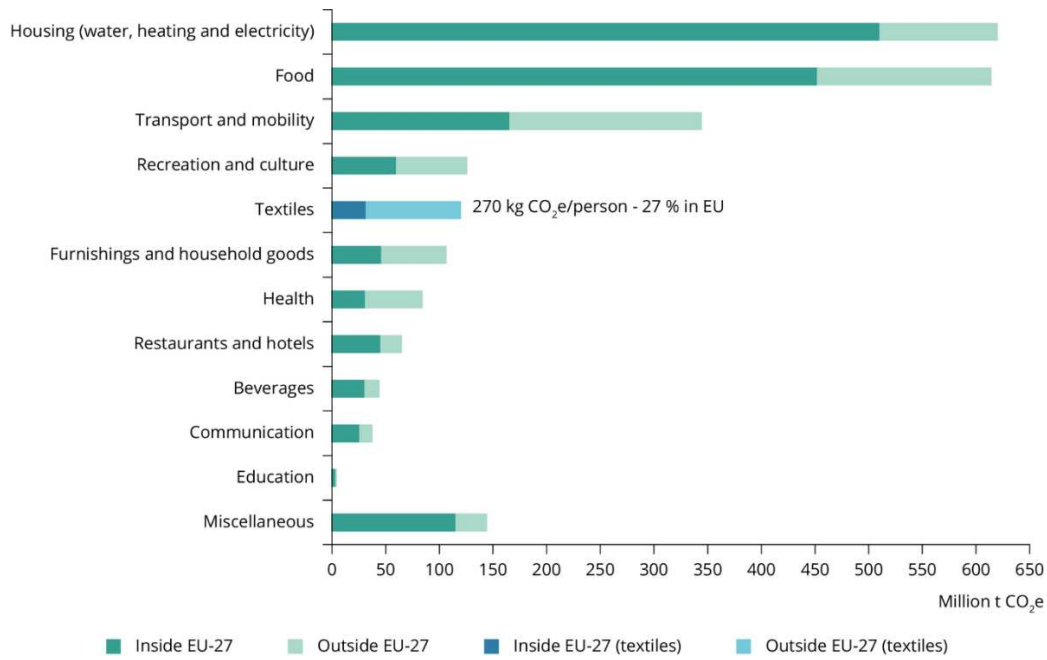*Figure 5. Greenhouse gas emissions in the upstream supply chains of EU-27 household consumption domains in 2020 (million tones CO2e), (source: https://www.eea.europa.eu/publications/textiles-and-the-environment-the).*

Chapter 2   Materials and methods of characterization

2.1. Materials

In the following chapter, all the used materials are listed and briefly described according to the state of the art. All the results for the specific experimental are described in separate chapters.

Table 2. Overview of the materials used in the experiments.

	Materials	Aim	Chapter
Traditional	Glass fiber Polypropylene Surgical mask FFP masks	Reference, commercially available filters; evaluation of Particulate Filtration Efficiency	3.Mechanical filters
Fabricated	Electrospun filters: PLA PLA+P-MCC PLA+W-MCC CA	Fabrication of biodegradable filters; evaluation of Particulate Filtration Efficiency	
Traditional	Activated carbon	Reference, commercially available powdered activated carbon; evaluation of VOCs adsorption	4.Adsorbents
Fabricated	Coffee grounds-derived biochar Coffee grounds-derived activated carbon Olive stones-derived activated carbon	Fabrication of adsorbents from alternative feedstock; evaluation of VOCs adsorption	
Traditional	TiO_2 P-25 TiO_2 KronoClean 7404	Reference, commercially available; evaluation of photocatalytic degradation	5.Photocatalysis
Fabricated	Potassium vanadate	Evaluation of photocatalytic degradation within collaboration with another research group	
Traditional	Activated carbon filter Air purifier system	Commercially available single filters or multi-layer systems for air purification; evaluation of filtration/adsorption/ photocatalytic degradation in lab-scale or pilot-scale	

Fabricated	Potassium vanadate and zeolite composites Electrospun nanofiber composites Innovative finishing	Fabrication of materials with combined properties; evaluation of filtration/adsorption/ photocatalytic degradation in lab-scale or pilot-scale	6.Combined systems

2.1.1. Alternative materials

List of alternative materials (precursors) and the purpose of their synthesis and application are shown in Table 3.

Table 3. List of alternative materials used for experiments.

Type of waste	Material	Purpose	Chapter
Textiles	Clothes	Microcrystalline cellulose extraction	3. *Mechanical filters*
Food	Coffee grounds	Activated carbon and biochar preparation	4. *Adsorbents*
Food	Olive stones	Activated carbon and biochar preparation	4. *Adsorbents*
Biomass ashes	Fly and bottom combustion ashes	Traditional aggregate substitution in innovating finishing	6. *Hybrid systems*

2.1.1.1. Waste textiles for cellulose extraction

As part of an innovative circular strategy, the main goal of this work was to study the possibility to transform the extracted cellulose from textile wastes by acid hydrolysis and freeze-drying and further transform it into cellulose-based filters. This part of the research was performed in the collaboration with Rida Jbr, Phd student, where during the Short-Term Scientific Mission (funded by Cost Action) in the University of Vienna he studied possible ways of cellulose extraction from waste cotton. Briefly, clean and dried white clothes (100 % cotton) collected from the domestic sources were cut into 1 cm x 1 cm pieces and used as a precursor of microcrystalline cellulose (MC). The procedure and results were described in chapter 3.

Figure 6. Waste textiles.

2.1.1.2. Food waste precursor for sorbents preparation

The most widely used carbonaceous materials for the industrial processing of activated carbons are wood, coconut shells, and coal. Since most of these precursors are imported and highly expensive, it is crucial, especially for poor nations, to locate affordable and useful feedstock for the production of activated carbon for industrial application. In this work, coffee grounds (CG) and olive stones (OS) were chosen as sustainable precursors of porous carbons. Both selected precursors, are rich in cellulose, hemicellulose, and lignin [24], [25], which makes them another potential source for carbonous sorbents preparation. The procedure and characterization were described in chapter 4.

Figure 7. Coffee grounds and (b) olive stones.

2.1.1.3. Biomass ashes as alternative aggregates

Biomass ashes collected from Italian biomass-to-energy valorization plant, located in Rieti (Lazio), have been used an unconventional aggregate to prepare an Italian Patented (No.102017000033750) innovating finishing, 'malta multifunzionale'. The procedure, characterization and depolluting properties evaluated in the laboratory and pilot scales were described in chapter 6.

Biomass ash constitutes the waste from combustion processes, specifically wood chips or other types of wood waste, for the production of energy in power plants. They are a mixture of mineral elements and unburned organic components. The elements that typically make up ash are silica, calcium, potassium, phosphorus, manganese, iron, zinc, sodium and boron. These elements are not found in elementary form but in the form of oxides, silicates and nitrates. The ashes can be divided into bottom ash and fly ash based on their density and therefore their ability to accumulate at the bottom of the combustion chamber or to move away from it using the flow of combustion fumes. Fly ash consists of the particulate solid which is separated from the combustion fumes by means of electrostatic or mechanical filters, whereas bottom ash is made up of heavier particles deposited at the base of the furnace.
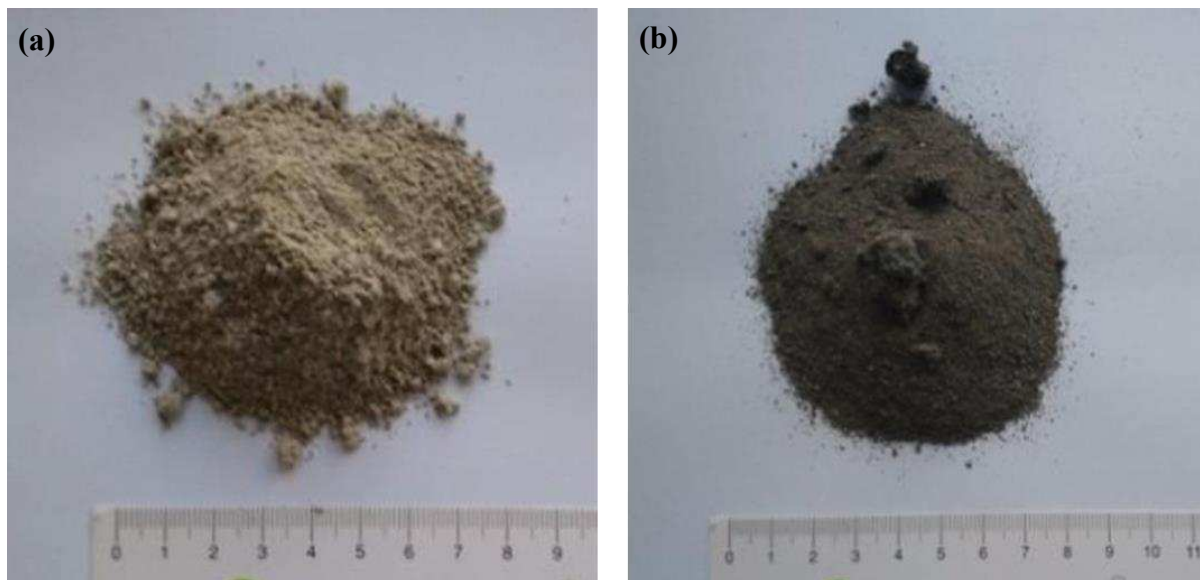

Figure 8. (a) fly and (b) bottom ashes.

2.1.2. Mechanical filters

Five different types of filters were characterized, and Particulate Filtration Efficiency has been compared (chapter 3). Commercially available filters were used as reference. In particular, glass fiber, polypropylene, surgical and FFP masks. Electrospun membranes were also fabricated.

2.1.2.1. Glass fiber

Glass microfiber filters without binder are used for difference weight analysis. They have a high thermal and chemical stability and are commonly used in determination of total suspended solids, or for gravimetric analysis of particles in air and hot fumes. It is a commonly used material used for HEPA filters, which can filter out particles as small as 0.3 microns.
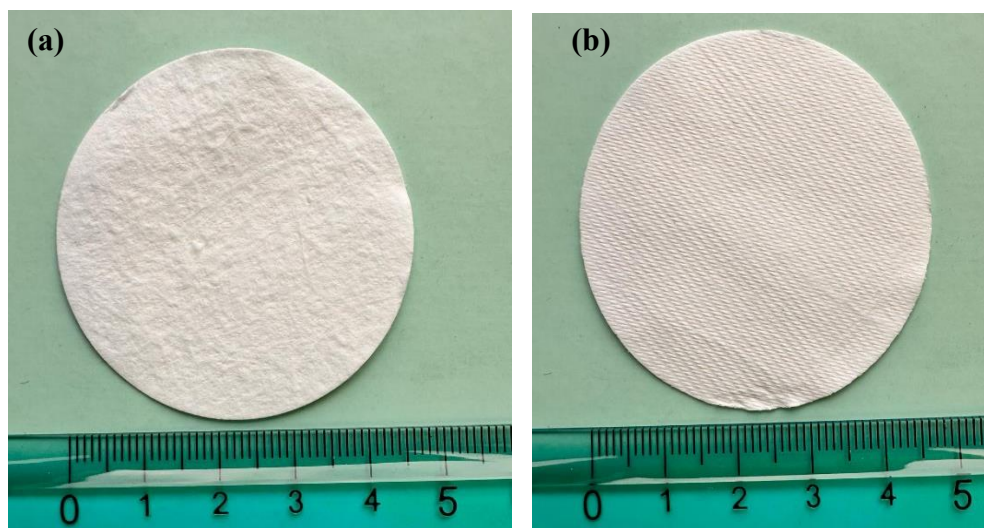

Figure 9. Glass fiber (a) front and (b) back side.

2.1.2.2. Polypropylene

Polymer based filters, most often polypropylene, are durable and reliable materials that can be used to make filters, which are often washable. It is commonly used material for the production of filtering masks.
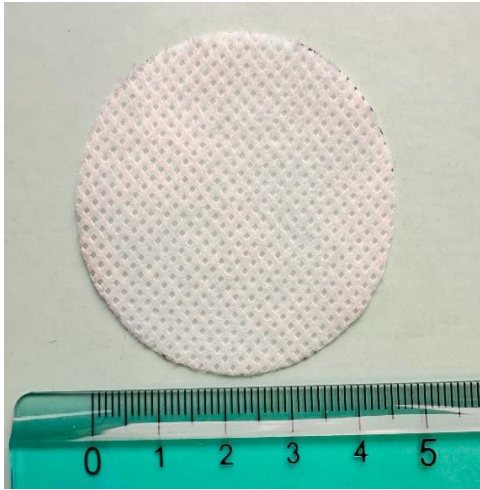
Figure 10. Polypropylene filter.

2.1.2.3. Surgical mask

Certified surgical masks are classified as personal protective equipment (PPE) used by healthcare professionals that serve as a mechanical barrier that interferes with direct airflow in and out of respiratory orifices (i.e. nose and mouth). They are tested and approved according to the European Standard EN 14683. The outward-facing side of the mask (usually spunbond non-woven polyester) is typically colored (usually blue, green, or yellow) and is fluid-repellent. The middle melt-blown polymer material (most commonly polypropylene) acts as the filter that stops microbes from penetrating and exiting the mask (highly efficiency layer). The inner spunbond layer of the mask (non-woven fabric e.g. cotton) captures and absorbs moisture, reducing the chance of any mucus or bacteria from leaving the mask when the wearer coughs or talks.

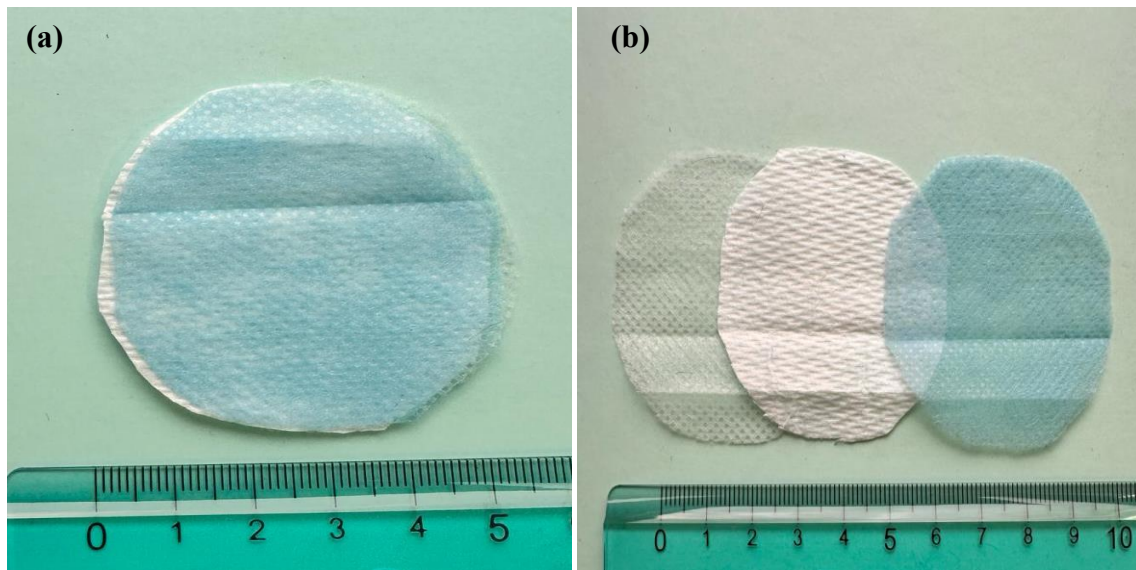*Figure 11. Surgical mask (a) overlapped layers and (b) 3-layers.*

2.1.2.4. Filtering Face Pieces

Filtering Face pieces (FFPs) are another type of PPE and protect against particulate pollutants such as dust, smoke and aerosols. They are available in the three protection levels FFP1, FFP2 and FFP3. The higher the number, the higher filtering efficiency against particles. In this thesis, FFP1 and FFP2 mask have been tested. Certified FFP masks meet requirements of the European Standard EN 149, or additionally EN 14683 (masks with exhalation wave).

The total leakage for the airborne particles with an aerodynamic diameter of 0.3 µm for an FFP1 mask is a maximum of 22%. At least 80% of contaminants are filtered out of the inhaled air. They are designed to protect the wearer from non-toxic dust particles and aerosols and are commonly used in industries. While, the total leakage of an FFP2 mask is a maximum of 8% and at least 94% of contaminants are filtered out of the inhaled air. FFP2 provides protection against solid (dust) and liquid (mist) particulates in concentrations up to 10 times the TLV.

The FFP1 and FFP2 masks consist of 3 layers made of synthetic fibers. The outer is the polypropylene material and inner layers are non-woven spun-bond fabric, and between them is melt-blown material. Nonwoven spun-bond fabrics are fibers that are bonded by chemical or physical treatment such as mechanical processing, heating, or using solvents. Polymeric materials such as polypropylene, polyethylene, and polyamides are commonly known as good raw materials for their production. Nonwoven melt-blown fabrics are porous materials that are

produced in a single process of polymer fiber spinning, air quenching/drawing, and web formation.
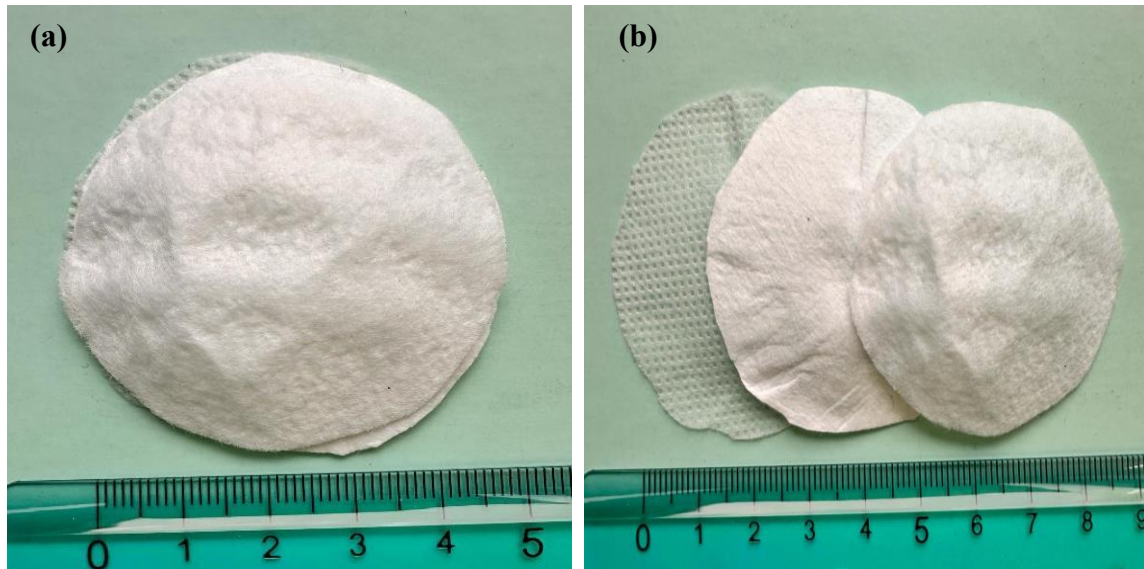
Figure 12. FFP1 mask.

2.1.2.5. Electrospun filters

Electrospun filters were prepared by dissolving biopolymers in organic solvents and produced by electrospinning technique.

The biopolymers used in this thesis are: Polylactic Acid (PLA), Cellulose Acetate (CA) and two types of Microcrystalline Cellulose (MC): commercial pure one (P-MC) and extracted from waste textiles (W-MC).

Produced electrospun filter were placed between 3D printed PLA support as shown in the figure below.

Figure 13. (a) electrospun PLA filter between 3D printed support and (b) 3D printed PLA support.

2.1.3. Adsorbents

Three different types of adsorbents were characterized and analyzed in terms of adsorption capacity (chapter 4). Biochar and activated carbon were produced from the food and the carbonization/activation experiments were conducted during Short Term Scientific stay (funded by Greenering Cost Action, CA18224) in the Dep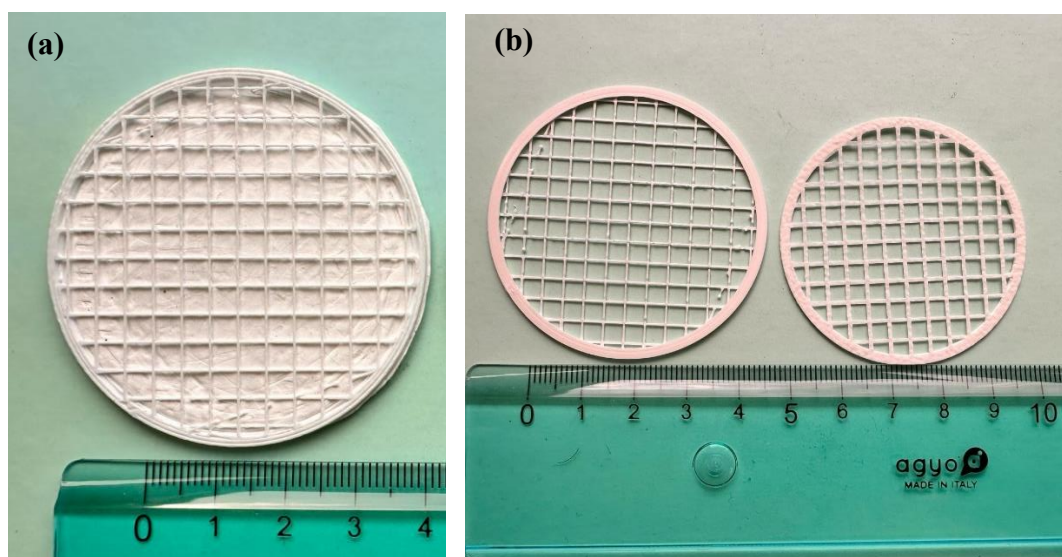artment of Chemistry, NOVA University of Lisbon in Portugal, under the supervision of Dr. Maria Bernardo. One type of commercial activated carbon was used for comparison.

2.1.3.1. Commercial activated carbon

Carbosorb PCF (COMELT S.p.A) is commercial activated carbon with particle size from 20 to 250 μm, produced via the physical activation of selected vegetable raw material. The main characteristics are reported in Table 4.

Table 4. General properties of Carbosorb PCF.

Specific surface area	Iodine number	Ash content	Bulk density	pH
1200 m^2/g	1000 mg/g	6%	400-500 kg/m^3	alkaline

2.1.3.2. Waste derived-activated carbon and biochar

The activated carbons were prepared from coffee grounds and olive stones via the chemical activation method, using potassium carbonate (K_2CO_3) as an activation agent, and through the physical activation method using CO_2 an as activation agent. Biochar was produced by pyrolysis of coffee grounds.
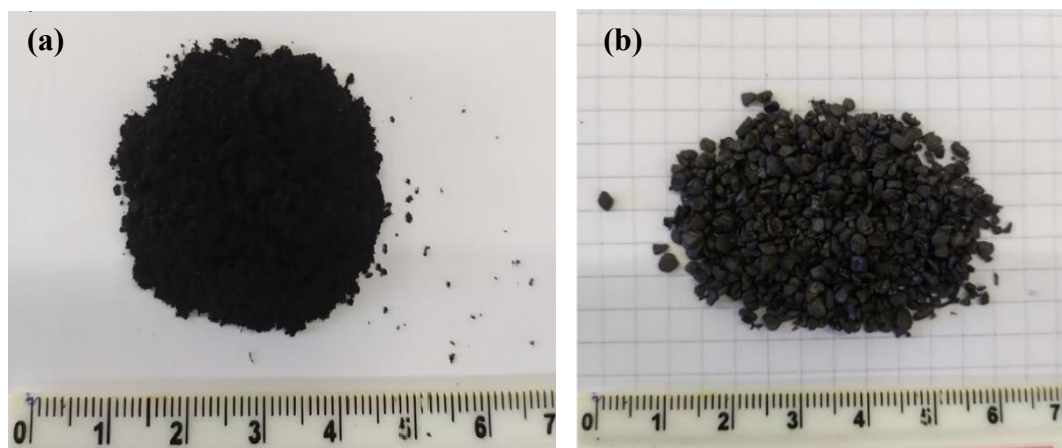

Figure 14. (a) coffee grounds-derived activated carbon and (b) olive stones-derived activated carbon.

2.1.4. Photocatalytic agents

Different commercially available and novel photocatalytic agents have been tested and compared in this thesis and are described in chapter 5.

2.1.4.1. Commercial Titanium Dioxide

Aroxide produced by Evonik® and KRONOClean 7404 by Kronos®.
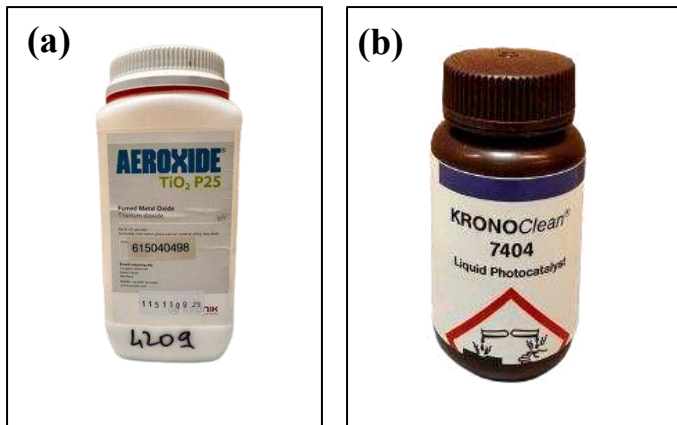
Figure 15. Commercial photocatalytic agents (a) P-25 Aeroxide by Evonik® and (b) KronoClean 7404 by KRONOS®.

2.1.4.2. Potassium vanadate

Potassium Vanadate (non-hydrated KV_3O_8) was synthesized by research group [26]-[27], from Faculty of Applied Physics and Mathematics, Institute of Nanotechnology and Materials Engineering, Gdańsk University of Technology in Poland, as described in previous study [28].

Figure 16. KVO sample.

2.1.5. Combined system

2.1.5.1. Commercial air purifying system

Portable air purifier system consisted of 5 types of filters: Pre-filter, HEPA, bipolar ionization device, photocatalytic TiO_2 filter, UVC lamp and activated carbon filter. It was tested in terms of particulate matter removal in a pilot-scale test room (section 6.3.).

Figure 17. Portable air purificator.

2.1.5.2. Commercial activated carbon filter

Liquifil 259, manufactured by Purification Products Limited, is the commercial activated carbon filter used as a reference (section 6.4). It is an air laid web material consisting of powdered activated carbon and cellulose wood pulp fibers, bound onto a cotton backing with a modified acrylonitrile copolymer latex. It is described as a strong, high carbon content filter for heavy duty or intense filtration applications.
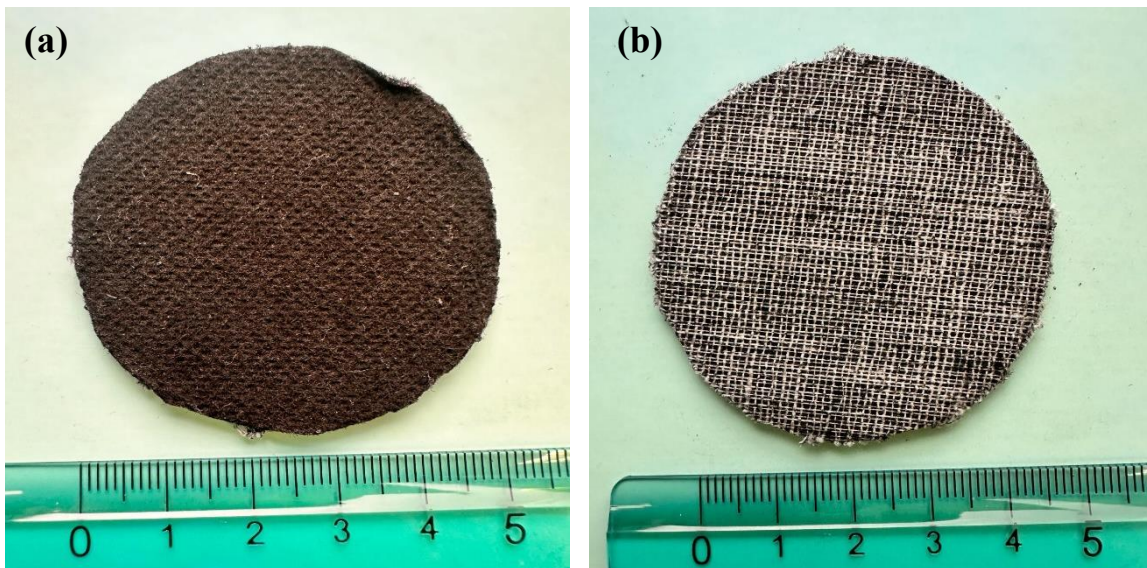

Figure 18. Commercial activated carbon filter (a) front and (b) back side.

The main characteristics are reported in Table 5.

Table 5. General properties of Liquifil 259 filter.

Basis weight	Thickness	Max Pore Size	Mean Pore Size	Carbon Content
1000 g/m^2	2.44 mm	42 µm	23 µm	50% (500 g/m^2)

2.1.5.3. Electrospun nanofiber composites

Some of the electrospun filters were selected, to be combined with the adsorbent and/or photocatalyst and the results are presented in section 6.4. Electrospun hybrid filters with activated carbon were produced by spraying two types of activated carbon: commercial (Carbosorb PCF) and the one derived from coffee grounds (AC-K$_2$CO$_3$-CG). Additionally, to enhance the removal process TiO$_2$ photocatalytic agent was sprayed over activated carbon layer creating second layer.
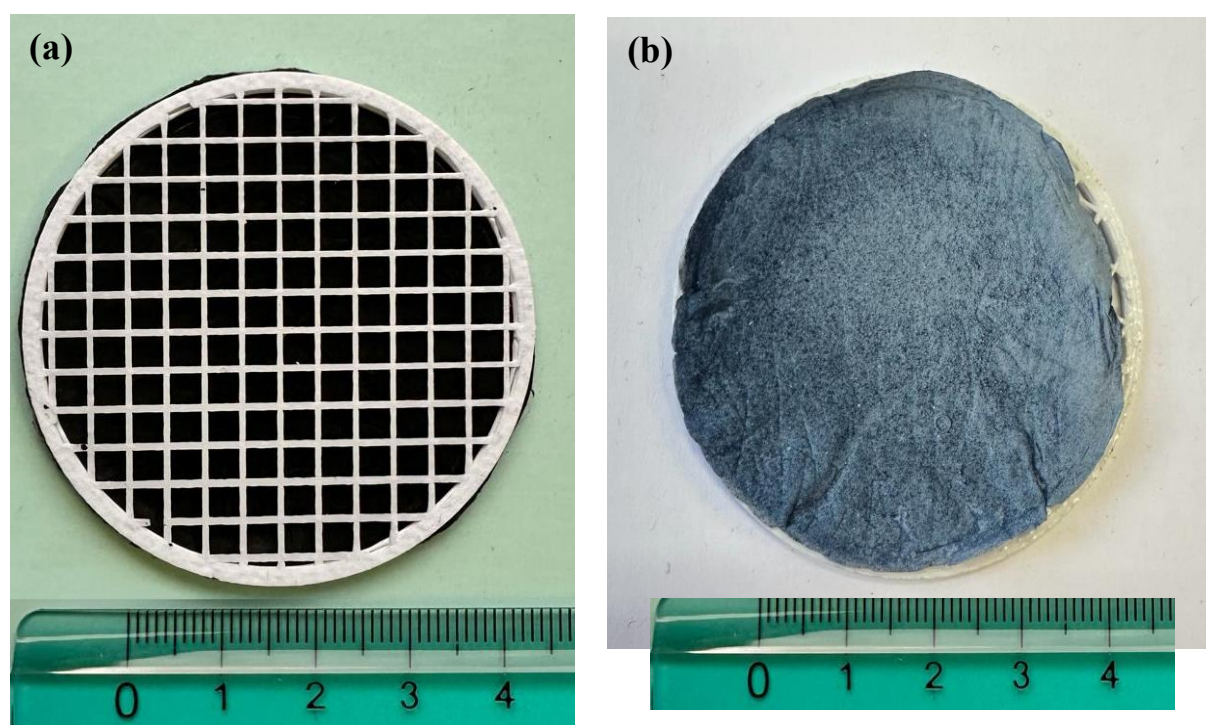

Figure 19. (a) electrospun PLA+AC filter and (b) electrospun PLA+AC+TiO2 filter.

2.1.5.4. Potassium vanadate and zeolite composites

As described in section 2.2.4.1 potassium vanadate samples are made up of vanadium oxide (V$_2$O$_5$) and potassium formate (CHOOK). Further characteristics and photocatalytic and adsorptive properties are presented in section 6.5.

52

Figure 20. Potassium vandate and zeolite composites.

2.1.5.5. Innovative finish

The innovative finish is an Italian Patented (No.102017000033750) containing lightweight unconventional aggregates not generally adopted for the preparation of mortar or finishes in the building sector and prepared with a commercial natural hydraulic lime (NHL) as a binder, which is named i.pro CALIX BLANCA NHL 3,5 (Heidelberg Materials – Italcementi), according to the standard UNI EN 459-1, with a declared density of 2700-3000 kg/m^3. Prepared innovative finish was analyzed in the lab and pilot scale in terms of depolluting properties and the results are presented in section 6.6.

2.2.   Material characterization

2.2.1. Morphology and elemental analysis

Morphological and elemental analysis were conducted via optical microscope (Keyence VHX-6000 digital light microscope) and scanning electron microscope (ZEISS SUPRA 40) equipped with an energy-dispersive X-ray spectroscope (Bruker Quantax 200-Z10).

Figure 21. Scanning Electron Microscope.

2.2.2. Thermogravimetric properties

To determine the thermal stability of the material, thermogravimetric (TGA/DTG) analysis was undertaken from 25 °C to 1000 °C under an inert atmosphere with a heating rate of 10 °C/min flow of N_2 using a TGA/SDTA851 (Mettler Toledo) instrument.

Figure 22. TGA/SDTA851 instrument.

2.2.3. Textural properties

Textural properties including the specific surface area (SSA) were determined using the Brunauer–Emmett–Teller (BET) equation, the total pore volume (V_{total}) was determined by the amount of N_2 adsorbed at $P/P_0 = 0.95$, the micropore volume (V_{micro}) was determined using the t-plot method, and the mesopore volume (V_{meso}) was determined by the difference between V_{total} and V_{micro} of the obtained samples; the above metrics were retrieved from the N_2

adsorption–desorption isotherms at -196 °C (77 K) using ASAP 2010 Micromeritics equipment. Before analysis, the samples were degassed for 2h at 200 °C.

Figure 23. Micromeritics equipment.

CO_2 adsorption–desorption isotherms (Anton Paar Quantachrome Instruments, Boynton Beach, FL, USA) were obtained to characterize the narrowest pores at 0 °C (273 K) using Automated Gas Sorption Data software. The surface area and pore size were evaluated according to the DFT model. Pore size distributions and the average pore diameter were obtained by applying the non-local density functional theory (NLDFT) and DFT methods to the N_2 and CO_2 adsorption data. Before analysis, the samples were degassed under a vacuum for 12 h at 150 °C. CO_2 adsorption–desorption isotherms within the relative pressure (P/P_0) range from 0–0.03 were collected to evaluate CO_2 uptake.

Figure 24. Anton Paar Quantachrome Instruments.

2.2.4. XRD phase identification

X-ray diffraction analysis was performed on the carbons to determine the degree of crystallinity or amorphousness of the samples. Measurements were performed using a Bruker AXS D8 Advance instrument at an angle of diffraction (2θ) between 10° and 60°, with the radiation source Cu-α having a wavelength λ = 1.5406 Å, an operating voltage of 40 kV (current of 40 mA), step = 0.02, and scan speed = 2 sec/step at room temperature.
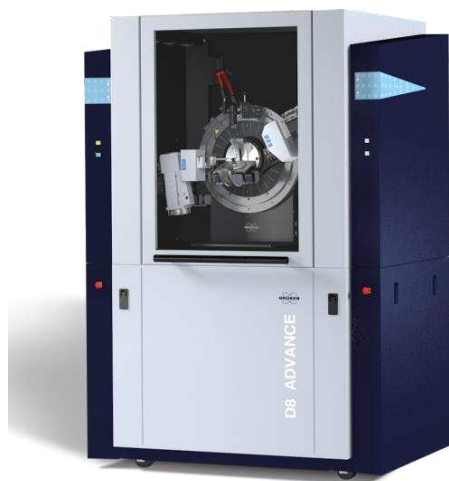

Figure 25. Bruker AXS D8 Advance instrument.

2.2.5. Proximate analysis

Ash, fixed carbon, and moisture content in the obtained samples were analyzed via thermogravimetric analysis, according to the ASTM *Standard Test Method for Compositional Analysis by Thermogravimetry* (E 1131-08), with slight modifications. The analysis was conducted on a Mettler Toledo TGA/SDTA 851 instrument, with a heating rate of 10 °C/min from room temperature to 900 °C under a N_2 atmosphere (20 mL/min). About 10 mg of the sample was heated from room temperature at 25 °C to 110 °C in nitrogen and held isothermally at 110 °C for 10 min, until complete dehydration was accomplished. The temperature was then raised to 900 °C and held isothermally for 10 min to determine the quantity of volatile matter. The atmosphere was then changed to be oxidizing to create the environment for combustion; this temperature was held for 30 min until the sample's weight remained unchanged. The weight lost during this period was due to the reaction of the fixed carbon with oxygen, and the remaining residue was ash.

2.2.6. Chemical structure

Fourier transform infrared (FTIR) spectroscopy was used to study the molecular structure of the materials in transmission mode using a Perkin Elmer FTIR spectrometer. The FTIR spectra were recorded between 4000 cm^{-1} and 450 cm^{-1}, with a spectral resolution of $4cm^{-1}$ and 32 scans.

Figure 26. Perkin Elmer FTIR spectrometer.

2.2.7. pH point of zero charge

The surface functional groups and pH point of zero charage (pHpzc) are important characteristics as they indicate the acidity/basicity of the material. It was determined according to the reverse mass titration method proposed by Noh and Schwarz [29]. Shortly, 0,1g of sample was mixed with 1ml of deionized water in different flasks. After that N_2 gas was inserted in case to keep the inert conditions. The solutions were stirred for 24h to reach equilibrium, and the final pH measured with a Crison pH 2001 m.

Chapter 3   Mechanical filters

Commercial polymers

CELLULOSE
ACETATE

POLYLACTIC ACID

Cellulose extraction

Electrospinning

Sustainable filtering media

Kitchen hoods

Air purifier

PPE
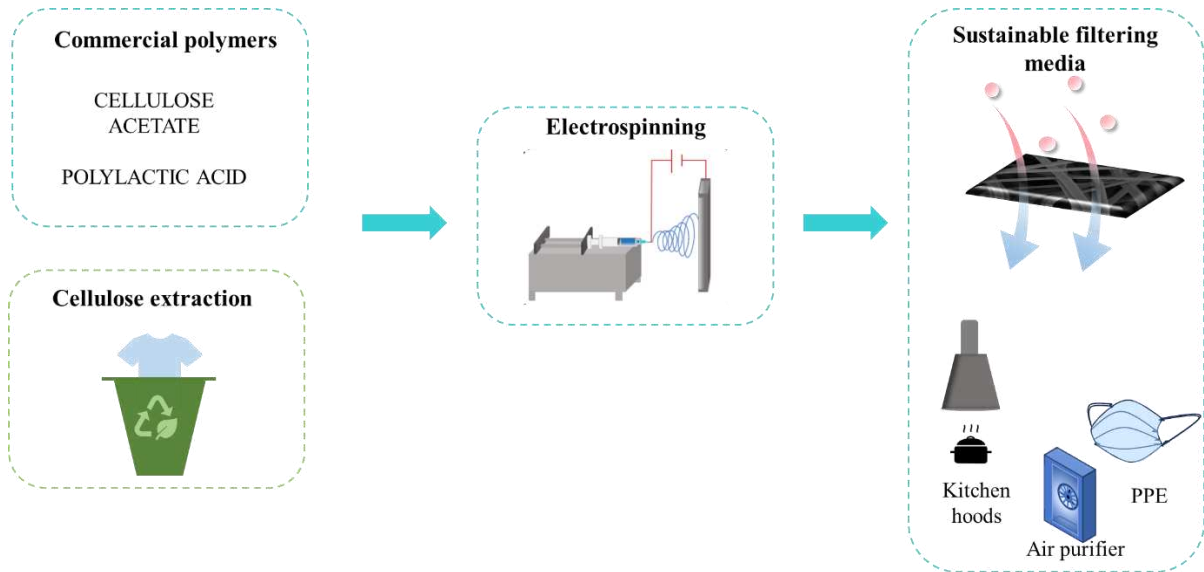
3.1. Background

Filters are systems commonly used in the retention of particles and are one of the strategies to improve indoor air quality. This chapter introduces issues related to mechanical filters. Among others, industrial techniques of filters manufacturing were also presented. For finer particles such as $PM_{2.5}$ (fine particulate matter) or smaller like PM_1, $PM_{0.5}$, $PM_{0.3}$, suitable air filter media are recommended, such as nanofibers, which have diameters on the nanometer scale. One of the techniques to produce nanofibers is electrospinning. In the following theoretical part, examples of biopolymers used in this part of the thesis are introduced.

3.2. Aims and objective

The goal of this work was to develop filters for PM capture utilizing polymers with less environmental impact and electrospinning technique. Different methods of filtration efficiency evaluation and different flow rates have been applied, depending on the potential application.

Firstly, part of the fabricated filters was evaluated as a sustainable personal protective equipment and compared with the traditional surgical and FFP masks.

In the subsequent experiments different formulation has been prepared and the influence of the commercial microcrystalline cellulose (MCC) addition (2.5 – 5 %) to the PLA matrix has been studied. To follow the European Standard EN 149:2001+A1:2009, the flow rate of 95 L/min has been applied.

Microcrystalline cellulose is well known for its potential use as a reinforcement for PLA materials [30], [31] and it can be derived from renewable and environmentally friendly resources. In the last section the development of waste-derived MCC and PLA composites has been evaluated. Both as a reinforcement agent (5%) and as a substitute of PLA (5-20 %) have been studied.

The fabrication parameters, fiber morphology, and filtration efficiency of fabricated filters were analyzed.

3.3. Fabrics

Woven fabric is a type of textile that is made by interlacing two or more sets of fibers at right angles to each other. It characterizes regular, repeating pattern of interlocking threads.

Knitted fabric is a textile that results from knitting, the process of inter-looping of yarns or inter-meshing of loops.

Nonwoven fabric is the other important category of fibrous materials. Nonwoven fabrics are made out of fibers without any restriction. They can be very short fibers of a few millimeters length, ordinary fibers as used in the traditional textile industry, or very long filaments. The fibers are bonded together through various methods, such as heat, chemicals, or pressure.

Figure 27. The structural differences between nonwoven and woven fabrics [22].

Nonwoven fabrics can be made from a variety of materials, including natural fibers like cotton and wool, as well as synthetic fibers like polypropylene and polyester. They are used in a wide range of applications, including disposable medical products like face masks and surgical gowns, wipes, filters, insulation, and more. Woven fabric is better suited for applications where strength, durability stretching, and customizability characteristics are relevant., e.g. clothing, home decor, medical textiles (bandages), filters, transportation (seat covers, carpeting, insulation) and others. Nonwoven fabrics instead, can be produced quickly and at a lower cost than traditional woven fabrics, as they require fewer manufacturing steps. Additionally, nonwoven fabrics can be designed to have specific properties, such as being water-resistant, flame-retardant, or breathable, depending on the intended use. Nonwoven fabrics are commonly used for disposable medical products (surgical masks), packaging, geotextiles, insulation and filters.

3.4. Industrial techniques of filters manufacturing

Primary methods of filtering manufacturing are described below.

3.4.1. Fibrillation

Filaments composed of a single component are longitudinally separated into finer fibers (fibrils) usually from 50 to 500 nm by means of high-pressure water streams, ultrasound or strong mechanical means.

3.4.2. Spun-bond

Spun-bond is one of the basic methods of nonwoven fabric manufacturing. A spinning jet forms fibers of 10–30 micrometers in diameter. The formed fibers either cool down on their own or get dried in the forming system. The latter technique improves mechanical qualities of the fibers — they extend in length and get thinner when subjected to powerful air flow.
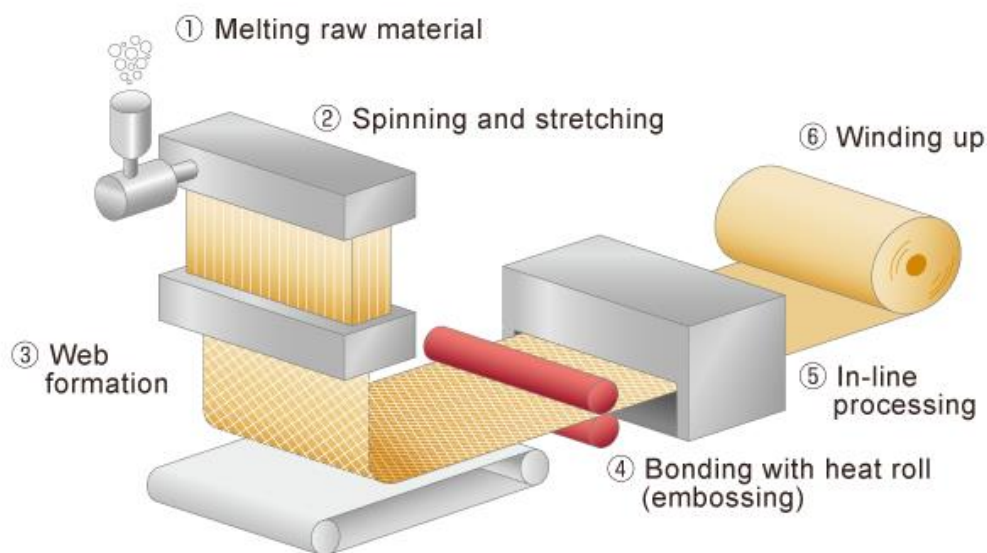

Figure 28. Spun-bond technique. (source: https://www.unitika.co.jp/nonwoven/e/about/manufacturing-process.html).

3.4.3. Melt-blowing

Melt-blowing is a unique, one-step process in which the melting of a polymer emerging from orifices is blown into super-fine fibers by hot, high-velocity air. A molten polymer is blown into ultrafine fibers and collected on a moving rotary drum or a forming belt with a vacuum underneath the surface. Conventional melt-blown process produces fibers with diameter from 5 to 10 µm with the shape of non-woven [32].
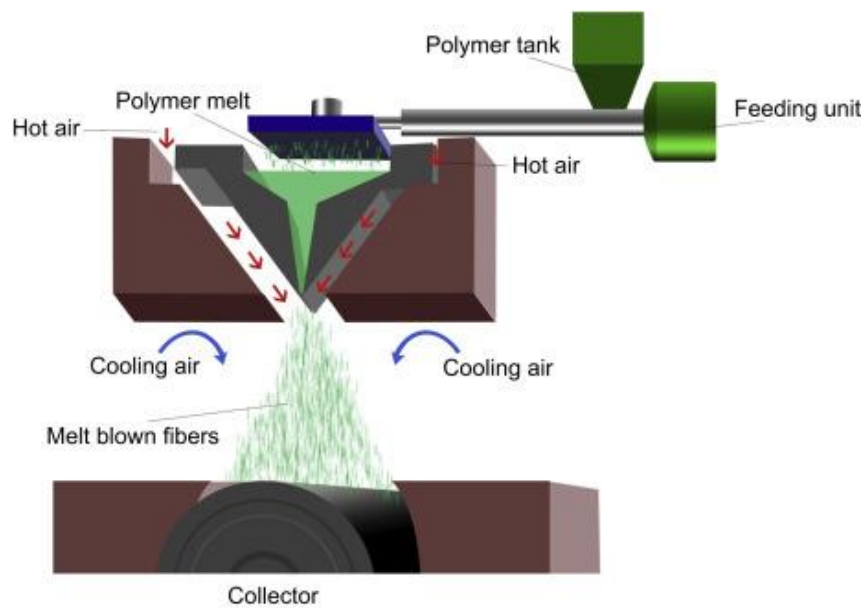

Figure 29. Melt-blowing process [24].

3.4.5. Wetlaid

Wetlaid materials find application for personal hygiene care, beauty care, medical care, household wipe cleaning or filters (HEPA). Wetlaid air filter media is made similarly to the process to make paper using glass fibers instead of cellulose fibers.
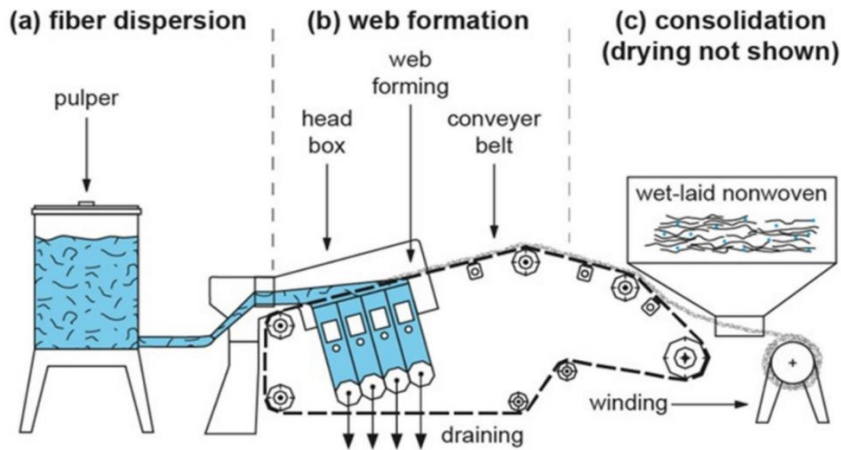
Figure 30. Wetlaid technique [25].

3.4.6. Electrospinning

Electrospinning technique uses an electrical charge to generate ultrathin (ranging from tens of nanometers to several micrometers) fibers from a liquid. Figure 31a shows the electrospinning set-up. The major components include a high-voltage power supply, a syringe pump, a spinneret (usually, a hypodermic needle with blunt tip), and a conductive collector. The power supply can be either direct current (DC) or alternating current (AC). When a sufficiently high voltage is applied to a liquid droplet, the body of the liquid becomes charged, and electrostatic repulsion counteracts the surface tension and a stream of liquid erupts from the surface, until it is finally deposited on the grounded collector. In general, the electrospinning process can be divided into four consecutive steps:

1. Charging of the liquid droplet and formation of Taylor cone or cone-shaped jet;
2. Extension of the charged jet along a straight line;
3. Thinning of the jet in the presence of an electric field and growth of electrical bending instability (also known as whipping instability);
4. Solidification and collection of the jet as solid fibers on a grounded collector.

The electrospinning process and morphology of the fibers can be controlled by different parameters which were presented in Table 6. For example, when sufficient viscosity of the solution is not achieved, electrospraying process occurs (Figure 31). During electrospinning, the jet can be kept in a continuous form to produce fibers instead of breaking into droplets (for the formation of particles) as with electrospraying [33].
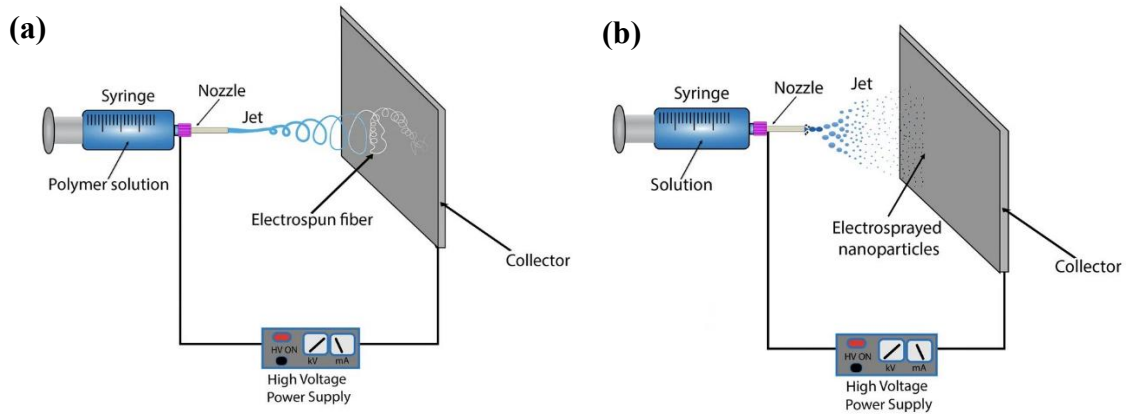
Figure 31. Schematic process of (a) electrospinning and (b) electrospraying. (source: https://3dprintingindustry.com/news/uk-researchers-create-low-cost-electrospray-and electrospinning-device-using-fdm-3d-printing-170897/).

Porous, hollow, helical, aligned, multilayer, core-shell, and multichannel fibers can be fabricated for different applications. Besides filtration media manufacturing, electrospun fiber membranes find extensive applications like tissue engineering, energy, biotechnology, sensors, and other sectors.

Table 6. Effect of electrospinning parameters on fiber morphology [27], [28], [29].

	Parameter	Effect on fiber morphology	
		Higher ↑	Lower ↓
Solution parameters	Molecular weight	↑ fiber diameter	electrospraying
	Concentration (viscosity)	↑ fiber diameter	↓ fiber diameter bead defect formation
	Conductivity	↓ fiber diameter bead defect formation unstable jet	↑ fiber diameter bead defect formation electrospraying
	Solvent volatility	fibers exhibit micro-texture (pores on the surface)	fused fibers
Operating conditions	Spinning distance	↓ fiber diameter unstable electric field	↑ fiber diameter
	Voltage	↑ fiber diameter bead defect formation electrospraying	spitting of polymer bead defect formation
	Flow rate	↑ fiber diameter ↑ porosity	↓ fiber diameter

		bead defect formation	needle obstruction due to premature solvent vaporization
Ambient conditions	Humidity	↓ fiber diameter ↑ porosity Instability of the jet	↑ fiber diameter
	Temperature	needle obstruction due to premature solvent vaporization	more uniform fiber diameter distribution

3.5. Filtration mechanism

The main filtration mechanisms in air and gas filtration include direct interception, inertial impaction, diffusional interception, electrostatic attraction, gravity and straining.

- *Interception* → the particles tend to follow the air currents, but secondary forces can be established with the filter such as van der Waals forces.

- *Inertial impact* → occurs when particles of larger dimensions and therefore with greater weight are unable to follow the trend of the air flow impacting on the obstacle, i.e. the filter, instead of passing around it unlike smaller particles.

- *Diffusion* → captures small particles that move according to Brownian motions or the disordered movements of these particles, which could consequently come into contact with the filter.

- *Electrostatic interaction* → if the particles and the filter have electric charges these will be attracted and blocked.

- *Gravity* → particles with larger diameters will be more affected by the force of gravity and could settle on the filter.

- *Straining* → occurs when a particle enters a filter whose pores are smaller than the diameter of the particle itself.
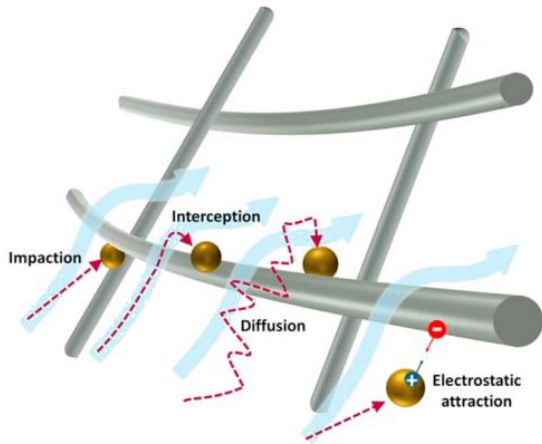
Figure 32. Common filtration mechanisms [30].

For particles with diameter below 100 nm, the dominant mechanism of capture is diffusion. Brownian motion, which is the chaotic movement of particles in still air, causes the aerosol to collide with the fibers of the filter material [34]. Particles with a diameter of 0.23–0.3 μm show the lowest efficiency to be captured by filter fibers, and they are described as the most penetrating particle size (MPPS) (Figure 33). The key role in capturing particles larger than 1 μm is attributed to inertial impaction and interception. Inertial impact changes the direction of the particles in the air stream. In this case, as the diameter and face velocity increase, the inertia increases; thus, the particles are easier to retain by the filter medium. On the other hand, the interception mechanism occurs when a particle is moving toward the air streamline and meets the surface of the fiber.
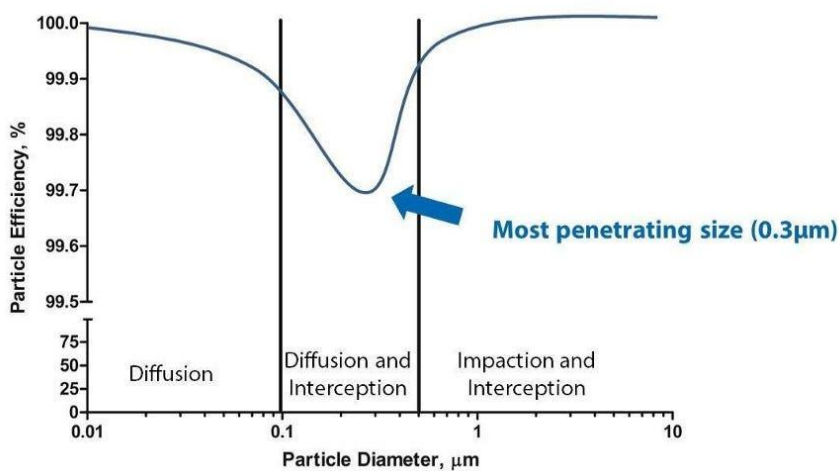

Figure 33. Most Penetrating Particles (source: https://medium.com/@climeclabs/an-overview-of-the-efficiency-of-a-fibrous-filter-hepa-against-particles-of-different-sizes-9305a38299f8).

Table 7. Comparison of filtration efficiency with studies in literature.

Material	Methods of fabrication	Characteristics	Source of PM	Flow rate	Efficiency	Ref.
Polypropylene	Melt-blown	Average diameter 2.9 μm, thickness 1.53 mm	NaCl (10 – 750 nm)	5 cm/s 10 cm/s 15 cm/s	97.52% 96.37% 93.81%	[34]
Polypropylene	Melt-blown		Incense	14.1 cm/s	$PM_{2.5}$ 82.1 % PM_{10} 96.1%	[35]
Glass fiber	/	Average diameter 0.5 μm, thickness 0.4 mm	NaCl	5 cm/s	≥ 99.95% (0.3 μm)	[36]
Glass fiber	Flame blowing	Average diameter (μm) G1 1.680 G2 1.157 G3 1.014 G4 0.913 G5 0.644	Dust disperser 0.97 – 176 μm	1.75–14 cm/s	For particles 4 μm G1 86,40 G2 96 G3 100 G4 100 G5 100	[37]
Glass fiber filter paper	Chopped glass fiber and glass microfiber were dispersed together to prepare the filter paper	Chopped glass fiber with uniform diameter of 6 μm and length of 6 mm, glass microfiber average diameter 2.6 μm and 1.0 μm	NaCl 2% (mean diameter 0.26 μm)	5.3 cm/s	/	[38]

3.6. Biopolymers

Polymers can be synthesized from a variety of sources. The raw materials used may originate from fossil fuels (non-renewable resources such as oil, natural gas, or coal), natural substances like cellulose or starch, or renewable resources (non-fossil, naturally occurring resources like biomass or organic waste). The last two types of polymers are classified as biopolymers, which are attractive materials, and they can replace petroleum based synthetic polymers for the fabrication of filtering media. Polymers derived from renewable resources (synthetic) are distinct from natural polymers as their synthesis is deliberately initiated by a chemical agent or microorganisms. Not depending on the source of the raw materials, certain biopolymers are biodegradable. This implies that, if they are appropriately collected and processed with organic waste, they can undergo organic recycling. However, it's important to

note that just because polymers are derived from renewable resources, it doesn't necessarily mean they are biodegradable.
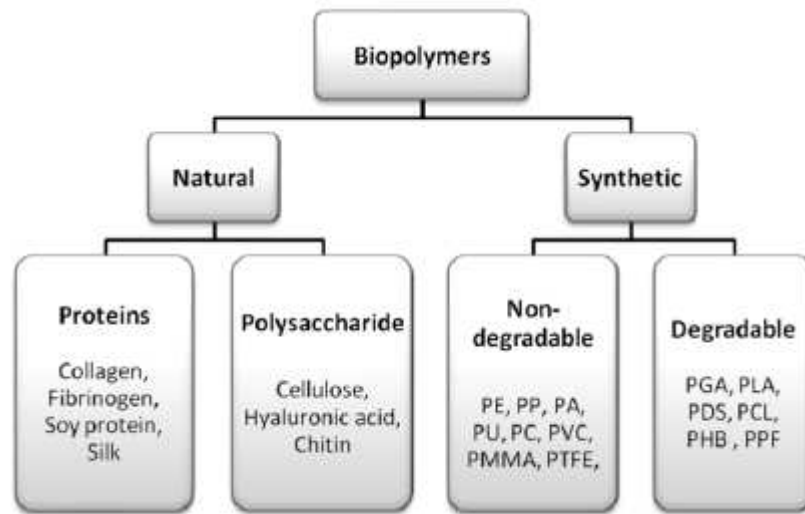

Figure 34. Classification of biopolymers.

In this thesis the following biopolymers were selected for the biodegradable filters' fabrication: cellulose (in form of microcrystalline), cellulose acetate, hydroxypropyl methyl cellulose and polylactic acid and are briefly described in the next subchapters.

3.6.1. Cellulose

Cellulose is the natural most abundant renewable polymer on earth [39], renewably obtained from cell walls of plants. It is a polydisperse linear polysaccharide consisting of β-1,4-glycosidic linked d-glucose.
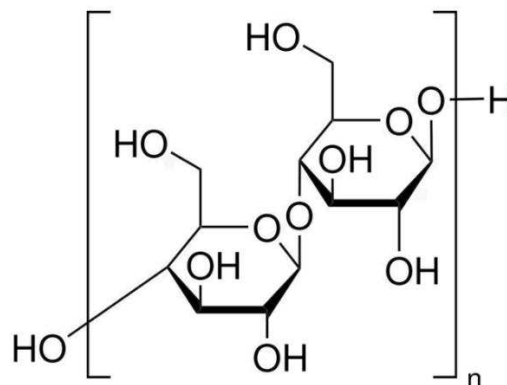

Figure 35. Cellulose chemical structure.

Owing to the unique characteristics, such as environmental sustainability, biocompatibility, low price, mechanical properties, and biodegradability, cellulose and its derivatives are receiving a lot of attention in several applications.

The main commercial sources of cellulose are wood (pines, eucalyptus, etc.) – used in paper production, while cotton is used in the manufacturing of textiles.

According to the type of treatment (chemical or mechanical) that cellulose sources are submitted to, cellulose microfibril can be classified in four types, corresponding to different microstructures features and properties such as microcrystalline cellulose (MCC) and nanocrystalline cellulose (NCC), nanofibrillated cellulose (NFC) and cellulose derivatives.
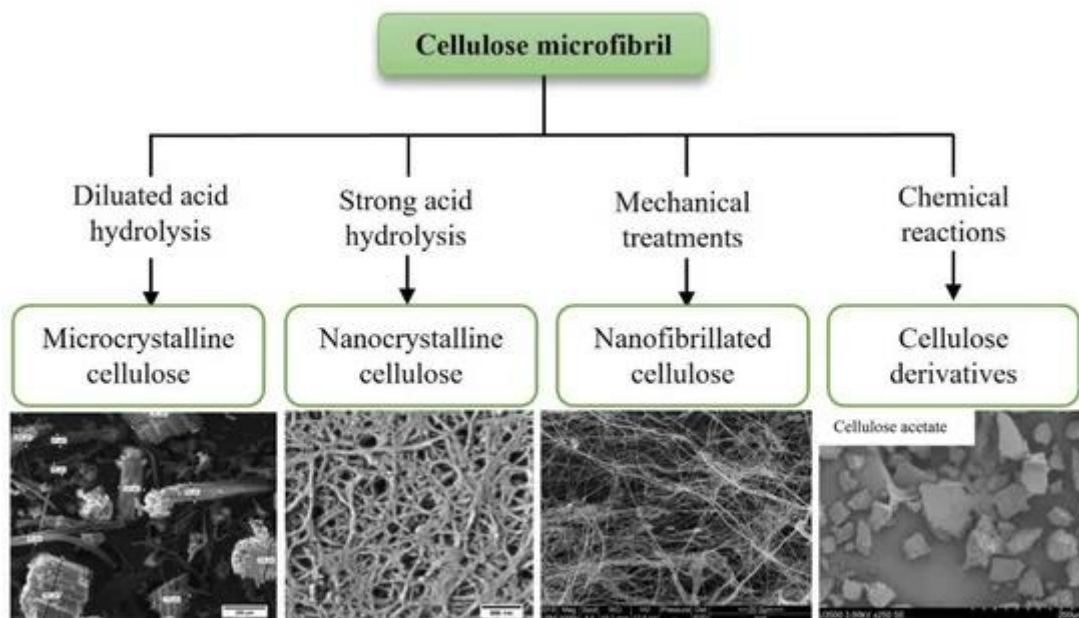

Figure 36. Examples of cellulose forms [37].

3.6.1.1. Cellulose fibrils

Cellulose fibers are made of microfibrils. Nanofibrillated cellulose consists of fibers with 20–100 nm in diameter and several micrometers in length [40].
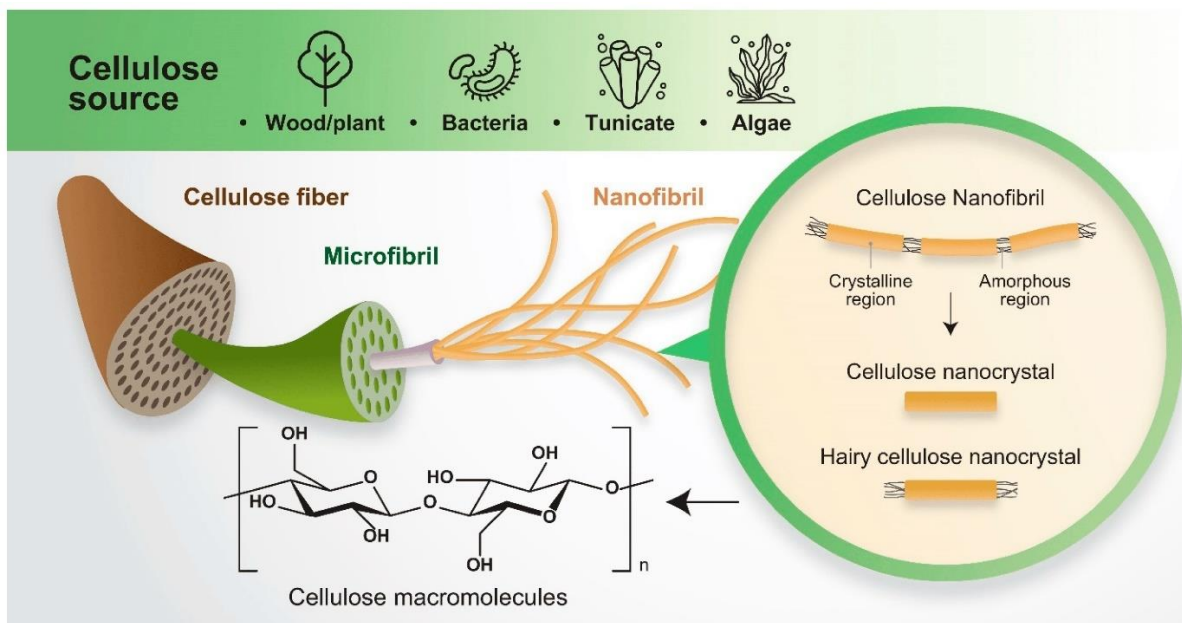
Figure 37. Schematic illustration of hierarchical structure of cellulose [38].

3.6.1.2. Microcrystalline and nanocrystalline cellulose

Microcrystalline cellulose and nanocrystalline cellulose are purified partially depolymerized non-fibrous forms of cellulose. Both of them are produced by purification and hydrolysis process. During the purification step, lignin is destroyed and removed in raw materials using alkaline treatment. This step aims to remove the lignin, which can inhibit acid penetration during the next step (hydrolysis). The hydrolysis process aims to remove the amorphous parts of cellulose giving short rod-like fibrils of high crystallinity [41]. Crystalline cellulose is most commonly extracted from cellulose fibers via acid hydrolysis, however, it can be also isolated by enzymatic hydrolysis.

Depending on the hydrolysis conditions like type of acid and concentration, crystalline cellulose can be obtained of micro- to nano- diameter. Nanocrystalline cellulose have a diameter smaller than 10 nm and lengths 100-500 nm, while microcrystalline cellulose has lengths from 50 to 200 µm [39].

The use of cellulose micro- and nanocrystals as reinforcement in composites has attracted attention due to the increasing interest in developing new sustainable and environmentally friendly materials.

In this thesis, microcrystalline cellulose was used in two ways: as a reinforcing material (adding in various concentrations to PLA) and as a filler (substituting PLA).

70

3.6.1.3. Cellulose derivates

The cellulose derivatives include various esters and ethers, such as cellulose acetate (CA), cellulose nitrate (CN), cellulose sulfate (CS), ethyl cellulose (EC), methylcellulose (MC), carboxymethyl cellulose (CMC), hydroxyethyl cellulose (HEC), hydroxypropyl cellulose (HPC), hydroxypropyl methylcellulose (HPMC), and others. Cellulose acetate and hydroxypropyl methylcellulose will be further discussed, as both of them were selected for electrospinning.
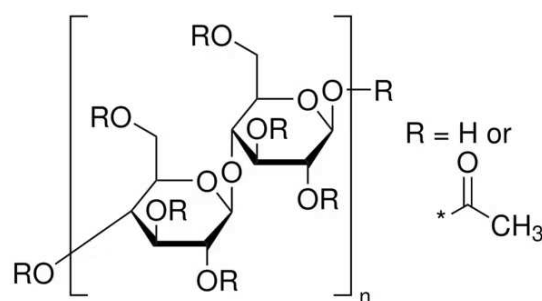
Cellulose acetate

Figure 38. Cellulose acetate chemical structure.

Cellulose acetate is a biodegradable, partially acetylated cellulose, in which the acetyl content ranges from 29.0% to 44.8%.

The commercial production starts from the activation of cellulose by aqueous acetic acid to ensure uniform acetylation. It is then dehydrated and reacted with acetic anhydride using a catalyst (e.g., sulfuric acid) in a solvent (e.g., anhydrous acetic acid).

The CA is considered one of the most important cellulose derivatives due to its broad application possibilities such as plastic films, textile fibers, filtration membranes, paints, cigarette filters, coats, dialyzes, drugs and biomedical utilities.

Hydroxypropyl methylcellulose

Hydroxypropyl methylcellulose is another common cellulose derivative that has been used in the food industry as thickening agent, emulsifier and stabilizer. It's also a potential film

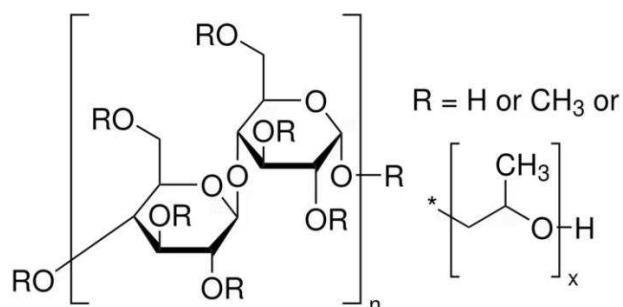forming material with low flavor and aroma properties, high solubility in water and good barrier properties.

Figure 39. Hydroxypropyl methyl cellulose chemical structure.

3.6.2. Polylactic acid

Polylactic acid is a biodegradable a recyclable aliphatic polyester produced from renewable feedstock. The monomer, lactic acid (LA), is obtained from bacterial fermentation of polysaccharides extracted from corn, sugarcane, potatoes, and other agricultural sources. Due to its eco-friendly properties, PLA has a proven potential to replace conventional petrochemical-based polymers for widespread applications.
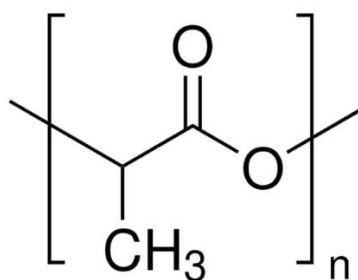

Figure 40. Polylactic acid chemical structure.

In recent years, this biopolymer has been used in various sectors due to its characteristics such as mechanical resistance, biocompatibility and ease of processing. Among the sectors we find the medical/biomedical industry, packaging production, pharmaceutical, and textile industries.
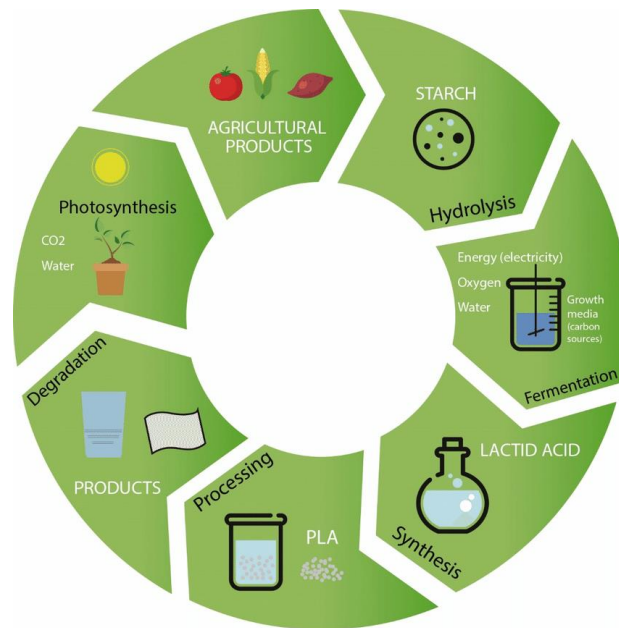
Figure 41. Schematic diagram of polylactic acid synthesis [40].

Because PLA in a thermoplastic, and it becomes a liquid at melting point from 150 to 160 °C, it may be processed using common techniques to create fibers, films, and sheets, including extrusion, injection molding, film blowing, thermoforming.

Although, despite number advantages, PLA characterize also some imperfections that limit its use in certain applications, mainly: 1) poor toughness - PLA is a very brittle material with less than 10% elongation at break, and 2) slow degradation rate - PLA degrades through the hydrolysis of backbone ester groups and the degradation rate depends on the PLA crystallinity, molecular weight and its distribution, morphology, water diffusion rate into the polymer, and the stereoisomeric content [42]. The degradation rate is often considered to be an important selection criterion for biomedical applications, 3) low melting point.

One strategy to improve PLA mechanical properties is the addition of reinforcements like microcrystalline cellulose.

3.3. Materials and methods

3.3.1. Materials

Biopolymers used in this experiment to produce electrospun fibers are listed below:

- Polylactic acid PLA (Total Corbion Luminy LX930)

- Cellulose acetate CA (Codex)

- Hydroxypropyl methylcellulose HPMC (Sigma Aldrich)

- Microcrystalline cellulose: commercial pure one P-MCC (Merc Millipore, microcrystalline cellulose for gas chromatography) and recovered from waste textiles W-MCC

Acetone (Sigma Aldrich, ≥99.5%) and ethanol (Sigma Aldrich, ≥99.8%) were used to dissolve the polymers. Produced filters were tested and compared to the selected reference filters: polypropylene, surgical mask, FFP1 and FFP2 mask and glass fiber.

All the filters (fabricated and traditional ones) and textile waste precursor were briefly described and presented previously in chapter 2.2.

3.3.2. Recovery of cellulose from waste textiles

Microcrystalline cellulose was isolated from textile wastes via controlled acid hydrolysis. The recovery procedure is briefly described. 5g of cotton waste were chemically treated by mixing with 200ml of 20% H_2SO_4 for 5h at 80 °C. After chemical treatment, the reaction mass was centrifuged (10 min, at 3500 rpm min^{-1}) to remove supernatant. The sediment was neutralized under magnetic stirring using a sodium hydroxide solution. The mass was then filled up to its original volume and second centrifugation was provided. The samples were frozen at approximately -27 °C and lyophilized. Obtained cellulose powder (W-MCC) was then sieved (Retsch vibration screening machine) to obtain faction of particles < 100 μm.

3.3.3. Fabrication of electrospun bio-based filters

Bio-based filters were produced by electrospinning technique. The preparation procedure involves the addition of the solvent to the polymer, followed by stirring until a homogeneous solution was obtained. The solution was subsequently loaded in a syringe and mounted in the electrospinning instrument (Spinbox ®, Bioinicia)

Four different formulations are proposed:

a) *Polylactic acid (PLA)*
b) *Cellulose acetate (CA)*

c) *Polylactic acid + Pure microcrystalline cellulose (PLA:P-MCC)* – preliminary investigations regarding addition of MCC to the electrospinning solution have been done using P-MCC. In the first set of experiments, cellulose was added from 2.5% to 5 wt% (based on 13% PLA weight). The solutions were prepared by first dispersing P-MCC in acetone and followed by adding measured PLA pellets.

d) *Polylactic acid + Waste-derived microcrystalline cellulose (PLA:W-MCC)* - the solutions were prepared as previously described with the addition of W-MCC in 2.5% and 5%. Moreover, substitution in 5 – 20 % was studied, while constant total polymer concentration was kept at 13% w/w.

Considering the stability of the process while applying 13% w/w PLA solution in acetone, this concentration was considered as a reference for the preparation of PLA-MCC composites and employed for the trials with the both P-MCC and W-MCC as additive and substitute polymers.

A list of fabricated electrospun filters and the electrospinning conditions are shown in table X.

Samples have been labelled as (X) Y% Z:Z (R:R) where:

X = single (S) made up from 10ml or (D) double layer made up from 20ml of polymer or (I) which have been distinguished as they were fabricated using less than 10ml of polymer.

Y = total concentration of the polymer in the solution

Z = short name of the polymer/s

(R:R) = the ratio between two polymers

Table 8. List of parameters applied for electrospinning.

Total conc.	Solv.	V	T	RH	Flux	Dist.	Needle Ø	ml	Type of collector	Sample label
(w/w)		(kV)	(ºC)	(%)	(mL/min)	(cm)	(mm)			

Polylactic acid

Total conc.	Solv.	V	T	RH	Flux	Dist.	Needle Ø	ml	Type of collector	Sample label
10%	Acetone	20	20	45	0.07	10		20	Horizontal	(D) 10% PLA
12%	Acetone	20	20	39	0.07	10		20	Horizontal	(D) 12% PLA
13%	Acetone	20	22	29-38	0.07	10	0.91	9	Horizontal	(I) 13% PLA
14 %	Acetone	20	20	41	0.08	10		10	Rotary	(S) 14% PLA (D) 14% PLA*

Cellulose acetate

Total conc.	Solv.	V	T	RH	Flux	Dist.	Needle Ø	ml	Type of collector	Sample label
14%	Acetone	15	19-21	52-56	1	9	1.6	9	Horizontal	(I) 12.5% CA and (II) 12.5% CA*

Hydroxypropyl methylcellulose

Total conc.	Solv.	V	T	RH	Flux	Dist.	Needle Ø	ml	Type of collector	Sample label
5%	Ethanol	18	25	56	0.016	15		2	Horizontal	5% HPMC1
5%	Ethanol	18	27	57	0.09	10		4.8	Horizontal	5% HPMC2
5%	Ethanol	13	27	57	0.09	10		4.8	Horizontal	5% HPMC3

Polylactic acid + Pure microcrystalline cellulose

Total conc.	Solv.	V	T	RH	Flux	Dist.	Needle Ø	ml	Type of collector	Sample label
13.3% (13% PLA 0.3% P-MCC)	Acetone	20	19	48	0.07	10	0.72	8	Horizontal	(I) 13% PLA:P-MCC (100:2.5)
13.5% (13% PLA 0.5% P-MCC)	Acetone	20	21	30	0.07	10	0.72	5	Horizontal	(I) 13.5% PLA:P-MCC (100:5)
13.5% (13% PLA 0.5% P-MCC)	Acetone	20	26	56	0.07	10	0.72	10	Horizontal	(S) 13.5% PLA:P-MCC (100:5)

Polylactic acid + Waste-derived microcrystalline cellulose

Total conc.	Solv.	V	T	RH	Flux	Dist.	Needle Ø	ml	Type of collector	Sample label
13.5% (13% PLA 0.5% W-MCC)	Acetone	20	24	47	0.07	10		10	Horizontal	(S) 13.5% PLA+W-MCC (100:5)
13.5% (13% PLA 0.5% W-MCC)	Acetone	20	21	50	0.07	10		20	Horizontal	(D) 13.5% PLA+W-MCC (100:5)
13%	Acetone	20	23	51	0.07	10		20	Horizontal	(D) 13% PLA+W-MCC (95:5)

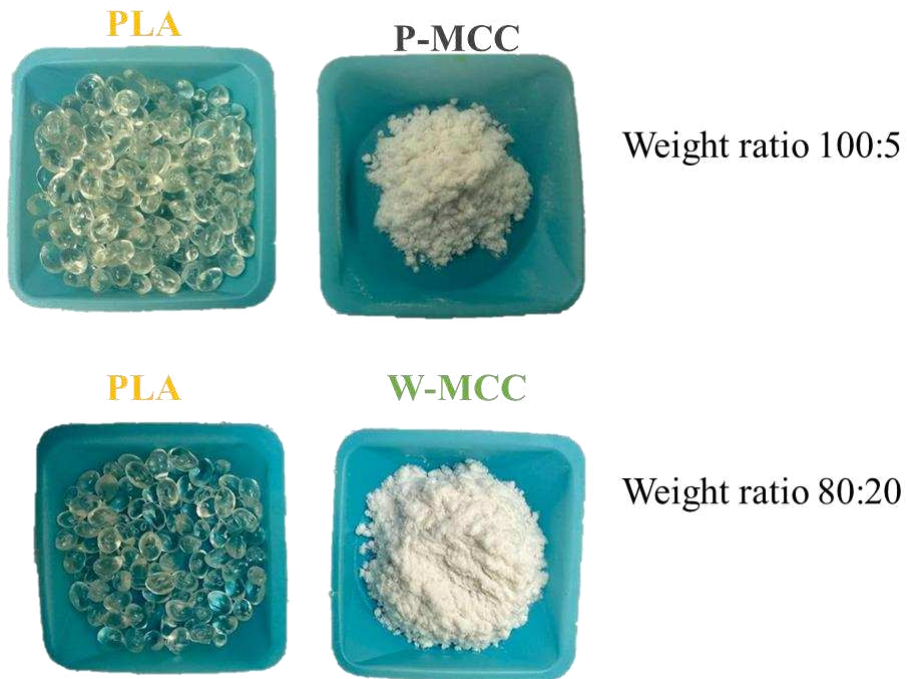| (12% PLA 1% W-MCC)										
13% (10% PLA 3% W-MCC)	Acetone	20	21	45	0.07	10		20	Horizontal	(D) 13% PLA+W-MCC (80:20)

*sample made by overlapping two single (S) layers

Figure 42. PLA and P-MCC and W-MCC in different weight combinations.

Figure 43. Solution of 13% PLA:W-MCC (100:5) prepared for electrospinning.

3.3.3. Characterization

Morphology of recovered cellulose fractions and pure microcrystalline cellulose (P-MCC) were characterized by optical and SEM analysis. FTIR spectroscopy was provided to analyze the chemical structure of the waste-derived MCC, and it has been compared to the P-MCC.

To study the morphology of the electrospun and commercial filters SEM analysis was provided. The average diameters and the diameter distribution were calculated using ImageJ based on at least 20 random diameter measurements from the corresponding SEM images. Scanning electron microscope and elemental composition (SEM+EDX) analysis was also provided to support the filtration tests (trapped particles by the filtering media). Some of the commercial filters were observed under optical microscope, for the preliminary analysis.

Detailed methods of characterization were described previously in section 2.3.

3.3.2. Particulate filtration efficiency test

To test the Particle Filtration Efficiency of the filters lab-build system has been designed and assembled (Figure 44). It consists of PVC pipe in which the filter can be placed using a 3D printed PLA based filter support with a 5.3 cm diameter; the air is drawn out of 15 m^3 of the room with a pumping system connected to the tube. The flow rate was adjusted by variable transformer, and air velocity was measured by rotating aerometer (Testo 417). The humidifier (Medisana) with a 2-3% w/V NaCl solution was placed inside the room, and it disperses tiny droplets of the solution in the air (aerosolization); as the water evaporates it leaves the NaCl particles suspended, actually generating PM in the air. For sampling of indoor conditions, at a height of 1.05 m from the ground, a circular hole with a diameter of 5 cm was provided, into which a cylindrical tube of the same diameter was inserted. The moisture was removed during the test using a commercial sorbent. The pressure drop between the filter was measured by differential manometer (Trotec TA400 or MPXV7002DP (NXP Semiconductors, Eindhoven, Netherlands). Concentration of the PM after the filter was measured following initially *procedure 1*, and in subsequent tests *procedure 2*, which are described below.
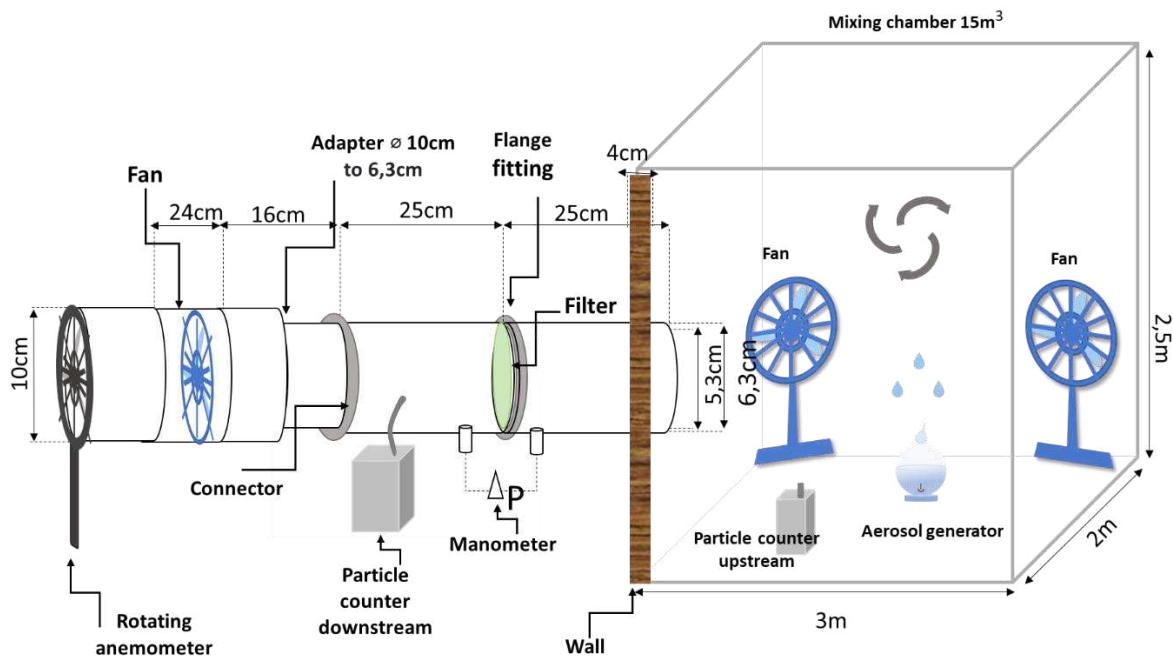

Figure 44. Schematic diagram of testing room (not to scale).

Procedure 1 – shown schematically on Figure 45. The test started when the initial conditions (PM concentration below 100 µg/m³) measured by portable aerosol spectrometer (OPC, GRIMM Aerosol Technik GmbH, model 1.108, Ainring, Germany) within the diameter range of 0.23 µm to 20 µm, were ensured. Once the aforementioned concentration has been reached, humidifier has been turned on and aerosol generation continued till concentration of PM reached around 25000 µg/m³. After that humidifier was turned off. When the concentration dropped to 20 000 µg/m³ the filter with the support has been inserted in the tube and the test has been carried out for 7 min. After that the filter was removed and the concentration has been measured for another 5 min.
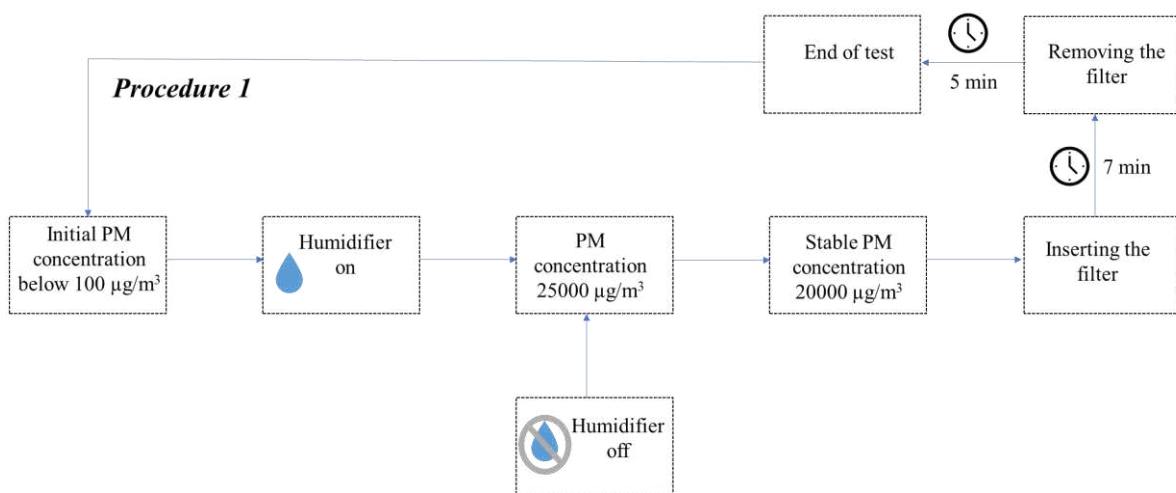

Figure 45. Schematic flow diagram of filtration efficiency test (procedure 1).

Procedure 2 – two particles counters (Trotect BQ21) were used to measure the PM concentration before the filter (upstream concentration) and after the filter (downstream concentration). The device has two channels, which are designed to measure particles of sizes 2.5 µm and 10 µm, respectively; these sizes correspond to the internationally recognized categories of fine particulate matter, $PM_{2.5}$ and $PM_{10.}$
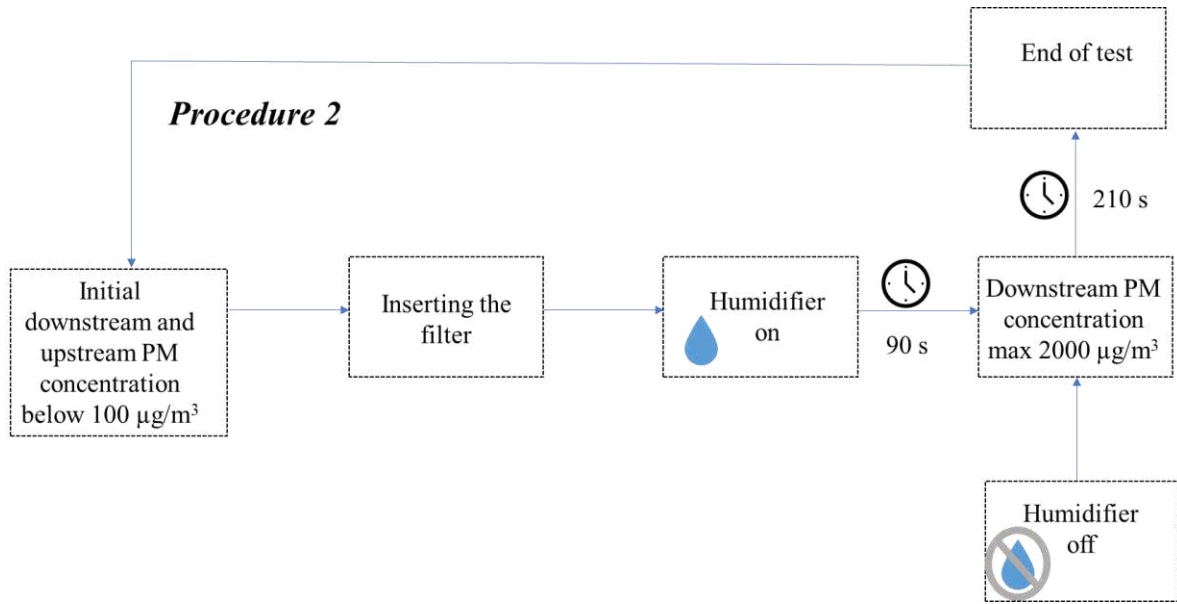
Figure 46. Schematic flow diagram of filtration efficiency test (procedure 2).

The filtration efficiency (η) was evaluated as follows:

$$\eta = 1 - \frac{Cdownstream}{Cupstream} \; x \; 100 \tag{1}$$

Where $C_{downstream}$ is the average concentration of NaCl aerosol after filtration, and $C_{upstream}$ is the average concentration of NaCl aerosol before filtration.

Therefore, the quality factor for each PM removal efficiency was provided to compare the different filtering media. Eq. (2) defines the quality factor (QF):

$$QF = \frac{-ln\,(1 - \eta)}{\Delta P} \tag{2}$$

Where η is the filtration efficiency, and ΔP is the pressure drop.

Filters were divided into three series depending on the potential application. I and II series were tested in terms of filtration efficiency by applying procedure 1. The difference between both series was the flow rate.

To carry out the tests for the samples from the series II, the European standard EN 149:2001+A1:2009 was consulted. The solution to be used to reproduce the particulate involves the use of NaCl, the air flow sucked in by the fan must be equal to 95 L/min and following the test the acceptable pressure drop range is between 210 and 300 Pa as shown in Table 9.

Table 9. Extract from EN 149:2001+A1:2009 regulation, which reports the maximum penetration of aerosol and breathing resistance values for the three categories of masks.

Mask classification	FFP1	FFP2	FFP3
Maximum penetration of aerosol (sodium chloride test, 95 L/min)	20%	6%	1%
Maximum permitted resistance (at inhalation flow rate 95 L/min)	210 Pa	240 Pa	300 Pa

For the series III, the second procedure was followed where the higher flow rate was applied (200 L/min) for the potential applications in purifying devices. Two particle counters were applied to measure the concentration downstream and upstream.

3.3. Results and discussion

All the solutions, apart from HPMC were successfully electrospun and further characterized in terms of filtration efficiency. In order to distinguish the specimens, all the filters (traditional ones and the fabricated ones) have been color-coded and listed in Table 10.

For HMPC using as prepared solution and with the electrospinning parameters applied as shown in Table 8, the problems with fibers formation appeared and the deposition of the polymer on the aluminum foil was very inhomogeneous and scattered, probably due to the emerging process of electrospraying, instead of electrospinning. Further attempts to optimize the parameters were abandoned and focus was placed on the remaining polymers.

Table 10. List of filters tested.

Filter		ID	Procedure and flow rate applied	Series number
Traditional filtering media	Polypropylene		Procedure II 95 L/min	II
	Surgical mask		Procedure I and II 120 L/min and 95 L/min	I
	FFP1		Procedure II 95 L/min	II
	FFP2		Procedure I 120 L/min	I
	Glass fiber		Procedure III 200 L/min	III
Novel fabricated filtering media	(D) 10% PLA		Procedure III 200 L/min	III
	(D) 12% PLA		Procedure III 200 L/min	III
	(I) 13% PLA		Procedure II 95 L/min	II
	(S) 14% PLA		Procedure I 120 L/min	I
	(D) 14% PLA		Procedure I 120 L/min	I
	(I) 14% CA		Procedure II 95 L/min	II
	(II) 14% CA		Procedure II 95 L/min	II
	(I) 13% PLA:P-MCC (100:2.5)		Procedure II 95 L/min	II
	(I) 13.5% PLA:P-MCC (100:5)		Procedure II 95 L/min	II

(III) Sandwich*		Procedure II 95 L/min	II
(S) 13.5% PLA:W-MCC (100:5)		Procedure III 200 L/min	III
(D) 13.5% PLA:W-MCC (100:5)		Procedure III 200 L/min	III
(D) 13% PLA:W-MCC (95:5)		Procedure III 200 L/min	III
(D) 13% PLA:W-MCC (80:20)		Procedure III 200 L/min	III

*multi-layer filter made by overlapping two (I) 14% CA and the middle of (I) 13.5% PLA:P-MCC (100:5)

3.3.1. Microcrystalline cellulose characterization

Morphology

Optical microscopy (Figure 47) was used for the preliminary experiments. SEM analysis of W-MCC was done to further characterize the morphology of the particles and compared with the P-MCC (Figure 48). Both MCCs characterize rod-like structure. P-MCC characterize particle length from 37 to 157 µm, and W-MCC ranged from 3.8 µm to 162 µm. Additionally, particle size distribution has been performed for W-MCC and the results showed the median particle size of 33.8 µm (Figure 49).
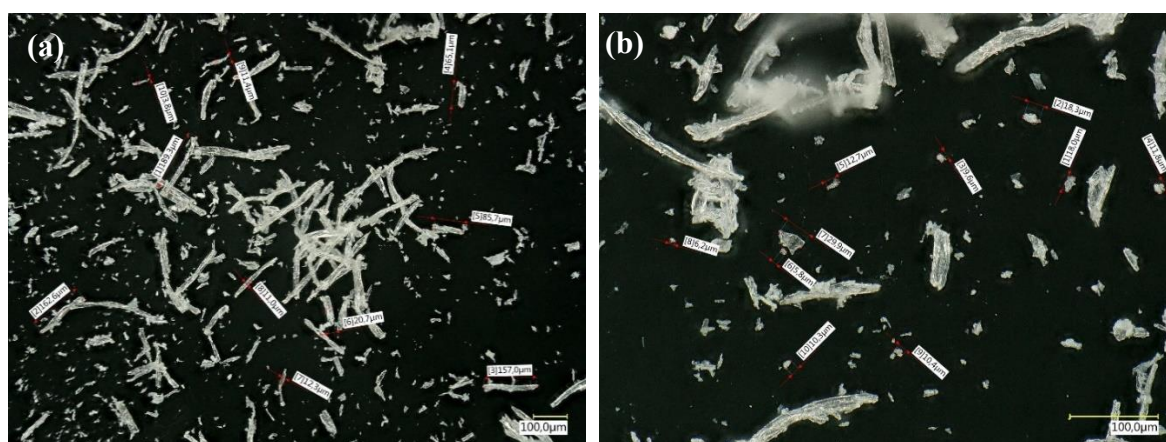
Figure 47. Optical Microscope Images of the W-MCC, (a) 200x and (b) 500x magnification.
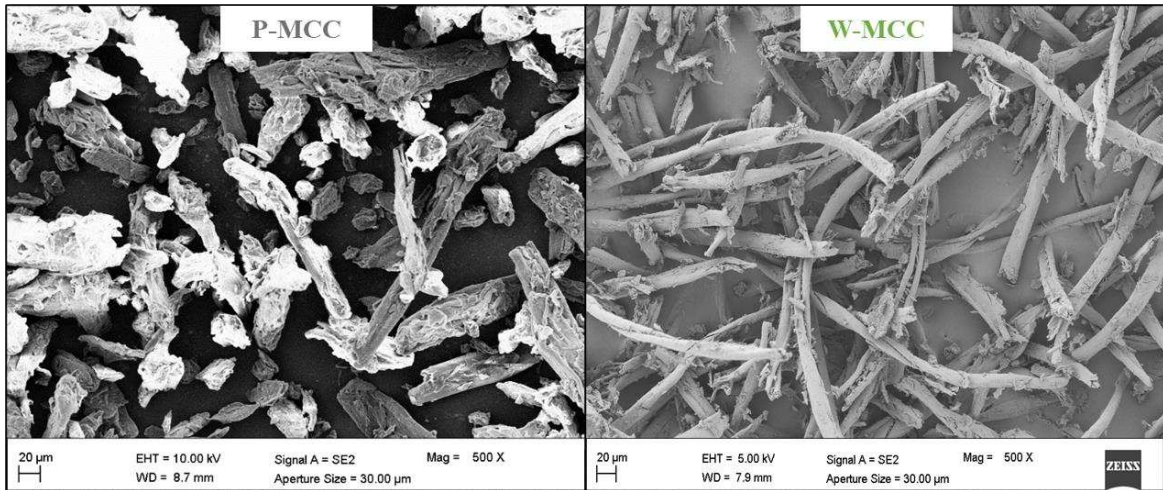
Figure 48. SEM images of P-MCC and W-MCC.
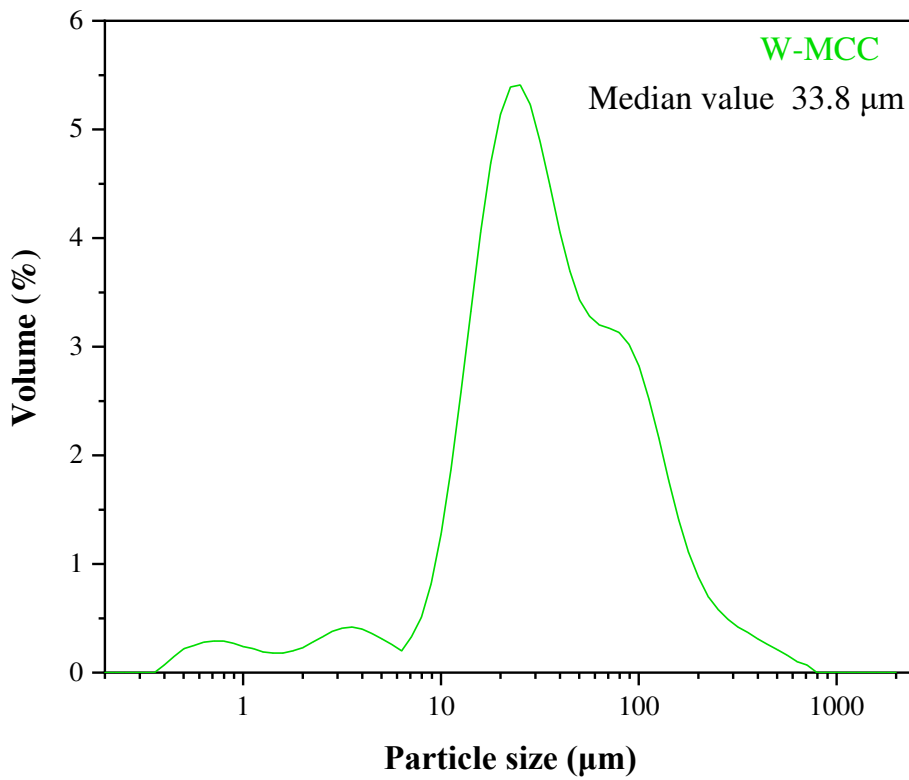
Figure 49. Particle size distribution for W-MCC.

Crystallinity

To investigate the crystalline properties of the obtained W-MCC and P-MCC, their XRD diffraction patterns and crystallinity are shown in Figure 50. All the patterns present sharp

peaks around 2θ = 15°, 17° and 23°, which are the characteristic peaks of cellulose. For W-MCC additional peaks appeared: 19°, 28°, 29° and 32°.
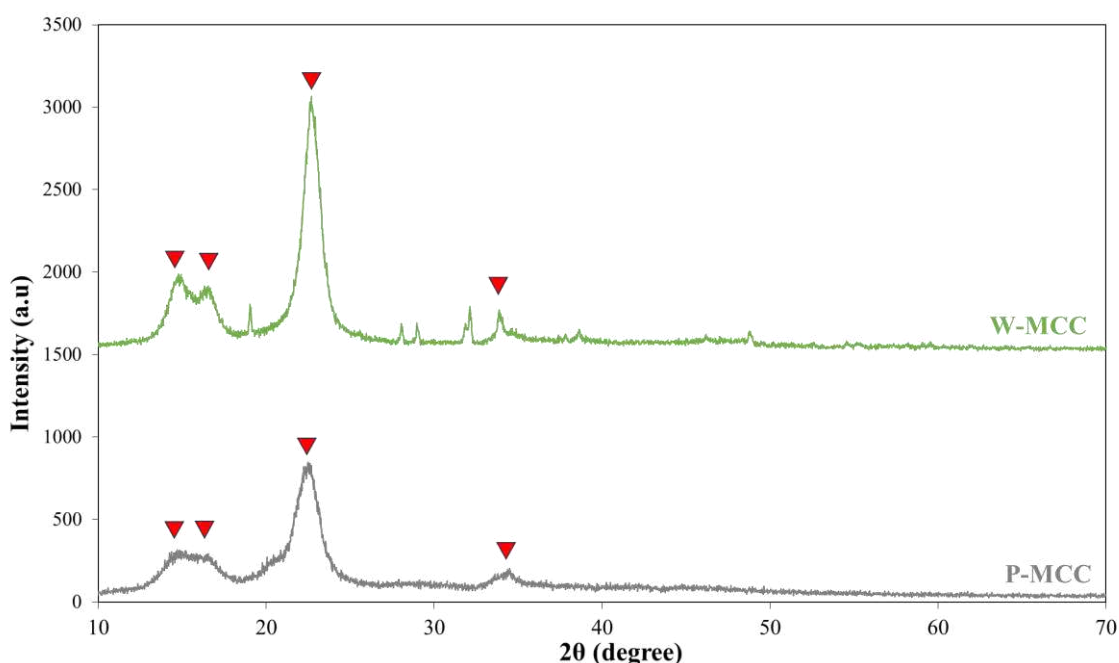
Figure 50. X-ray diffraction pattern of pure and waste-derived microcrystalline cellulose.

Chemical structure

Figure 51 shows the FT-IR spectra of cellulose (data from the library), P-MCC and W-MCC. All samples displayed similar spectra, which indicated that the extraction process did not modify the chemical composition of the samples. In addition, the spectra revealed similarities in functional groups.

The stretching vibration of O–H and asymmetric stretching vibration of the C–H bond appeared at 3337 and 2890 cm^{-1}, respectively. The peak observed at 1645 cm^{-1} corresponds to the C=O stretching vibration. Peaks at 1428 cm^{-1}, 1371 cm^{-1}, and 1315 cm^{-1} can be attributed to the bending of C–H, CH$_2$, and OH, respectively, which are typical for polysaccharides. The peak at 1029 cm^{-1} is characteristic of the asymmetric vibration of (C–O–C). The peak at 897 cm^{-1} is characteristic of cellulose with β-glycoside bonds of the glucose ring.
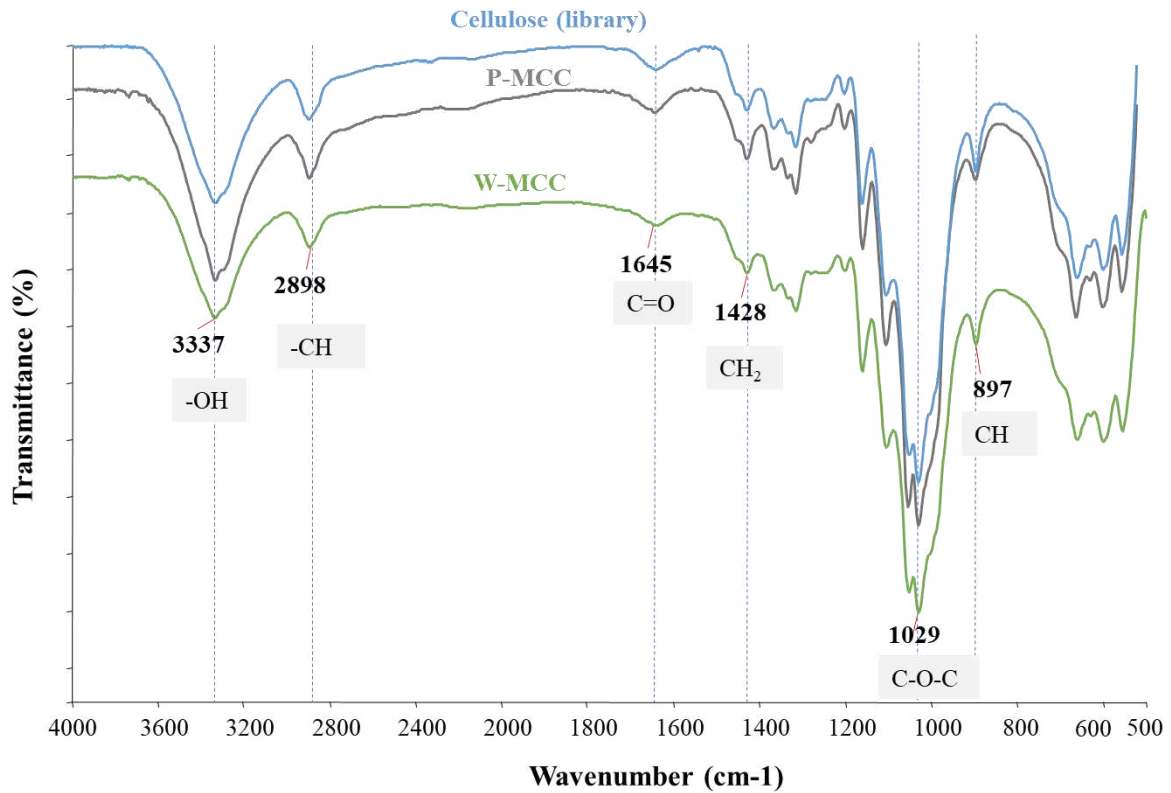
Figure 51. FTIR spectra.

3.3.2. Filters characterization

Analysis of morphology

The efficiency of filtering materials depends on their fiber structure, morphology, and porosity. SEM analysis was performed to analyze the morphology of traditional and fabricated filters. The images are presented below.
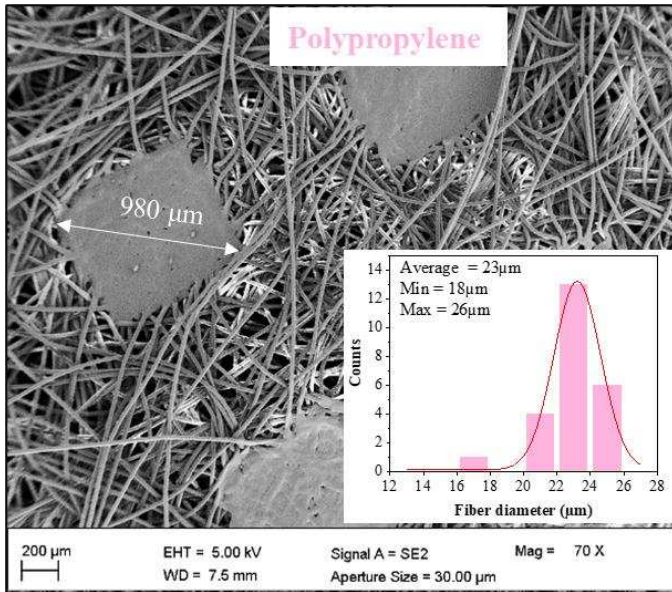
Figure 52. SEM image of traditional polypropylene filter.
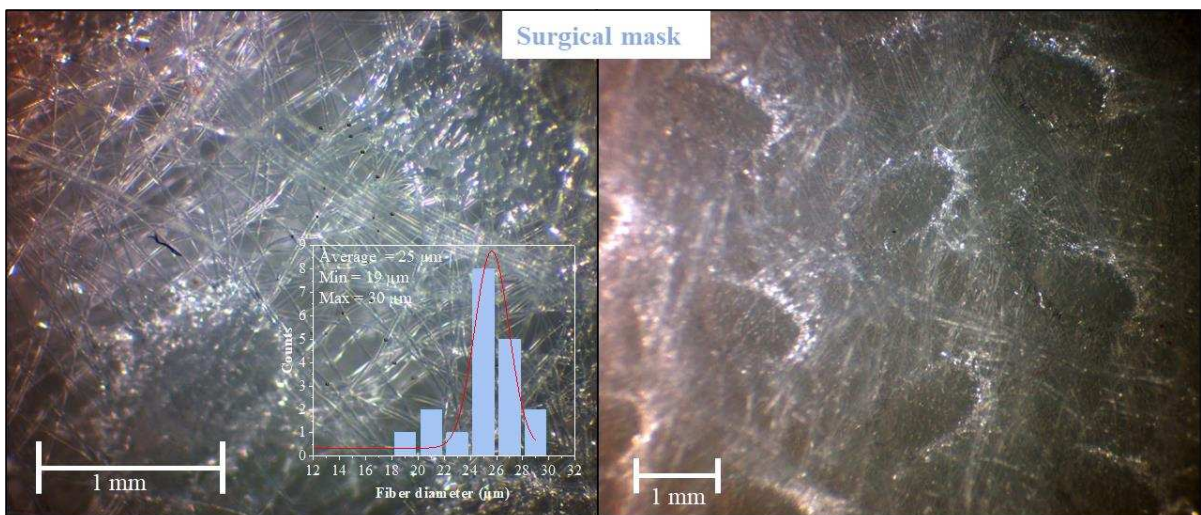
Figure 53. Optical images of surgical mask.
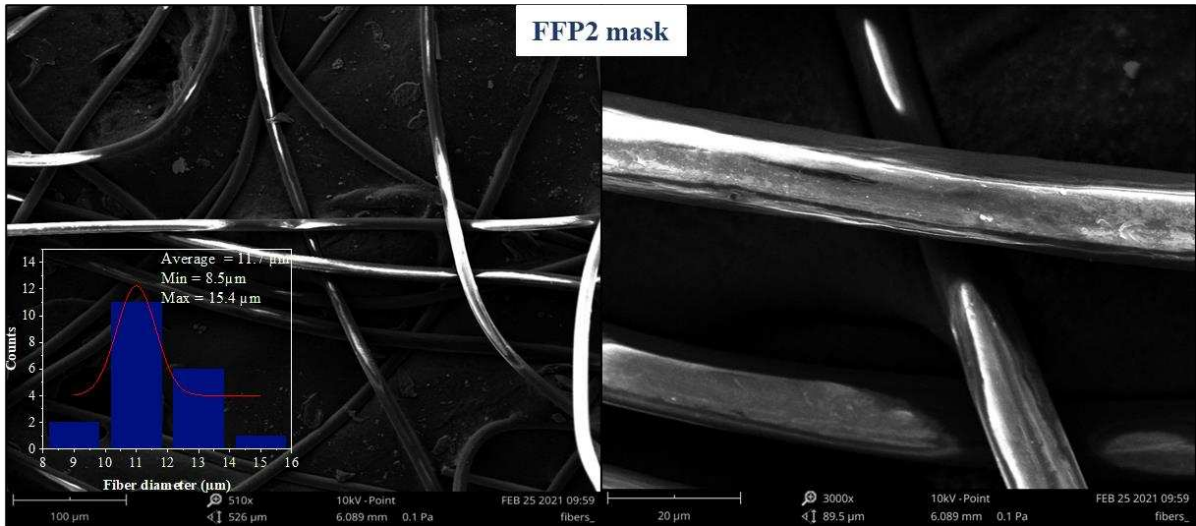
Figure 54. SEM images of traditional FFP2 mask.

Polypropylene filter (Figure 52) characterizes randomly orientated fibers with a range diameter from 18 to 26 µm and rhombus-shaped parts of 980 µm length. The average fiber diameter of polypropylene and surgical mask is similar and amounts to 23 µm and 25 µm, respectively. In fact, one of the surgical mask layer consists of the polypropylene filter (section 2.2.2.3). The fiber distribution for surgical mask ranged from 19 to 30 µm.

The fibers of FFP2 mask characterizes smaller fibers' diameter (9 – 15 µm) with an average of 12 µm.

Glass fiber filtering medium consists of randomly oriented fibers with a very wide range of diameter, from 116 nm to 5.53 µm.
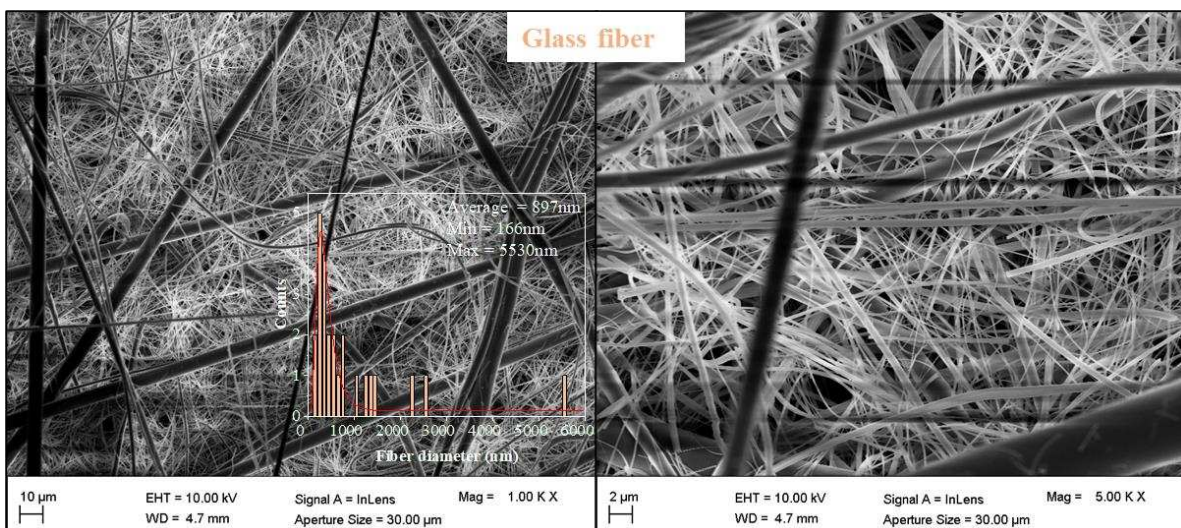
Figure 55. SEM images of glass fiber.
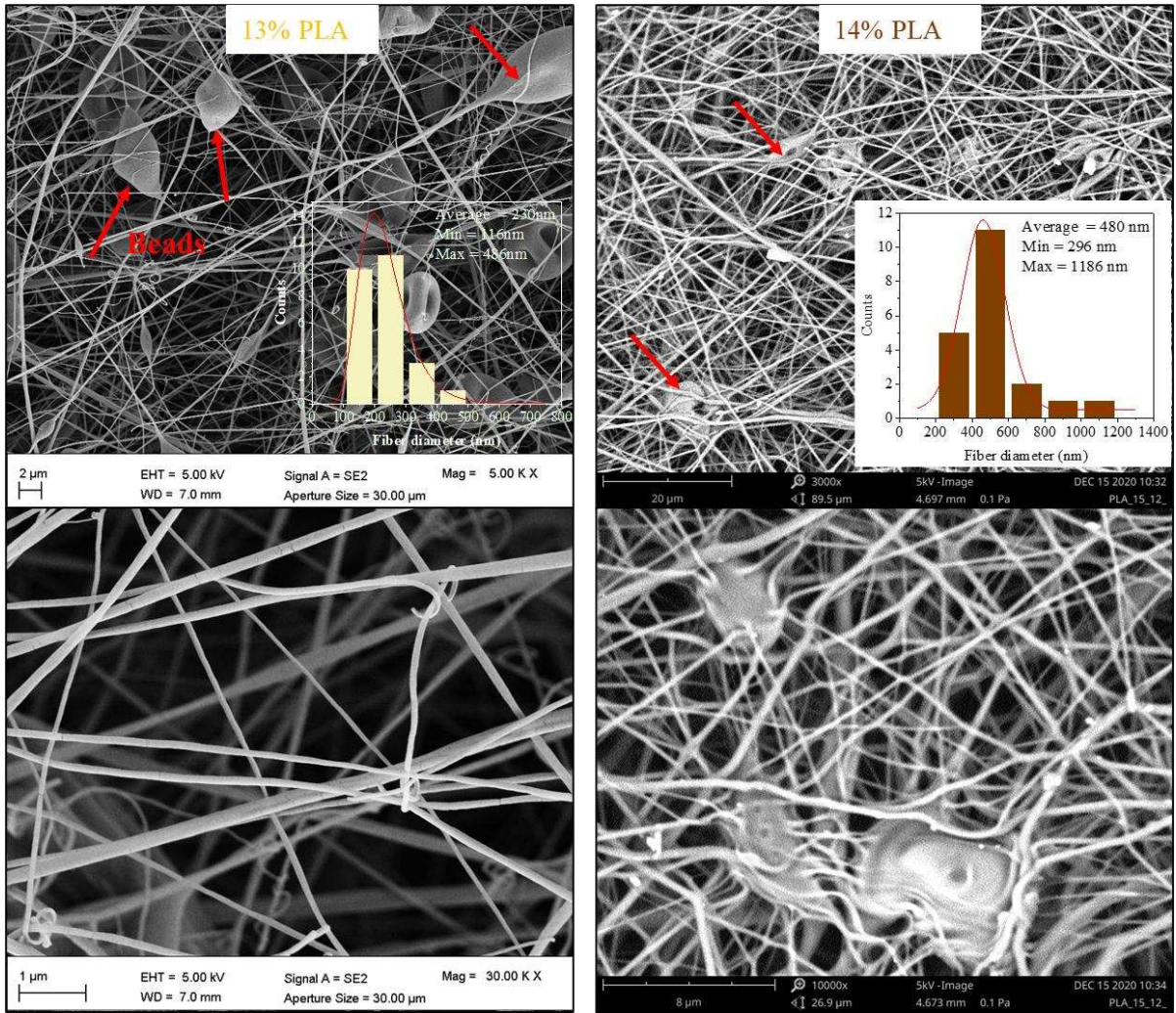
Figure 56. SEM images of 13% and 14% PLA nanofibers.

The fibers obtained from electrospinning of 13% PLA (Figure 56) are heterogeneous, and the diameter ranges from a minimum of 116 nm to a maximum of 486 nm, with the average diameter of 230 nm. Visible accumulations of polymer (beads marked with red arrows on the figure) are present, which will have played a role in the efficiency of the filter and in the pressure drop, given that the spaces between the fibers are reduced by these imperfections. Several fibers are broken or twisted, and this series of which may indicate not optimal electrospinning conditions.

Increasing the polymer concentration up to 14% PLA, and flow rate to 0.08 mL/min (Figure 56) resulted in more homogeneous fibers, however the average fiber diameter increased double, from 230 nm to 480 nm. Few beads are present. The formation of beaded fibers has been observed widely, and it is related to the instability of the jet of polymer solution [43].
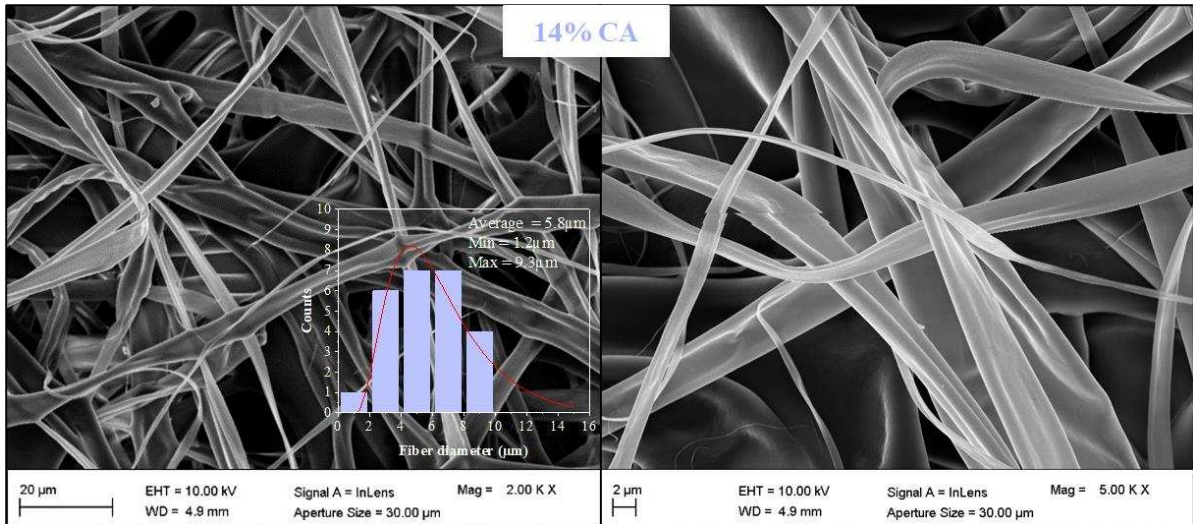
Figure 57. SEM images of 14% Cellulose acetate fibers.

Fibers obtained from the 14% solution of cellulose acetate characterize flat-ribbon morphology with the average diameter of 6 µm. Much larger fiber diameter compared to the 13% and 14% PLA fibers, is a result of high flow rate as shown in Table 11.
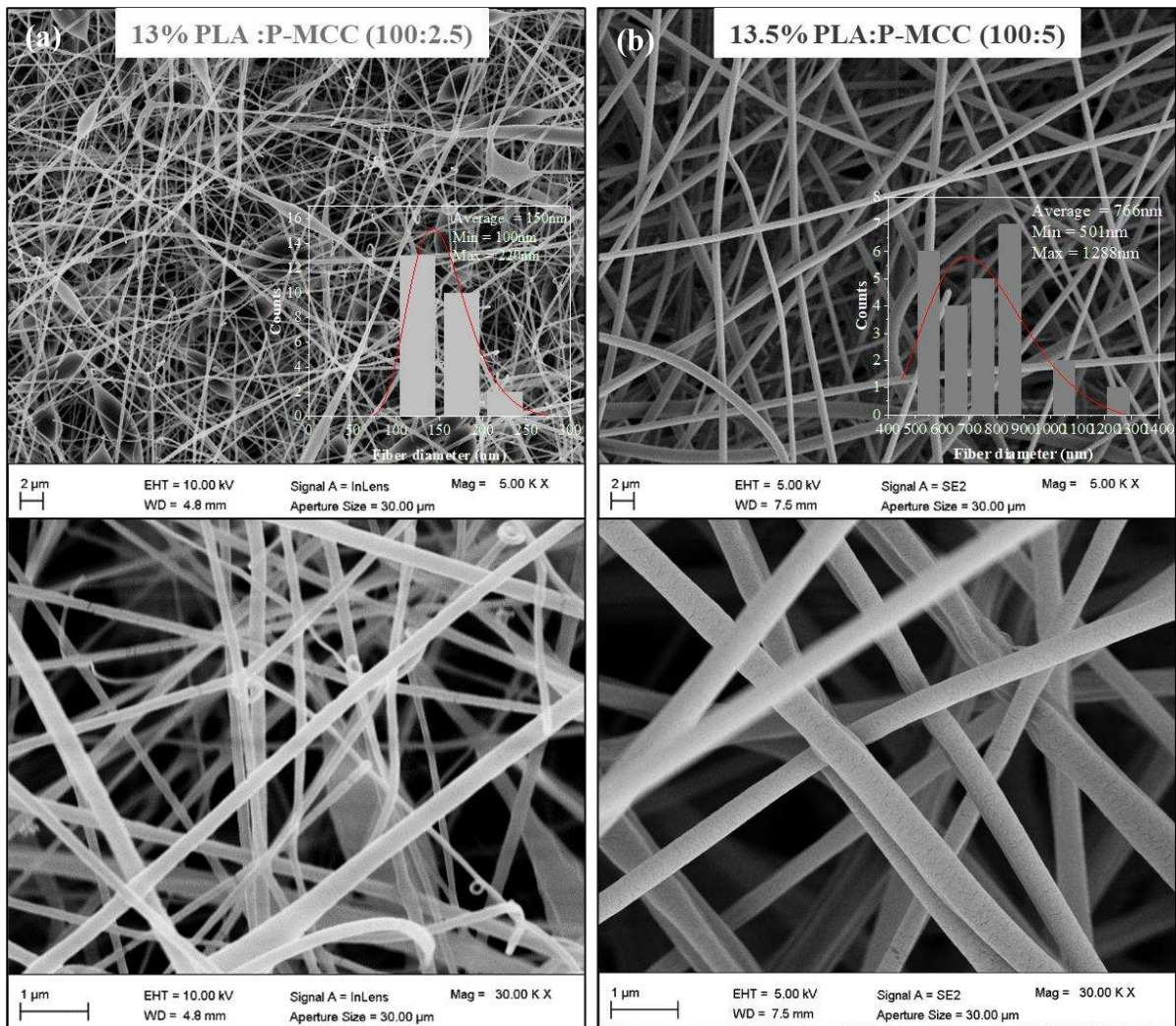
Figure 58. SEM images of 13% PLA reinforced with (a) 2.5% and (b) 5% of W-MCC.

Adding 2.5% microcrystalline cellulose to the 13% of PLA matrix resulted in a decrease in the average fiber diameter (150 nm) and in a reduction of fiber diameters. In fact, the minimum fiber diameter is 100 nm, while the maximum 220 nm. Whereas addition 5% of MCC resulted in increase of the total polymer concentration to 13.5% and in smooth defect-less fibers. The average fiber diameter increased to 766 nm and the range is from 501 nm to 1288 nm. The MCC particles are not present on the images, suggesting that they arranged inside and along

the fibers. Moreover, sample 13.5% PLA:P-MCC (100:5) characterize porous surface of the fibers.

This result confirms that addition of MCC can improve the mechanical properties, however further tensile test should be performed.
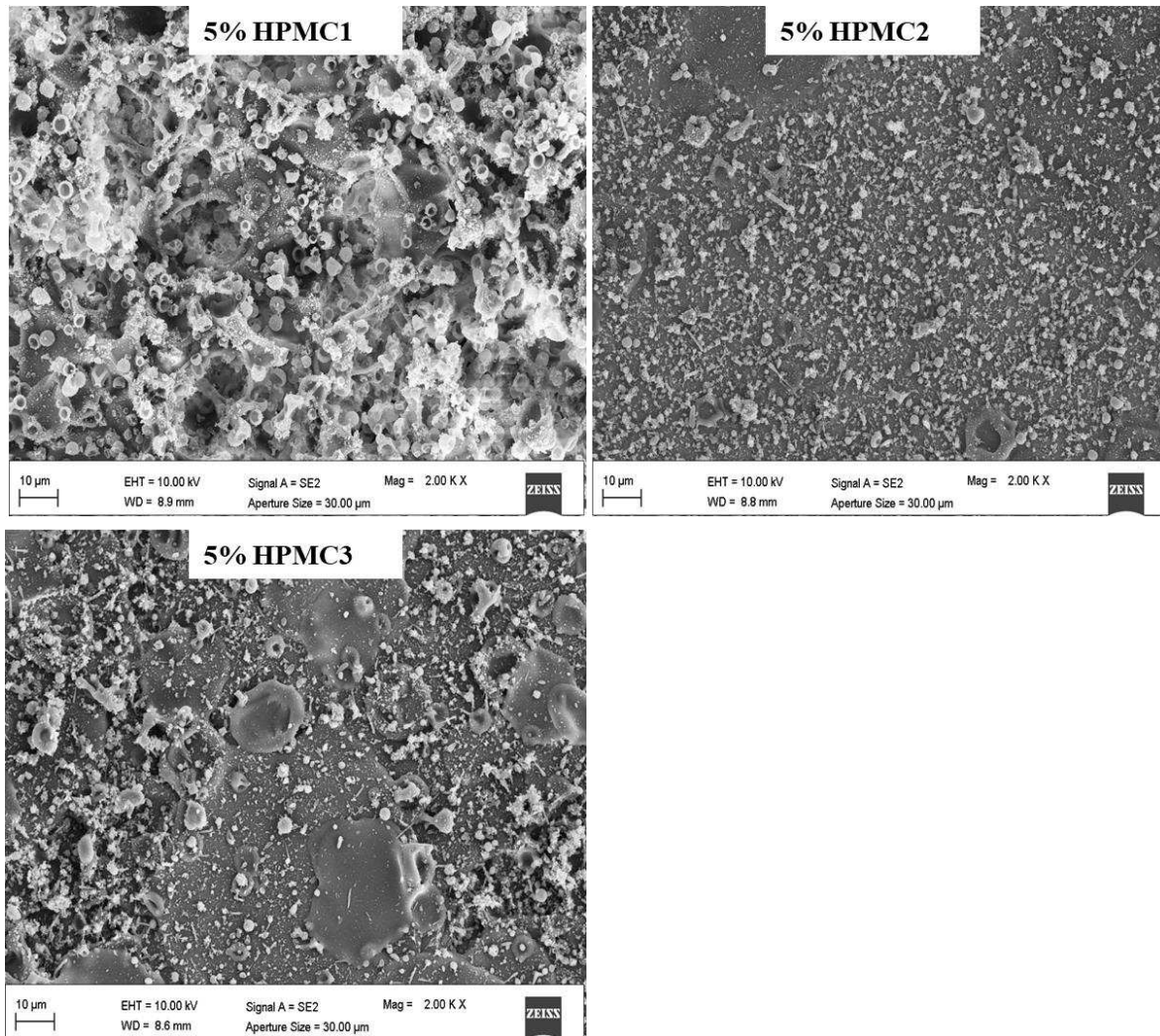
Figure 59. SEM images of HPMC samples.

The images of HPMC samples (*Figure 59*) confirmed, the hypothesis that from 5% HPMC solutions the fibers cannot be produced.

Table 11. Average fiber diameters of the filters.

Sample	Average fiber diameter
Polypropylene	23 μm
Surgical mask	25 μm
FFP2 mask	12 μm
Glass fiber	897 nm
13% PLA	230 nm
14% PLA	480 nm
14% CA	6 μm
13% PLA:MCC (100:2.5)	150 nm
13.5% PLA:MCC (100:5)	766 nm
5% HPMC1	No fibers
5% HPMC2	No fibers
5% HPMC3	No fibers

3.3.1. Particle efficiency filtration test

Results obtained for series I are presented in Figure 60 and Table 12. To measure the smallest particles, three particulate channels have been monitored: PM_1, $PM_{0.5}$ and $PM_{0.23}$. The (S) 14% PLA achieved a filtration efficiency similar to the surgical mask (from 60% for the $PM_{0.23}$ and to about 70% for the PM_1). The factor that influenced the differences in filtration efficiency between (D) 14% PLA and the surgical mask was fiber diameter. In short, the filtration efficiency increases when the fiber diameter decreases. A lower penetration of the particles can be found in filters with a significantly small diameter (0.27 μm) [25] due to the increase in surface area. In accordance with the concept of most penetrating particle size (MPPS), the smaller particles penetrate the filters more, resulting in a decreased of filtration efficiency for $PM_{0.3}$ compared to larger particle sizes.

Multi-layer electrospun fibers (double-PLA) had increased filtration efficiency of $PM_{0.3}$, $PM_{0.5}$ and PM_1 by about 35% compared to single-layer fibers due to the increase in thickness of the filter medium. However, this came at the cost of a decrease in air permeability. In fact, the pressure drop increased from 107 Pa to 132 Pa.

Both of these factors, filtering efficiency and pressure drop, affect the final value of the quality factor. Thus, the key is to design a highly effective mask suitable for everyday use for humans, while ensuring proper air circulation when inhaling and exhaling.

Results from this part of the experiment have been published [44].

Figure 60. Particle filtration efficiency test results (series I). Dashed lines indicate the filtration efficiency of traditional filters.

Table 12. Results obtained from the particle filtration efficiency test.

Filter	Efficiency $PM_{0.23}$	Efficiency $PM_{0.5}$	Efficiency PM_1	Pressure Drop
Surgical mask	58.87%	69.39%	71.67%	87
FFP2 mask	97.07%	97.37%	97.28%	128
(S) 14% PLA	60.57%	63.58%	71.61%	107
(D) 14% PLA	93.76%	94.28%	93.96%	132

Figure 61 and Table 13 present the results from the particle filtration efficiency test for series II. PM_{10}, $PM_{2.5}$ and PM_1 concentrations have been measured. For the filters produced with the addition of 2.5% P-MCC ((I) 13% PLA:P-MCC (100:2.5)), the average efficiency for PM_{10} and $PM_{2.5}$ is around 63% and 57%, respectively.

Figure 61. Particle filtration efficiency test results (series II). Dashed lines indicate the filtration efficiency of traditional filters.

Table 13. Average efficiency, standard deviation and pressure drop for each type of filter tested.

Filter	Eff.% PM_1	Eff.% $PM_{2.5}$	Eff. PM_{10}	St. Dev PM_1	St. Dev. $PM_{2.5}$	St.Dev. PM_{10}	Pressure Drop
Polypropylene	39%	57%	59%	7.2%	6.4%	5.9%	24
FFP1	72%	79%	80%	9.6%	13.2%	10.5%	48
Surgical mask	45%	59%	61%	15.0%	9.0%	7.9%	39
(I) 13% PLA	59%	78%	82%	12.0%	11.1%	10.0%	52
(I)14% CA	49%	65%	70%	19.3%	16.4%	15.1%	57
(II)14% CA	55%	74%	78%	10.2%	10.0%	7.0%	57
(I)13% PLA:P-MCC (100:2.5)	40%	57%	63%	7.8%	7.1%	5.7%	56
(I)13% PLA:P-MCC (100:5)	57%	69%	72%	0.7%	2.1%	2.8%	55
(III) Sandwich	82%	90%	92%	11.4%	8.1%	6.9%	59

Results from series III have been presented in Figure 62 and Table 14. Two particulate matter sizes have been monitored: $PM_{2.5}$ and PM_{10}. All electrospun filters characterize high filtration efficiency, over 90%, while commercial glass fiber filters show the highest removal efficiency

(over 99% for PM_{10} and $PM_{2.5}$). Applying lower flow rate during the test (95 L/min instead of 120 L/min) the pressure drop for all the filters decreased and ranged from 25 to 58 Pa.

The (S) 13.5 % PLA:P-MCC (100:5) demonstrated a good filtration efficiency, with a decrease of 4% (for $PM_{2.5}$) and 3% (for PM_{10}) circa with respect to the commercial glass fiber. Addition of 5% of waste-derived MCC (filter (S) 13.5 % PLA:W-MCC) resulted in decreasing by 7% ($PM_{2.5}$) and 6% (PM_{10}) with respect to the filter with the addition of the same amount of P-MCC, however the drop pressure decreased from 119 Pa to 117 Pa, which may indicate that the filter was slightly thinner. Moreover, filters produced from 10 ml of the solution were very thin, brittle and difficult to separate from the aluminum foil and to handle, hence subsequent filters (D) were produced from a double amount of solution (20 ml). This step did not significantly affect the drop pressure which ranged from 114 to 117 for double layer filters. The effect of this polymer concentration increase in the filter (D) 13.5 % PLA:W-MCC (100:5) is relevant, demonstrated by an excellent removal efficiency (95% for $PM_{2.5}$ 96% for PM_{10}) and hence, the increase in the filtration efficiency of 10.5% and 9% for $PM_{2.5}$ and PM_{10} respectively.

The next two filters, (D) 13% PLA:W-MCC (95:5) and (D) 13% PLA:W-MCC (80:20) concern the attempt of substitution of PLA with W-MCC in 5% and 20% respectively. Moreover, to understand the effect of MCC substitution filters filtration efficiency of 12% PLA and 10% PLA were compared. The results showed that in both cases the removal efficiency was comparable to the filter without W-MCC substitution with slightly decrease in the filtration efficiency (from 5% to 8%). Despite excellent filtration efficiency results, the (D) 10% PLA solution produced a very thin and difficult to handle filter.
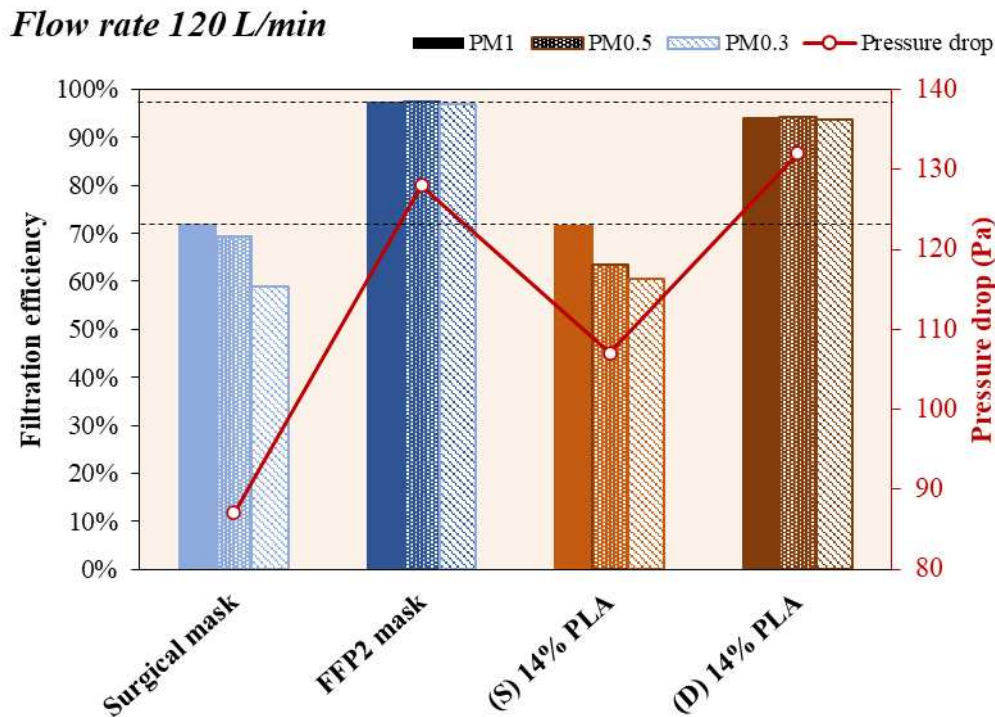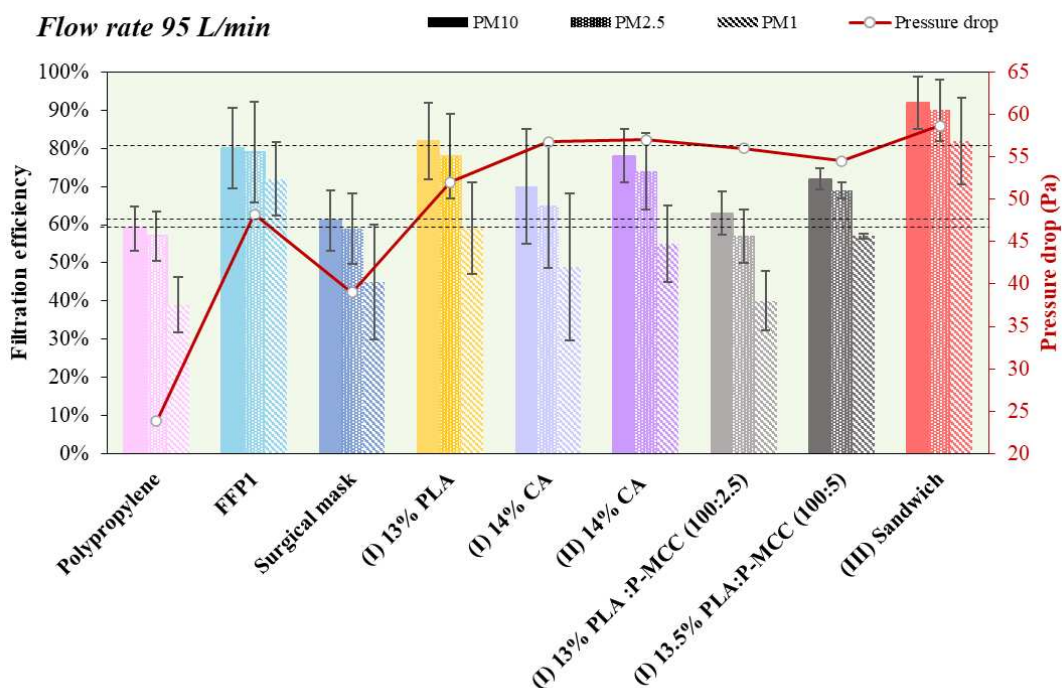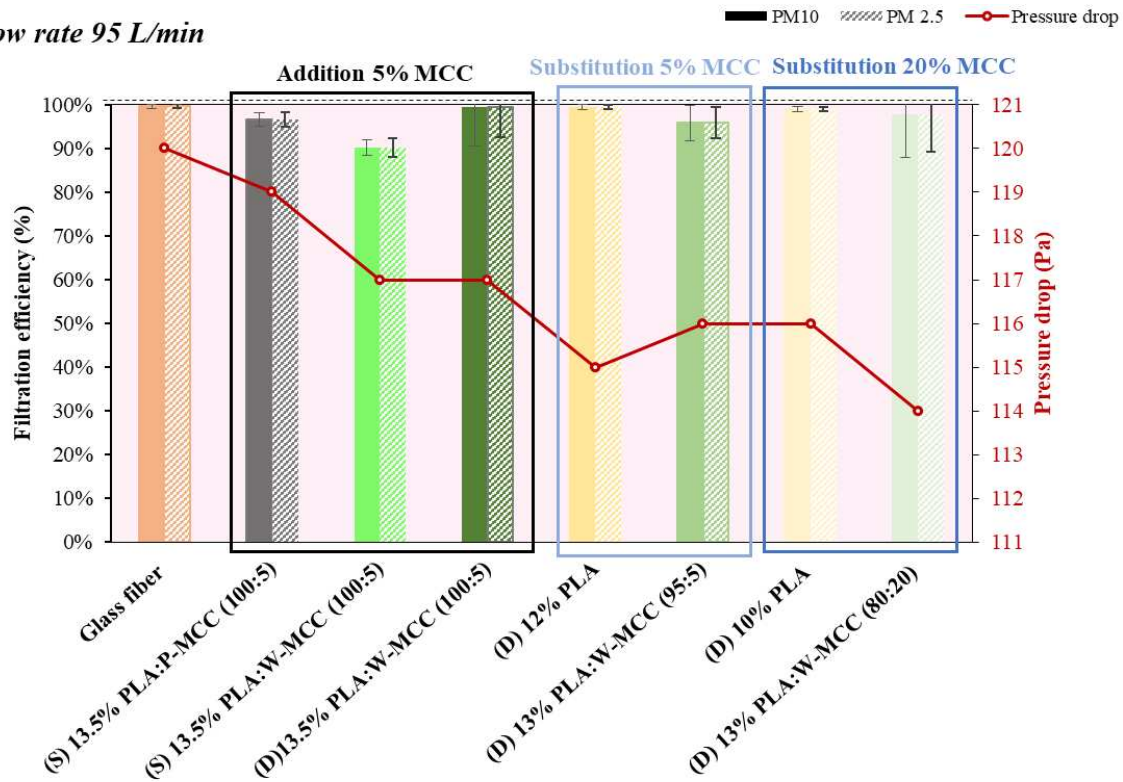
Figure 62. Filtration efficiency test results (series III). The dashed line indicates the filtration efficiency of the traditional filter.

Table 14. Average efficiency, standard deviation and pressure drop for each type of filter tested.

Filter	Eff. $PM_{2.5}$	Eff.% PM_{10}	St. Dev $PM_{2.5}$	St.Dev PM_{10}	Pressure Drop
Glass Fiber	99.19%	99.66%	0.56%	0.45%	120 Pa
(S) 13% PLA:MCC (100:2.5)	95.69%	96.73%	1.58%	1.65%	119 Pa
(S) 13.5 % PLA:W-MCC (100:5)	88.65%	90.27%	1.78%	2.20%	117 Pa
(D) 13.5 % PLA:W-MCC (100:5)	94.73%	96.07%	8.93%	6.81%	117 Pa
(D) 12% PLA	99.67%	99.53%	0.56%	0.53%	116 Pa
(D) 13% PLA:W-MCC (95:5)	95.14%	95.90%	4.06%	3.50%	115 Pa
(D) 10% PLA	98.54%	98.94%	0.51%	0.49%	114 Pa
(D) 13% PLA:W-MCC (80:20)	96.17%	97.72%	9.85%	8.42%	116 Pa

The SEM images of the Glass Fiber and 14% CA filters after the PM filtration test (Figure 63 and Figure 64) show the 0.5 – 2.7 µm sized NaCl particles (represented as PM) deposited on or around the fibers, confirming efficient capture.
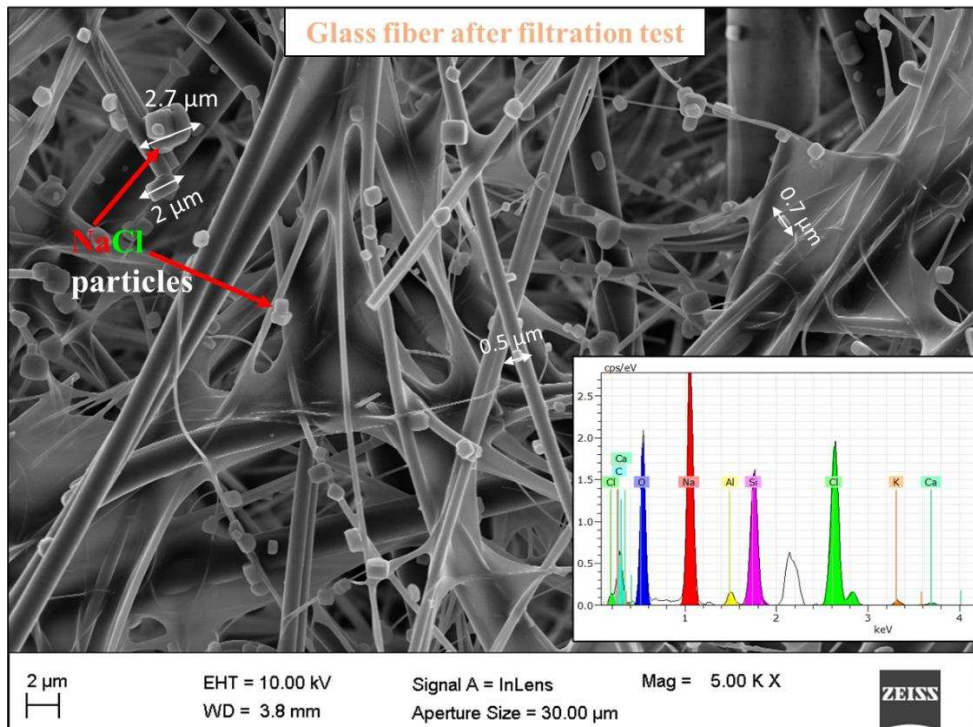
Figure 63. SEM image and elemental analysis of glass fiber filter after filtration test.
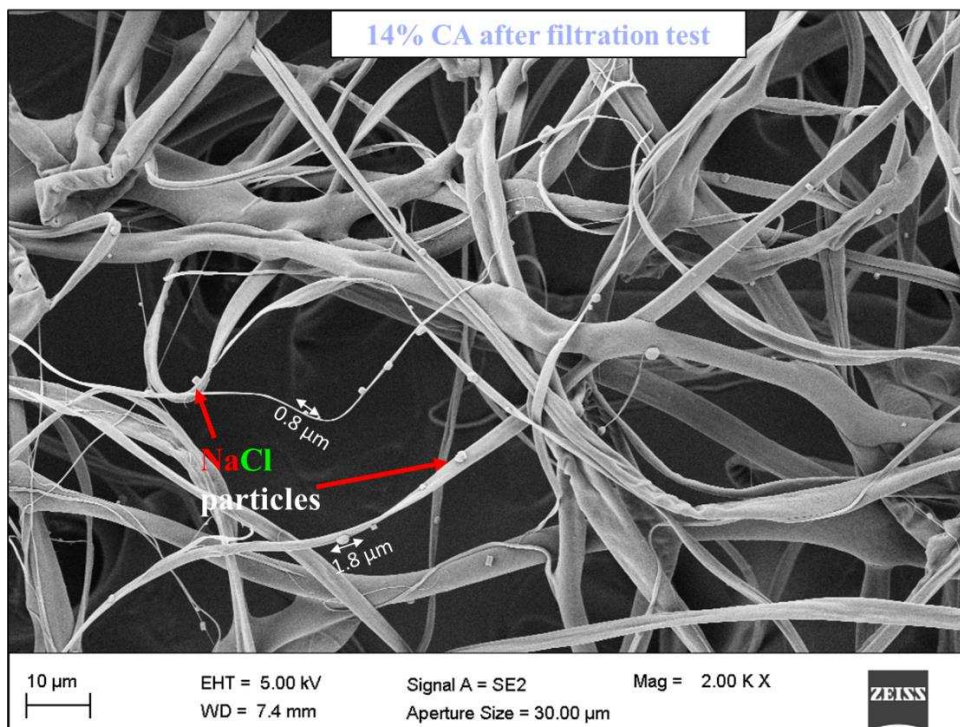
Figure 64. SEM image of 14% CA filter after filtration test.

Table 15. Elemental content of the glass fiber filter after filtration test.

Element	Content norm. (wt. %)	Content atom. (at. %)
Na	18.47	14.34
Cl	14.52	7.31
O	33.69	37.59
C	23.17	34.44
Si	8.42	5.35
Al	0.88	0.58
K	0.53	0.24
Ca	0.31	0.14

The filtration quality factor (QF), determined from filtration efficiency and pressure drop, is commonly used to assess the performance of the filters. QFs for $PM_{0.3}$, $PM_{0.5}$, PM_1 of series I for (D) 14% PLA is higher than surgical mask and (S) 14% PLA but slightly lower than FFP2 mask. For series II instead, where the lower flow rate was applied and PMs in the range of 1 µm to 10 µm were measured, the highest quality factor belongs to (III) layered sandwich filter. Filters from the last series (III), characterize quality factors for PM_{10} in the range from 0.019 Pa^{-1} to 0.048 Pa^{-1}. QF10 for (D)13.5% PLA:W-MCC (100:5) and (D) 12 % PLA are 0.045 Pa^{-1} and 0.044 Pa^{-1} respectively, and are comparable to the QF obtained by glass fiber (0.048 Pa^{-1})
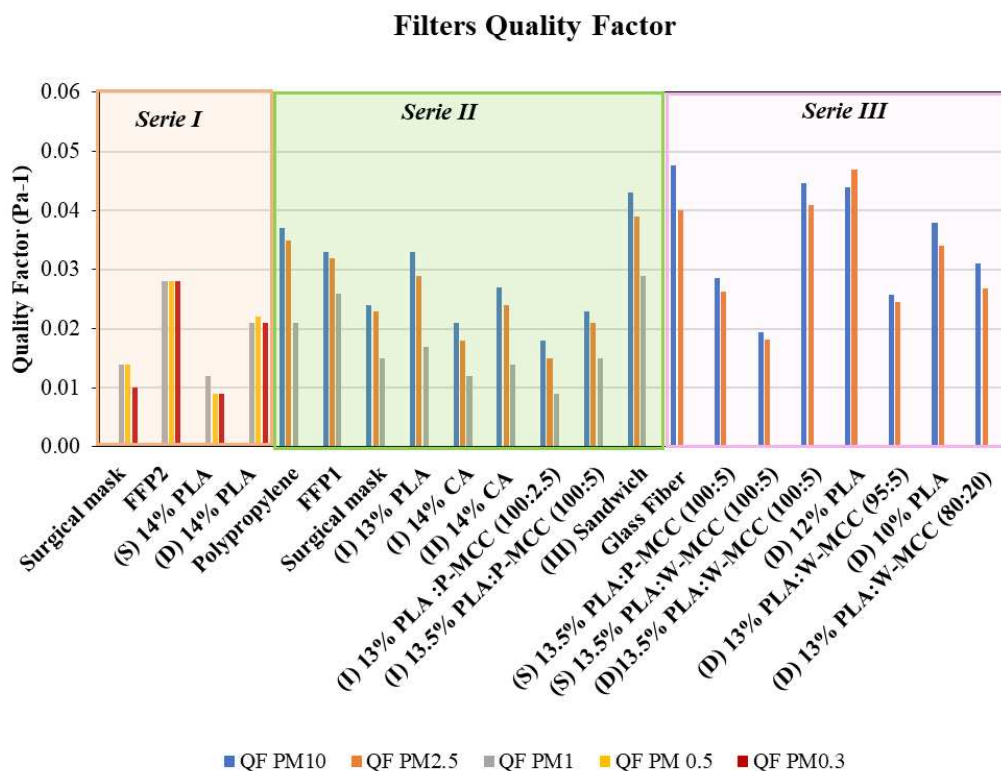
Figure 65. Quality factors of traditional and fabricated filters.

3.4. Conclusions

In this study, bio-based filters fabrication has been demonstrated. The utilization of eco-friendly materials, such as biodegradable and/or recovered polymers, may constitute an eco-friendly alternative solution for traditional filters, which very often end up in the landfills. According to filtration tests, the (S) 14% PLA exhibited a filtration efficiency more than 60%, comparable to the surgical mask, whereas the double-layered electrospun 14% PLA revealed similar performance to the FFP2 mask, retaining up to 95% of the particles with a diameter greater than 230 nm ($PM_{0.3}$).

Moreover, this study showed the contribution to sustainable development under the principle of a circular economy and possible way of preventing textile waste to be disposed in environment and an opportunity of second life for recovered polymer (MCC). A series of MCC-PLA fibrous nanocomposite were successfully electrospun by loading different concentrations of MCCs into a PLA matrix. When MCC was substituted instead of added to the PLA solution (5% addition and 5-20% substitution), the fabrication of the filter with the electrospinning method was still successful, however a slight decrease of the filtration efficiency (4-8% for $PM_{2.5}$ and PM_{10}) comparing to filters with the same percentage of PLA but without W-MCC has been noticed. Despite this, excellent filtration efficiency has been demonstrated (over 90% for $PM_{2.5}$ and PM_{10}). As a result, this research demonstrates a novel method of fabrication PLA-MCC filters with a quality factor comparable to the traditional glass fiber filter. To understand better the contribution of MCC in the PLA-MCC filtering composites further investigations regarding morphological and mechanical properties are required.

Chapter 4   Adsorbents
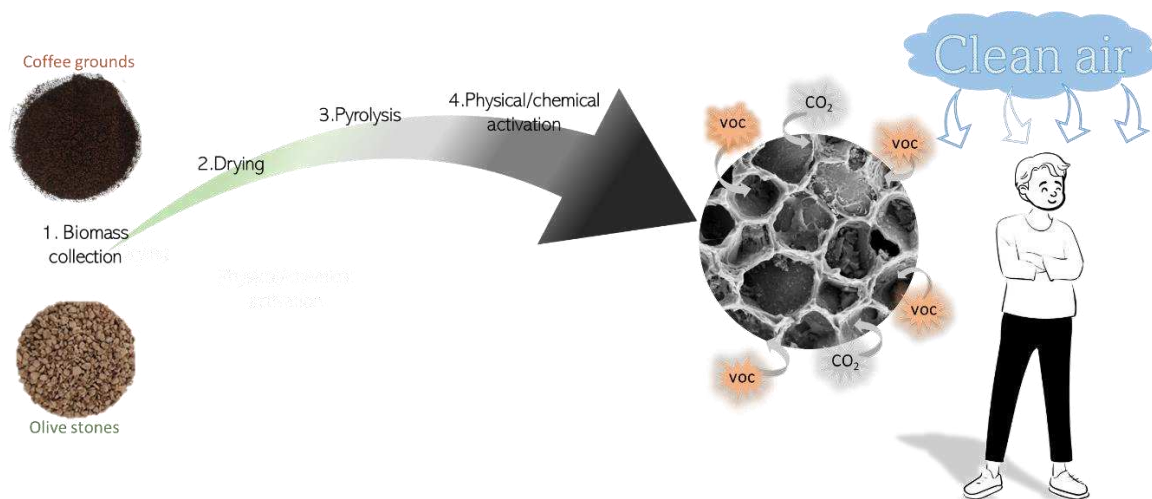
4.1. Background

A number of studies have been carried out to analyze the air pollutants and the negative impact which can imply during the exposure not only on human's health and environment but also on buildings, historical monuments, cultural heritage objects and artworks [45], [46], [47], [48], [49]. For this reason, many strategies have been developed to counteract the issues related to poor air quality. As a flexible, inexpensive, efficient, and simple method, adsorption can be used in the removal of air pollutants that are produced by various activities. The adsorbents used for VOCs gas capture are mainly porous materials such as:

- Metal Organic Frameworks (MOFs)
- Zeolites
- Mesoporous silica
- Carbon nanotubes
- Graphene
- Carbonaceous nanofiber membranes or
- Activated carbon

Activated carbon is one of the most commonly used adsorbent, with a very high specific surface area and a well-developed surface pore structure, which make it suitable for use as an adsorbent for the removal of gaseous pollutants.

However, the main issue present throughout the entire process of producing these materials is the use of nonrenewable precursors, such as petroleum residues, coal, peat, and lignite, which are associated with high costs and extensive energy consumption [50].

4.2. Aims and objectives

In this work, activated carbon and biochar have been produced from organic waste materials: coffee grounds and olive stones. To introduce the porous structure needed for VOCs adsorption, two types of activation were applied: chemical activation with potassium carbonate (K_2CO_3), and physical activation with carbon dioxide (CO_2). K_2CO_3 has been proposed as an eco-friendly activating agent [51], [52], [53]. Moreover, activated carbon obtained by K_2CO_3 activation is normally rich in micro- and narrow pores, and increases the carbon yield

(comparing to the one obtained by KOH) [54], [55], which increases its potential for production on a larger scale.

The influence of the activation process, type, and time of activation was also investigated. Characterization of materials and the adsorption capacity of the obtained porous carbons for volatile organic compounds (VOCs) in indoor conditions was studied.

As reported in Table 16, there are many studies regarding synthesis activated carbon from various waste precursors, however, regarding VOC adsorption, there are only a few data obtained in conditions similar to those used in our study (low concentration of VOCs, a static adsorption set-up) which try to simulate as better as possible a real indoor environment. Most adsorption data are collected under high concentrations (100 to 1000 ppm), which does not simulate the realistic indoor operating conditions (VOC concentrations in the range of the limits of TLV–TWA) at which gaseous indoor contaminant air cleaning devices/materials could be applied.

4.3. Activated carbon

4.3.1. Main properties

Activated carbon is known as a universal adsorbent due to its unique properties such as high porosity and specific surface area, adequate PSD (Particle Size Distribution) and high mechanical strength. The pores in activated carbons are scattered over a wide range of size and shape. The pores are classified by their sizes (Figure 66) usually into three groups:

(i)   macropores having average diameter more than 50nm;
(ii)   mesopores with diameter 2–50nm;
(iii)   micropores having average diameter less than 2nm.

The last group, micropores, is often divided into two subgroups: supermicropores (0.7–2 nm) and ultramicropores (<0.7 nm).

Activated carbon is widely employed as an adsorbent material for pollutant removal applications due to its advantages such as low cost, easy regeneration, moisture resistance and high adsorption capacity at ambient conditions. It can be classified both in terms of physical properties, such as particles dimension, and in terms of precursor material.

Based on particles dimension, activated carbon can be classified in the following categories:

- **GAC (Granular Activated Carbon):** has a relatively larger particle size compared to powdered activated carbon and, consequently, presents a smaller external surface.
- **PAC (Powdered Activated Carbon):** the ASTM classifies particles passing through an 80-mesh sieve (0.177 mm) and smaller as PAC.
- **EAC (Extruded Activated Carbon):** combines powdered activated carbon with a binder, which are fused together and extruded into a cylindrical shaped activated carbon block.
- **ACFC (Activated Carbon Fiber Cloth):** easy regeneration with high flexibility, but high manufacturing cost.
- **CA (Carbon Aerogels):** combines activated carbon with aerogel effects. Aerogels are a class of synthetic porous ultralight materials derived from a gel, in which the liquid component of the gel has been replaced with a gas, without significant collapse of the gel structure.
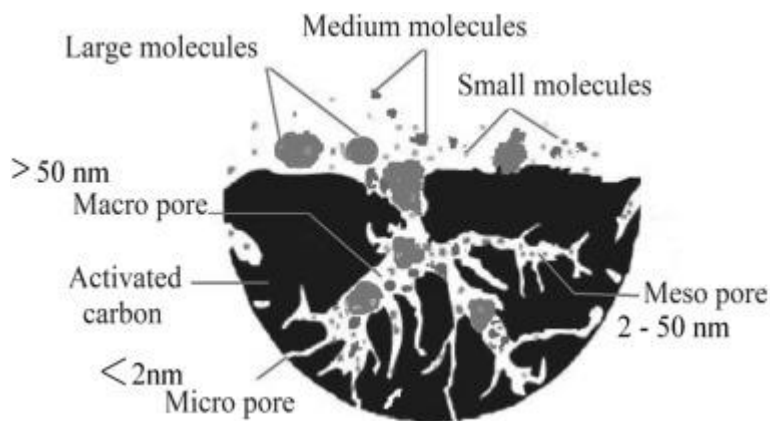
Figure 66. Classification of pores in activated carbon [55].

4.3.2. Process of preparation

In general, there are three main processes for the preparation of activated carbon:

1) Physical activation - the raw precursor is carbonized, and then simultaneously activated (single-step process) or the obtained char from the carbonization step is collected and subsequently submitted to activation (two-step process) by using oxidizing gases like CO_2 [56], or steam [57], among others.

2) Chemical activation - consists of a single-step process, where the raw carbonaceous material is first mixed or impregnated with the chemical agent. Frequently used activating agents are classified as bases such as KOH and NaOH [58], acids like H_3PO_4 [59] and H_2SO_4, or even salts such as K_2CO_3 and $ZnCl_2$ [60], followed by heating in an inert atmosphere. After cooling, the obtained product is rinsed with distilled water or mild acid to remove the remaining activating agent. Many activating agents like alkali hydroxides are hazardous, expensive and corrosive [61], while $ZnCl_2$ is unfriendly to the environment and may create waste disposal problem, which makes difficult to implement production on the industrial scale.

3) The combination of both - is performed by chemical activation step followed by physical activation.

Table 16. Comparison of biomass-derived carbons for air pollutant adsorption.

Carbon precursor	Sample nomenclature	Activation conditions		Specific surface area	Adsorbate	Ads. Capacity	Experimental conditions	Ref
		Activation agent	Time and temperature	[m²/g]				
Rice husk	KOH-AC	KOH (impregnation)	2 h 750 °C	1439	CO_2	251 mg/g	P=1 bar T=0 °C	[62]
Arundo donax	KLB2	KOH		1122	CO_2	277 mg/g	P=1 bar T=0 °C	[56]
Coffee grounds	CG800-1	K_2CO_3 (mixing)	1h 800 °C	1692	CO_2	102 mg/g and 316 mg/g	P=0.15 bar and P=1 bar, T=0 °C	[63]
The stems of *Diplotaxis acris*	AC	1. Pyrolysis 2. 85% H_3PO_4 (impregnation)	2 h 550°C	40	Benzene	5.4 mg/g	Static adsorption test in 25 °C, initial conc. 313ppm	[64]
Buckwheat Hull	Unactivated adsorbent and K2CO3-activated adsorbent	None and K_2CO_3 (impregnation)	2h 800 °C	240 (biochar) 1300 (AC)	Toluene	18% removed by biochar and 36% by AC, during 90 min exposure	Static adsorption test in Tedlar® bag, Initial concentration 230ppm T=15–16 ℃ m_{AC}= 0.2g	[65]
Commercial coal based	CAC	-		842	Toluene	65 mg/m3	Dynamic adsorption (fix-bed reactor),	[66]

Precursor	Sample	Activating agent	Conditions	Surface area	VOC	Capacity	Adsorption	Ref
							Initial concentration 32 ppm, T=39 ºC, ambient pressure	
Sewage-sludge	SB-P-AGK-AW	KOH (mixing)	1h 700 °C	990	Toluene, MEK Limonene	350 mg/g 220 mg/g 640 mg/g	Dynamic adsorption, initial concentration 100 ppm for toluene and 50ppm for MEK and limonene	[67]
Black cumin		ZnCl$_2$ (impregnation)	1 h 550 °C	1213	BTX: Benzene, toluene, xylene	495 mg/g 580 mg/g 674 mg/g	Dynamic adsorption, single and multi-component system, initial conc.20 mg/L	[68]
Banana peel		KOH (impregnation)	3 h 800 °C	3746	Benzene, toluene	2149 mg/g 2195 mg/g	T = 25 °C, Pressure 12.7 Kpa (for benzene) and 3.8 Kpa (for toluene)	[69]

4.4. Materials and methods

4.4.1. Precursor selecting and characterization

In this work, coffee grounds (CG) and olive stones (OS) were chosen as precursors of porous carbons. Around 500 g of CG were collected from a cafeteria located in Senigallia (Italy). Open-air pre-drying was conducted, and then the samples were oven-dried at 50 ºC for 8 hours. In the next step, all coffee grounds were sieved until the material passed 500 µm. An olive mill located in the Alentejo region of Portugal provided 1 kg of crushed OS with a diameter of 2–3 mm; the stones were then dried at 50 °C for 8 hours.

Morphological and elemental analyses were conducted via a scanning electron microscope, thermal properties were evaluated by TGA method and chemical structure by FTIR spectroscopy as described in chapter 2.3.

4.4.2. Preparation of activated carbon and biochar

A lab-scale pyrolysis reactor (Figure 67) of tubular design with the following dimensions: an outer diameter of 2.5 cm and a length of 50 cm. The quartz reactor was placed in the electric vertical (in the case of physical activation) or horizontal (in the case of chemical activation) tube furnace (Resiprel Lda.) controlled by a PID programmable temperature controller (RKC, REX-P96). Since an inert environment is required for the pyrolytic process, nitrogen flow was supplied throughout the entire process and the gas flow was controlled by an Omega flow meter. Carbon samples were obtained via chemical or physical activation or without activation step.
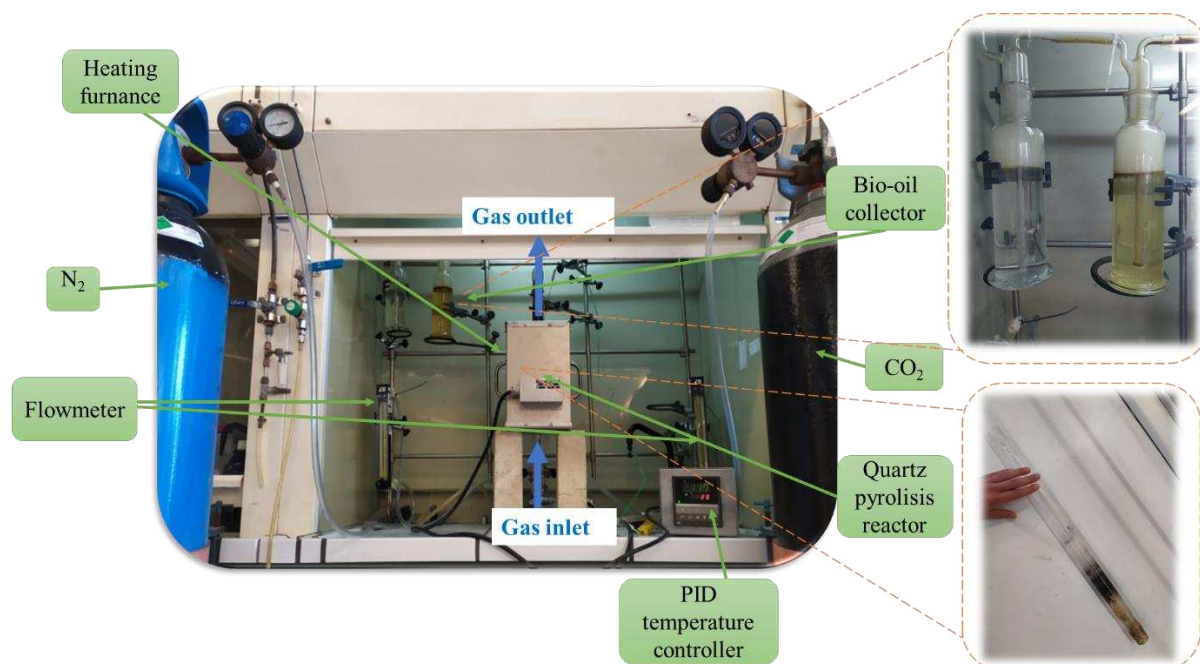
Figure 67. Experimental pyrolysis reactor.

Via chemical activation each type of biomass, coffee grounds (CG) or olive stones (OS), was mixed with K_2CO_3 (Riedel-de Haën, min. 99% purity) at a mass ratio of 1:3. The prepared mixture was transferred to the reactor and heated up to 800 °C at a heating rate of 10 °C/min in a flowing stream of N_2 (150 mL/min), shown as Step I in Figure 68. The activation process was maintained for 1 hour (Step II). After cooling, the obtained product was washed with

distilled water until the washing water presented a pH of around 5.7 (the pH of the deionized water used for the washing). The as-prepared activated carbon was oven-dried at 105 °C for 24 hours. The obtained samples were referred to as follows: AC-K$_2$CO$_3$-CG for the coffee grounds and AC-K$_2$CO$_3$-OS for the olive stones.
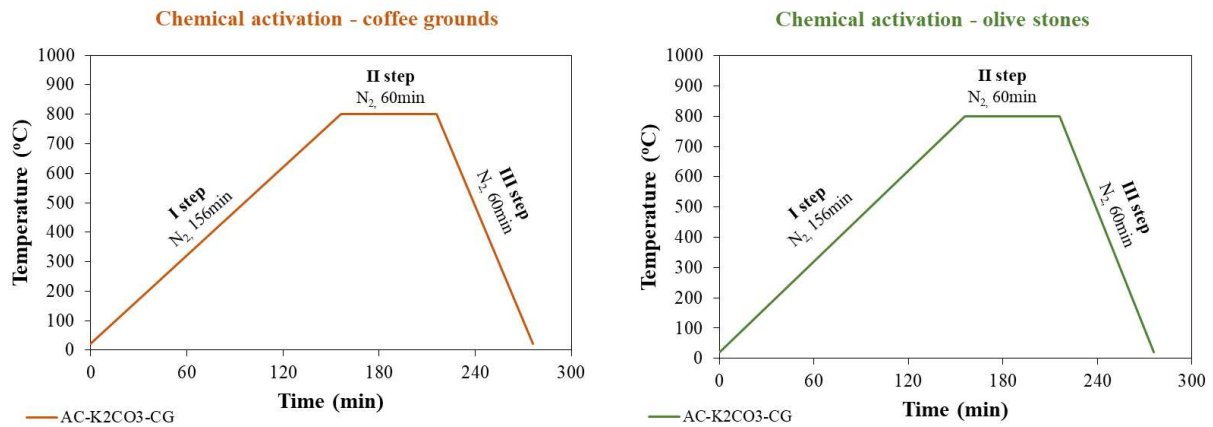
Figure 68. The chemical activation process for coffee grounds and olive stones.

Figure 69. (a) Coffee grounds and (b) olive stones mixed with potassium carbonate and (c) vacuum filtering to remove chemical activation agent.

Via physical activation, 10 g of biomass was placed into the reactor and heated at 5 °C/min under an N_2 flow of 150 mL/min (Step I in Figure 70). After reaching 500 ºC, the temperature was kept constant to facilitate the pyrolysis (carbonization) process for 1 hour (Step II). In Step III, the temperature was raised to 800 °C at a heating rate of 10 °C/min. After reaching 800 °C, the N_2 flow was stopped, and the CO_2 was turned on with a flow of 100 mL/min (Step IV). The activation process lasted from 1 to 2 hours in the case of coffee grounds and for 3 hours in the case of olive stones. After that, CO_2 was changed again to N_2 until room temperature was

reached. The obtained samples were labeled AC-CO_2(1h)-CG and AC-CO_2(2h)-CG for the coffee grounds and AC-CO_2-OS for the olive stones.
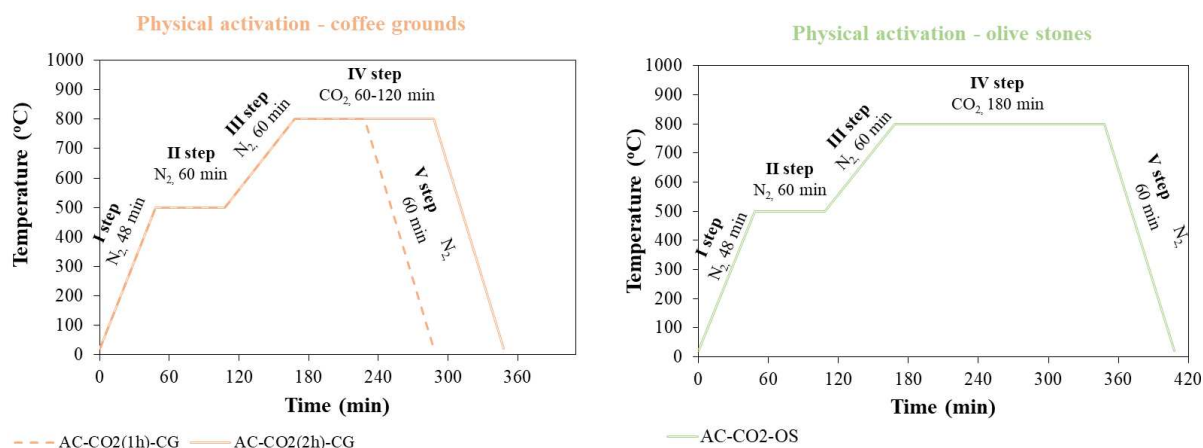
Figure 70. The physical activation process of coffee grounds and olive stones.

To study the influence of the activation on one of the precursors, coffee grounds were subjected to the carbonization process at 500 ºC with retention times of 15 minutes and 2 hours, without any further activation steps. Obtained biochars were labelled as B(15')-CG and B(2h)-CG.

All the prepared samples were sieved again and milled until the material passed 500 μm; they were then kept in air-tight containers at room temperature (20 °C). The preparation conditions of the different activated carbons used in this study are summarized in Table 17.

Table 17. List of prepared samples and experimental conditions.

Sample name	Type of precursor	Type of activation	Activation time (h)	Process time[a] (min)	Activation or carbonization temperature (°C)
AC-K_2CO_3-CG	Coffee grounds	chemical	1	216	800
AC-K_2CO_3-OS	Olive stones	chemical	1	216	800
AC-CO_2-OS	Olive stones	physical	3	348	800
AC-CO_2(2h)-CG	Coffee grounds	physical	2	288	800
AC-CO_2(1h)-CG	Coffee grounds	physical	1	228	800
B(2h)-CG	Coffee grounds	-	-	168	500
B(15')-CG	Coffee grounds	-	-	63	500

[a] Time considered from the beginning of heating up to the end of the pyrolysis or activation process.

The yield (%) of each sample, which is defined as the weight of the final product divided by the mass of the raw material [70], was calculated using Eq.   (3):

$$Yield\ (\%) = \frac{W0}{Wp} * 100$$

(3)

Where W_0, is the mass of the raw material and W_p is the mass of the sample at the end of the process.

4.4.3. Characterization of biochars and activated carbons

Morphology (SEM), thermal properties (TGA/DTG), textural properties (BET, applying N_2 and CO_2), phase identification (XRD), chemical surface (FTIR and pHpz), moisture, volatile matter and ash content were analyzed according to the procedures described in chapter 2.3.

4.4.4. Depolluting properties evaluation

The VOC adsorption properties of each sample were tested at a controlled temperature (20 ± 2 °C) and a relative humidity (RH) of 50 ± 5%. To ensure that all the samples had a homogeneous distribution of sorbent, a fixed mass of 50 mg was first mixed with 5 ml of distilled water in a beaker and placed in the ultrasound bath. After 5 min, the mixture was poured into a Petri dish and the beaker was washed with an additional 2 ml of water to make sure that all content had been transferred; it was then placed in the oven at 105 °C for 12 hours. Depolluting properties were then evaluated following the procedure shown in Figure 71 by means of MEK and toluene adsorption. The VOC adsorption properties of each sample were tested at a controlled temperature (20 ± 2 °C) and a relative humidity (RH) of 50 ± 5%. Depolluting properties were evaluated in terms of the adsorbent properties in a batch reactor, according to the modified method used in previous works [71], [72], [73]. Briefly, after drying, each sample was placed on the sample holder in the 17 L sealed glass chamber (reactor). 1μl of one type of VOC was injected into the reactor utilizing a micro-syringe to ensure an initial concentration of around 16 ppm (± 1 ppm) for MEK and 14 ppm (± 1 ppm) for toluene, after evaporation. A fan was placed in the bottom of the reactor to guarantee continuous air

recirculation. To monitor changes in the VOCs concentration over time, a photoionization detector (PID) (Aeroqual, Series 900, 0–30ppm range) was used. A blank test was performed before each analysis to control the concentration during the analysis.
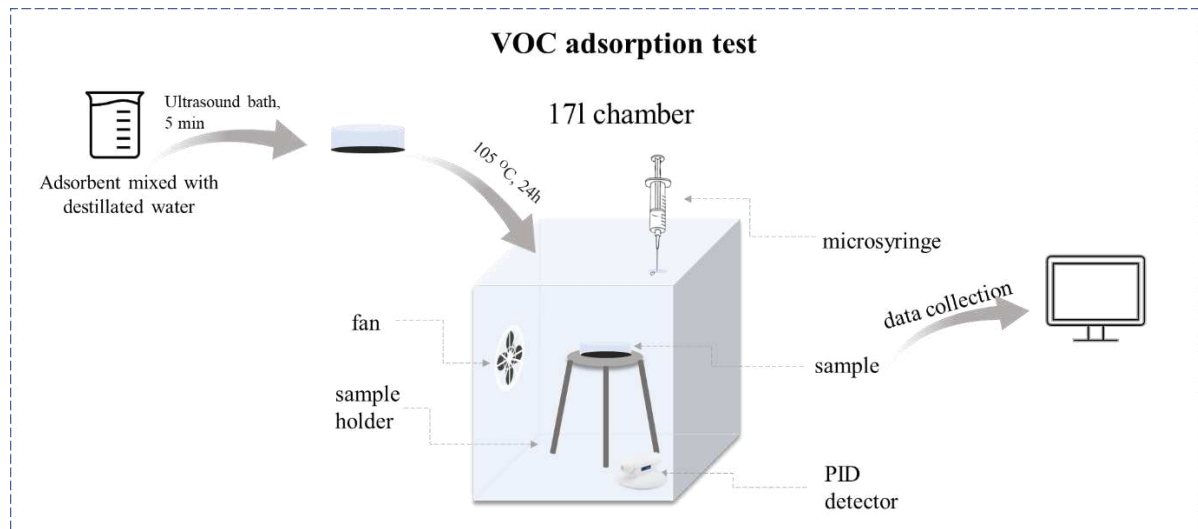
Figure 71. Experimental chamber for VOC adsorption.

The percentage of each adsorbed VOC was calculated according to the difference between the concentrations after the end of monitoring (C_t) and the concentration recorded at the beginning of the test (C_0) according to Eq. (4):

$$VOC\ adsorbed\ (\%) = \frac{Ct - C0}{Ct} \times 100 \qquad (4)$$

The value of VOCs uptake (mg/g) after the end of test is determined using Eq. (5) [7]:

$$qe = \frac{C0 - Ce}{W} \times V \qquad (5)$$

Where C_0 (ppm) is the initial gas phase concentration of VOCs and C_e (ppm) is the gas phase concentration of VOCs at equilibrium; V is the interior volume of the test chamber in liters (17 L), and W is the mass of the sample (0.05 g).

The reusability of the samples was evaluated after their exposure to VOCs for 90 min (Cycle I). The used samples were dried at 100°C for one hour and then reused to assess their performance (Cycle II).

4.5. Results and discussion

4.5.1. Thermogravimetric analysis

Figure 72 shows the evolution of the sample mass (TGA) and its derivative (DTG) over time during the pyrolysis of CG and OS under inert conditions (N_2).

The thermal degradation can be divided into three (in the case of OS) and four (in the case of GC) regions. Both TGA curves of coffee grounds and olive stones first present a mass loss of around 10 % up to 150 °C, which is related to the loss of moisture and highly volatile organic compounds [74]. Two peaks in the DTG plot of the olive stones, with the maxima at 276 °C and 324 °C, and two peaks in the DTG plot of coffee grounds at 304 °C and 346 °C represent the degradation of hemicellulose and cellulose, respectively. As previously reported, hemicellulose mainly decomposes at 220–315 °C, and cellulose mainly decomposes at 315–400 °C [9]. The simultaneous degradation of lignin, the third main component of the biomass, occurred in the temperature range of 160–900 °C [75] with the maximum peak at 391 °C representing the fourth degradation region of the coffee grounds. The devolatilization of biomasses is related to the differences in the elemental and chemical compositions of the two samples. Under higher temperatures, the material is quite stable, with an insignificant loss of mass (3%) corresponding to the loss of oxygen molecules. The following results provide insight into the carbonization temperature range required for the production of activated carbon and indicate that 800 °C is sufficient to completely remove the volatile matter, as, after 500 °C, both materials show only slight weight loss, as also reported in [59] and [76].
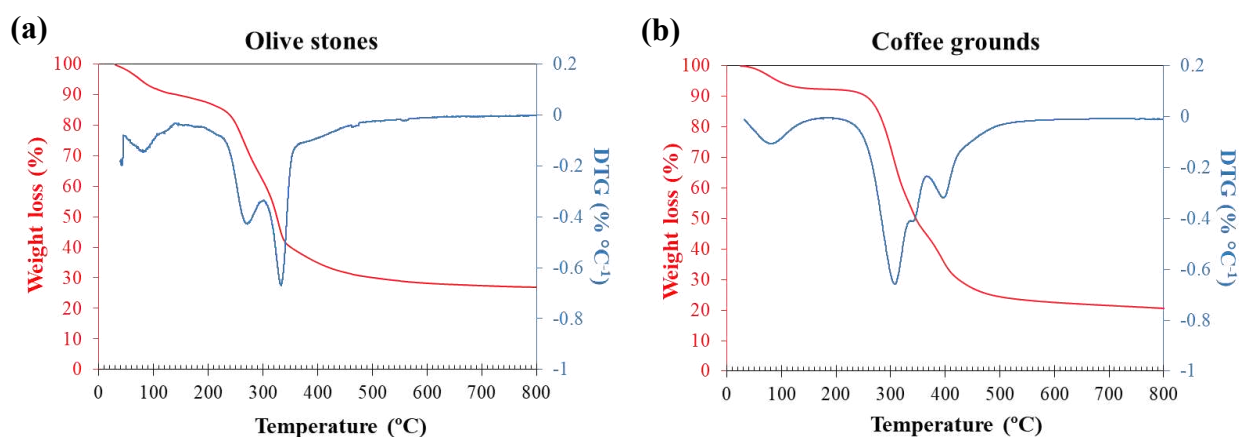
Figure 72. Thermogravimetric analysis (TGA) and differential thermogravimetry (DTG) curves of (a) olive stones and (b) coffee grounds.

4.5.2. Morphology and elemental study

Figure 73 shows SEM pictures of coffee grounds, olive stones, biochars, and activated carbons (physical/chemical). Coffee grounds (Figure 73a) and olive stones (Figure 73h) have a bulky morphology with a rather smooth surface and no pores. After the thermal treatment, there was a change in the morphology in all the samples, and a porous structure featuring large cavities with an entrance of several micrometers was formed, exhibiting a heterogeneous structure. These cavities result from the reaction of activating agents and carbon atoms in the precursors [77] and serve as channels, allowing the molecules of the adsorbate to reach pores located in the interior of the carbon [78]. In the case of olive stones, the structure is characterized by a thick wall structure with rough edges [79]. The pore dimensions of AC-K_2CO_3-CG, shown in Figure 73d and Figure 73e, are smaller than those of the rest of the carbon samples. As a result, an increasing number of activating agents causes the structure to exhibit a merging of the micropores and the development of mesopores. Similar results were observed previously in [80].

It was reported that, after dispersion on the surface, K_2CO_3 undergoes crosslinking condensation reactions with the cellulosic internal structure of the precursor in an inert environment above 600 °C, leaving the non-penetrating pores [60]. According to the reported literature, the associated reaction is presented as follows:

K_2CO_3 +2C → 2K + 3CO

115
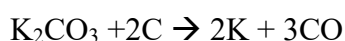
The metallic potassium could further develop porosity via intercalation through carbon sheets to enlarge the pores [81].

In contrast, during physical activation, at high temperatures, carbon atoms and CO_2 activator form $CO + H_2$ or CO to form a porous structure [82].
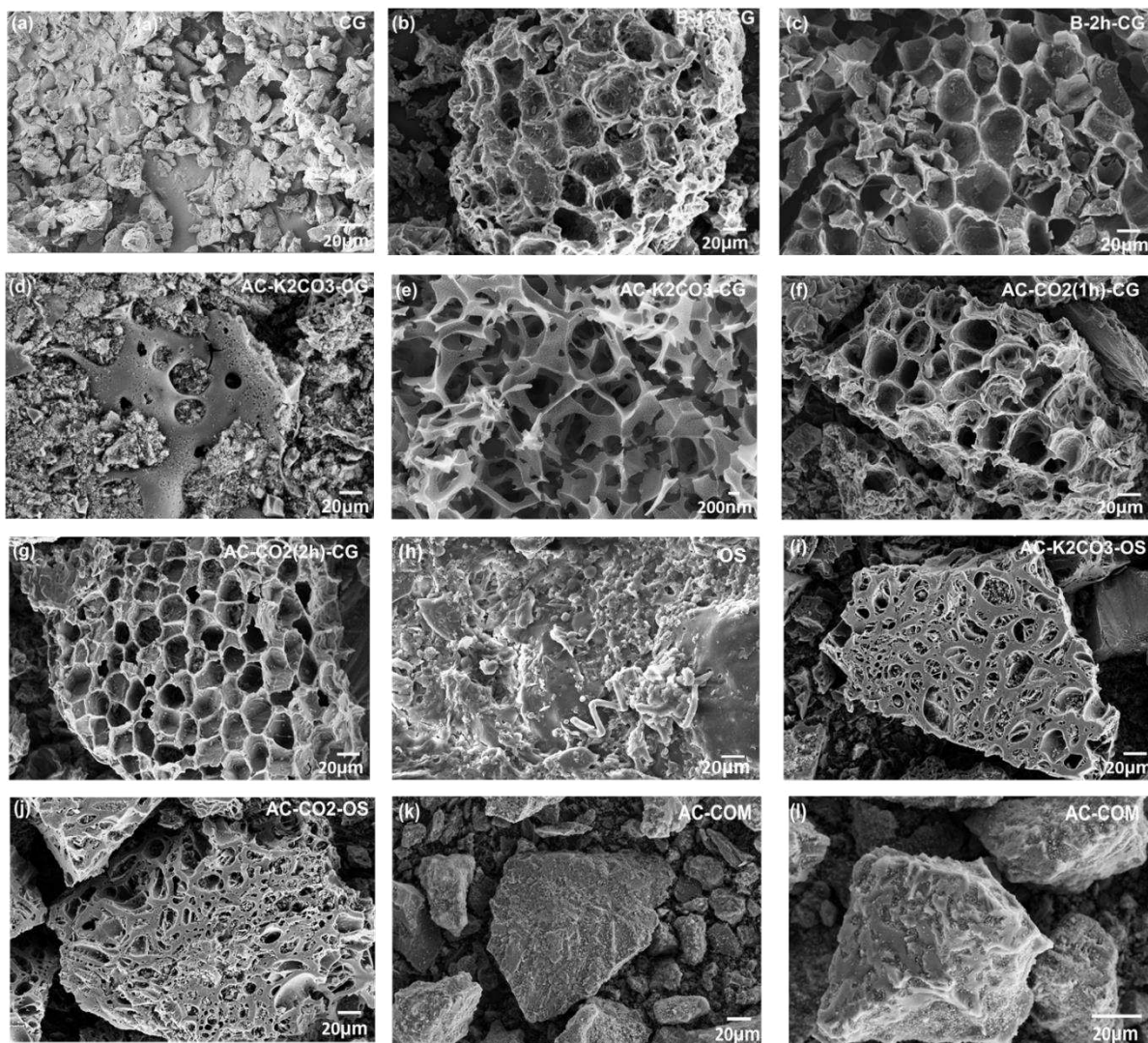
Figure 73. SEM images of (a) CG, (b) and (c) CG—biochars, (d) and (e) CG after chemical activation, (f) and (g) CG after physical activation; (h) OS, (i) OS after chemical activation, and (j) OS after physical activation; (k) and (l) commercial activated carbon at MAG 1.00Kx.

Appendix Table 4.1. summarizes the elemental analysis and O/C atomic ratios of all the samples. Figure 74a shows the main elements contained in the samples, selected from those detected via EDX (C, O, Mg, K, S, Ca, P). As expected, carbon and oxygen are the main elements of the biomass precursors composed of lignocellulosic components. Both types of

biomasses have high carbon content, at approximately 60%. After pyrolysis and activation, the carbon content increases to 80–90% and the content of oxygen decreases from 41 to 45 to 10–14%. The activation time did not significantly affect the carbon content (differences between 3 and 7% are considered negligible). The highest carbon content characterizes AC-K$_2$CO$_3$-CG (88.89%) and AC-K$_2$CO$_3$-OS (88.74%), while the lowest was obtained for biochar B-2h-CG (82.11%). The atomic ratio O/C was used to evaluate the hydrophilicity and polarity of the carbons, which, after carbonization and activation, decreased from 0.51–0.54 O/C to 0.08–0.12 O/C, indicating the successful removal of oxygen-containing functional groups and the hydrophobic nature of the produced carbonaceous samples. The low potassium content in the chemically activated carbons, which was comparable to other samples, indicates sufficient washing. Figure 74b clearly shows that, after activation and with the increasing duration of the process, the carbon content slightly increases; however, when comparing all the activated samples, the process time exhibits no dependence on the carbon content.
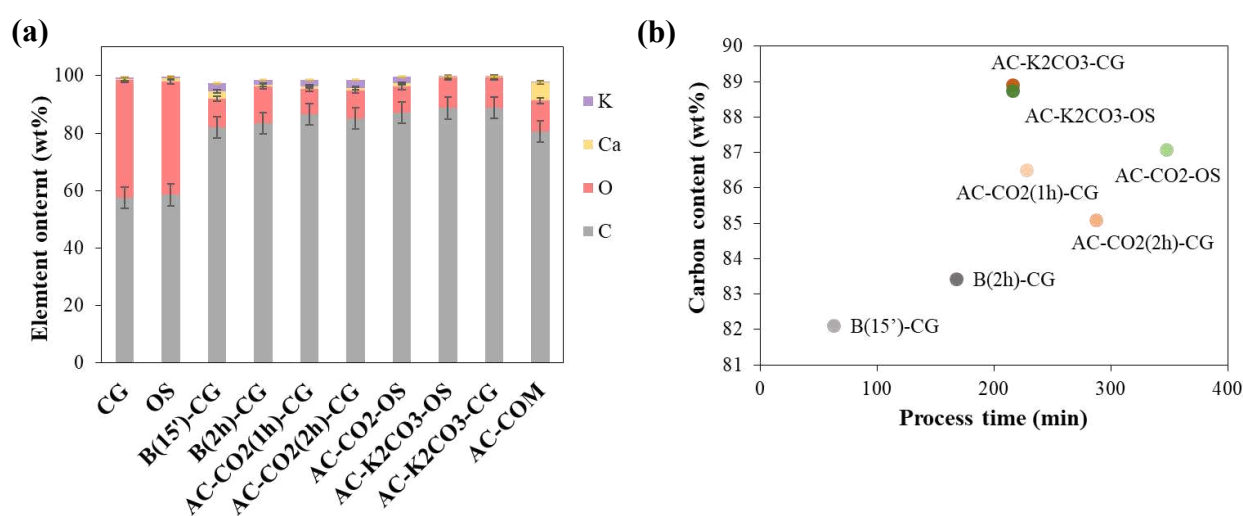
Figure 74. Elemental analysis (a) and (b) effect of the process time on the carbon content.

4.5.3. Process yield and proximate analysis

From the industrial point of view, it is important to evaluate the carbon yield to determine whether the material is feasible for large-scale applications. The mass yields of the obtained samples (Table 18) ranged from 17% to 30%. An increase in the pyrolysis time from 15 minutes to 2 hours decreased the yield of the product from 28% to 24%. These values are similar to those previously obtained [83] from the pyrolysis of coffee grounds at 450 °C and a retention time of two hours. Despite the use of different precursors, the duration of physical

activation did not influence the product yield of the activated carbon samples, which ranged from 20% to 21%. In this work, the highest product yield was observed when using the chemical activation of olive stones as a precursor (30%); comparing it to biochar samples with similar yields indicates that the activation exerted a slight influence. This conclusion was also confirmed by the authors of [74], who proved that the solid fraction (biochar) is reduced rapidly during the initial stages of the pyrolysis process (between 200 °C and 400 °C) while the quantity of gas and oil increases, and the application of higher temperatures resulted in a progressive but less significant reduction in the solid fraction. The same precursor, when activated by physical activation, resulted in a 9% lower product yield (21%). In the case of coffee grounds, the yields of the product activated via both methods were similar: 17% in the case of chemical activation and 20% in the case of physical activation.

The proximate analysis data collected in Table 18 shows the high volatile fraction of the precursors (77%–78%), which was significantly reduced after pyrolysis (28%–35%), chemical (18%–19%), and physical (16%–23%) activations. The key parameters influenced by the volatile matter content were the temperature and process time. The lowest volatile matter content was found in $AC-CO_2-OS$, which was produced over the longest process time (three hours). Increasing the duration of carbonization would release the volatile compounds that were still left. On the other hand, after the thermal treatment, the fixed carbon content increased from 12%–14% to 56%–69%. The experimental results also show that, because of volatile matter release, the ash content of the CG-derived carbons increased from 0.6% to 5.7%, but, after chemical activation, it was only two times higher. This difference in ash content was much lower in the case of the olive-stone-derived samples that underwent chemical (1.6%) and physical (0.9%) activation and raw olive stones (0.6%). A high ash content was observed in the biochar samples (4.1%–4.5%) and physically activated carbons (5.6%–5.7 %), since no washing was performed on the resulting carbons.

pH_{pzc} is the parameter that indicates the carbon sample's inherent acidic or basic nature and the degree of oxidation. After chemical activation ($AC-K_2CO_3-CG$ and $AC-K_2CO_3-OS$), the samples exhibit a neutral character. Meanwhile, the samples that underwent physical activation, as well as the biochars, show significantly alkaline characteristics; this is mainly related to their higher ash content.

Table 18. Yield (wt%), proximate analysis (wt%), and pHpzc of the precursors and carbon samples.

Sample	Yield (%)	Moisture (wt%)	Volatile Matter (wt%)	[a]Fixed Carbon (wt%)	Ashes (wt%)	pH$_{pzc}$
AC-K$_2$CO$_3$-CG	17	22.1	19.2	57.5	1.2	6.7
AC-K$_2$CO$_3$-OS	30	11.7	17.9	68.8	1.6	7.7
AC-CO$_2$-OS	21	10.3	15.5	73.3	0.9	9.3
AC-CO$_2$(2h)-CG	20	10.5	23.2	60.6	5.7	10.4
AC-CO$_2$(1h)-CG	20	9.9	22.4	62.1	5.6	9.4
B(2h)-CG	24	5.7	27.8	62.0	4.5	10.7
B(15')-CG	28	5.4	34.5	56.0	4.1	10.5
CG	-	9.4	78.0	12.0	0.6	n.d.
OS	-	8.0	77.0	14.0	0.5	n.d.
AC-COM	-	6.9	11.0	76.0	6.1	[b]Basic

n.d. = not determined

[a] fixed carbon= 100 - (moisture + volatile matter + ashes)

[b] declared in the datasheet

4.5.4. Textural properties

Textural properties, such as the specific surface area (SSA), total pore volumes (V$_{total}$), micropore volume (V$_{micro}$), and mesopore volume (V$_{meso}$), obtained from N$_2$ adsorption–desorption isotherms, are listed in Table 19. The SSA and V$_{total}$ followed the pattern of AC-K$_2$CO$_3$-CG > AC-CO$_2$-OS > AC-K$_2$CO$_3$-OS > AC-CO$_2$(2h)-CG. As expected, the use of a chemical activation process led to the development of higher porosity, indicating that K$_2$CO$_3$ is a more effective activating agent than CO$_2$, and these samples resulted in a higher surface area. The activation via K$_2$CO$_3$ does not have the same effect on the two biomasses, being much more effective for coffee grounds that exhibit the highest surface area of 1597 m^2/g and the highest total pore volume of 0.736 cm^3/g. However, as reported by Hayashi et al. [60], the structure of carbon depends on the precursor used in the production process. K$_2$CO$_3$ is reduced more easily by disorganized carbon than by crystalline carbon. Consequently, it can be assumed that coffee grounds have a less crystalline structure, so that K$_2$CO$_3$ was able to remove more carbon as CO gas, leading to the formation of a higher specific surface area. This hypothesis was later confirmed by the XRD spectra shown in Figure 77.

All the materials possess significant micropore content, ranging from 79–80% for the chemically activated carbons and 82–92% for the physically activated carbons. On the other hand, the biochars (B(2h)-CG and B(15')-CG) appeared to be non-porous or microporous

materials due to very low amounts of adsorbed N_2. Adsorption and desorption isotherms of N_2 are shown in Figure 75. According to the IUPAC (International Union of Pure and Applied Chemistry) classification, all the isotherms exhibited Type I behavior, confirming a predominance of micropores. AC-K_2CO_3-CG features a small hysteresis loop of type H4 and low levels of deviation from the plateau region in the isotherm plots, which is related to the micro-/mesoporous structure of carbon [84]. The hysteresis loops of AC-K_2CO_3-OS, AC-CO_2(1h)-CG, and AC-CO_2(2h)-CG were not closed, perhaps due to the lower content of mesopores [16]. The high adsorption values occurred at a low value of relative pressure: nearly 0.1 for AC-CO_2-OS and 0.05 for the rest of the carbons. The isotherms remain nearly horizontal over a range of P/P_0, approaching unity, and the total pore volume is well-defined [85].
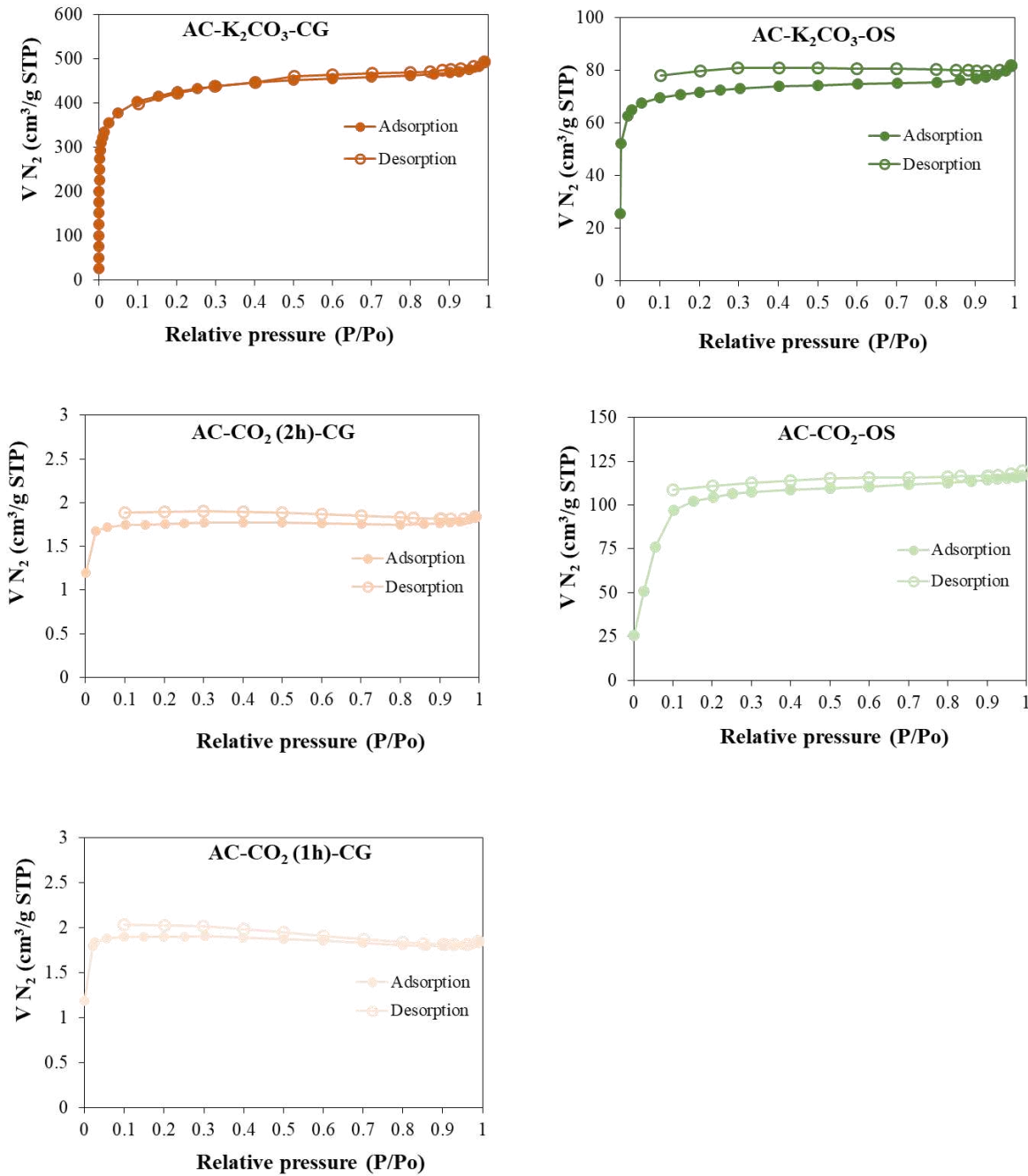
Figure 75. Adsorption-desorption isotherms.

The highest specific surface area (1487 m^2/g) and total pore volume (0.527 cm^3/g) obtained from CO_2 adsorption were exhibited by AC-K_2CO_3-CG, followed by AC-K_2CO_3-OS, AC-CO_2-OS, AC-CO_2(2h)-CG, AC-CO_2(1h)-CG, B(2h)-CG and B(15')-CG, with values of 870 m^2/g, 778 m^2/g, 716 m^2/g, 649 m^2/g, 331 m^2/g, and 251 m^2/g, respectively. The differences in the obtained values for pore volume and specific surface area between N_2 and CO_2 adsorption result from the different kinetic diameters of the two molecules: N_2 0.364 nm and

CO_2 0.330 nm [86]. These results indicate that the microporous carbon samples contain narrow micropores (<0.7 nm) that only CO_2 can penetrate, while nitrogen cannot access them under cryogenic conditions. On the other hand, because of the high saturation pressure of CO_2 at 273 K, low-pressure (up to atmospheric pressure) experiments are limited to the analysis of pores <1.5 nm [87], hence the lower values of SSA and V_{total} of AC-K_2CO_3-CG, in which larger pores were also developed.

Table 19. Textural properties of the samples.

Sample	N_2				CO_2		
	[a]SSA m²/g	[b]V_{total} cm³/g	[c]V_{micro} cm³/g	[b]V_{meso} cm³/g	[d]SSA m²/g	[d]V_{total} cm³/g	[d]V_{narrow} cm³/g
AC-K_2CO_3-CG	1597	0.736	0.580	0.156	1487	0.527	0.24
AC-K_2CO_3-OS	274	0.121	0.097	0.024	870	0.221	0.17
AC-CO_2-OS	432	0.181	0.148	0.033	778	0.205	0.16
AC-CO_2(2h)-CG	159	0.063	0.057	0.006	716	0.184	0.14
AC-CO_2(1h)-CG	173	0.064	0.059	0.005	649	0.159	0.13
B(2h)-CG	n.d.	n.d.	n.d.	n.d.	331	0.088	0.07
B(15')-CG	n.d.	n.d.	n.d.	n.d.	251	0.070	0.05
AC-COM	[e]1200						

SSA= specific surface area, V_{total} = total pore volume, V_{micro} = micropore volume; V_{meso} = mesopore volume; n.d. = not determined
[a] Determined via the BET equation (P/Po < 0.1).
[b] Single-point adsorption total pore volume of pores smaller than 40.6 nm at P/P_0=0.95.
[c] Measured using the t-plot method.
[d] Determined via the DFT method.
[e] Declared in the datasheet.

The type of activation had a significant effect on the specific surface area and pore structure. Compared with non-activated samples B-(15')-CG and B-(2h)-CG, the specific surface area of the physically and chemically activated carbons, was two to three and three to six times higher, respectively. Moreover, the curves of the pore size distribution (Figure 76) obtained according to the DFT (density functional theory) method from N_2 (Figure 76a) and CO_2 (Figure 76b) adsorption indicate that most of the pores of all samples have sizes smaller than 2 nm and are located in the microporous region. Additionally, the presence of narrow pores in the range of 0.3–0.7 nm illustrates the highly tunable nature of carbon. Samples AC-K_2CO_3-OS, AC-CO_2-OS, AC-CO_2(2h)-CG, AC-CO_2(1h)-CG, B-(2h)-CG, and B-(15')-CG exhibit two distinctive peaks, which indicate the presence of two pore fractions (Figure 76b). The first is distributed between 0.30 nm and 0.45 nm and the other between 0.45 nm and 0.75 nm.

Meanwhile, AC-K$_2$CO$_3$-CG is characterized by a wider pore size distribution, up to 3 nm, with the main fraction distributed between 0.45 nm and 0.75 nm.
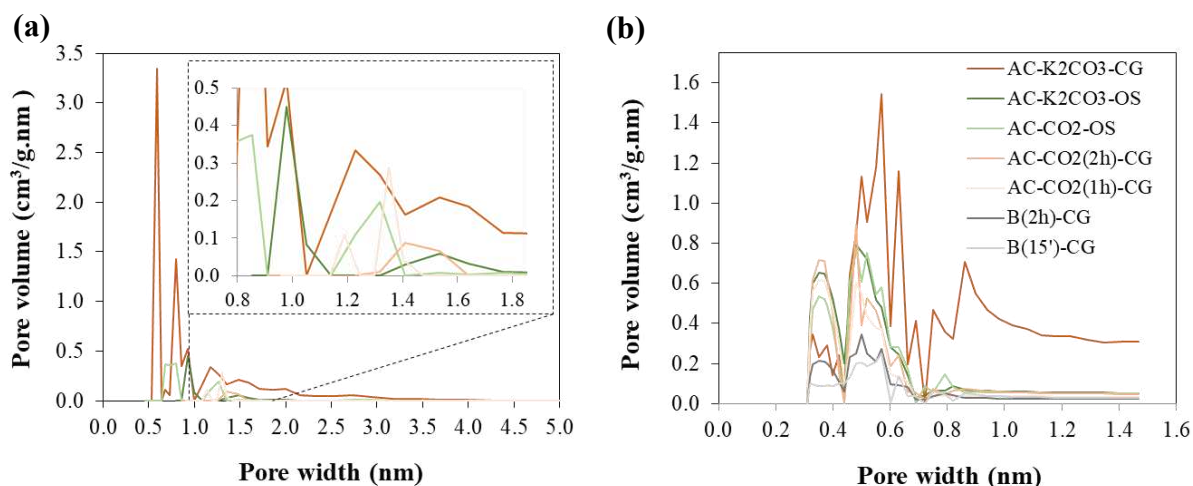
Figure 76. The pore size distribution of the produced samples was measured with (a) N$_2$ and (b) CO$_2$ using the DFT method.

4.5.5. X-ray diffraction phase identification

Figure 77 displays the XRD spectra of the carbon materials. Two broad diffraction maxima, attributed to the amorphous carbon and graphite, are demonstrated by broad peaks at 23–25° and 43–44°, corresponding to the diffraction of C (002) and C (101), respectively [88]. In the case of the biochar samples (B(2h)-CG and B(15)'-CG), no peak was found at 43°, and, for AC-K$_2$CO$_3$-CG, AC-CO$_2$(1h)-CG, and AC-CO$_2$(2h)-CG, the intensity of the peak was very low. The intensity of the peak at 43° of the commercial activated carbon (AC-COM) is equal to that detected for AC-K$_2$CO$_3$-OS and A-CO$_2$-OS. The difference in the XRD patterns between the other samples suggests that the activation process, the time of the process, and the type of precursor affected the microcrystalline structure.
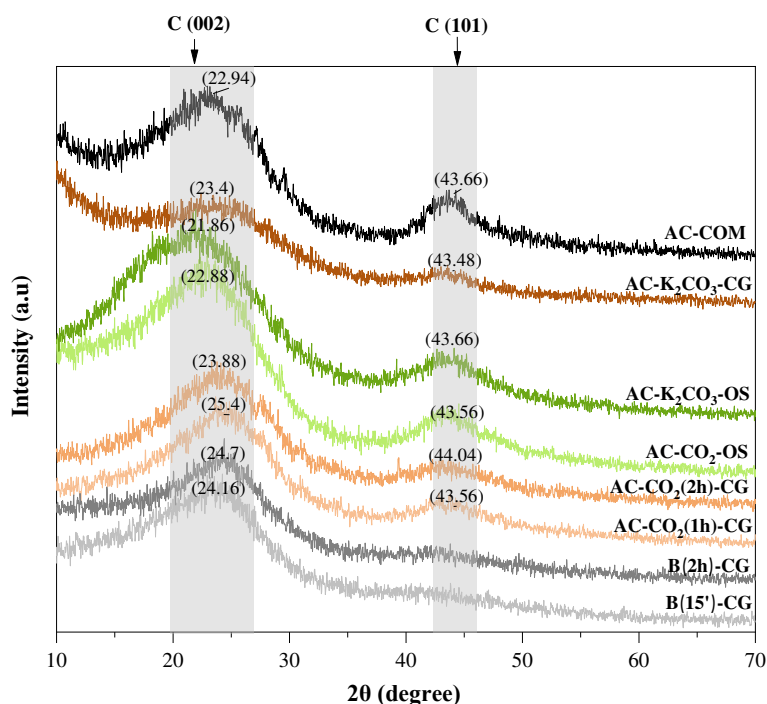
Figure 77. XRD spectra of commercial activated carbon and of the samples obtained from olive stones and coffee grounds.

4.5.6. Chemical surface analysis

The FTIR spectra are presented in Figure 78 and Figure 79, where the established functional groups contained in the coffee grounds, olive stones, and produced samples are identified. As reported in [65], due to the strong infrared absorption of carbon, the background absorption is highly significant; as such, it is quite difficult to identify the intrinsic peaks of the surface functional groups. However, it can be observed that, after carbonization and activation, the functional groups on the surface changed. The broad bands with peaks observed at approximately 3369 cm^{-1} (for coffee grounds) and 3445 cm^{-1} (for olive stones), which are assigned to the O-H stretching of the cellulose, absorbed water, hemicellulose, and lignin, slowly disappear during pyrolysis (biochar samples), as the pyrolysis time increases and after the chemical activation. In the case of physical activation, the intensity is much lower with respect to the raw biomass. In the AC-CO_2-1h-CG sample, the peak is in fact centered at about 3000 cm^{-1}, indicating OH groups held by intramolecular H bonds; meanwhile, in the AC-CO_2-2h-CG sample, the peak is shifted to 3500 cm^{-1}, indicating OH groups free from H bonds. Therefore, this spectral trend is indicative of a conformational variation in molecules.

The bands at 2925 cm^{-1} and 2855^{-1} cm^{-1} for CG, 2918 cm^{-1} and 2851 cm^{-1} for B-(15')-CG, and 2957 cm^{-1} and 2929 cm^{-1} for OS, indicate the symmetric or asymmetric C-H stretching vibration of saturated aliphatic groups (alkane/alkyl) [89], which disappears after the activation step.

In the FTIR spectra of the olive stones, the peak of the carbonyl group is at 1743 cm^{-1}, and it is reduced considerably after activation, almost disappearing, to be replaced by the peak at 1569 cm^{-1}; this is prevalent in the AC-K$_2$CO$_3$-OS and AC-CO$_2$-OS samples. This spectral pattern could indicate an important structural variation in the molecule that can result from two factors: during the chemical activation, the carbonyl is replaced by the C=N group (1569 cm^{-1}) via a reaction with an amino group, or the molecule is arranged in such a way as to expose the surface aromatic groups, clearly visible with ATR spectroscopy, rather than the carbonyl groups. The band around 1500–1700 cm^{-1} could also correspond to aromatic C=C stretching. Similar findings were reported by Wei et al. [90]. The band around 1100–1300 cm^{-1} corresponds to the aromatic C-O stretching mode of C-OH and the carboxyl groups.

Moreover, small peaks at around 800 cm^{-1}, with higher values after the pyrolysis and activation processes, can be assigned to the vibration of an aromatic group and to the bending vibrations of C-H groups. Similar spectra for activated carbon samples are commonly reported in the literature [91], [65].

All activated carbons had similar IR transmittance spectra; however, the peak intensities were different, indicating that the produced ACs had similar surface chemical properties. Progressive changes in functional groups appear in both precursors, due to the degradation of hemicellulose, cellulose, and lignin, which are the main components of coffee grounds and olive stones. Successful aromatization caused by the decomposition and condensation of volatile matters after the carbonization and activation process [92] was also noted through the appearance of aromatic groups.
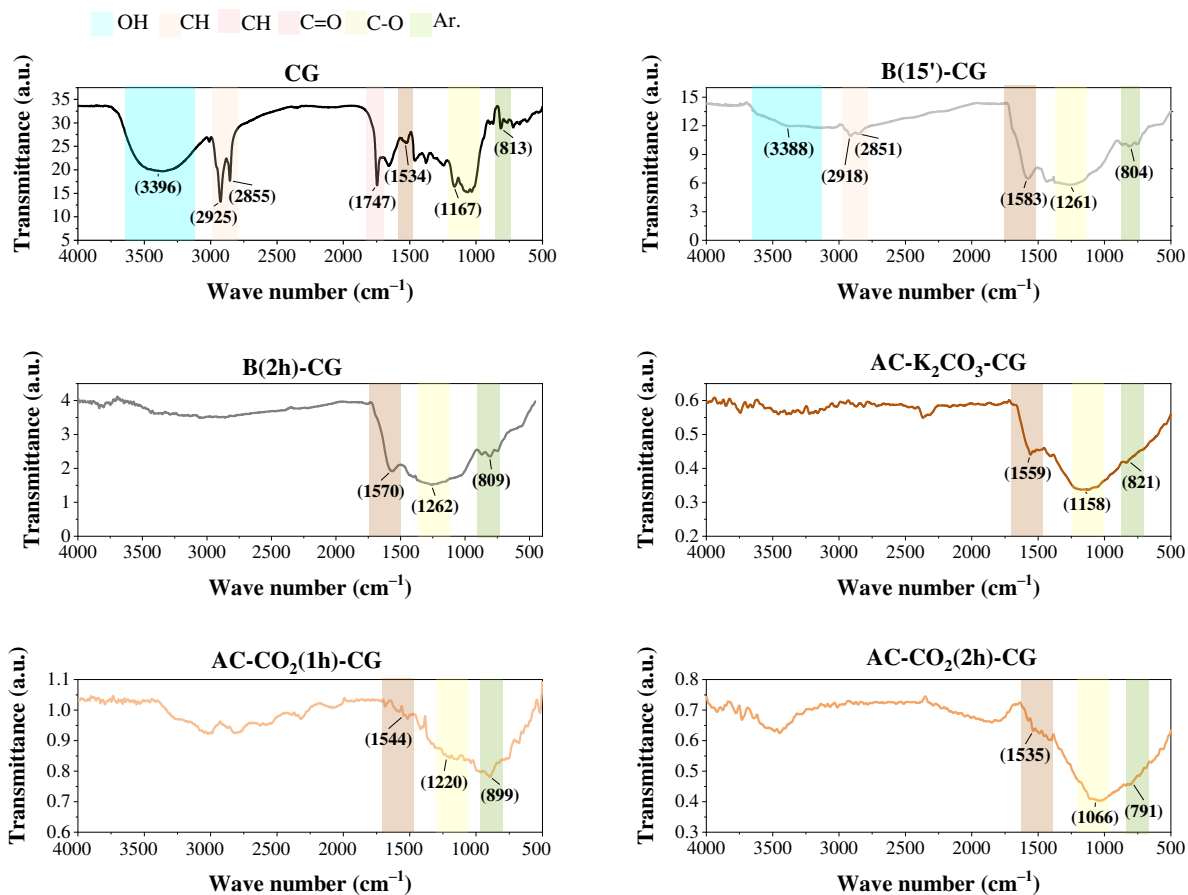
Figure 78. FTIR spectra of coffee grounds and produced biochars and activated carbons.
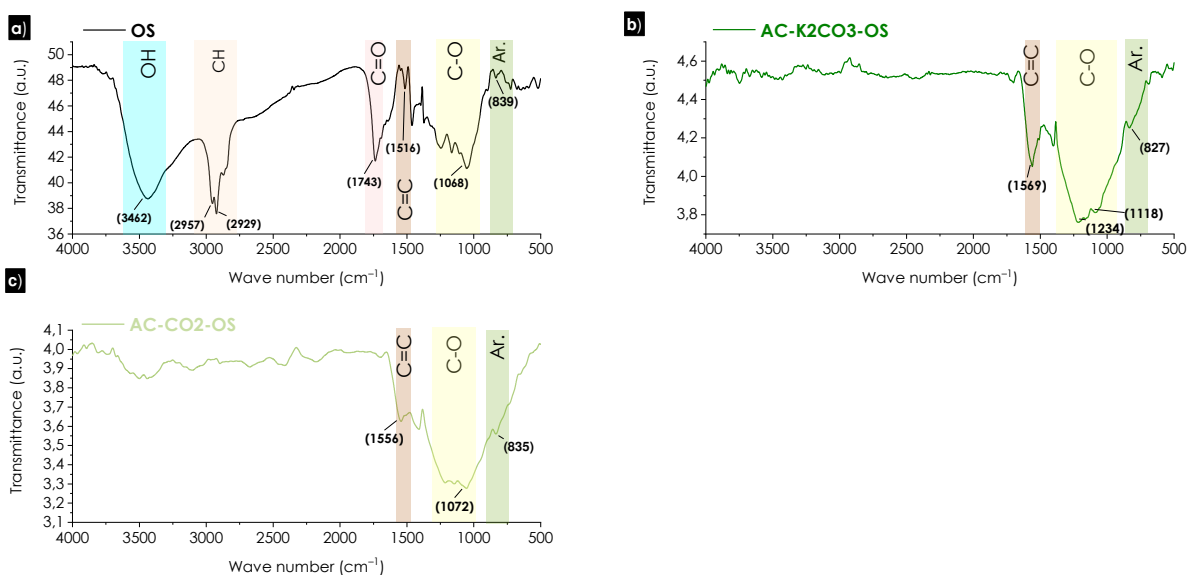
Figure 79. FTIR spectra of olive stones and produced activated carbons.

4.5.7. Depolluting properties

4.5.7.1. CO_2 adsorption

Figure 80 presents the CO_2 adsorption–desorption isotherms of the carbon samples under different conditions, at 273 K and under low relative pressures (P/P_0 <0.03). The desorption curves do not show hysteresis, indicating that the adsorption is fully reversible. The adsorption capacities are collected in Table 21. The sequence of the highest amount of adsorbed CO_2 is AC-K_2CO_3-CG > AC-K_2CO_3-OS > AC-CO_2-OS > AC-CO_2(2h)-CG > AC-CO_2(1h)-CG > B-(2h)-CG > B-(15')-CG. These results correlate with the textural parameters. The biochar samples showed the weakest ability to adsorb CO_2 molecules because they have relatively small surface areas: 251 m^2/g and 351 m^2/g for B-(15')-CG and B-(2h)-CG, respectively. The highest CO_2 uptake is observed for AC-K_2CO_3-CG which has the highest surface area and micropore volume, as shown in paragraph 4.8.4; this finding highlights that a large surface area and a high micropore volume are major factors in increasing CO_2 adsorption properties.

The CO_2 adsorption capacity of AC-K_2CO_3-CG reached 253 mg/g, a value 60% higher than that reported by [63], where the experimental conditions for the activated carbon samples were similar to those used in our research and the CO_2 adsorption properties were examined at 0 °C and 0.15 bar.

A similar CO_2 uptake has been obtained [62] where activated carbon produced via KOH impregnation reached 251 mg/g at higher pressures (1 bar). These values are aligned with those derived from the carbon material produced [56] from *Arundo donax* (plant-based precursor) via KOH activation at 1 bar and 273 K, and they are slightly lower than the activated carbon obtained similarly from coffee grounds [63], as presented in Table 16.
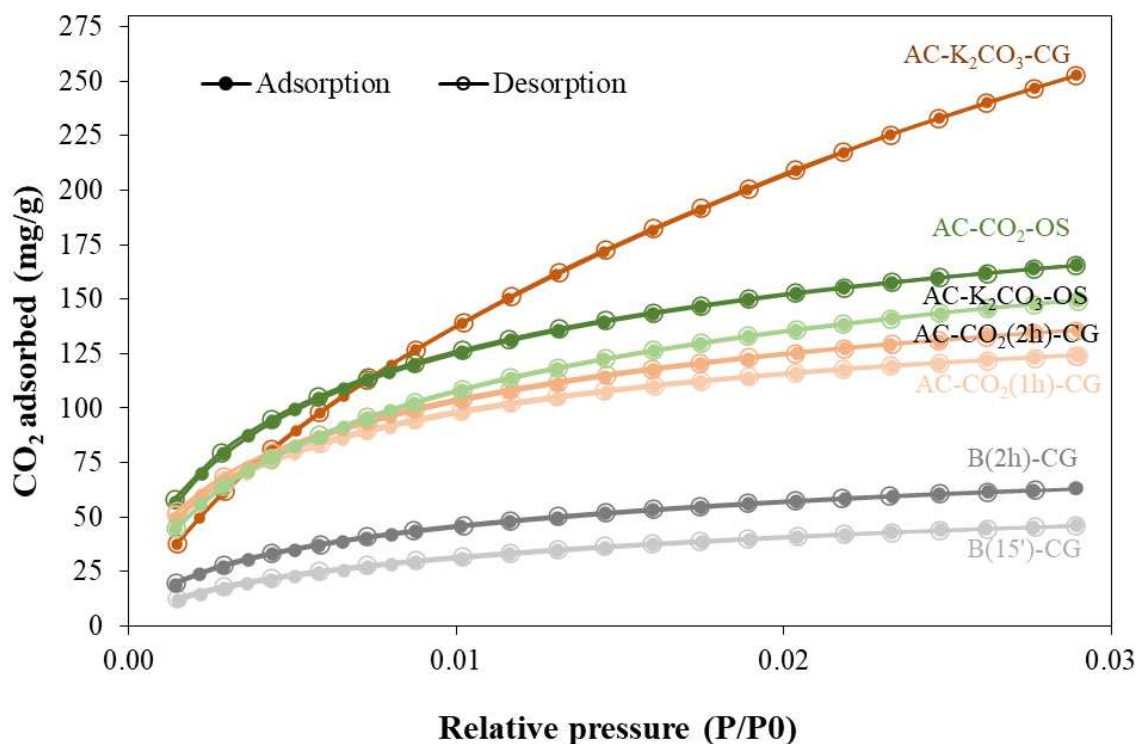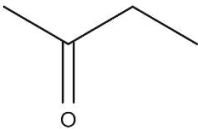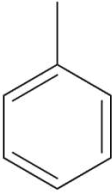
Figure 80. CO_2 adsorption–desorption isotherms at 0^oC (DFT method) and a relative pressure range from 0.00 to 0.03.

4.5.7.2. VOCs adsorption

Based on a chemical data sheet from the Occupational Safety and Health Administration (OSHA) [93], [94], [95] and from the American Conference of Governmental Industrial Hygienists (ACGIH) [96], [97], [98], acceptable levels of VOCs in the workplace and the physical properties of the adsorbates used in this work are collected in Table 20. Threshold limit values (TLVs®) refer to airborne concentrations of chemical substances and are based solely on health factors; they are determined by a non-governmental scientific association (ACGIH). They represent conditions to which it is believed that nearly all workers may be repeatedly exposed, day after day, over a working lifetime, without experiencing adverse health effects, while the PELs (permissible exposure limits) constitute the regulatory limits on the concentration of a substance in the air set by OSHA. These limit values are given as a TWA (time-weighted average) and refer to the concentration for a conventional 8-hour workday and a 40-hour workweek to which it is believed that nearly all workers may be repeatedly exposed, day after day, for a working lifetime, without experiencing adverse effects.

Whereas, as mentioned previously in chapter 1 (Table 1), ANSES indicates the following permissible limits of toluene concentrations 6 ppm (24h-mean) and 5 ppm (annual-mean).

Table 20. Physical properties and acceptable concentration limits of the selected adsorbates.

Adsorbate	Carbon dioxide	Methyl ethyl ketone	Toluene
Molecular structure	$O = C = O$		
Molecular weight	44 g/mol	72 g/mol	92 g/mol
Boiling point	-78.5 °C	79.6 °C	110.6 °C
Dipolar moment	0 D	2.76 D	0.31 D
Vapor pressure at 20 °C	716	71	21
Relative vapor density (air = 1)	1.53	2.42	3.14
[a]Kinetic diameter	0.330 nm	0.504 nm	0.568 nm
OSHA PEL - TWA	5000 ppm	200 ppm	200 ppm
ACGIH TLV - TWA	5000 ppm	75 ppm	20 ppm

OSHA = The Occupational Safety and Health Administration, PEL - TWA = Permissible Exposure Limits – Time Weighted Average, ACGIH = American Conference of Governmental Industrial Hygienists, TLV - TWA = Threshold Limit Values - Time Weighted   Average [a] [99]

The initial toluene (14 ppm) and MEK (16 ppm) concentrations applied in the adsorption tests, corresponded to 7% and 8% of the PEL–TWA limits (200 ppm for MEK and toluene) set by OSHA and to 70% and 21% of the TLV–TWA limits (75 ppm for MEK and 20 ppm for toluene) set by ACGIH.

Adsorption of MEK and toluene on produced samples has been shown on Figure 81 and Figure 82 for the first cycle of exposure and for the second cycle, after the regeneration of the materials, to evaluate the reusability of the activated carbon.

For sample AC-K$_2$CO$_3$-CG, the concentrations after 90 min of exposure to MEK were reduced to around 7 ppm, representing 59% of the initial concentration. These results are comparable to those obtained from commercial AC-COM, and AC-CO$_2$-OS which removed 56% and 55% of MEK. AC-K$_2$CO$_3$-OS, AC-CO$_2$(2h)-CG, AC-CO$_2$(1h)-CG presented lower adsorption properties: 48%, 40% and 36% respectively. Both biochar samples (B-15'-CG and B-2h-CG) show a negligible adsorption capacity: 7% and 5%, respectively.

The chemically activated samples' (AC-K$_2$CO$_3$-CG, AC-K$_2$CO$_3$-OS) and AC-COM's ability to adsorb non-polar toluene is similar to that for polar MEK, suggesting that chemical activation promotes polar and non-polar groups at carbons' surfaces. In the case of physically activated carbons, we noted a decrease in the adsorption: -15% for AC-CO$_2$-OS, -11% for AC-CO$_2$(2h)-CG, and -16% for AC-CO$_2$(1h)-CG.

Methyl Ethyl Ketone adsorption

Figure 81. (a) MEK adsorption (first and the second cycle) and (b) the relationship between specific surface area and adsorbed MEK.

Toluene adsorption

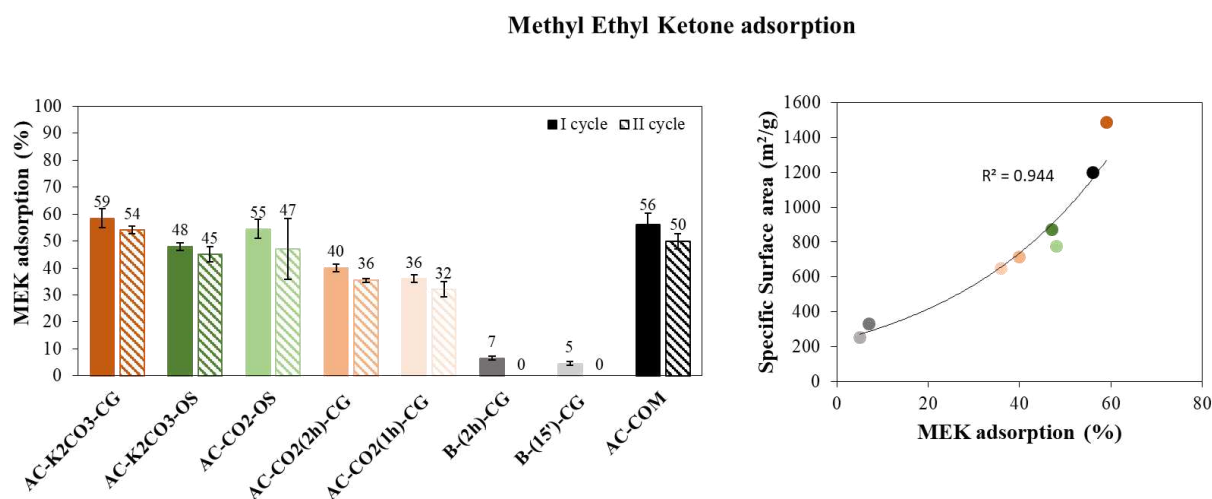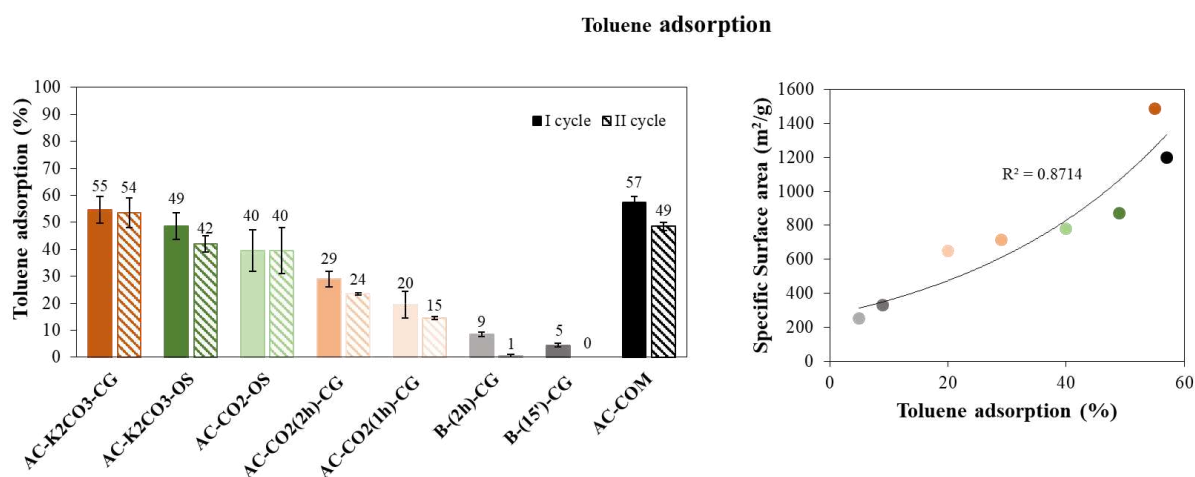*Figure 82. (a) Toluene adsorption (first and the second cycle) and (b) relationship between the specific surface area and adsorbed toluene.*

Other research study [100] specified that physical adsorption was noted to occur in three stages: (a) the adsorption of VOC molecules at the external surface of the adsorbent via convection,

axial dispersion, and particle diffusion. This rate is determined by the specific surface area. (b) The pollutant molecules can then diffuse through the porous structure of the activated carbon onto smaller pores. As reported elsewhere, the extent of the diffusion is dependent on the size of the molecules and the pore structure and volume of the activated carbon [101]. (c) In the final stage, the adsorbate is adsorbed onto the adsorbent and, when equilibrium occurs, the ratio of the micro-, meso-, and macropore volume is the dominant factor.

Adsorbent recyclability is another important indicator, as it determines the cost of the adsorption process and the possibility of commercialization.

Results obtained from adsorption by regenerated samples (Cycle II) still represent a fairly good ability to capture VOCs, implying that the spent materials can be reused in an eco-friendly way without much loss (maximum of 8%) in activity after the treatment. Similar results were obtained by Shah et al. [102], who found regeneration efficiencies greater than 90% at temperatures above 120 ºC for MEK; however, this was after a longer regeneration period (two hours), which is associated with higher energy consumption.

As demonstrated in Figure 81b and Figure 82b, the correlation coefficients are 0.94 and 0.87, indicating that the adsorption capacity of the VOCs increases with the increase of the specific surface area of the adsorbent. This is related to the fact that a larger specific surface area determines the presence of more pores on the carbon's surface, and VOCs can be captured more easily. Although micropores play a key role in the adsorption of VOCs at low concentrations (ppbv and ppmv) in indoor environments [78], mesopores in the AC-K2CO3-CG sample could also enhance the diffusion of the VOC molecules in the micropores [67], thus increasing the adsorption capacity.

The kinetic diameters of MEK and toluene are 0.504 nm and 0.568 nm, respectively. To better understand and illustrate which pores are able to capture both of these molecules, Appendix Table 4.2. presents the volume and percentage of pores larger than the kinetic diameter of MEK (>0.50 nm) and toluene (>0.57 nm) that were obtained using the previous DFT method. All the samples show a higher adsorption capacity for MEK, which is the adsorbate with the highest dipole moment. It has been also demonstrated that, for each type of produced carbon, there is a greater content of pores > 0.50 nm than >0.57 nm, which means that there are more possible active sites for MEK molecules than for toluene. In fact, a decrease of 11–16 % in toluene removal and 36–51 % in the adsorption capacity was observed for AC-CO_2-OS, AC-CO_2(2h)-CG, and AC-CO_2(1h)-CG. This phenomenon was not observed for AC-K_2CO_3-CG, AC-

K_2CO_3-OS, or AC-COM, for which the percentages of adsorbed MEK and toluene after 90 min reached almost the same values; however, the adsorption capacity decreased by around 11–18%.

The adsorption mechanisms of volatile organic compounds may be controlled by the following interactions: the hydrophobic effect, π–π bonds, hydrogen bonds, Van der Waals interactions, and covalent and electrostatic interactions [103]. Changes in adsorption can be explained by the presence of heteroatoms, which determine the apparent acidity or basicity of the activated carbon surface. As a result, molecules that interact with carbon in a specific way can adsorb more strongly and in greater amounts when the functional groups are present [104]. The adsorption performance of aromatic molecules with benzene rings takes place via the electron donor–acceptor reaction, involving π electrons on the activated carbon surface, aromatic rings, and basic functional groups (π-electron-rich functional groups), as demonstrated in [82] and [105]. On the other hand, the electron-withdrawing carbonyl group found in the produced sample may reduce its surface electron density on the graphite-like activated carbon layer, thus weakening the π–π conjugated effect between toluene and the adsorbent [106], [107].

The lower toluene adsorption recorded for the physically activated carbons may also be related to their lower aromaticity. The FT-IR results (Figure 78 and Figure 79) indicate that the intensity of the peaks associated with the aromatic C=C stretching for the AC-CO_2-OS, AC-CO_2(2h)-CG, and AC-CO_2(1h)-CG samples are lower than for AC-K_2CO_3-CG and AC-K_2CO_3-OS, indicating a larger number of aromatic groups, which may be responsible for the higher adsorption capacity.

Table 21. CO_2 and VOCs adsorption capacity.

Sample	CO_2 (mg/g)	MEK (mg/g)		Toluene (mg/g)	
		I cycle	II cycle	I cycle	II cycle
AC-K_2CO_3-CG	253	3210	2765	2618	2547
AC-K_2CO_3-OS	166	2611	2304	2332	1999
AC-CO_2-OS	145	2992	2406	1904	1880
AC-CO_2(2h)-CG	136	2176	1818	1380	1119
AC-CO_2(1h)-CG	124	1958	1638	952	690
B-(2h)-CG	63	381	0	428	24
B-(15')-CG	46	272	0	238	0
AC-COM	-	3046	2560	2618	2309

Table 16 compares the type of precursor, processing parameters, type of activating agents, and surface area of various activated carbons with depollution properties. The results obtained for the adsorption of VOC under static conditions were found to be comparably higher than the results of most other adsorbents in the literature. However, regarding VOC adsorption, there are only a few data obtained in conditions similar to those used in our study (low concentration of VOCs, a static adsorption setup) which try to simulate as better as possible a real indoor environment. Most adsorption data are collected under high concentrations (100 to 1000 ppm), which does not simulate the realistic indoor operating conditions (VOC concentrations in the range of the limits of TLV–TWA) at which gaseous indoor contaminant air cleaning devices/materials could be applied. In the study conducted by Takada [65], activated carbon produced from buckwheat hulls with an SSA of 1300 m^2/g was able to remove 36% of toluene after 90 min of exposure. However, a higher initial concentration was applied (220 ppm), and the adsorption capacity also depends on the initial concentration. As indicated in the literature, when the contaminant concentration in the air phase is low, the diffusion rate decreases. The VOC molecules instantly adsorb onto the particle surface, and they may not reach the innermost pores [108].

For instance, Shen [69] investigated the adsorption behaviors of ACs derived from banana peels on benzene and toluene at 25 °C. The adsorption capacities of the obtained carbons were 2149 mg/g and 2195 mg/g for benzene and toluene, respectively. However, a dynamic method of adsorption measurements was applied. Batur and Kutluay [68] produced AC from black cumin via chemical activation and explored its adsorption capacity for benzene, toluene, and xylene (BTX) vapors at low initial concentrations (20 mg/l for single- or 20 mg/l + 10 mg/l for multi-component systems). They observed that activated carbon shows a lower adsorption capacity in the multi-component system due to competitive adsorption, which depends on the properties of the VOCs (e.g., polarity, boiling point, molecular weight).

4.6. Conclusions

This work focuses on the valorization of biomass waste such as coffee grounds and olive stones in the frame of physical and chemical activation, as a sustainable approach to obtain activated carbon. The following conclusions were drawn based on the presented study:

a) The chemical activation of coffee grounds by K_2CO_3 (AC-K_2CO_3-CG) at 800 °C is the most effective process condition in establishing the highest degree of porosity and development of the high surface area (1487 m^2/g), and total pore volume (0.527 cm^3) obtained from CO_2 isotherms.

b) The pore size distribution of the activated carbons resides mainly in a very narrow region of ultra-micropores (0.5–0.6 nm).

c) It has been demonstrated that by chemical activation of coffee grounds, it is possible to obtain textural properties and capacity for VOCs adsorption comparable to commercial activated carbon, measured under ambient conditions.

d) VOC adsorption results indicated the high adsorption capacity for activated carbons (MEK 3210 – 1958 mg/g and toluene 2618–952 mg/g) and removal efficiency (MEK 59% – 36% and toluene 55%-20%) of the prepared ACs in low MEK and toluene concentrations (14 – 16 ppm).

e) It was observed that the adsorption capacity of toluene was always lower for each sample, which could be affected by toluene's higher kinetic diameter.

f) Regeneration at 100 °C for 1 h promoted the effective removal of MEK and toluene.

g) Chemically activated carbon produced from the coffee grounds showed promising results for CO_2 uptake (253 mg/g), however further adsorption tests under indoor conditions are needed.

Overall, the AC-K_2CO_3-CG sample was selected as the best-performing sample, and it could potentially be applied for the removal of VOCs and improve indoor air quality, as its high specific surface area, total pore volume, adsorption capacity could be beneficial for air purification through filters integrated with ventilation systems or other materials.

Chapter 5   Photocatalytic agents

5.1. Background

Earlier chapters presented two different mechanisms for removing air pollutants. Although they have been shown to be effective, all of these technologies suffer in that the target pollutant is transferred from one medium to another and is not completely eliminated. Photocatalytic oxidation (PCO) has garnered the most interest among all the techniques because of its high efficiency in the removal of typical indoor pollutants, even at low concentrations, with maximum efficiency and minimum energy. The advantages of photocatalytic oxidation for air remediation are:

- Possibility of using a renewable source of energy (solar energy) instead of a fossil one.
- The oxidation in the presence of a catalyst requires milder conditions and can be carried out under normal temperature and pressure.
- Light irradiation can lower the energy barrier of the rate limiting step in some catalytic systems or change the absorption and desorption behavior of reaction intermediates on the catalyst surface, thereby exhibiting higher activity and ideal reaction selectivity under solar driven conditions.

Various metal oxides (TiO_2, ZnO, WO_3, etc.) and metal sulfide-based (e.g., ZnS, CdS, etc.) semiconductor materials are utilized as catalysts for the photocatalytic oxidation of pollutants. TiO_2 is a commonly used semiconductor as it has the characteristics of chemical and biological stability, low toxicity, high durability, low cost, resistance to photocorrosion and high photocatalytic activity. Although TiO_2 has these merits, it has some disadvantages, such as high band gap energy (~3.2 eV), which restricts its usage under simulated or natural solar light irradiation, poor adsorption capacity, low surface area, and a high recombination rate of photogenerated charge carriers that limit the practical applicability of TiO_2 materials. In order to overcome those disadvantages and to improve the visible light utilization and carrier mobility of photocatalysts, the development of visible light-driven photocatalysts has become a new goal.

Thus far, many new photocatalytic agents have been developed. Recent studies demonstrate that metal vanadates exhibit promising visible-light photocatalytic reactivity in decomposing pollutants. However, research on development of different metal vanadates for photocatalytic applications is limited, with most reports focusing on bismuth vanadate [109] or silver vanadate [110]. In the previous study [28], Nadolska et al. proposed simple method based on liquid-phase exfoliation with ion exchange to synthesis potassium vanadates ($K_2V_6O_{16} \cdot nH_2O$

nanobelts and KV_3O_8 microplatelets). Synthesized potassium vanadates characterized narrow band gap energy of 1.80 eV ($K_2V_6O_{16} \cdot nH_2O$) and 1.91 eV (KV_3O_8) and high photocatalytic degradation under visible light. Obtained, KV_3O_8 exhibited the greatest photocatalytic activity, resulting in more than 90% degradation of the dye within the first 30 min.

Based on the above research the novel potassium vanadate is considered promising photocatalytic agent, however to the best my knowledge any research is focused on the KVO application for air pollutants photocatalytic degradation. Therefore, this research was conducted to fill this knowledge gap.

5.2. Aims and objectives

This chapter focuses on the initial phase (standalone photocatalytic test) of the experimental research and the aim was to select the best performing activating agent for the innovative multifunctional finish preparation (described in chapter 6 in details). In collaboration with another research group [26], [27], from Faculty of Applied Physics and Mathematics, Institute of Nanotechnology and Materials Engineering, Gdańsk University of Technology (Poland), possible application of novel potassium vanadate photocatalytic agent for indoor air pollutants (NO_x and VOCs) abatement have been considered. Obtained results were compared to the commercial TiO_2 agents. Different testing methods have been evaluated.

5.3. Principal mechanism of photocatalysis

In the photocatalytic process, a semiconductor catalyst and an irradiation source are employed. Upon excitation of the semiconductor with photon energy equal to or greater than its band gap energy, an electron in an electron-filled valence band (VB) is excited to a vacant conduction band (CB) and electron–hole pairs are generated. While surface-adsorbed reactive species undergo oxidation reactions by the photogenerated holes at the top of the valence band, reduction reactions occur through the photogenerated electrons at the bottom of the conduction band. Therefore, the conduction band of the semiconductor must have more negative potential than the reduction potential of the chemical species, and the valence band of the semiconductor must have more positive than the oxidation potential of the chemical species to allow photoreduction and photooxidation processes, respectively. In case of TiO_2 the conduction band position of anatase form is reported to be -0.51V at pH 7, which lies slightly above the reduction potential of molecular oxygen, which is an abundant and green oxidant in the

environmental atmosphere; moreover, in principle, most VOCs have less positive oxidation potentials than the positive potential of the TiO_2 valence band, which allows them to be oxidized upon UV light illumination. Therefore, TiO_2 is considered an efficient photocatalyst for VOCs removal.
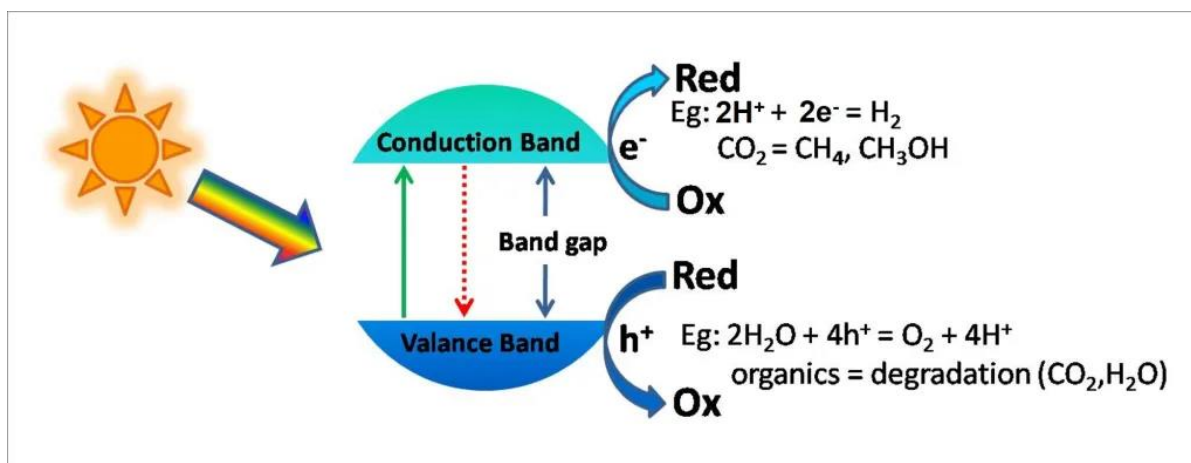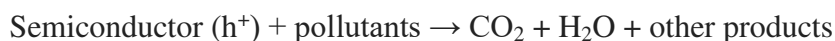
$$\text{Semiconductor} + h\upsilon \ (\lambda \geq \text{band gap energy}) \rightarrow \text{Semiconductor } (h^+) + \text{Semiconductor } (e^-)$$

$$h^+ + H_2O \rightarrow \text{Semiconductor} + H^+ + {}^{\bullet}OH$$

$$\text{Semiconductor } (h^+) + \text{-OH} \rightarrow \text{Semiconductor} + {}^{\bullet}OH$$

$$\text{Semiconductor } (e^-) + O_2 \rightarrow \text{Semiconductor} + O_2^{\bullet -}$$

$$O_2^{\bullet -} + H^+ \rightarrow HO_2^{\bullet}$$

$$HO_2^{\bullet} + e^- \rightarrow HO_2^-$$

$$HO_2^- + H^+ \rightarrow H_2O_2$$

$$HO_2^{\bullet} + HO_2^{\bullet} \rightarrow H_2O_2 + O_2$$

$$H_2O_2 + h\upsilon \rightarrow 2\ {}^{\bullet}OH$$

$$H_2O_2 + \text{Semiconductor } (e^-) \rightarrow \text{Semiconductor} + OH^- + {}^{\bullet}OH$$

$$\text{Semiconductor } (h^+) + \text{pollutants} \rightarrow CO_2 + H_2O + \text{other products}$$
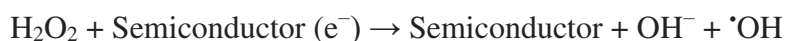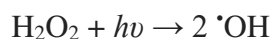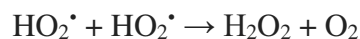
Figure 83. Schematic illustration of the photocatalytic mechanism for semiconductor photocatalysts under light irradiation. (source: https://chemistrydocs.com/photocatalysis-types-mechanism-and-applications/#google_vignette).

5.3. Materials and methods

5.3.1. Materials

Three different photocatalytic agents were investigated in this chapter, two commercial titanium dioxide: P-25 and KronoClean 7404 and novel potassium vanadate (labelled as KVO). P-25 is a combination of anatase and rutile crystal structure and is photoactive under UV-B radiation. The specific surface area measured by BET is 35-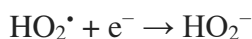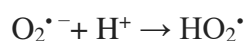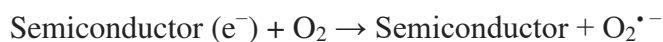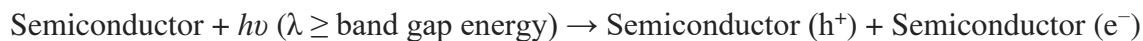65 m^2/g. The pH of a 4% water dispersion is 3.5–4.5, and the density 3.1 g/cm^3 as declared in the technical datasheet.

KRONOClean 7404 is a carbon-doped TiO_2 in the form of an aqueous suspension (40% TiO_2 and 60% water) with a pH of 7-8 and a density at 20 °C of approximately 1.4 g/cm^3 according to the technical data sheet. Produced in the form of anatase, photoactive under VIS and UV radiation.

KVO sample was synthesized by research group [26]-[27], from Faculty of Applied Physics and Mathematics, Institute of Nanotechnology and Materials Engineering, Gdańsk University of Technology in Poland, as described in previous study [28]. For the synthesis, LPE-IonEx method as applied and the procedure was as follows: 500 mg of V_2O_5 was added to 50 mL of a 1 M solution of potassium formate in deionized water. The mixture was vigorously stirred for 72 h, and the synthesis was conducted at 80 °C. From the obtained solution, orange precipitations were collected by centrifugation. After washing several times with deionized water, products were dried overnight at 40 °C under reduced pressure (0.01 bar). The obtained sample was labelled as KVO. Specific surface area of synthesized KVO, measured by BET, was 4.6 m^2.

5.3.2. Characterization

To investigate the morphology and elemental composition of novel KVO, SEM-EDX analysis (paragraph 2.3.1) was provided. Other physicochemical properties like, chemical composition, thermal stability, crystallographic parameters and chemical state were evaluated by FTIR, TGA, XRD, XPS, respectively and were described in previous studies [72], [28].

5.3.3. NOx degradation test

To evaluate photocatalytic degradation of NO_x 3 different samples were prepared, and the experiment was divided into two parts, using two different rectors to explore the best removal effect.

In the I part 1.2 g of commercial P-25 was dispersed in water to obtain slurries in the weight ratio $TiO_2:H_2O$ equal to 40:60 (the same concentration of KronoClean 7404 TiO_2 suspension). Then, the beakers containing aqueous slurries were subjected to 15-min ultrasound bath for even distribution, poured into three different petri dishes and dried for 24 h at 70 °C.
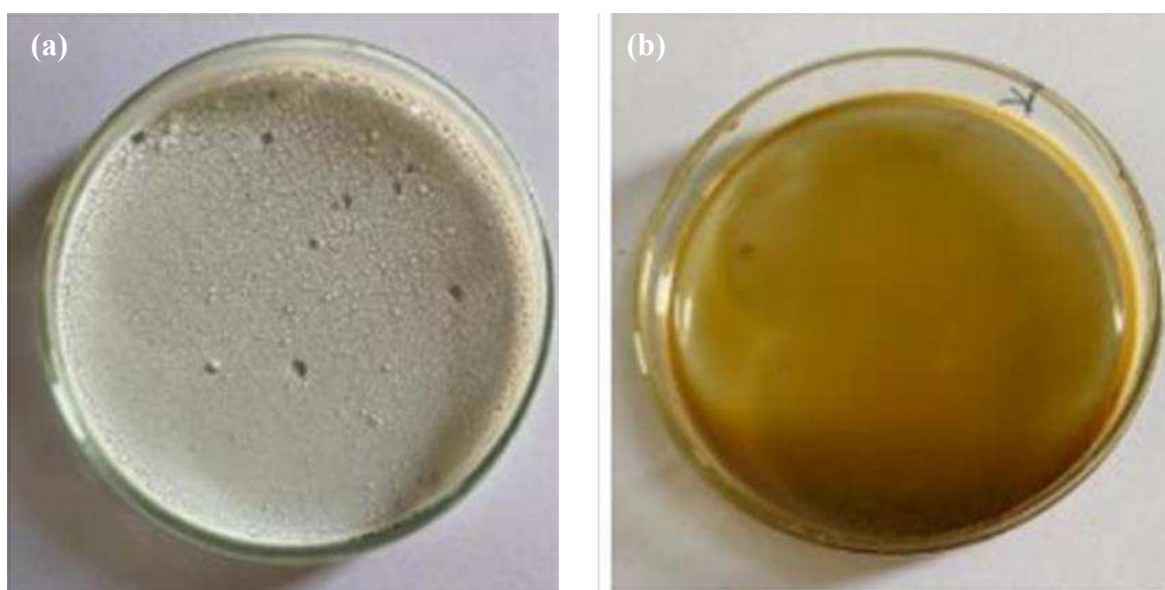
Figure 84. (a) P-25 and (b) KronoClean 7404 samples after drying.

18 mg of novel KVO was mixed with few drops of distilled water and subjected to 15-min ultrasound bath. After the preparation, the sample was poured on the glass support (55 cm^2) and dried under IR lamp until constant weight (changes in weight were lower than 1% of the total mass when 2 weight control after 1 hour were carried out).
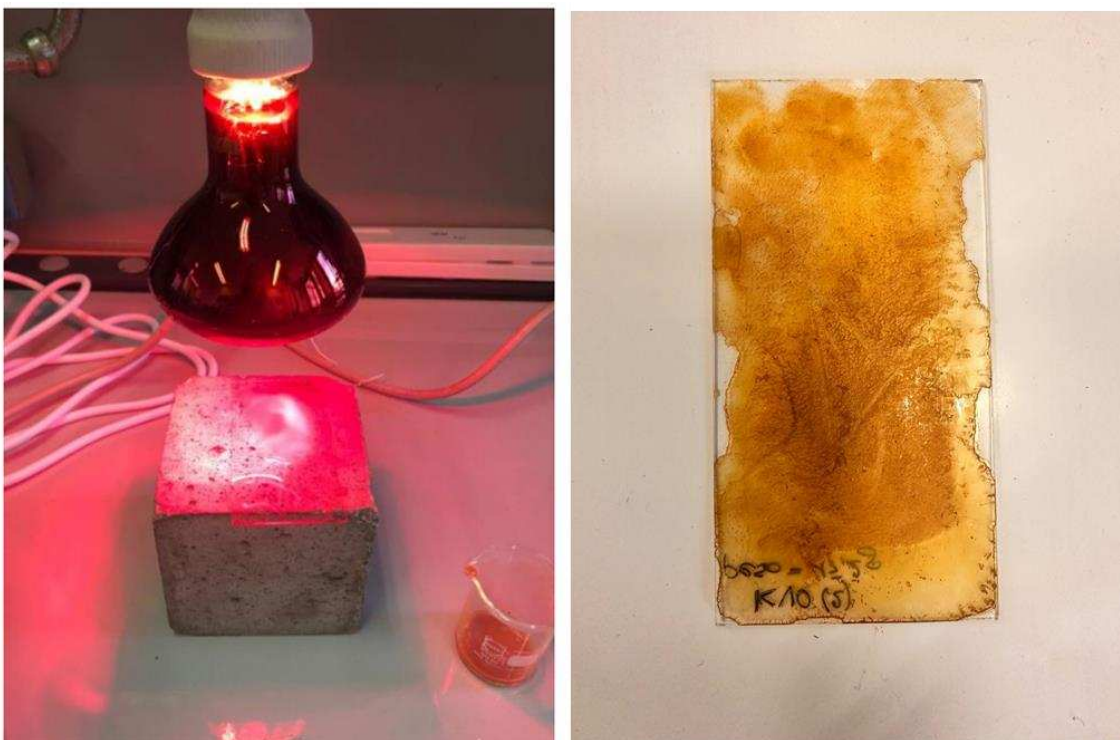
Figure 85. KVO sample.

Prepared samples were stored in the desiccator for further photocatalytic tests, which were carried out according to the procedure described below utilizing 3 L Pyrex reactor.

In the II part of the experiment, the commercial photocatalytic agent from the I part with the higher photocatalytic activity was selected for the further analysis, utilizing reactor of the smaller volume 0.13 L. 18 mg of P-25 was prepared according to the procedure described above for the KVO sample.
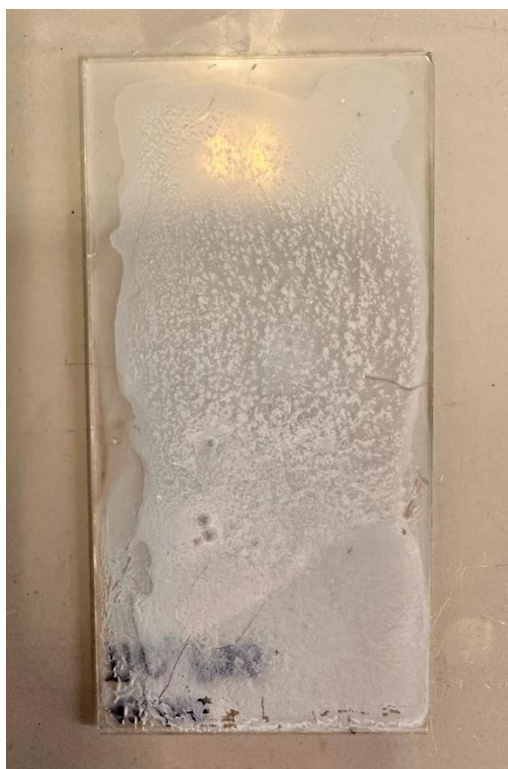
Figure 86. P-25 sample.

Photocatalytic properties of the samples were evaluated following the Italian UNI standard: 'Determination of the degradation activity of nitrogen oxides in the air by photocatalytic inorganic materials' (UNI 11247). NO_x removal was evaluated using the experimental apparatus, shown in Figure 87. The NO_x flux was supplied by a NOx tank, $\pm$ 1 ppm or $\pm$ 0.5 ppm NO (SAPIO S.r.l., Monza, Italy), and was kept constant with a dilution system (Calibrator 8188, Rancon Instruments S.p.A., Milan, Italy) by mixing with atmospheric air at $T = 25 \pm 2$ °C and RH between 40 and 50%. The samples under examination are positioned internally in the center of a reactor. Two types of chambers were used:

a) 3 L borosilicate glass reactor (Figure 88a)

b) 0.13 L reactor (Figure 88b) - a bipartite sample holder equipped with a bearing placed in the lower flap to allow better insulation of the internal environment during sealing, is made up of overlapping layers of polymethylmethacrylate (PMMA), each 1.5 mm thick, glued together; the internal box where we position the specimen has side walls in PMMA, upper and lower faces in 1.5 mm thick borosilicate glass. Box dimensions are 11.5 cm x 5.5 cm x 2 cm. The box is connected to the machinery by means of two pipes, which allow internal

recirculation of the pollutant and subsequent continuous transport to the analyzer for examination.

Figure 87. NOₓ apparatus.

During the test, reactor was covered with a curtain to eliminate the influence of external light. The concentration of NO and NO_x in the outlet of the reactor was measured using a chemiluminescence NO_x meter (nitrogen oxide analyzer model 8841, Monitor Labs, Englewood, CO, United States). Firstly, in dark conditions and then under the radiance of visible, UV or solar light adjusted by Delta Ohm HD 2101.1 photo radiometer (visible sensor LP 471 RAD 400 nm–1050 nm and UVA sensor LP 471 UVA RAD 315 nm–400 nm). As soon as the NO gas concentration was stable, the sample was placed inside the reactor and allowed to stay for a few minutes in the dark, in the absence of irradiation, until the equilibrium between the sample and the gas phase was reached, and NO concentration remained constant, according to UNI11247 standard (at least 10 min). This step allowed the elimination of the error related to the adsorption process to evaluate the only photocatalytic activity. The irradiation by VIS lamp lasted at least for 10 min, and when no photocatalytic degradation occurred, the time was elongated to 25 min to make sure that catalytic sites have been enough activated by irradiation. Then the source of light was turned off until the initial concentration was reached. The measurements were repeated three times (three cycles). The same procedure was followed in the case of the evaluation of photocatalytic capacity under UV or solar light. The temperature before and after turning on the lamp was monitored by means of thermocouple.
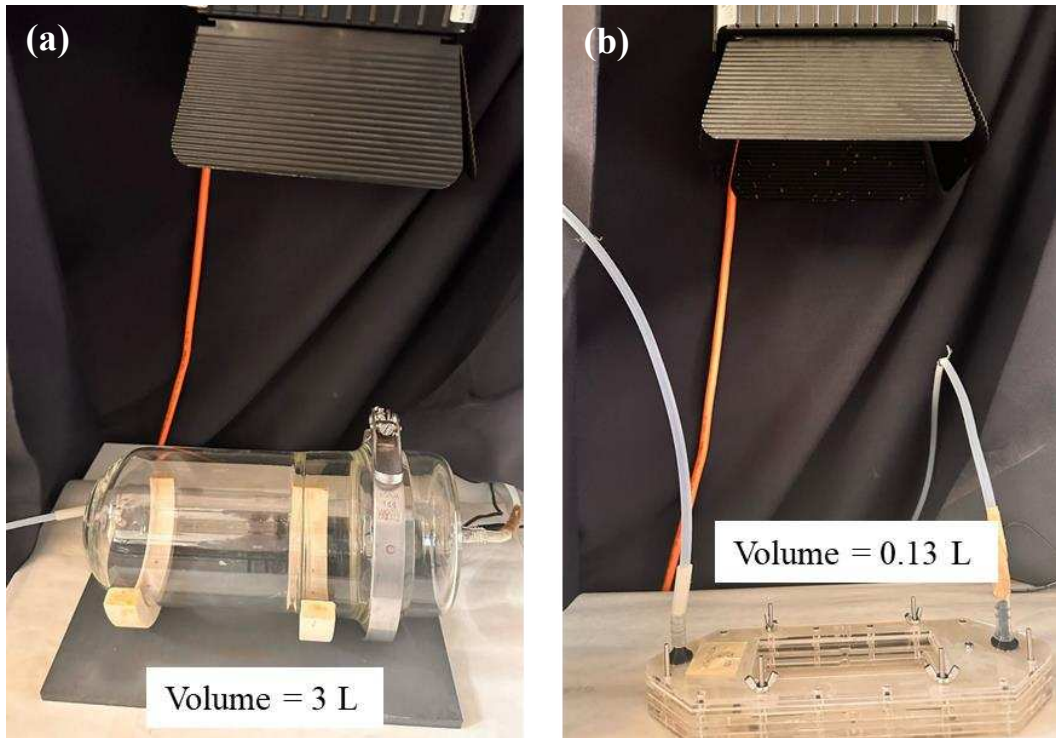
Figure 88. (a) 3 L and (b) 0.13 L NO$_x$ reactor.

For each specimen, the percentage measurement of the NO$_x$ removal efficiency (E$_{NOx}$) was calculated according to the formula referring shown below:

$$E_{NOx}(\%) = \frac{(NOx)_b - (NOx)_a}{(NOx)_b} \qquad (6)$$

Where:

(NO$_x$)$_b$ - arithmetic mean of the last three NO$_x$ concentration values before turning on the artificial light (dark conditions);

(NO$_x$)$_a$ - arithmetic mean of the three NO$_x$ concentration values after turning on the artificial light.

NO removal (E$_{NO}$) was calculated according to the formula:

$$E_{NO}(\%) = \frac{(NO)_b - (NO)_a}{(NO)_b} \qquad (7)$$

Where:

$(NO)_b$ - arithmetic mean of the last three NO concentration values before turning on the artificial light (dark conditions);

$(NO)_a$ - arithmetic mean of the three NO concentration values after turning on the artificial light.

The difference between E_{NOx} and E_{NO} corresponded to the formation (P_{NO2}) of the NO_2 reaction product:

$$P_{NO2} (\%) = E_{NOx} - E_{NO} \qquad (8)$$

5.3.3. VOCs degradation test

Samples for VOCs degradation tests were prepared as mentioned above and two support glasses were coated with 18 mg of KVO and P-25.

VOCs photocatalytic degradation test was performed in a batch reactor as shown in Figure 89. Methyl-ethyl-ketone was used as model pollutant and initial concentration was 12 ppm ($\pm$ 0.5 ppm) which was monitored through the whole test by Aeroqual software. The test was performed firstly, in dark conditions and when the adsorption equilibrium was reached, two types of radiation were provided:

- Visible – by turning on the lamp (Philips, 42W) with intensity adjusted by Delta Ohm HD 2101.1 photo radiometer (visible sensor LP 471 RAD 400 nm–1050nm);
- Ultraviolet - halogen lamp (Torcia, 400W) with measured light intensity measured by UVA sensor LP 471 UVA RAD 315 nm–400nm, at adjusted light intensity equal to 45 W/m^2

The temperature before and after turning on the lamp was monitored by means of a thermocouple.
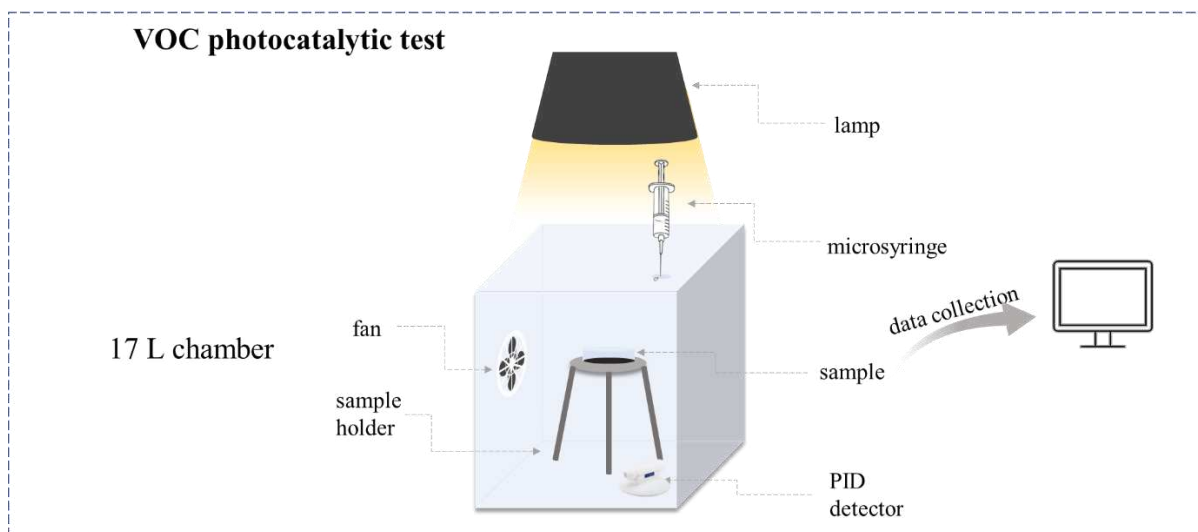
Figure 89. VOCs photocatalytic degradation test.

The percentage of degraded VOC was calculated according to the formula referring shown below:

$$VOC\ degraded\ (\%) = \frac{C_0 - C_t}{C_0} \tag{9}$$

Where:

C_0 – VOC concentration of in the reactor when the adsorption equilibrium was reached, before turning on the radiation source;

C_t – VOC concentration recorded at the end of the test.

5.4. Results and discussion

5.4.1. Morphology and elemental analysis

Morphology of the samples was analyzed by means of SEM observations. As shown in Figure 90, the structure of P-25 is composed of a well crystallized granular morphology. Particles are round and ovoid in shape, less agglomerated and with 27–40 nm size range. The morphology of nonhomogeneous KronoClean 7404 shows agglomeration with particles visible in different shapes, mainly oval, and size distribution is in the range between 28 and 85 nm.

KVO particles characterize different shapes and sizes: flat and hexagonal with a particle size from 1 to 12 μm (microplatelets) which corresponds to $K_2V_6O_{16} \cdot nH_2O$ and longitudinal-shaped much smaller, around 70 nm (nanobelts) which corresponds to KV_3O_8.
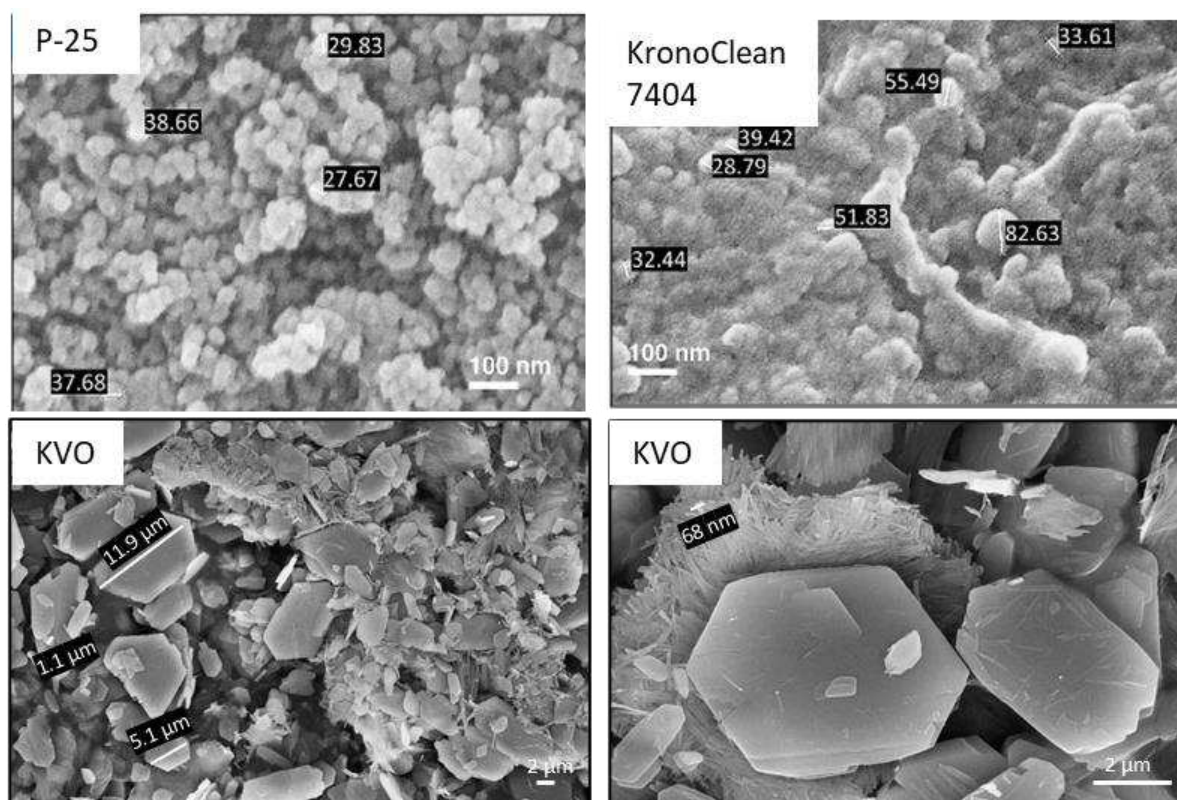

Figure 90. SEM images of commercial photocatalytic agents: P-25 and KronoClean 7404 [18], and novel KVO.

Table 22 and Figure 91 report the elemental composition and EDX spectra of the three different photocatalytic agents. The results show that P-25 contains a higher atomic percentage of titanium (35.31%) than KronoClean 7404 (21.78%), however less content of carbon which is 3.14% and 23.81% respectively. The elemental composition of potassium vanadate was analyzed in two different points as shown on figure x, and the average has been considered. The elemental composition is vanadium 31.45%, oxygen 38.17%, carbon 20.70% and potassium 9.65 %.

Table 22. Elemental composition.

Specimen	Atomic weight percentage (%)				
	Titanium	Oxygen	Carbon	Vanadium	Potassium
P-25	35.31	61.55	3.14	-	-
KronoClean 7404	21.78	53.56	23.81	-	-
KVO	-	38.17	20.70	31.45	9.65
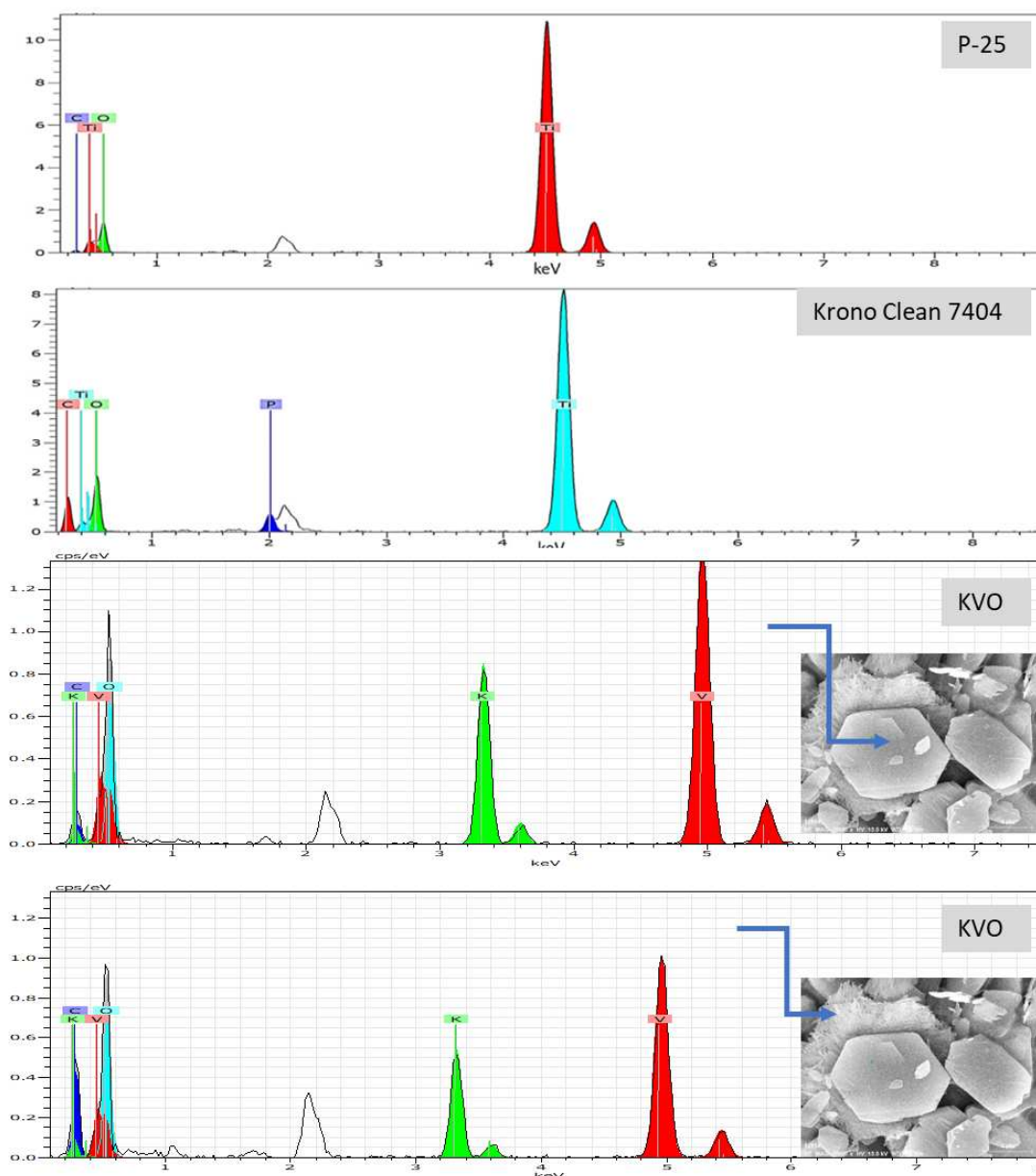
Figure 91. Figure. EDX spectra of P-25 and KronoClean 7404 [18], and novel KVO.

5.4.2. NO$_x$ degradation test

The profiles of photocatalytic oxidation of NOx are presented in Figure 92-96. Each test consists of the few steps:

1) Stabilization of the NOx concentration inside the reactor;

2) Opening the reactor, causing and inserting the tested sample – this step is necessary to eliminate the adsorption factor during the calculations;

3) Slight decrease of the NOx concentration;

4) Switching on the illumination source:

- VIS (Philips, 42 W) with the radiance 9 or 95 W/m^2 adjusted by Delta Ohm HD 2101.1 photo radiometer, visible sensor LP 471 RAD 400 nm–1050nm

- UV (Torcia UV, 400 W), measured light intensity 10 or 20 W/m^2 adjusted by UVA sensor LP 471 UVA RAD 315 nm–400nm;

5) Decrease in NOx and NO concentrations observed in all samples, except KronoClean 7404 under visible light and KVO under both, visible and UV light;

6) After stopping the irradiation, interruption of sites activation in photocatalyst surfaces and after few minutes NOx, NO and NO_2 concentration return to the same initial level;

7) The entire process by switching the lamp on and off was performed three times, unless no changes in the concentration has been noticed (KVO case).
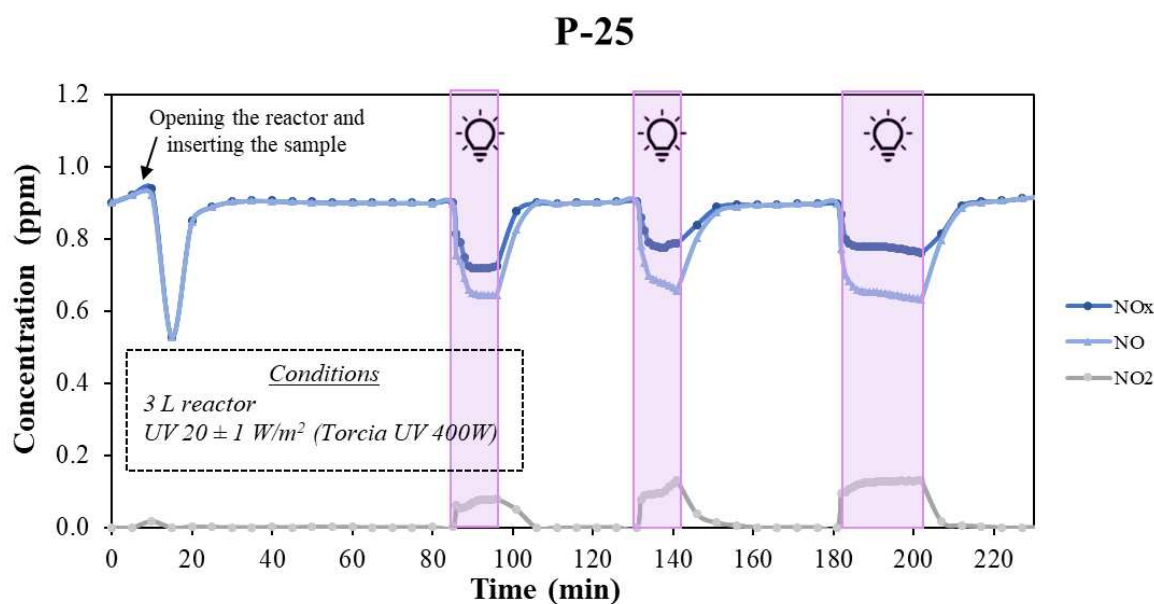
Figure 92. P-25 profile of photocatalytic oxidation of NO_x under UV light.
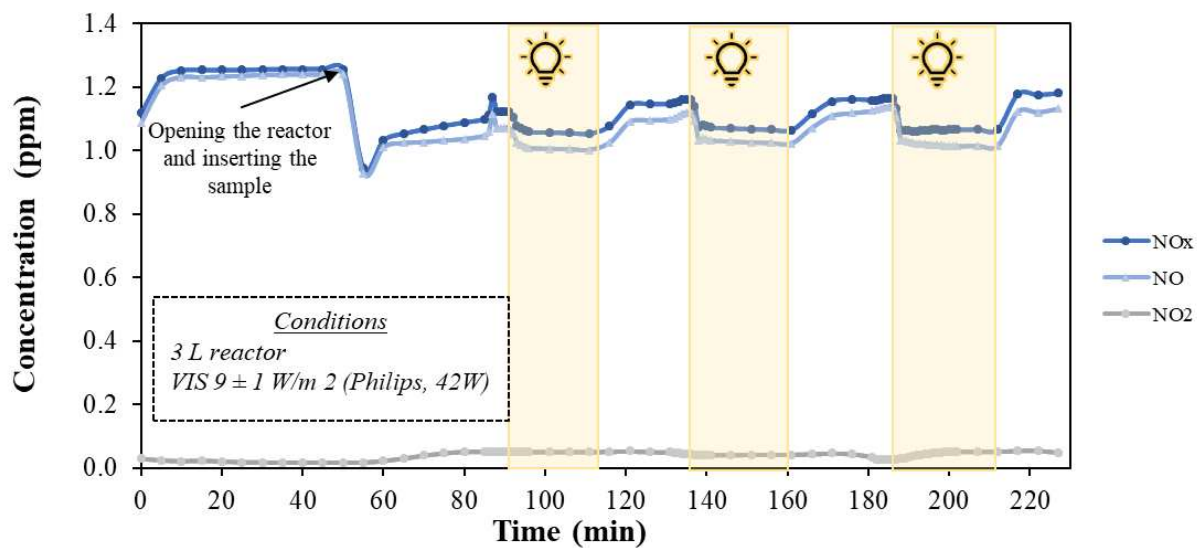
Figure 93. P-25 profile of photocatalytic oxidation of NO$_x$ under VIS light.

Figure 94. KronoClean7404 profile of photocatalytic oxidation of NO$_x$ under UV light.

KronoClean 7404

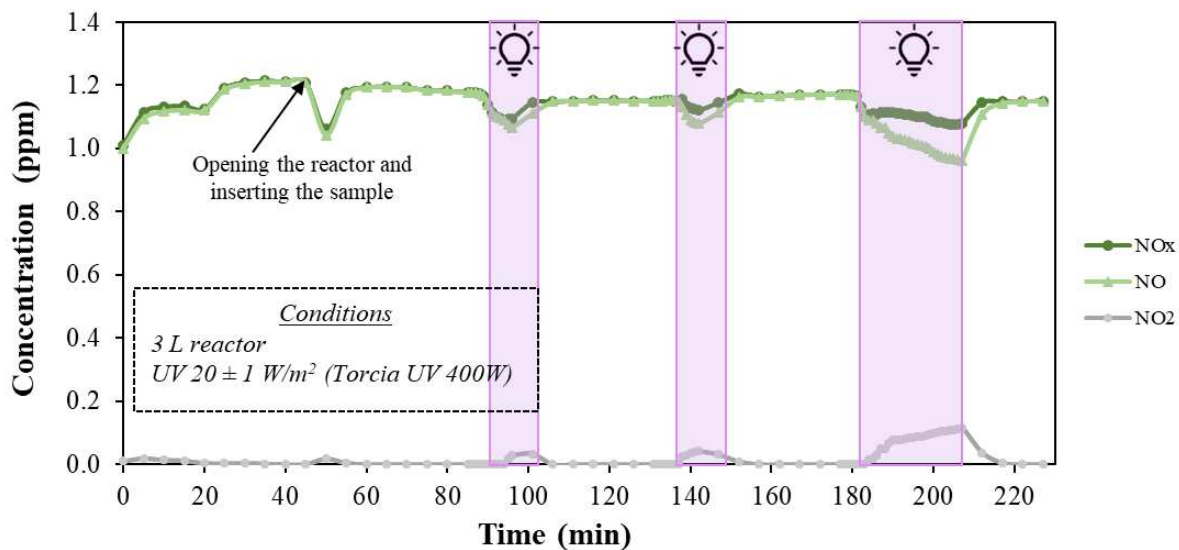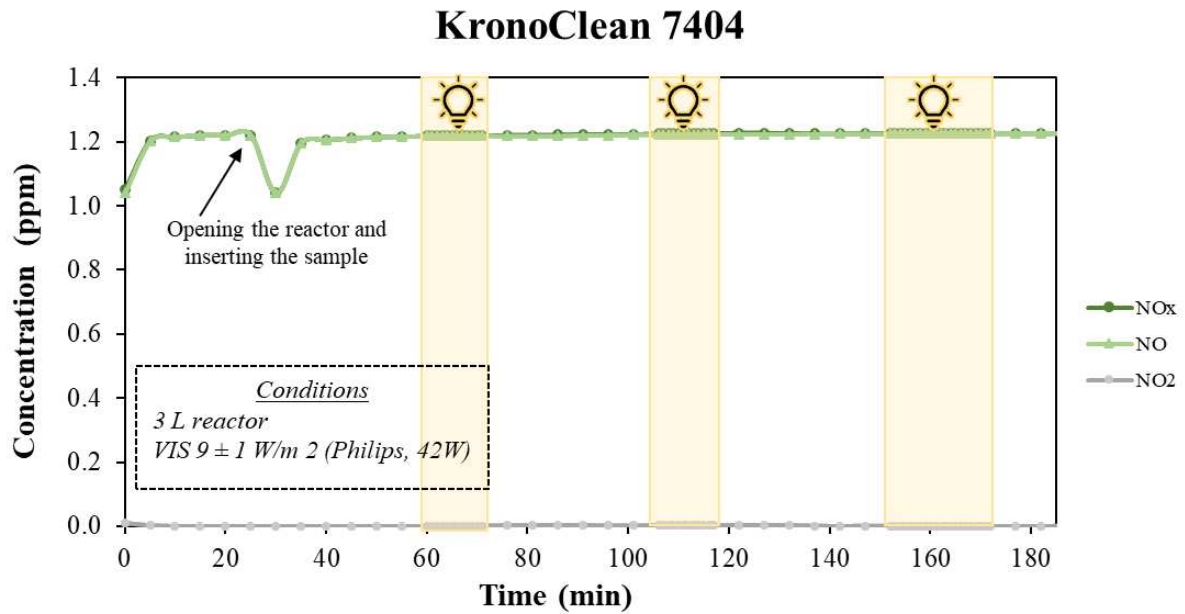*Figure 95. KronoClean7404 profile of photocatalytic oxidation of NO_x under visible light.*

KVO

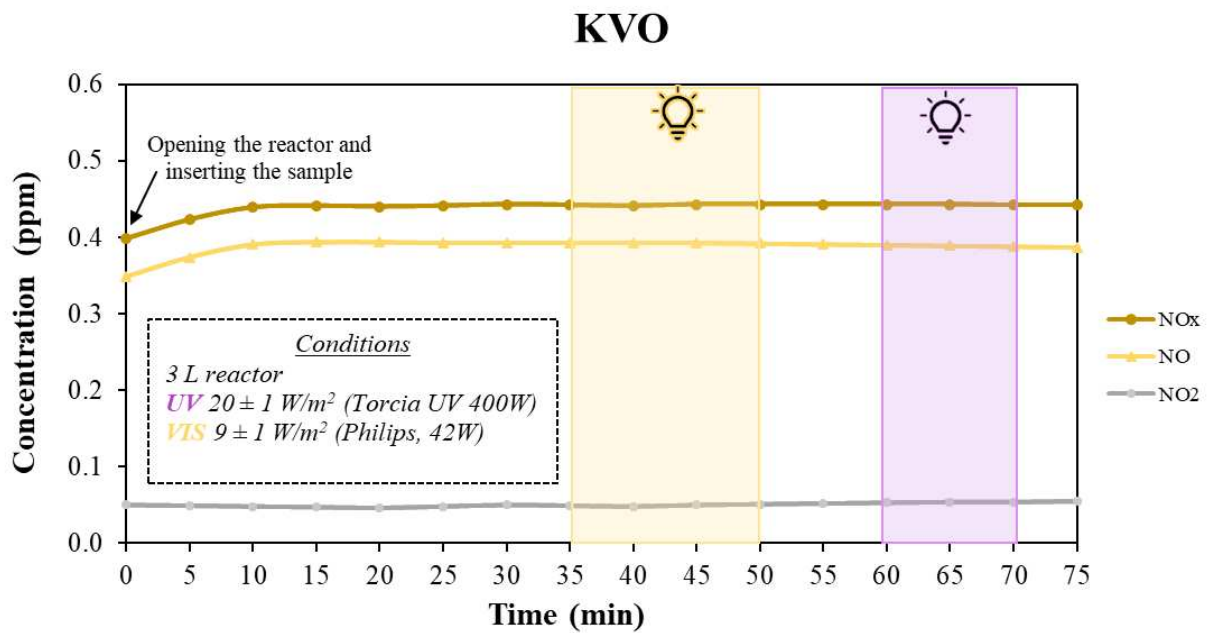*Figure 96. KVO profile of photocatalytic oxidation of NOx under visible and UV light.*
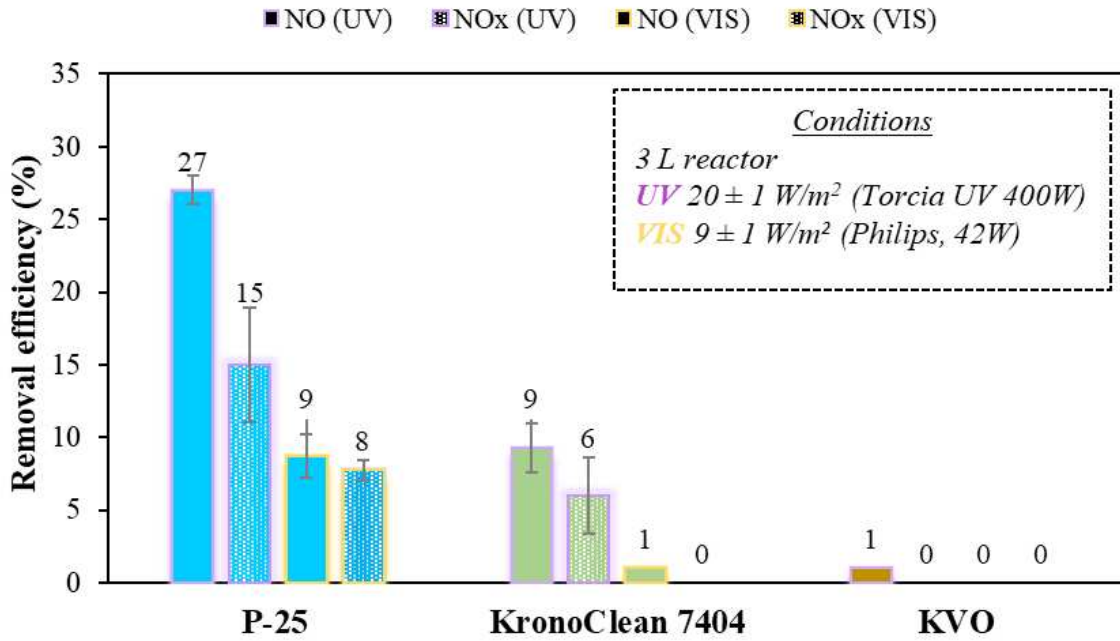
NOx test

NO (UV)   NOx (UV)   NO (VIS)   NOx (VIS)

Figure 97. NO$_x$ removal efficiency test results.

NOx test

NO2 (UV)   NO2 (VIS)
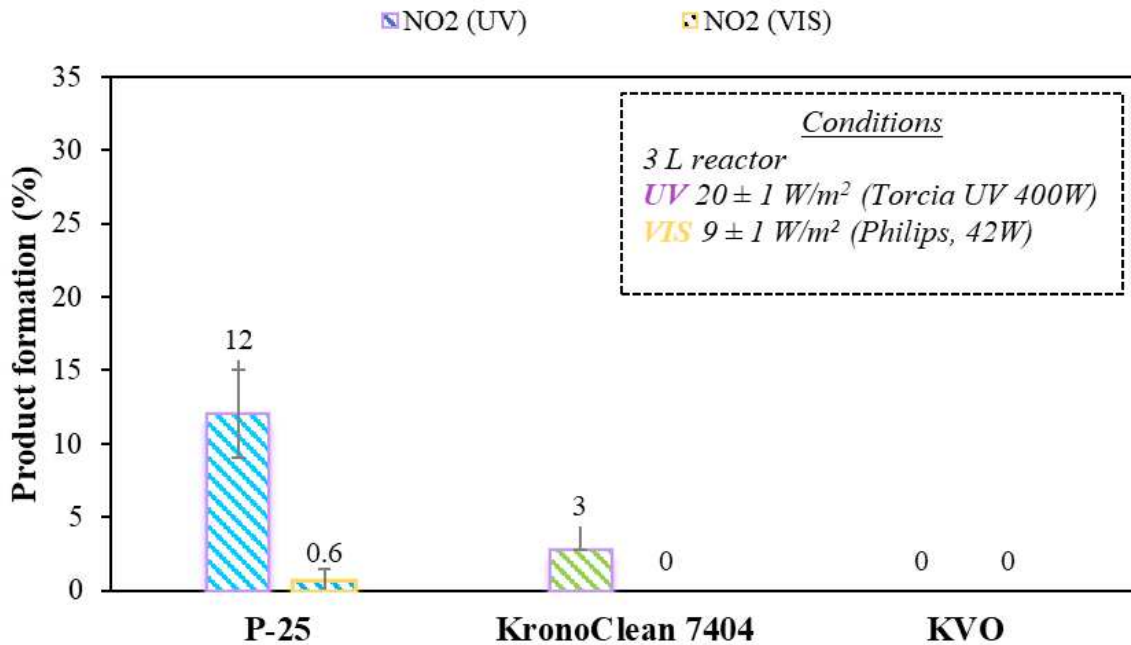
Figure 98. NO$_2$ formation results.

From the results presented on the bar charts (Figure 97 and Figure 98), P-25 appears to have greater photocatalytic activity than KronoClean 7404. Under UV irradiation NO degradation was 27%, while total NO_x 15%. KronoClean 7404 instead was able to remove 9% of NO, and 6% of NO_x. The difference between NO_x and NO is the percentage of NO_2 which is the by-product of photocatalytic reaction, which was 12% and 0.6% for P-25 under UV and VIS respectively. Moreover, KronoClean 7404 did not show the photocatalytic activity under VIS light as it is reported in the data sheet, while P-25 degraded 8% of NOx, while 1% was NO_2 production. KVO did not show the photocatalytic activity under the conditions applied. In order to increase the contact area with the pollutant, the volume of the reactor was decreased during the second part of the experiment and 0.13 L reactor has been used. In this case, the ratio between the exposed surface of the KVO sample to the volume of the reactor was increased from 18 cm^2/L to 423 cm^2/L. As reported in previous study [28], where KVO was investigated as photocatalysts for organic dye degradation under solar radiation in the following experiment also radiation conditions have been changed, and visible radiation has been increased to 95 W/m^2, while UV has been changed to 10 W/m^2 in order to avoid overheating of the sample in the reactor.

From results presented in Figure 99 it appears that by decreasing the volume of the reactor and changing radiance parameters, degradation of NO under UV lamp increased from 27 to 45% and from 0 to 3%, and under VIS, from 9 to 26% and from 0 to 3%, for P-25 and KVO respectively.
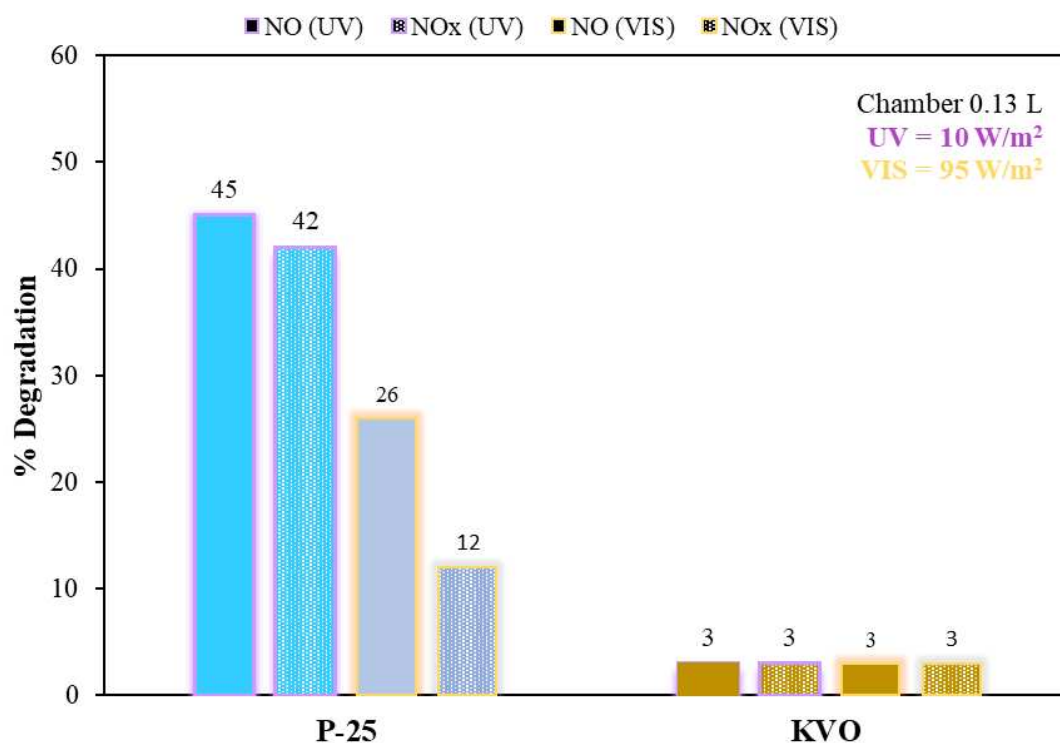
Figure 99. NOx degradation test results.

5.4.3. VOCs degradation test

In order to evaluate photocatalytic removal efficiency of organic compounds, another experiment has been conducted, and the results are shown on the Figure 100 and Figure 101. The ratio between the sample surface and reactor volume was equal to 3.2 cm^2/L and MEK concentration was monitored for 70 minutes. Before each test blank, test has been performed to eliminate the effect of a natural decay when the data were processed. The first part of measurement (with the light source switched off) concerns the adsorption process, which in the case of both investigated samples did not appear (the measurement lines of KVO and P-25 overlapped the blank one). After 32 minutes of the test, the UV lamp was switched on and in case of P-25 drop in the MEK concentration during the whole time of exposure was noticed. In this experiment, despite 30 minutes of UV exposure, the KVO also did not show photocatalytic activity. On the other hand, P-25 degraded 66% of MEK.

154
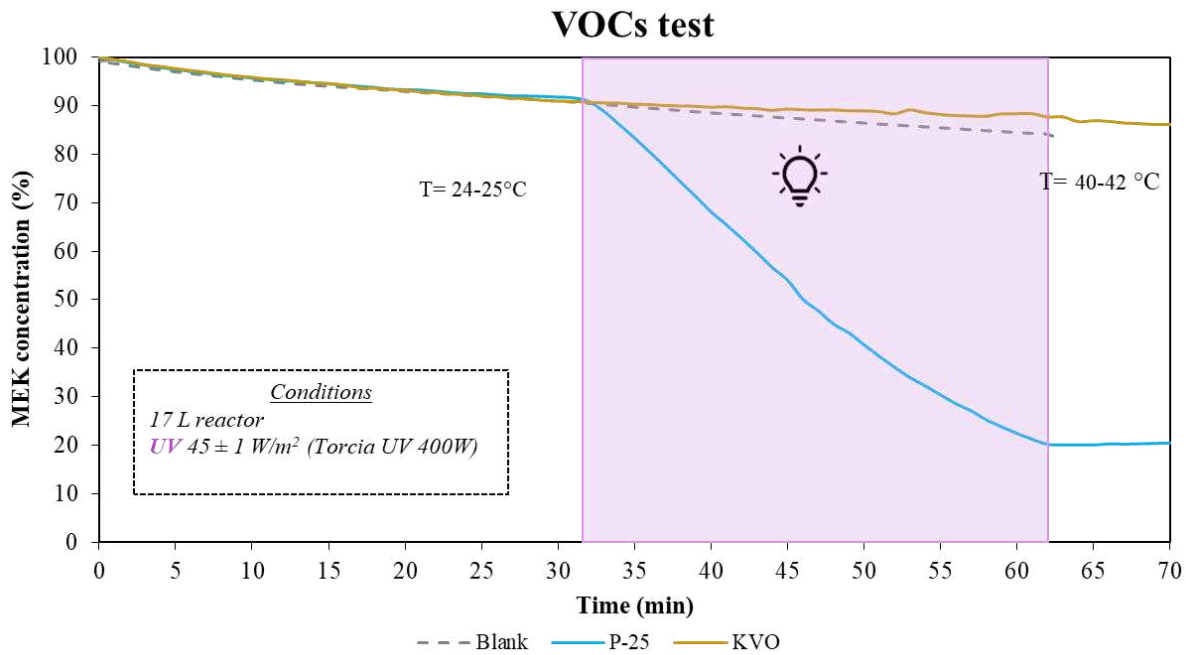
Figure 100. VOCs degradation test.
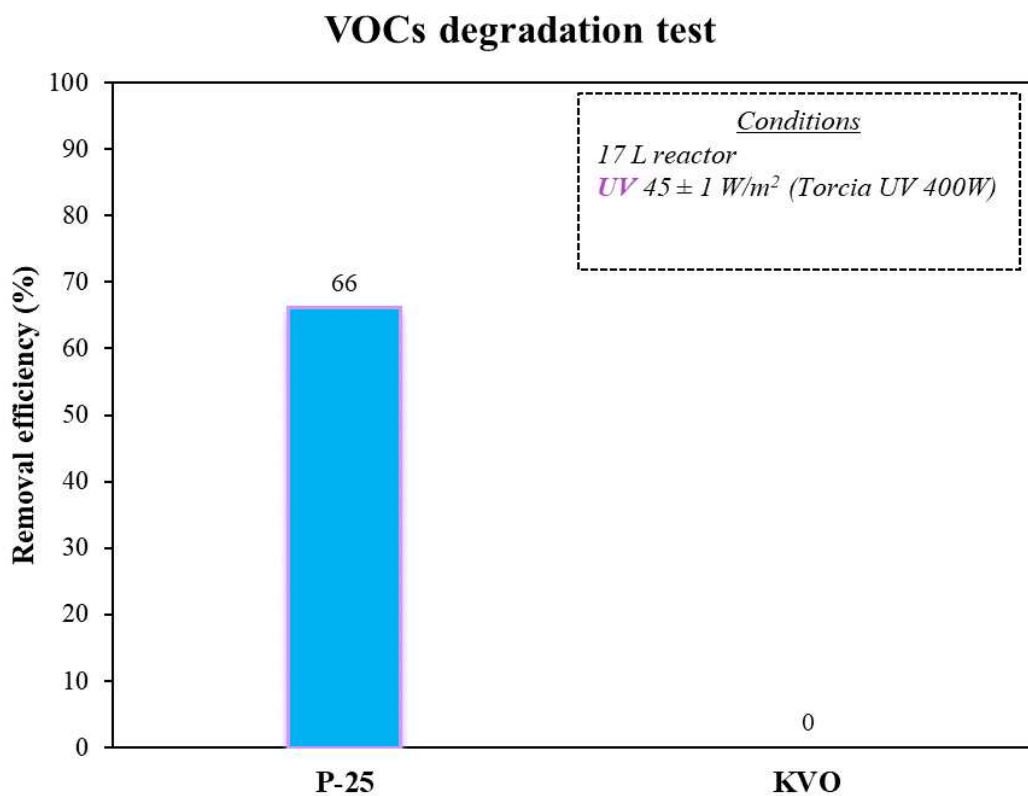
Figure 101. VOCs degradation test results.

The lack of the photocatalytic activity of KVO can be explained by the following factors:

1) The particle size – KVO characterize very wide range of particles, from micro to nano size (1−10 μm length and 150 nm width [28]). The particles of P-25 and KronoClean 7404 have smaller dimensions compared to the ones of KVO and are respectively 27-40 nm and 28-85 nm. This characteristic gives a significant advantage in photocatalysis when standalone photocatalytic properties are tested since the photocatalyst can guarantee a large contact surface [72]. In fact, nanoparticle sized photocatalysts shows higher efficiency toward gaseous pollutants' removal [111].

2) Reaction phase – reactivity in a liquid-phase is always higher than in the gas-phase [112].

3) The role of Reactive Oxygen Species (ROS) which play a dominant role during VOCs degradation [113], in case of the novel KVO has not been investigated in the literature;

4) Comparing FTIR spectra [28], [72] P-25 characterize wide and intense IR absorption in the region between 3000 and 3600 cm−1, which are attributed to the different types of hydroxyl groups and the OH stretching vibration of adsorbed water molecules, indicating its hydrophilicity, and tends to adsorb water molecules, which is an important factor during PCO process and prevents VOCs adsorption [114].

5.5. Conclusions

In this study, analyzed samples were characterized in terms of morphological properties and elemental composition using SEM and EDX. The photocatalytic degradation of MEK, under UV/VIS light illumination, was examined to evaluate the photocatalytic performance of prepared samples and compared with two commercial TiO_2. The aim of this study was to select the best performing photocatalytic agent for indoor finishing application. Both, inorganic (NOx) and organic (VOCs) photocatalytic degradation was investigated. The results from the first experiment showed that the novel KVO is characterized by low photocatalytic activity (3 % degradation of NO_x) under both types of radiation: UV (10 W/m^2) and VIS (95 W/m^2). The commercial P-25 acted as the most efficient photocatalyst and was able to degrade up to 27 % and 9 % of NO_x under UV (20 W/m^2) and VIS (9 W/m^2). Moreover, by decreasing volume of the reactor from 3 L to 0.13 L and decreasing UV and increasing VIS radiance, also the removal

efficiency increased to 45 % and 26 % of NOx under UV (10 W/m^2) and VIS (95 W/m^2), respectively.

VOCs degradation test showed that P-25 was able to remove 66% of MEK under UV (45 W/m^2) in 30 minutes, while KVO did not show the photocatalytic activity.

Chapter 6   Combined systems

6.1. Background

In the previous chapters, three different mechanisms to improve indoor quality have been presented. The application of combined technologies is a common technique to improve the efficiency of the process and to widen the group of the target pollutants. The most common configuration can be found in the commercial purifying devices where the first process (i.e., filtration) is followed by the second process (i.e., adsorption). Integrating the photocatalyst with the adsorbent material is a common way to enhance the efficiency of removal process, due to the increased specific surface area and facilitating adsorbed pollutant diffusion towards photocatalyst particles.

6.2. Aims and objectives

In this chapter, hybrid processes, combining adsorption, photocatalysis or filtration were investigated. More specifically, commercial air purificator, electrospun filters with activated carbon, potassium vanadate zeolite composites and multifunctional finishing were characterized, and synergistic effect was evaluated by means of pollutants removal.

6.3. Commercial air purificator

6.3.1. Materials and methods

Commercial active air purificator consists of 5 stages of filtration (Pre-filter, HEPA, bipolar ionization device, photocatalytic TiO_2 filter + UVC lamp and activated carbon filter). It was tested in terms of particulate matter removal in a pilot-scale test room according to the procedure described in the paragraph 3.3.2. with some modifications. Briefly, tested air purificator was placed inside a room (12 m^3) which was tightly closed, and the particulate aerosol was generated from 3% NaCl solution. The concentration of PM_2 and PM_{10} was measured by GRIMM spectrometer, which was placed inside the room.

Configurations tests are presented in Table 23.

Table 23. Filters configurations tested.

Filter type	Configuration number		
	1	2	3
HEPA F7	✓	✓	✓
Ionizator	✓	x	✓
UVA lamp	✓	✓	x
TiO$_2$ filter	✓	✓	✓
Activated carbon filter	✓	✓	✓

x – filter not present, ✓ - filter present.

Each test consisted of following steps:

1. Blank test (with active filtering system that is not present in the test room) - particulate generation was continued until the PM concentration reached 1600-1800 μg/m^3, at which point the generation is stopped, and natural decay is monitored.
2. When the active filtering system is present, it is switched on approximately 5 minutes after the generation reached 1600-1800 μg/m^3 and then stops to ensure homogeneous conditions inside the test chamber.
3. Combinations 2 and 3 were tested applying minimum flow rate (speed), while combination 1 was tested applying two different flow rates, minimum and maximum.

The removal efficiency is calculated as the difference between the detected concentration (PM$_2$ or PM$_{10}$) at the time of switching on the filtering system (C$_0$) and 15 minutes after its operation (C$_t$). The natural decay of particulate concentrations was subtracted from the data obtained.

$$PM\ removal(\%) = \frac{PM_0 - PMt}{PMo} \qquad (10)$$

Figure 102. PM removal test with commercial active system.

6.3.2. Results and discussion

Figure 103 report PM removal profiles for configurations 1-3 at minimum flow rate applied. A blank test is marked with a dashed line. It appears that, as regards the removal efficiency of PM_2 and PM_{10} at low speed, the different configurations adopted are not significantly influential. The ionization system and UV lamp (photocatalytic activation of TiO_2 filter), did not have an impact on the efficiency removal, indicating that HEPA filter is responsible for removing the most PMs. Indeed, tests from 3 different combinations showed that the concentration decreased to 300-400 $\mu g/m^3$ during 15 minutes of monitoring. From the results presented on the graph (Figure 103).

To assess the impact of the flow rate for the PM removal, configuration 1 (with all the filters present), was tested under maximum speed and the results are presented on Figure 104.
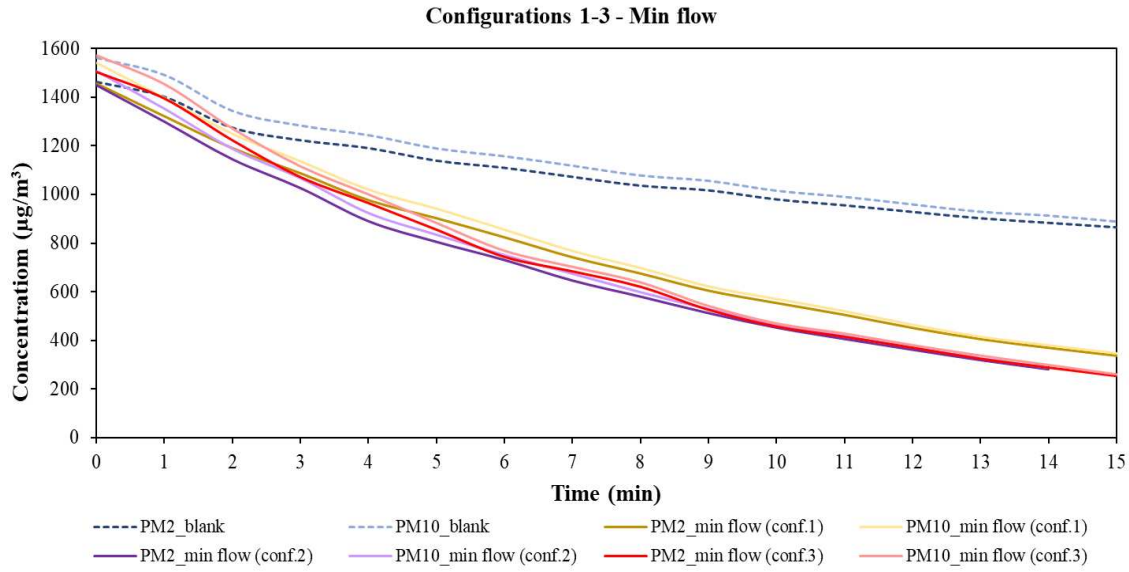
Figure 103. PM removal profiles for minimum flow rate (configurations 1-3).
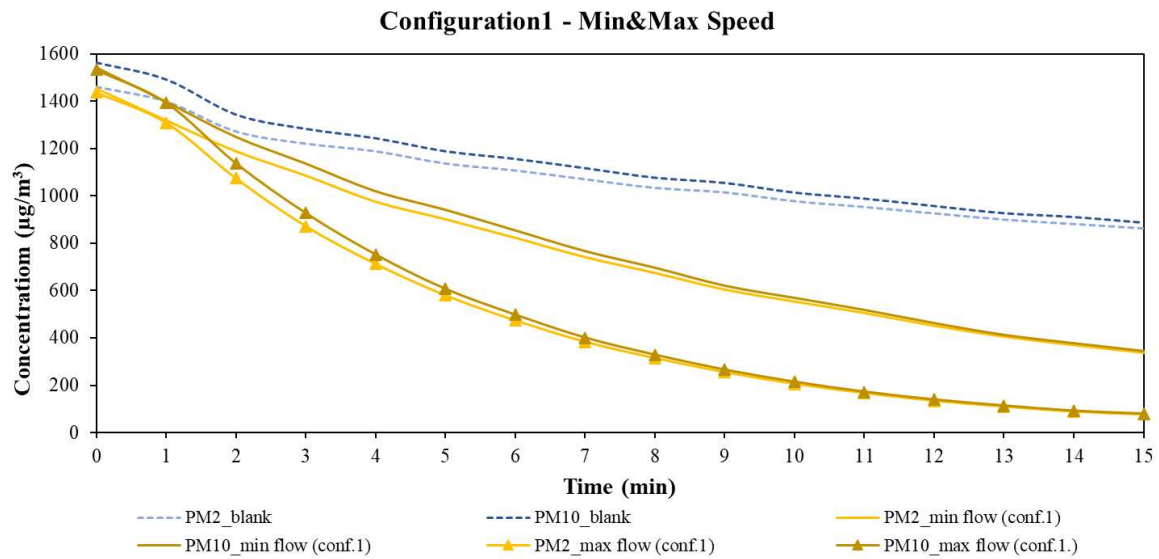
Figure 104. PM removal profiles for maximum flow rate (configuration 1).

All the configurations showed PM_2 and PM_{10} removal efficiency (Figure 105) from 36 to 40% and 39 and 43% respectively, during 15 minutes of monitoring test. On the other hand, the speed adopted is more influential. During maximum flow rate configuration, 1 showed 15% higher PM_2 and PM_{10} removal than when the minimum speed was applied.
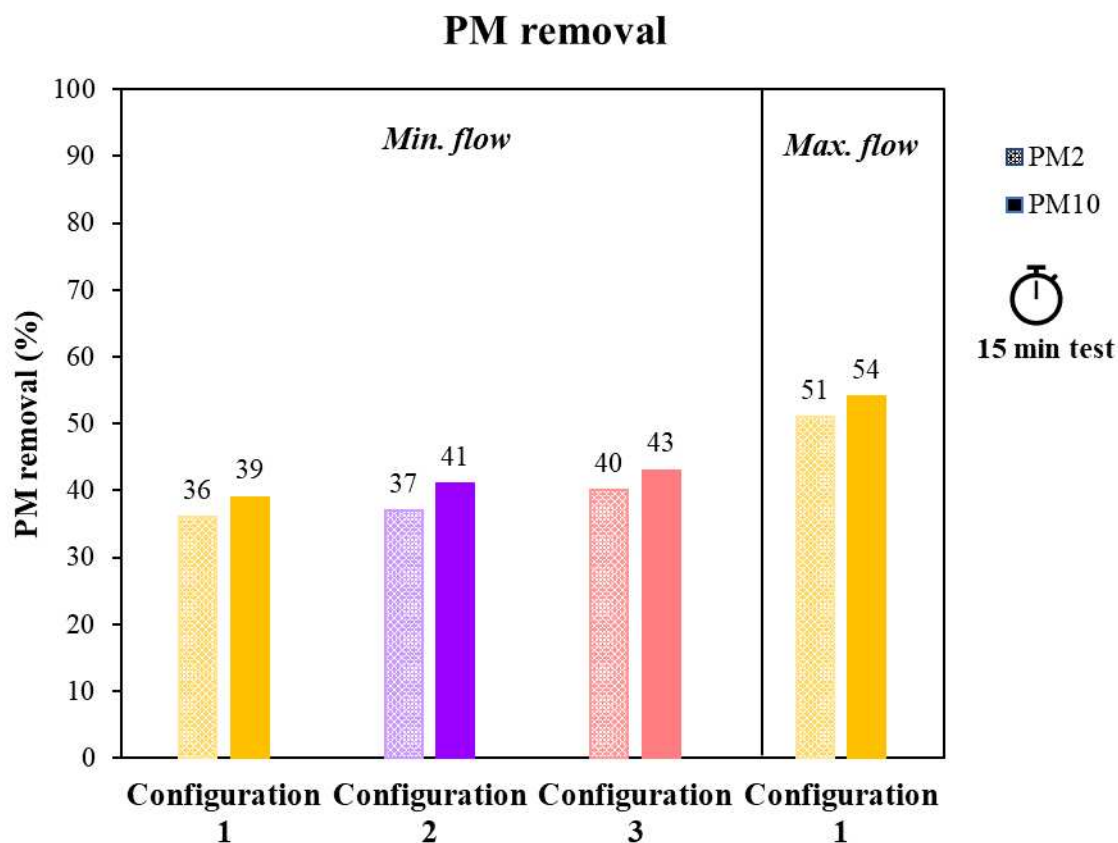
Figure 105. PM removal test results.

6.4. Filters with enhanced depolluting properties

6.4.1. Materials and methods

6.4.1.1. Materials

Electrospun filters previously tested in terms of particulate filtration efficiency (chapter 3) were selected to develop combined filters (imagine presented in paragraph 2.2.4.3.) with absorptive and photocatalytic properties. In order to reutilize polymer waste via electrospinning, samples fabricated from waste cellulose were selected (PLA-W:MCC). Three types of activated carbons (described previously in chapter 4) were used as adsorbents: commercially available AC-COM and AC-K_2CO_3-CG and to set a reference standard for the adsorption efficiency, the commercial activated carbon filter (paragraph 2.2.4.2.), labelled as AC Liquifil. Photocatalytic agent P-25 TiO_2 was applied in order to enhance VOCs removal.

6.4.1.1. Hybrid filters fabrications

Electrospun filters were fabricated as described previously in chapter 3. Activated carbon was sprayed on the electrospun surface by aerograph, creating the first layer (adsorptive one). The reason why activated carbon was not mixed together with the polymer solution before the electrospinning is to avoid blocking the pores present in the AC particles by the layer of the polymer [115].

The activated carbon was firstly crashed in the mortar to further decrease the dimension of the grains and break the thicker bulks; this was necessary to avoid the clogging of the airbrush during the spraying operation. The pure PLA filter was firstly weighted and then the crashed activated carbon was dispersed in the ethanol and sprayed with an airbrush on the filter surface. Ethanol was chosen as a solvent because it is not dissolving PLA, and it evaporates at a faster rate than water. After the complete evaporation of the solvent, the filter was weighted again to determine the quantity of activated carbon deposited to the polymeric base.

One of the filters was sprayed both with a first layer of activated carbon and a second layer of a TiO_2 solution to study a possible VOCs adsorption increase due to the synergistic effect of activated carbon adsorption and TiO_2 photocatalytic oxidation under visible and UV light. The method to spray the TiO_2 layer on the filter was the same used for the activated carbon.
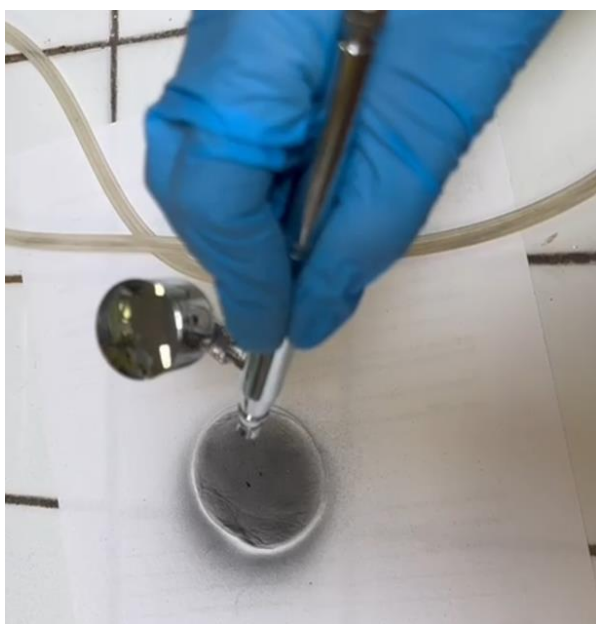
Figure 106. Polymeric Electrospun filter sprayed with activated carbon.

Figure 107. Polymeric Electrospun filter sprayed with activated carbon and TiO₂ P-25.

List of the tested filters and activated carbon and titanium dioxide contents are shown below. A Commercial AC filter (Liquifil 259) was used for comparison.

Table 24. List of the tested filters.

Filter	Label	Filter weight (mg)	Type of AC	AC (mg)	AC Content (%)	TiO₂ (mg)
AC Liquifil PLA:W-MCC (95:5)	Commercial AC filter PLA	2134	-	1067	*50%	-
PLA:W-MCC (95:5)	PLA+AC_COM	107.6	Commercial	22.7	21%	-
PLA:W-MCC (95:5)	PLA+AC_COM+TiO2	153.3	Commercial	22.7	15%	20
PLA:W-MCC (80:20)	PLA+AC_CG	93.7	AC-K₂CO₃-CG	13.9	15%	-

*declared in data sheet.

6.4.1.2. Depolluting properties evaluation

To test the adsorption of volatile organic compounds, the procedure described in paragraph 4.4.4. was followed with some modifications. Briefly, the filters were placed on the extremity of a PVC tube just after a small turbine; the turbine creates negative pressure and forces the air through the filter. The tube was then placed inside a sealed box (17 L). 1µl of MEK was injected into the reactor utilizing a micro-syringe to ensure an initial concentration of around 16 ppm (± 1 ppm), after evaporation. A fan was placed in the bottom of the reactor to guarantee continuous air recirculation. To monitor changes in the VOCs concentration over time, a photoionization detector (PID) (Aeroqual, Series 900, 0–30ppm range) was used. A blank test was performed before each analysis to control the concentration during the analysis.

For the filter with the further addition of the TiO_2, photocatalytic degradation of MEK was evaluated following the procedure described previously in paragraph 5.3.3. After 30 minutes of the test, the same reactor used for VOCs adsorption test (17 L) was irradiated by a visible light lamp (Philips lamp, 42W) with intensity equal to 12 ± 1 W/m^2 as detected by Delta Ohm HD 2101.1 photo radiometer (probe LP471 RAD 400 – 1050 nm). After 50 minutes of the test the VIS lamp was turned off and UV radiation was turned on (halogen lamp, 400W), with measured radiance of 12 ± 1 W/m^2 (probe LP471 UVA 315 – 400 nm).

6.4.2. Results and discussion

The results of the VOC adsorption are reported in Figure 108 as the C/C_0 ratio evolution during the test. PLA filter without addition of activated carbon does not show the adsorption properties and the monitoring line (green line) after 60 minutes of the test starts to overlap the blank line (dashed line). PLA does not adsorb and is used as a negative reference sample. Both the adsorption efficiency, and the trend of the MEK concentration decrease can be compared. The decrease follows an asymptotic trend in all the cases. For all the hybrid PLA-AC filters, the MEK concentration shows a sharp decrease in the first 20 minutes and then an almost constant plateau in the next 40 minutes of the test, indicating the adsorption sites are saturated after 20 minutes of the test and no further adsorption can take place. The Commercial AC filter does not present the flat trend after 20 minutes, but the adsorption carries on for the length of

the test. The amount of AC present in this commercial filter is indeed much higher, hence the adsorption sites are not easily saturated.
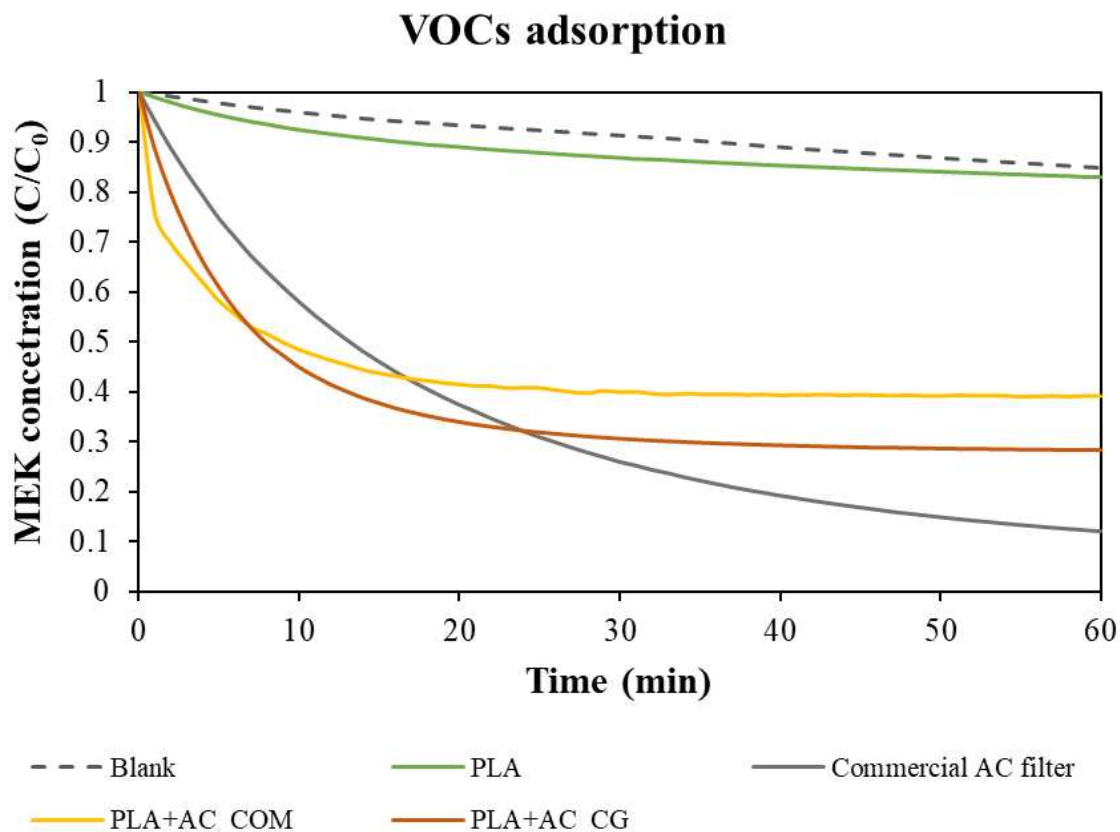
Figure 108. VOCs adsorption profiles.

In order to evaluate the photocatalytic activity, PLA+AC_COM+TiO_2 filter has been tested (Figure 109). In this case, two processes occurred: in the first phase adsorption, and later, photocatalysis. The result of all the samples tested were compared in Figure 110. The sample with the additional layer of TiO_2 was able to remove 36% of MEK within the 30 minutes of the test and showed 8% lower adsorption efficiency, than the same filter without addition of TiO_2 (PLA+AC_COM). The TiO_2 layer could have possibly limited the adsorption capacity of the activated carbon. After 30 minutes, when the sample reached equilibrium VIS lamp was switched on however, no changes in the concentration were noticed. Then, after turning off the VIS lamp, the sample was irradiated with a UV lamp and concentration was monitored for the next 30 minutes. The results showed slight photocatalytic activity under UV radiation (8%). Comparing this data with results obtained from standalone test (paragraph 5.4.3.), when 18 mg

of P-25 was tested under higher UV light intensity (45 W/m^2) it was able to remove 66% of MEK in 30 minutes of radiation. Experimental conditions were different, hence the results are not comparable, however several studies have investigated the use of AC as a support material for TiO$_2$ in removing VOCs from polluted air. For example, in the work of Ding et al. [116], TiO$_2$ was coated with AC by chemical vapor deposition and photocatalytic activities was determined through the degradation of phenol in water. The results showed that produces composites did not show the photocatalytic activity, indicating that activated carbon could act as an inhibitor of TiO$_2$. Similar finding were reported in work of Orlando et al. [117], where cellulose acetate electrospun fibers were modified with activated carbon and P-25 photocatalyst and examined for toluene removal. The results obtained showed that membranes that contained TiO$_2$ did not show a clear reduction of toluene concentration. However, when the CA/TiO$_2$ electrospray membrane was irradiated with UV, formaldehyde which is a typical by-product of PCO of toluene has been detected. Therefore, it can be concluded that in this case, photocatalytic reaction has been initiated in the set-up. Lastly, when the additives were combined onto the surface of the membranes (AC and TiO$_2$), it seems that the AC prevents the degradation of toluene from the catalyst. No formaldehyde production was recorded and therefore the TiO$_2$ might have been deactivated from AC, or the formaldehyde had been retained in the charcoal and could not be observed during the experiment.
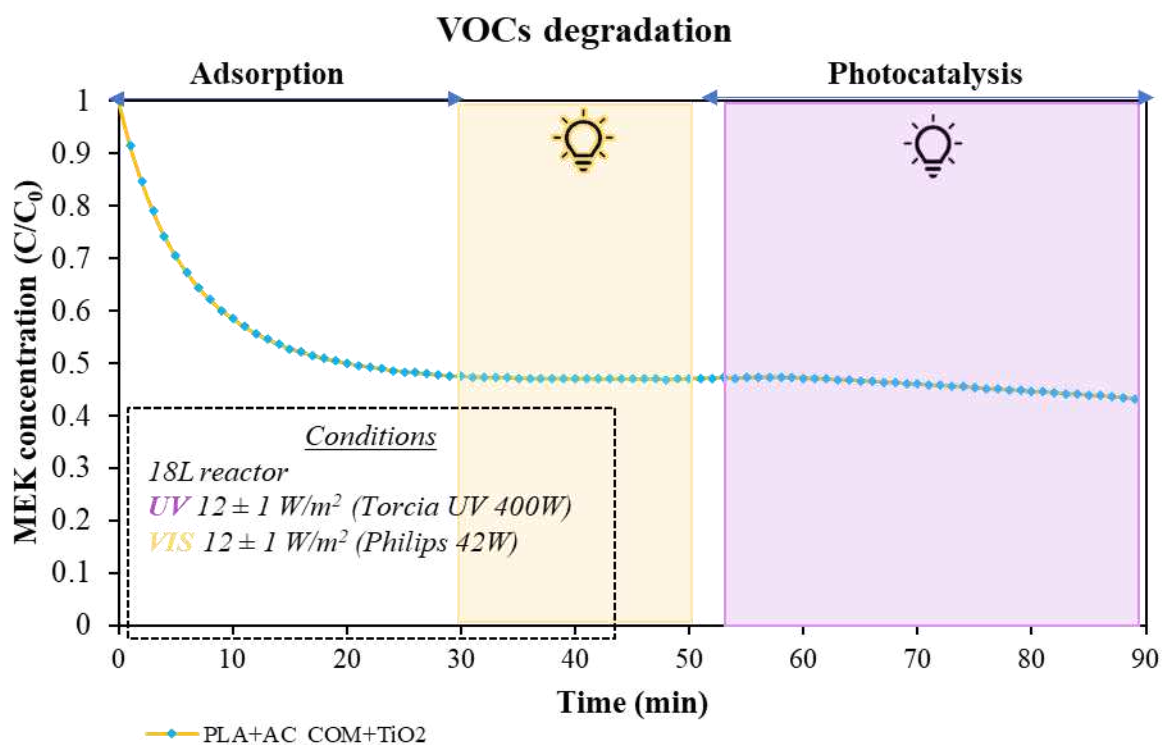
Figure 109. VOC photocatalytic degradation profile.
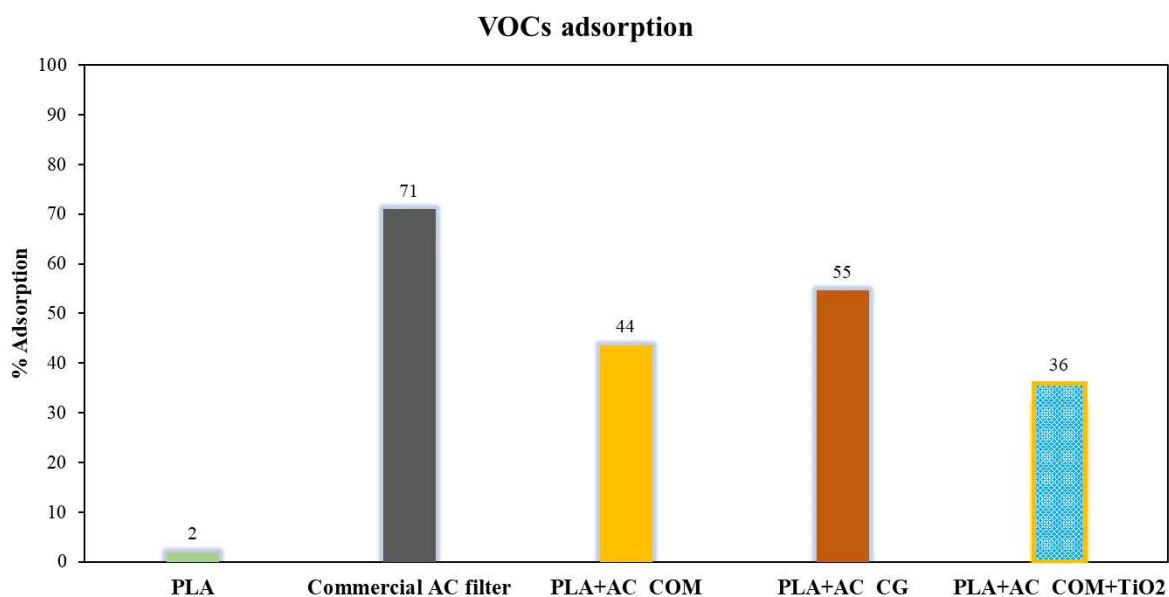
Figure 110. VOCs adsorption test results.

6.5. Photocatalytic agents with adsorptive properties

6.5.1. Materials and methods

Potassium vanadates and zeolite composites, prepared by another research group [28], were analyzed in terms of enhanced depolluting properties. The composites were prepared at 80 ^{O}C by mixing 500 mg V_2O_5 with 1M or 2M CHOOK. At the end of the reaction (after 72 hours), and after cooling down of obtained product, 100 – 500 mg of zeolite was added in the ambient temperature. Four different composites were prepared and labelled as KVO_ZEO1_1, KVO_ZEO1_5, KVO_ZEO5_1 and KVO_ZEO5_5, where the first number indicates the quantity in molar percentage of potassium formate:

- 1: 1 mol% of CHOOK;

- 5: 5 mol% of CHOOK;

and the second number that we find in the wording of the samples indicates the quantity in milligrams of zeolite:

- 1: 100 mg of zeolite;

- 5: 500 mg of zeolite.

Obtained results were compared with the commercial P-25 and KronoClean 7404 photocatalytic agents.

Morphology of obtained composites was analyzed through the SEM (according to the procedure from paragraph 2.3.). Textural properties including the specific surface area (SSA) were determined using the Brunauer–Emmett–Teller (BET) equation, the total pore volume (V_{total}) was determined by the amount of N_2 adsorbed at $P/P_0 = 0.95$ (paragraph 2.3.3.). The pore size distributions and pore areas are derived by the Barret – Joyner – Halenda (BJH) analysis with Halsey corrections in the range of $0.42 \leq p/p0 \leq 1$ of the adsorption branches for N_2 on the powders.

6.5.1.1. Depolluting properties evaluation

In order to evaluate depolluting (photocatalytic and adsorptive) properties NO_X and VOCs removal tests were performed according to the procedure previously described (paragraph 5.3.3). To confirm the successful mineralization during VOCs removal test CO_2 concentration was monitored by means of CO_2 K-30 Sensor (030-8-0006, 10.000 ppm) which was placed inside the 17 L reactor and connected to the Arduino Uno UART Interface. The concentration was registered Arduino IDE 2.2.1. software.
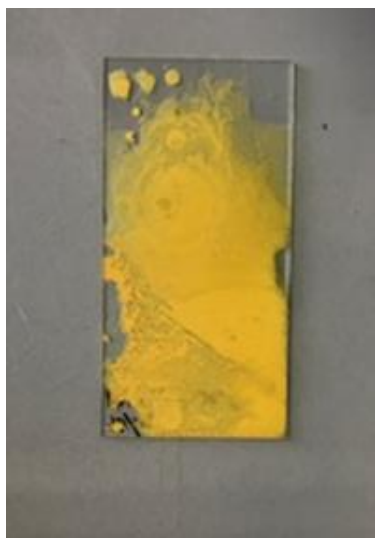
Figure 111. KVO_ZEO sample prepared for depolluting tests.

6.5.2. Results and discussion

6.5.2.1. Composites morphology and textural properties

Figure 112 collects the SEM images of tested samples.
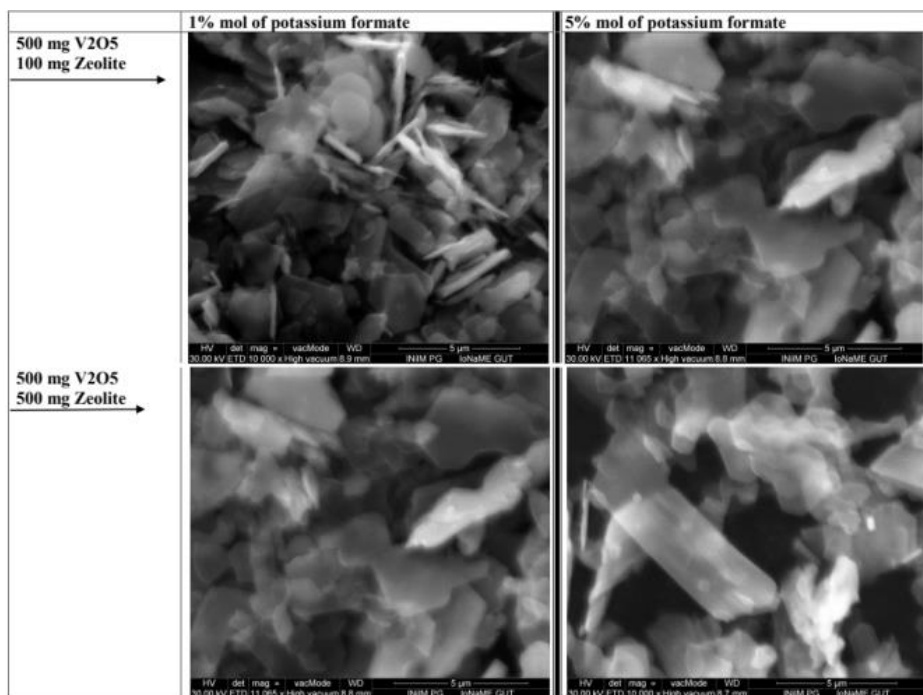
Figure 112. SEM images of potassium vanadate and zeolite composites.

Textural properties, such as specific surface area (SSA), total pore volumes (V_{total}) obtained from N_2 adsorption–desorption isotherms, of obtained composites are listed in Table 25. TiO_2 P-25 was measured as a reference sample. Figure 113 presents N_2 adsorption isotherms. BJH pore size distribution curves are shown in Figure 114-Figure 118.

BET N$_2$ adsorption isotherm
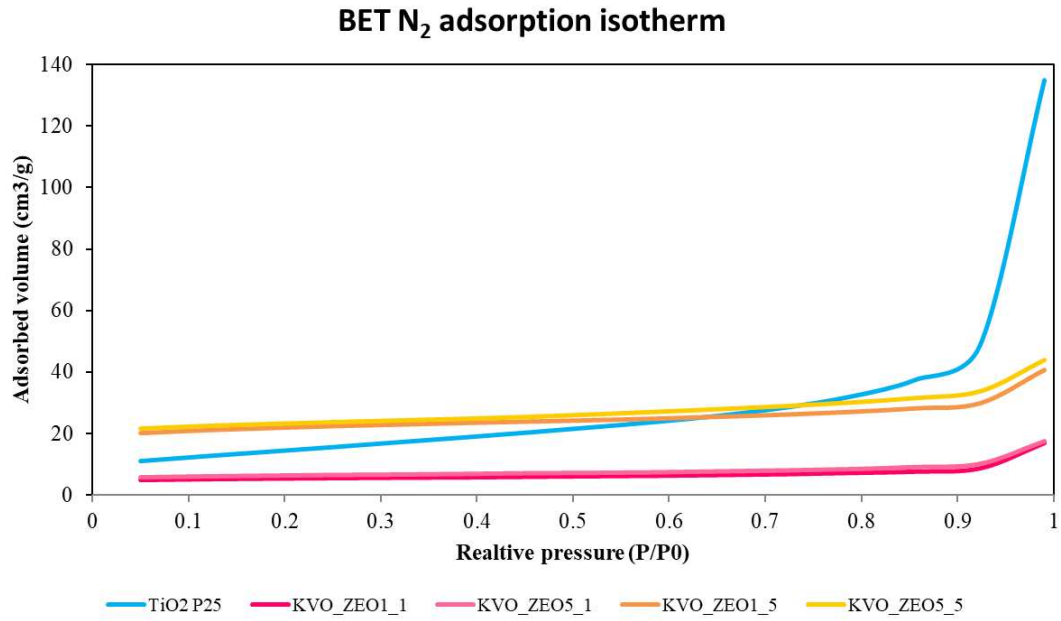
Figure 113. BET N$_2$ adsorption isotherms.

Figure 114. BJH pore size distribution curve of P-25.
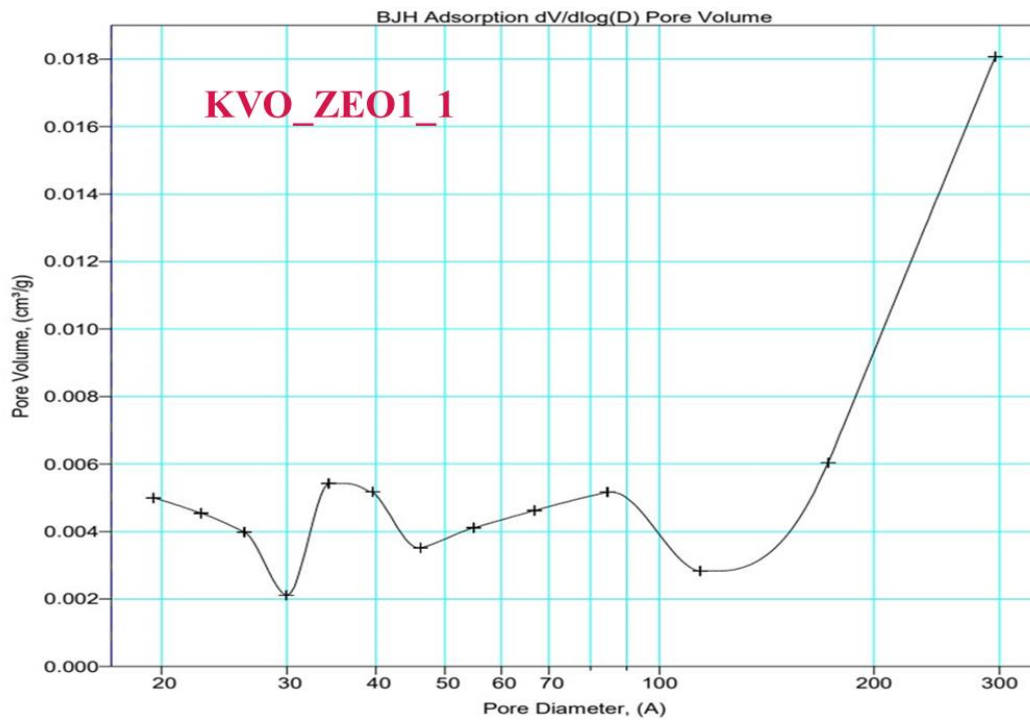
Figure 115. BJH pore size distribution curve of KVO_ZEO1_1.
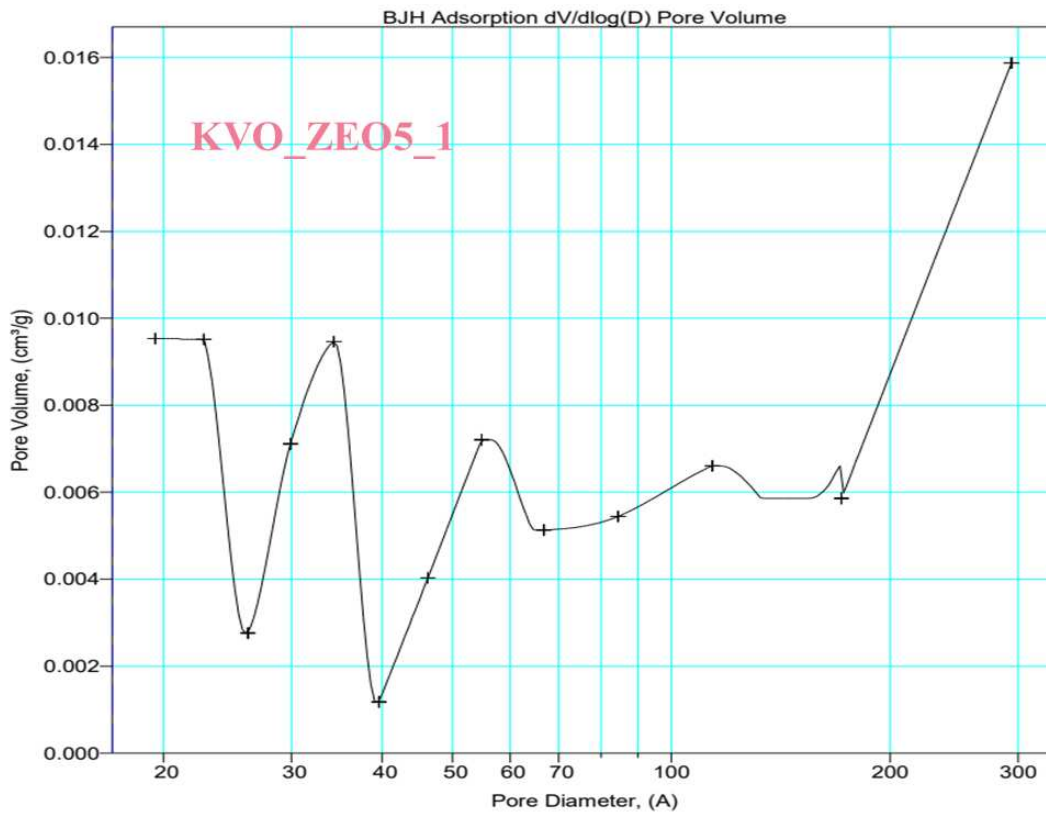
Figure 116. BJH pore size distribution curve of KVO_ZEO5_1.

Figure 117. BJH pore size distribution curve of KVO_ZEO1_5.
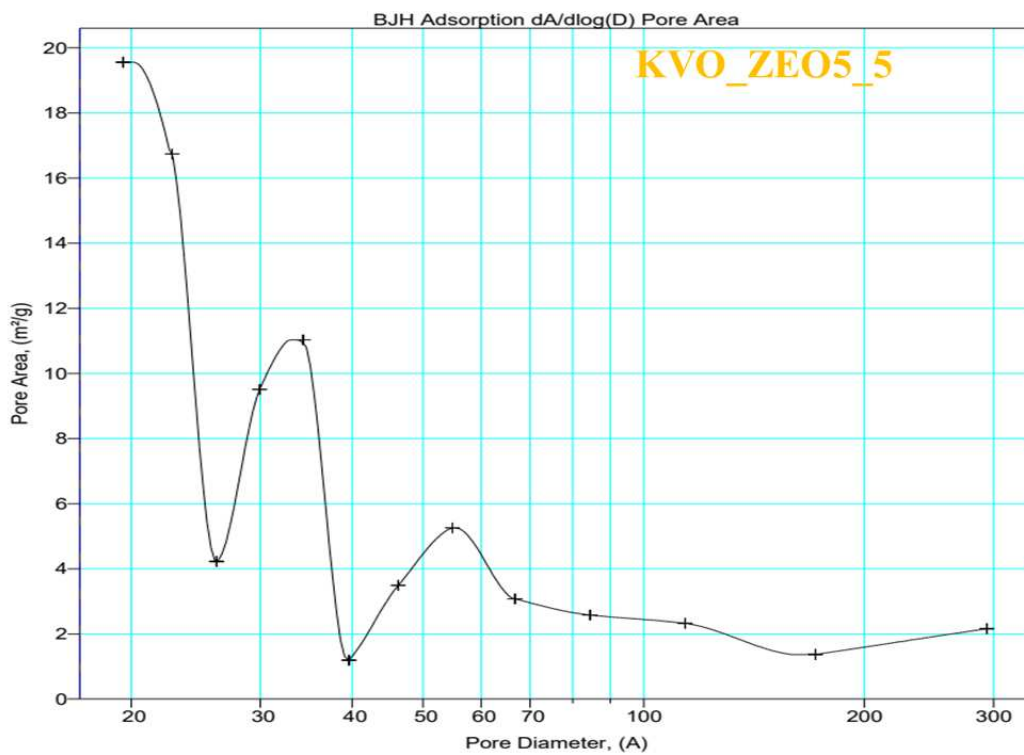
Figure 118. BJH pore size distribution curve of KVO_ZEO5_5.

174

Table 25. Textural properties of tested samples.

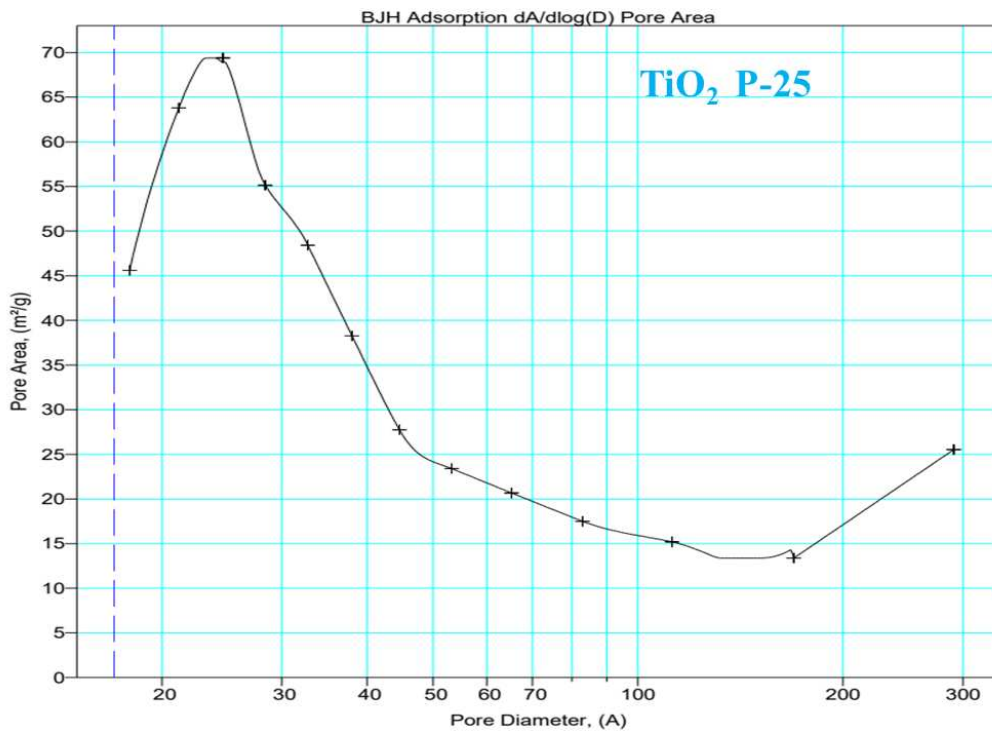| Sample	P-25	KVO_ZEO 1_1	KVO_ZEO 5_1	KVO_ZEO 5_5	KVO_ZEO 1_5
SSA (m^2/g)	52	18	31	76	72
Micropore area	0.36	12	13	13	49
Micro pore volume (cm^3/g)	-0.000146	0.0059	0.0064	0.0064	0.024
Average pore diameter (4V/A)	146 A	137 A	108 A	108 A	73 A

From the results collected in Table 25 we can see how in the KVO_ZEO samples the BET specific surface values are mainly influenced by the weight percentage of the zeolite, for KVO_ZEO1_5 and KVO_ZEO5_5 which have a quantity of zeolite 5 times higher than KVO_ZEO1_1 and KVO_ZEO5_1 the BET specific surface values are 3 times higher. We then notice a slight influence of potassium formate which at lower percentages has a slightly lower specific BET surface compared to a higher percentage.

6.5.2.2. NO$_x$ removal

NO$_x$ degradation test was performed in order to evaluate the photocatalytic activity. NOx concentration profiles are shown in Figure 119 – 124.
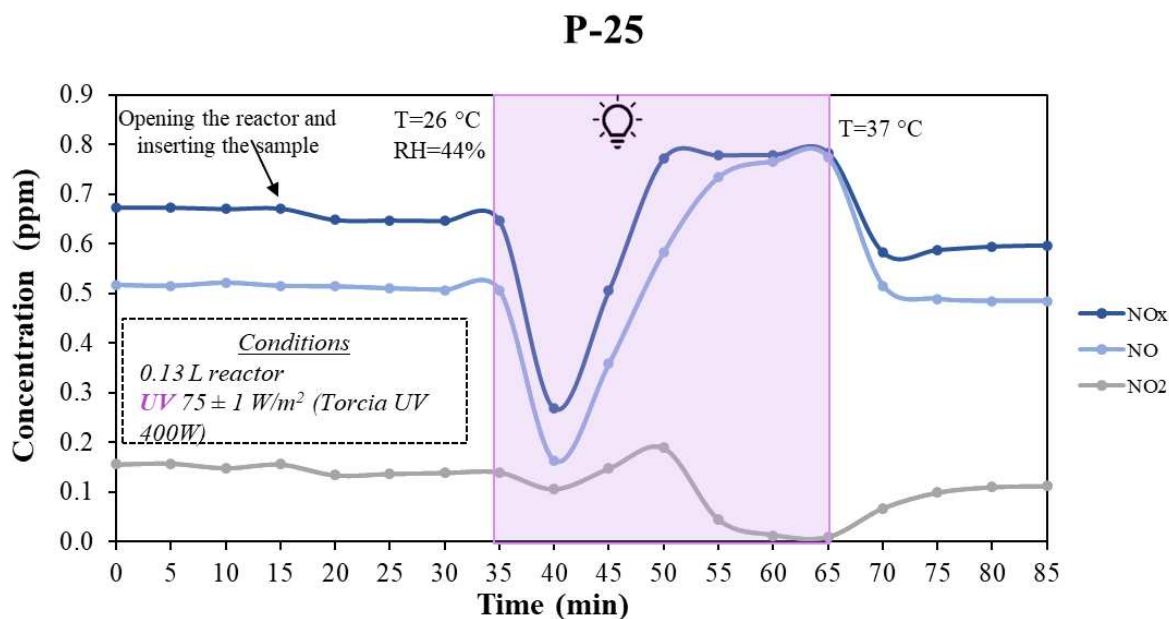
Figure 119. P-25 profile of photocatalytic oxidation of NO$_x$ under UV light.

After inserting the sample, the concentration of NOx decreased around 4%, which is caused because of the adsorption process. After 5 minutes of irradiation with UV lamp sharp decrease in the NOx and NO can be noticed, however after that time the concentrations starts to increase. The rapid increase in the concentration of NO_x, NO and NO_2 after could be caused due to the saturation of active sites but also desorption from the P-25 surface previously captured pollutant compounds due to the increasing temperature inside the reactor.
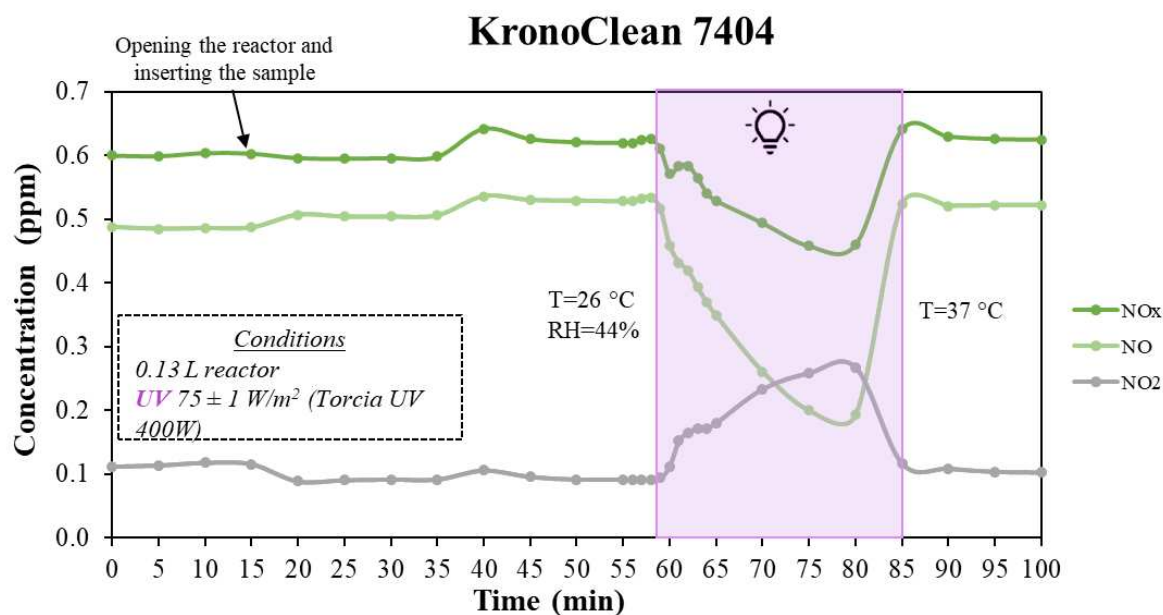
Figure 120. KronoClean 7404 profile of photocatalytic oxidation of NOx under UV light.

KronoClean 7404, the second commercial photocatalytic agent tested adsorbed 1% of NOx in the initial phase of the test. After the irradiation with UV lamp, contrary to NO_2 concentration the NOx and NO concentration decreased slowly and reached a peak after 20 minutes. 20 minutes After that time the NOx and NO concentration start to increase.
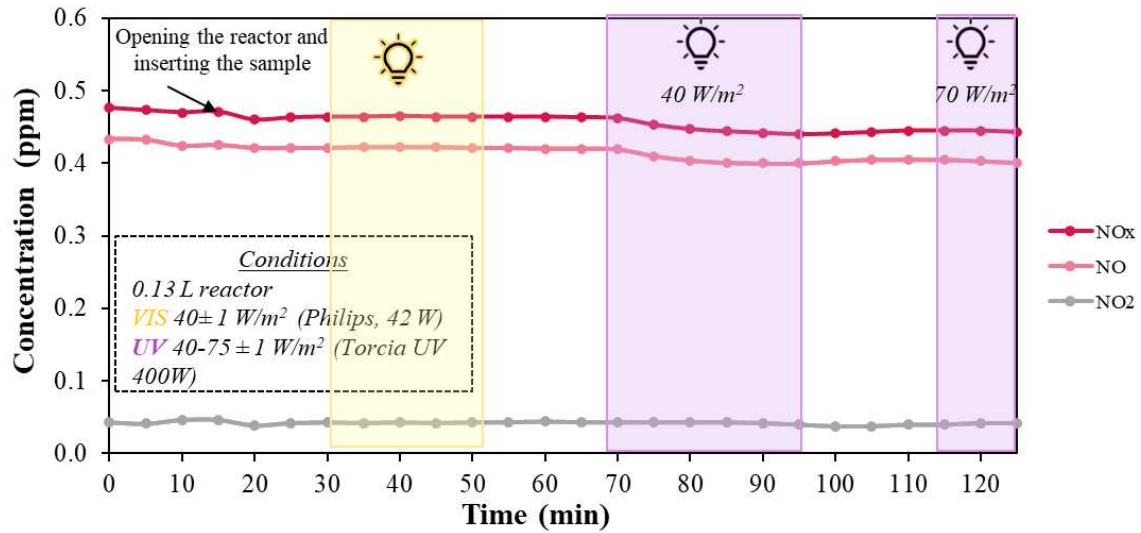
Figure 121. KVO_ZEO1_1 profile of photocatalytic oxidation of NOx under VIS and UV light.

Although KVO has been reported as a visible active photocatalytic agent, the first KVO_ZEO composite tested did not show any activity under visible light. Therefore, further tests were conducted under UV radiation initially with the irradiance 40 W/m^2 and then under 70 W/m^2. However, after the first UV radiation step KVO_ZEO1_1 showed just a slight decrease in NOx and NO concentration, and no further photocatalytic degradation probably to the saturation of the active sites.
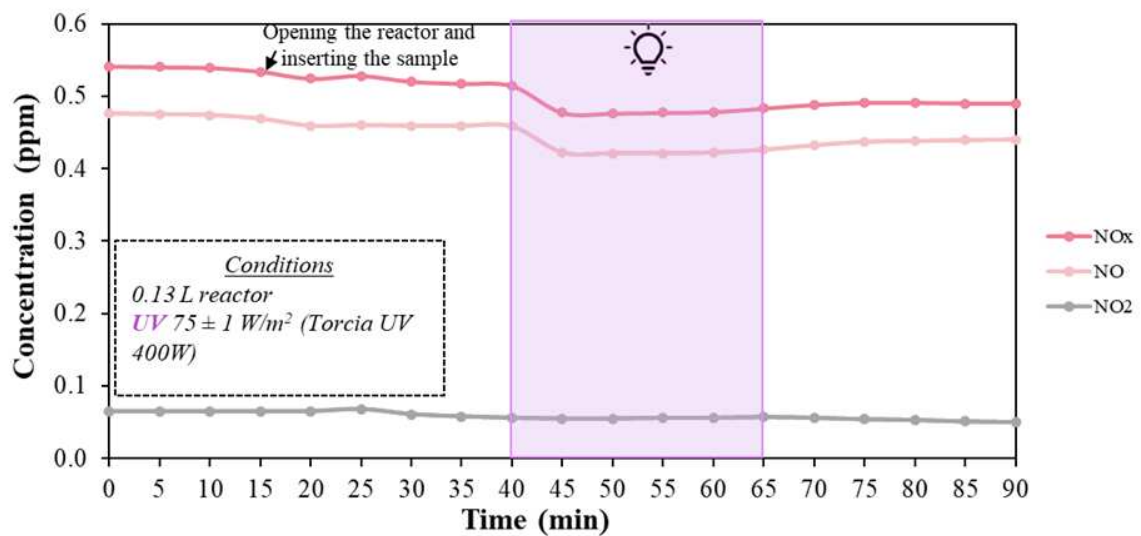
Figure 122. KVO_ZEO5_1 profile of photocatalytic oxidation of NO$_x$ under UV light.
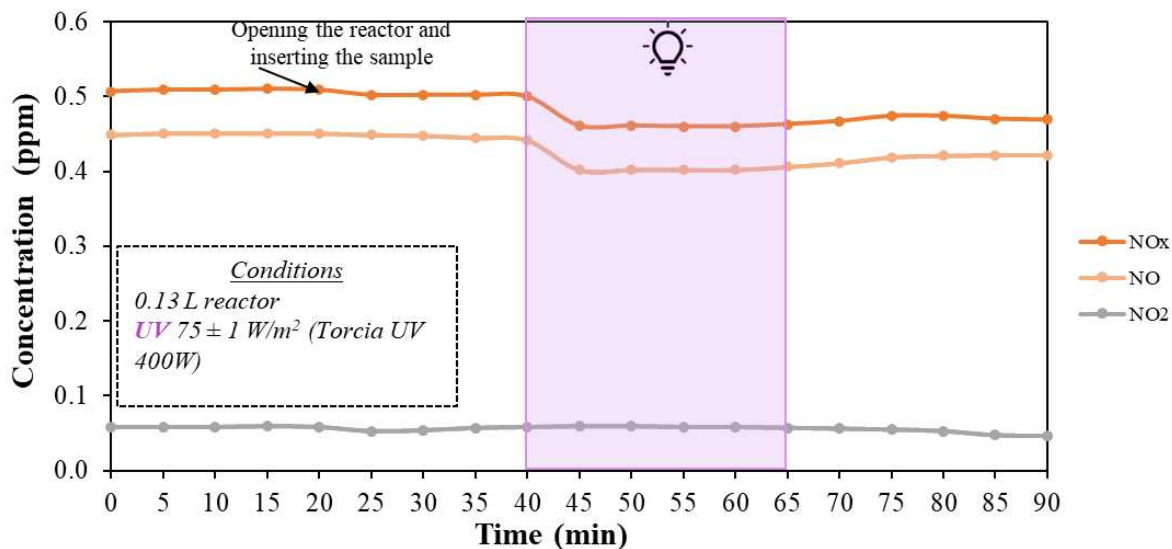
Figure 123. KVO_ZEO1_5 profile of photocatalytic oxidation of NO$_x$ under UV light.
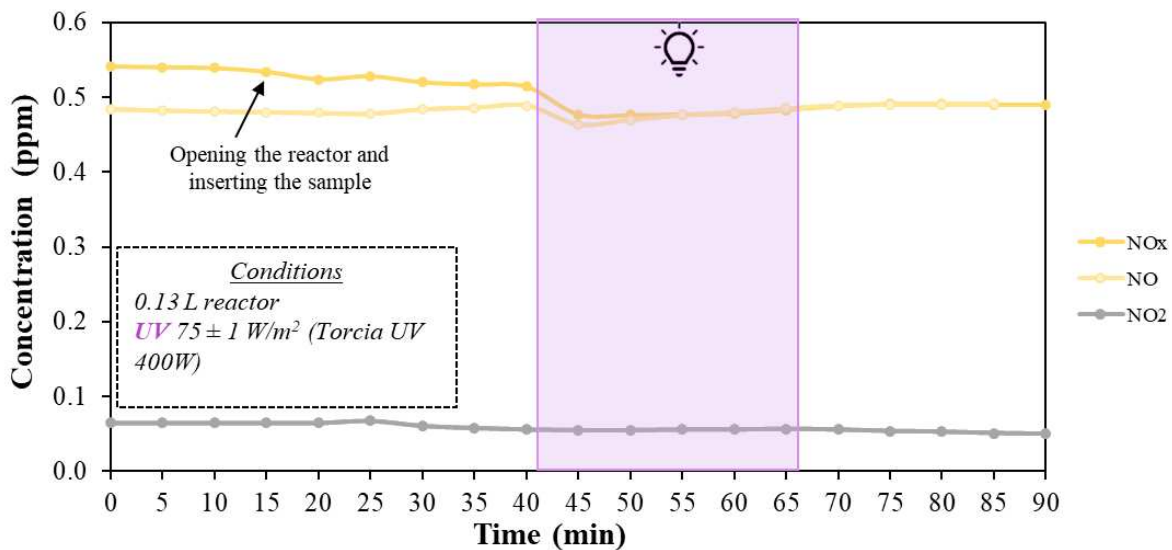
Figure 124. KVO_ZEO5_5 profile of photocatalytic oxidation of NOx under UV light.

Next two tests concern composites (KVO_ZEO1_5 and KVO_ZEO5_1) produced with higher zeolite content (500 mg) than previous ones. Both of them showed slight photocatalytic activity.

KVO
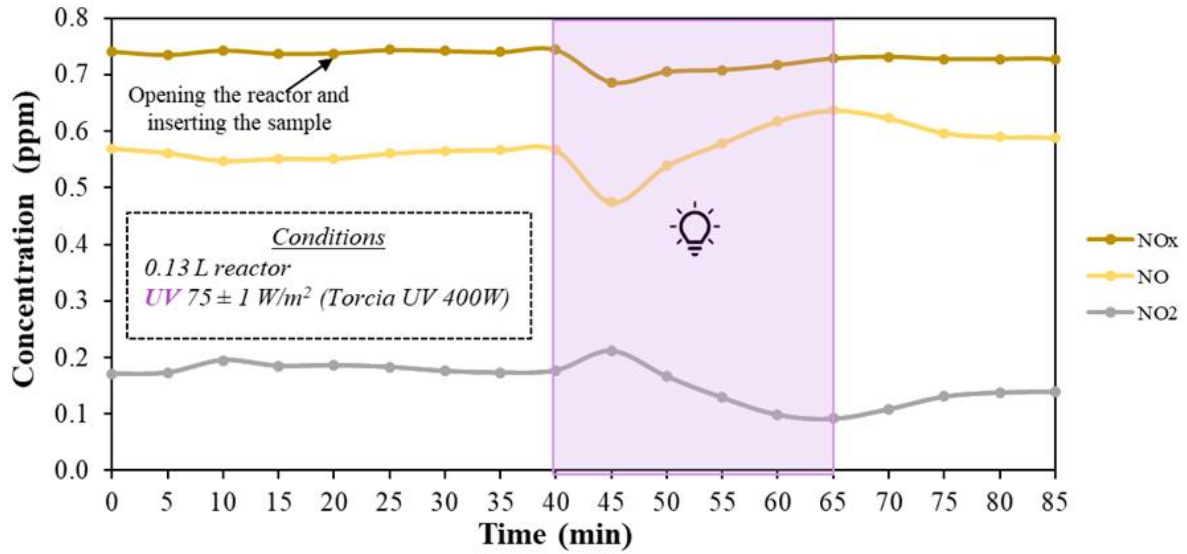
To compare obtained results, sample without zeolite KVO, has been tested in the same conditions as composite samples. The results showed after turning of the UV lamp concentration of NO_X and NO decreased in 5 minutes of irradiation, but very quickly after this time the concentration started to increase. This phenomenon was not present while testing KVO_ZEO composites, probably due to the enhanced specific surface area which trapped gaseous molecules, while KVO became saturated.

NOx degradation test
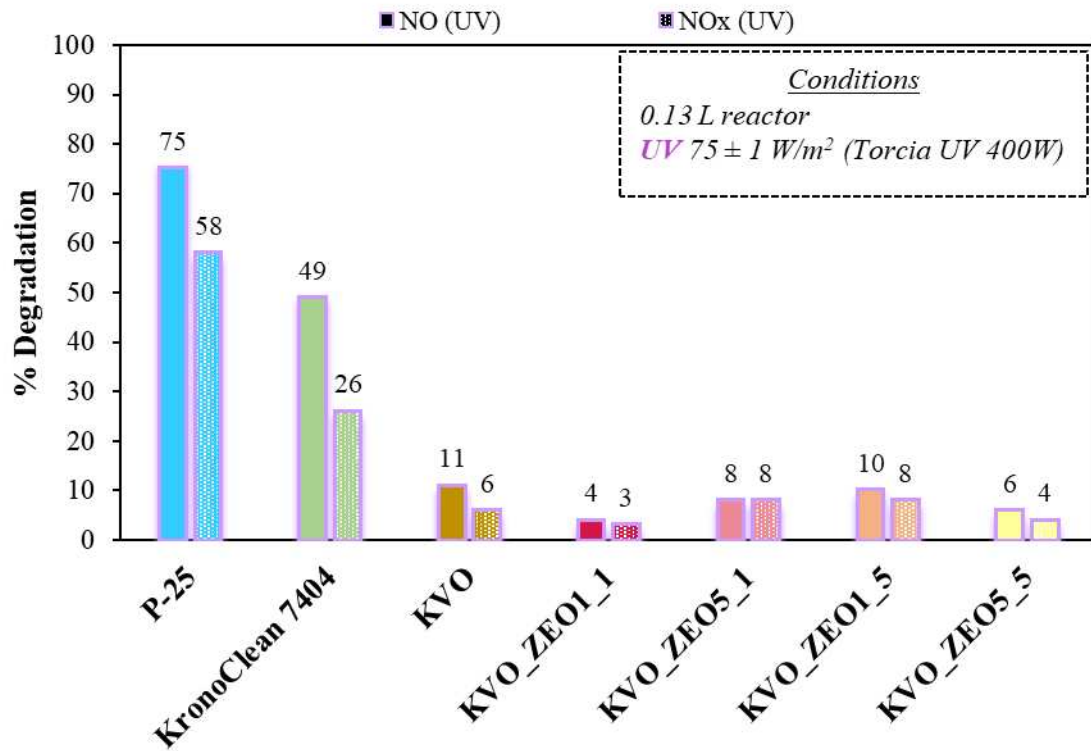
Figure 125. NO$_x$ degradation test results.

NOx removal/SSA
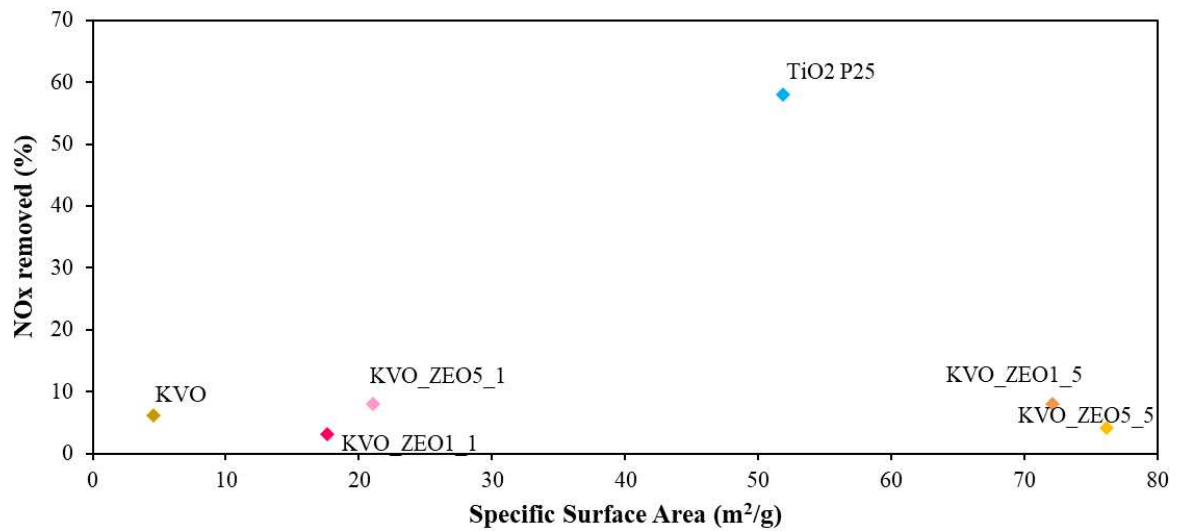
Figure 126. Correlation between NOx removal and Specific Surface Area.

The results from the NO_X test are presented in bar chart on Figure 125. For the KVO_ZEO composites and KronoClean 7404 photodegradation efficiency was considered after 25 min of illumination, while for the P-25 the value obtained after 5 min of illumination was considered during the calculations. Results showed that increasing UV radiation up to 75 W/m^2 photocatalytic NO_x degradation increased from 3% to 11%. KVO_ZEO composites did not show enhanced photocatalytic degradation compared to the KVO without zeolite. Between all the KVO_ZEO composites, KVO_ZEO1_5 showed the highest ability of NO_x removal (10%), KVO_ZEO5_1 with the same amount of zeolite but prepared with different molarity of potassium formate characterize lower photocatalytic degradation (6%), indicating that not the zeolite content (so adsorption properties) plays significant role in pollutant removal, but the method of preparation and V^{4+} content [28]. However, when we look closer on two KVO_ZEO composites prepared with the same molarity of the potassium formate KVO_ZEO1_1 and KVO_ZEO1_5 and KVO_ZEO5_1 and KVO_ZEO5_5 we can notice different photocatalytic activity between them indicating, that both factors: zeolite content and method of preparation could influence on the NO_x removal.

We can also notice that in case of zeolite composites, all the samples showed lower production of NO_2 compared to KVO. This fact can be explained by the presence of zeolite which could trap produced NO_2 molecules.

Moreover, to investigate the dependence of the specific surface area on the NO_x removal the Figure 126 has been presented. The results shows that SSA of specimens tested does not influence the NO_x removal.

6.5.2.3. VOCs removal

In order to evaluate VOCs degradation and adsorption another experiment has been performed. Separate results for every sample has been presented below. While figure Figure 133 and Figure 134 demonstrates the comparison of all the results collected during this test.
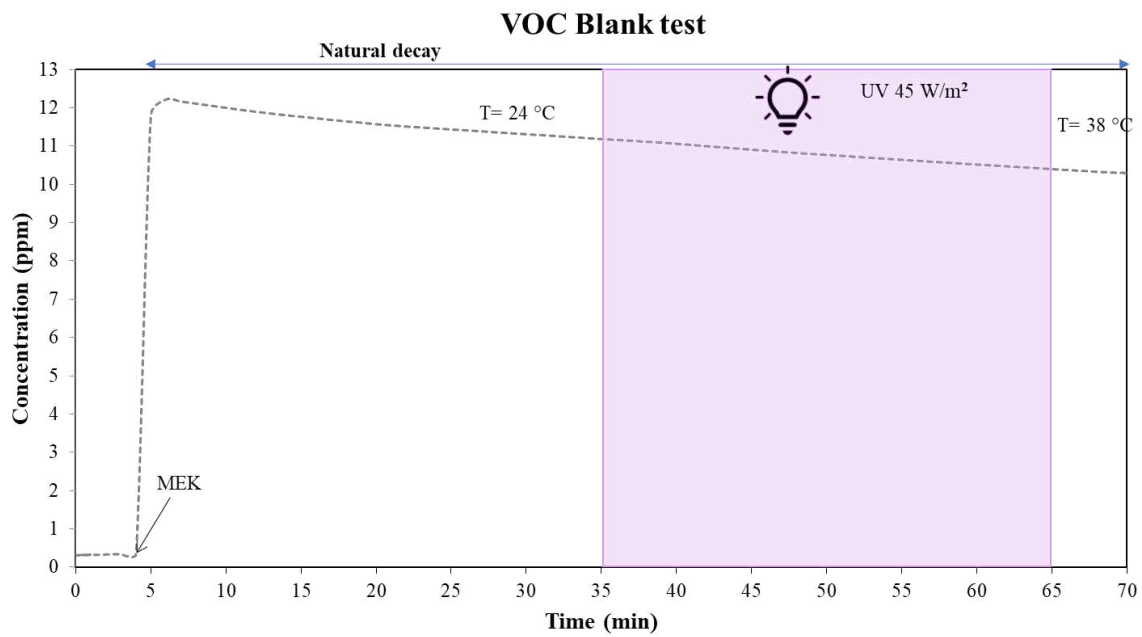
Figure 127. VOCs degradation blank test.
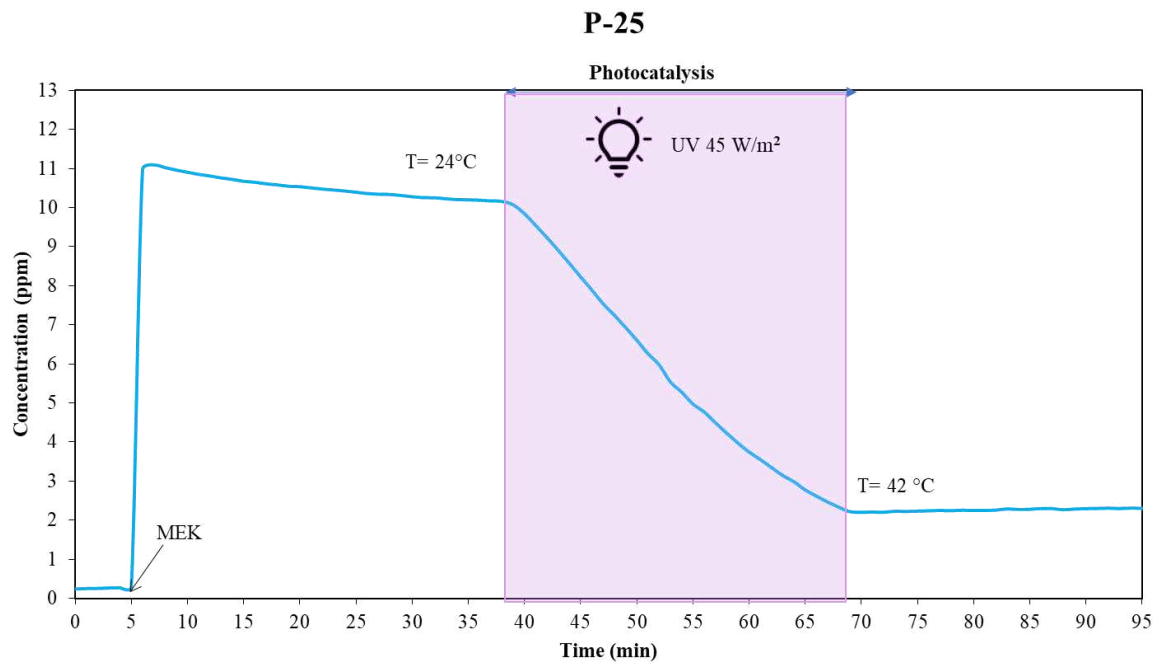
Figure 128. P-25 VOCs degradation profile under UV light.
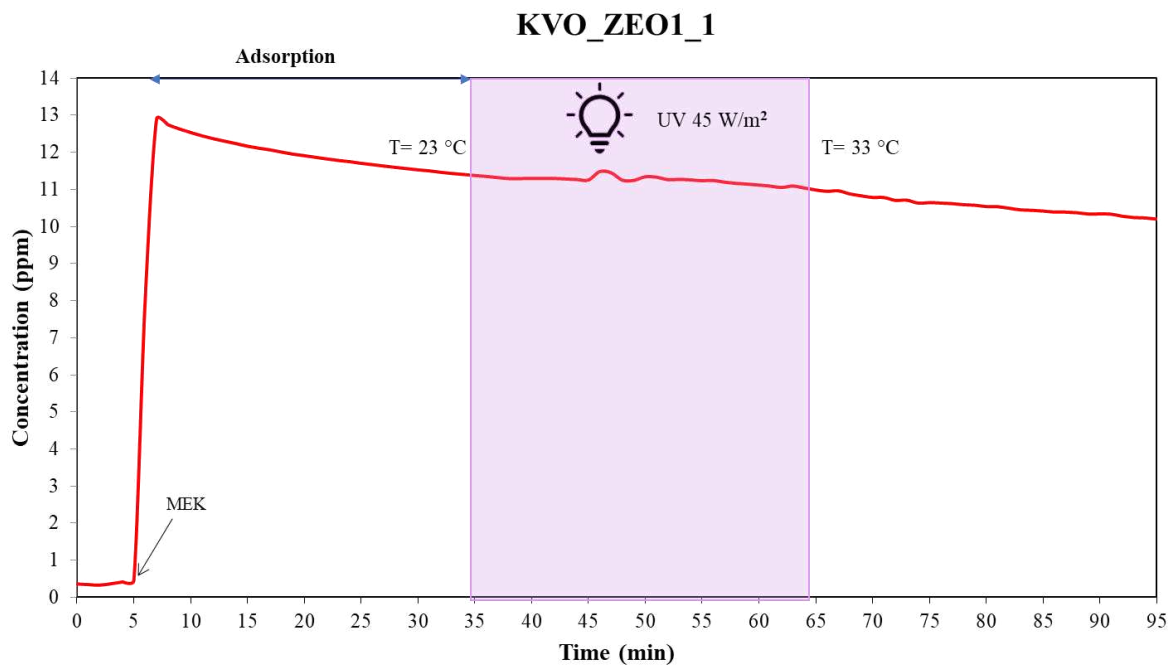
KVO_ZEO1_1

Figure 129. KVO_ZEO1_1 VOCs degradation profile under UV light.
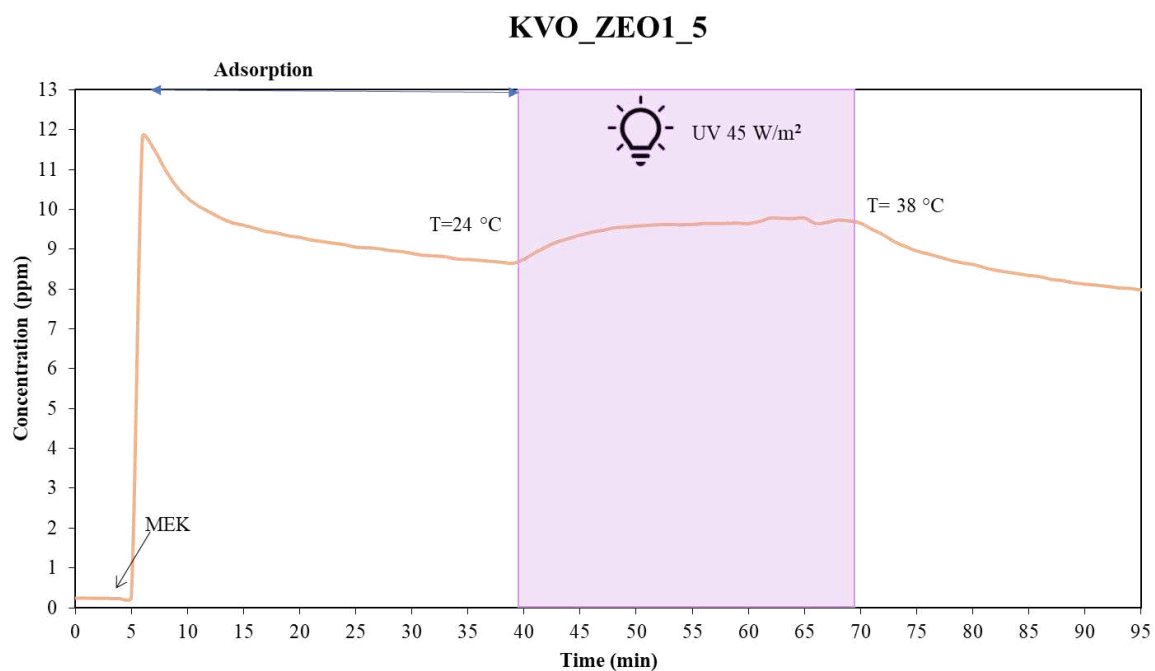
KVO_ZEO1_5

Figure 130. KVO_ZEO1_5 VOCs degradation profile under UV light.
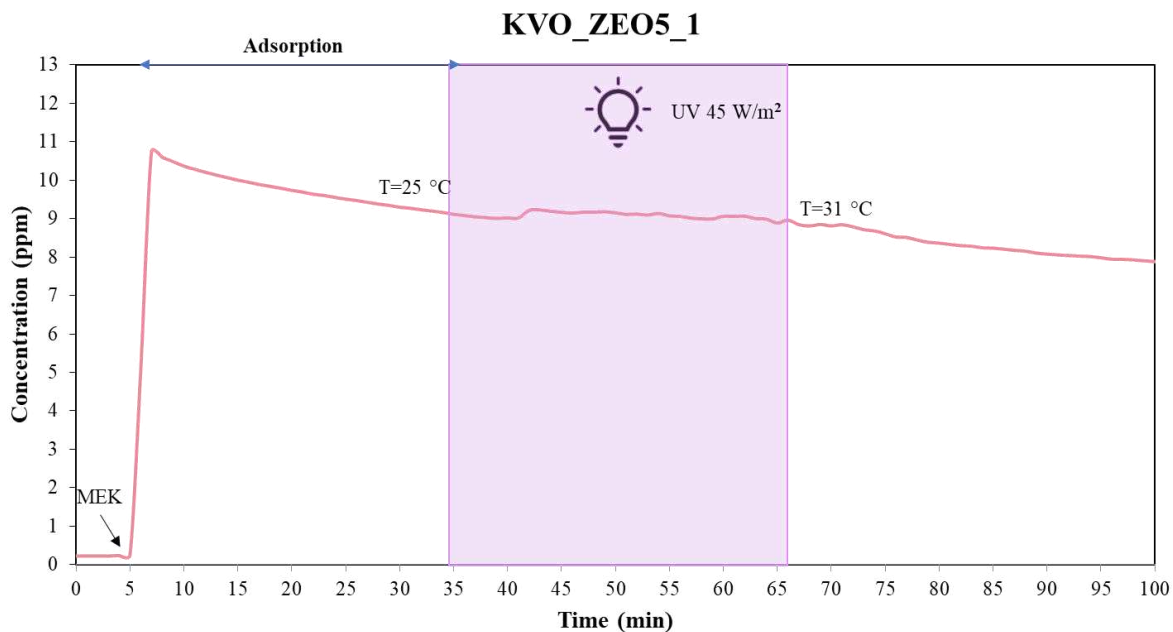
Figure 131. KVO_ZEO5_1 VOCs degradation profile under UV light.
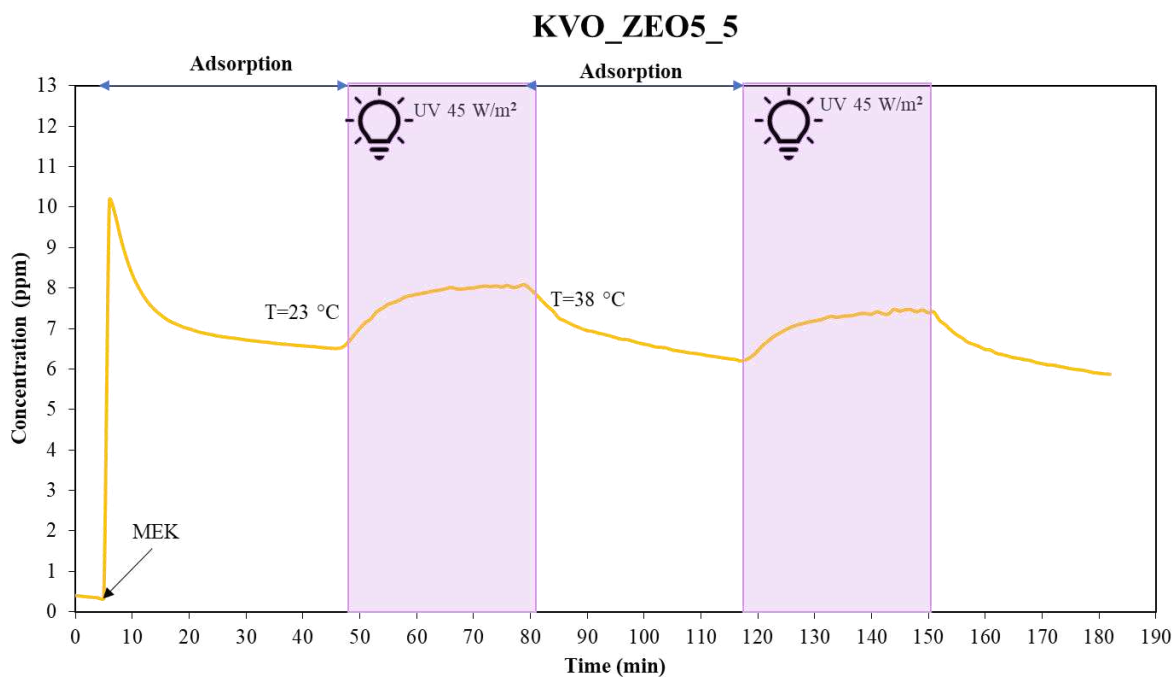
Figure 132. KVO_ZEO5_5 VOCs degradation profile under UV light.

To understand better the influence of the zeolite on the adsorptive properties the results were normalized by dividing the maximum value of the concentration during whole time of the test Figure 133).
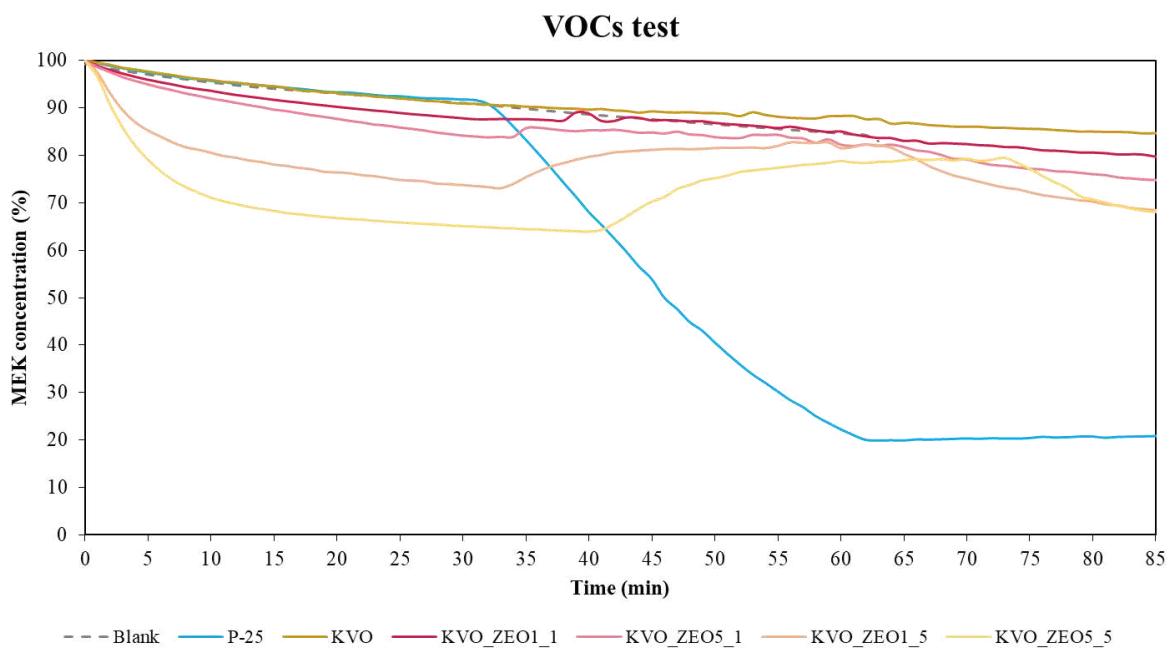
Figure 133. VOCs degradation profiles (normalized data).
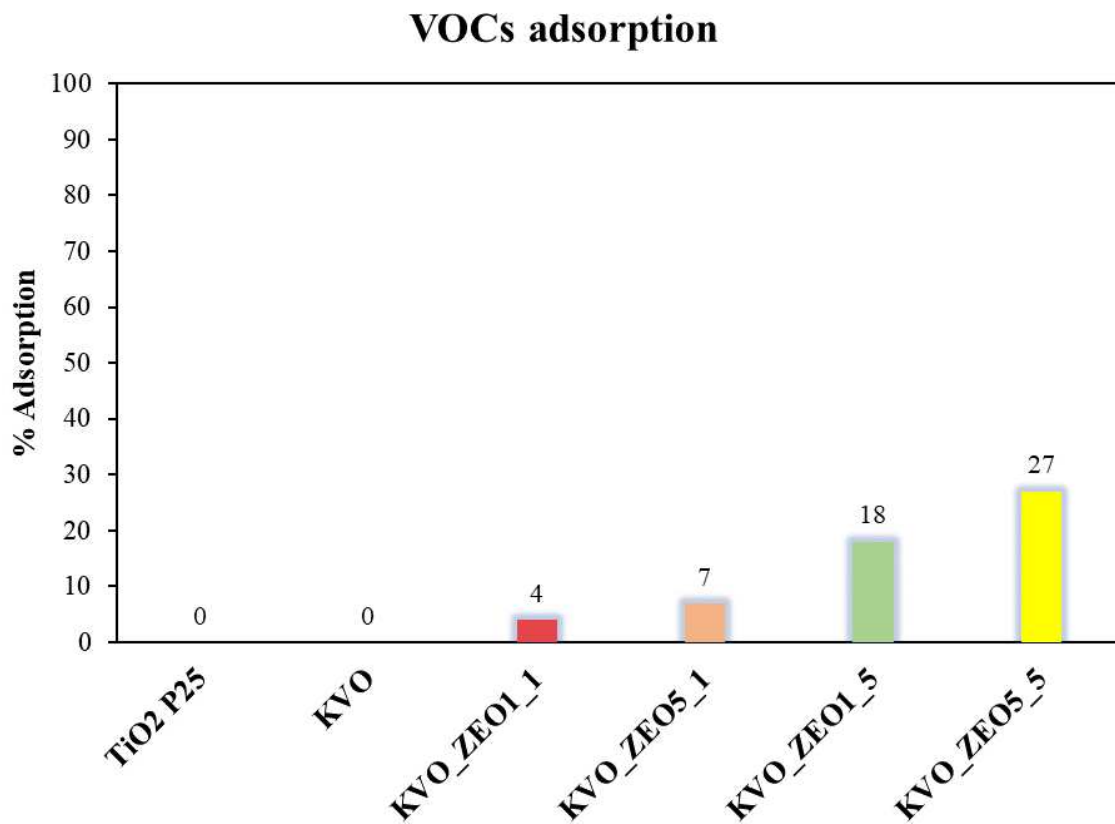
Figure 134. VOCs adsorption results.
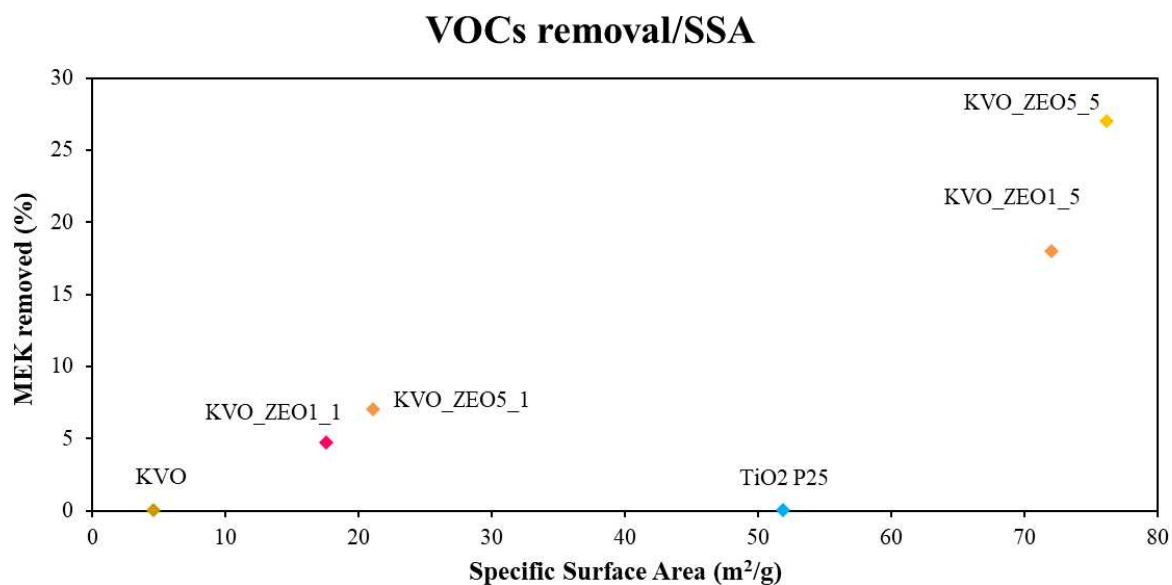
VOCs removal/SSA

Figure 135. Correlation between VOCs removal and Specific Surface Area.

The results were compared in bar chart in Figure 134. Zeolite addition enhanced adsorptive properties up to 27% (KVO_ZEO5_5) when added in 500 mg during composites synthesis and up to 7% when added in lower quantities (100 mg). We can see how in the KVO_ZEO samples Figure 135) the BET specific surface values are mainly influenced by the weight percentage of the zeolite, for KVO_ZEO1_5 and KVO_ZEO5_5 which have a quantity of zeolite 5 times higher than KVO_ZEO1_1 and KVO_ZEO5_1 the BET specific surface values are 3 times higher. We then notice a slight influence of potassium formate which at lower percentages has a slightly lower specific BET surface compared to a higher percentage. Commercial P-25 did seem to not be able to adsorb Volatile Organic Compounds. What is possible to notice is that once the UV lamp is turned on, the concentration of MEK tends to rise in case of KVO_ZEO composites reached almost the concentrations of the blank test. Immediately after turning off the lamp, the concentration decreases again. It can be explained by desorption process of the MEK molecules from the zeolite surface.
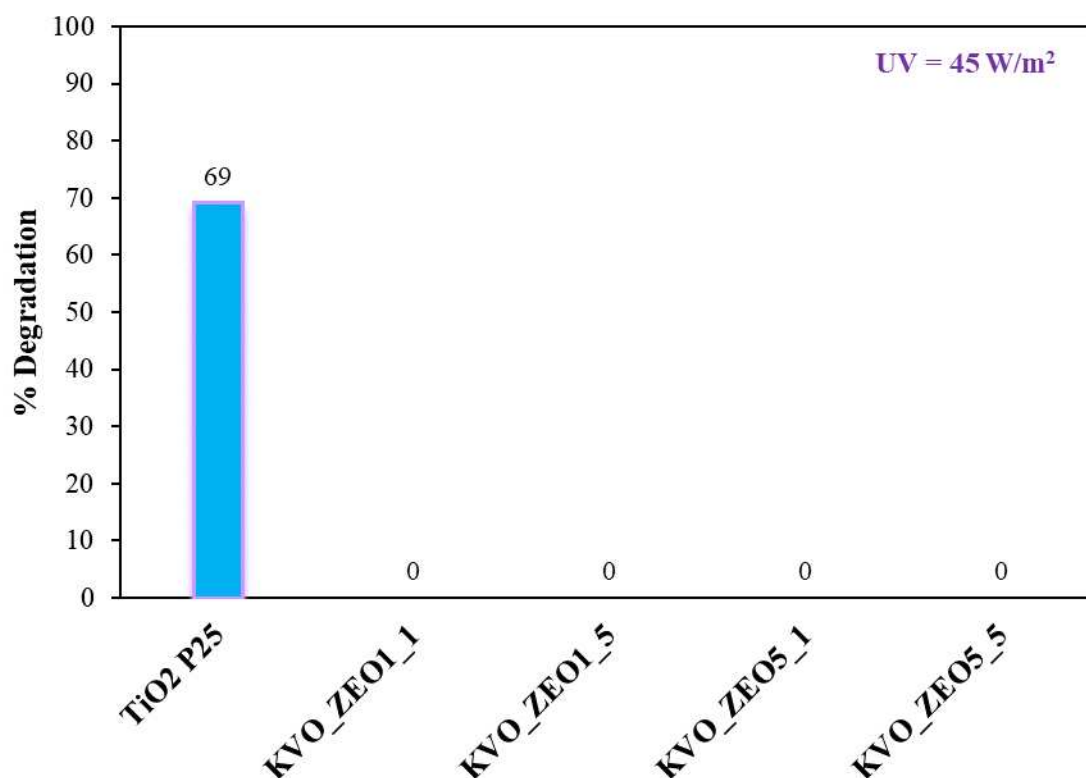
Figure 136. VOCs degradation test results.

In order to confirm the hypothesis regarding the lack of photocatalytic activity under applied conditions, CO_2 product of the mineralization was monitored. The results are presented on Figure 137 – 139. When P-25 was tested, the CO_2 concentration increased maximum 7% during the irradiation of the lamp confirming successful degradation of MEK, while for KVO_ZEO5_5 sample the CO_2 concentration was decreasing. It could be explained due to slight adsorption of CO_2, or not stable CO_2 concentration during the experiment. Additionally, to increase the initial concentration of MEK, and hence increase the potential mineralization product, the injected volume of MEK was increased to 50 µl. During the first 25 minutes of radiation no changes in the CO_2 concentration were observed, however later the concentration increased from 680 ppm to 704 ppm representing a slight increase of 3%, probably caused by photolysis process. After 5 minutes of turning off the lamp, the concentration turned to the initial values (around 680 ppm).
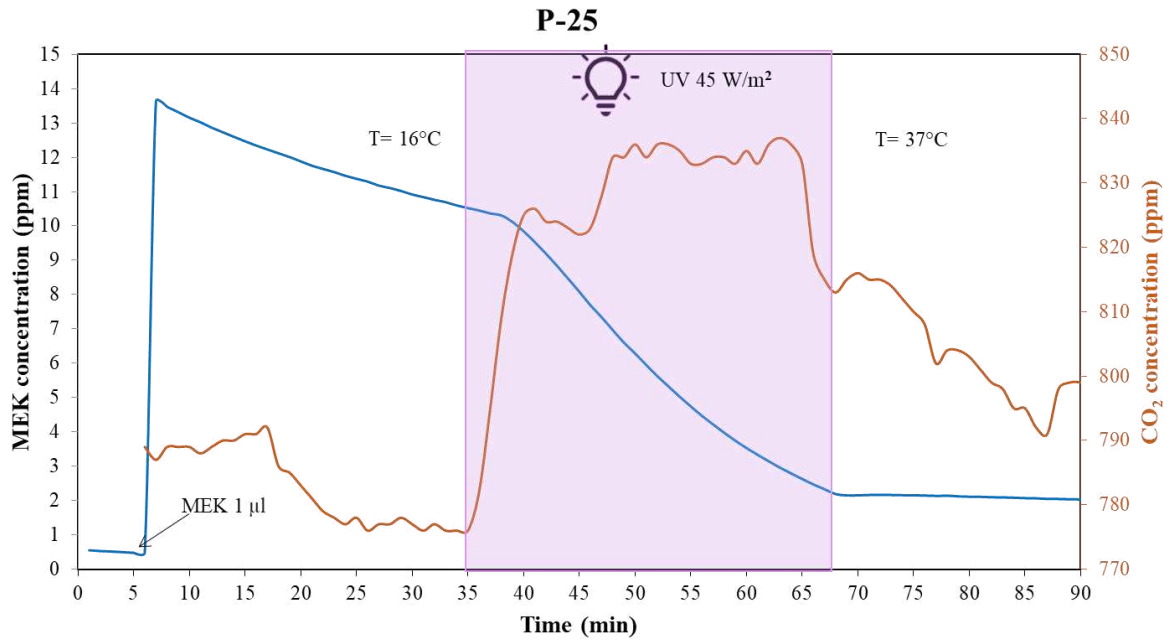
Figure 137. CO_2 concentration monitoring after injection of 1µl of MEK (sample P-25).
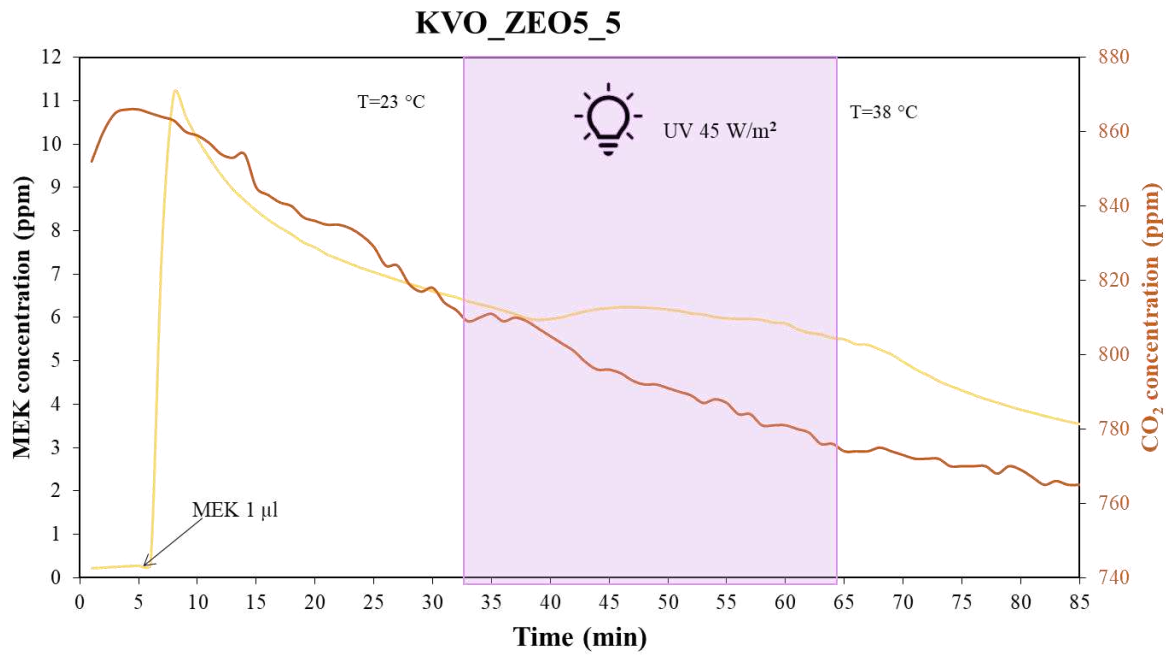
Figure 138. CO_2 concentration monitoring after injection of 1µl of MEK (sample KVO_ZEO5_5).
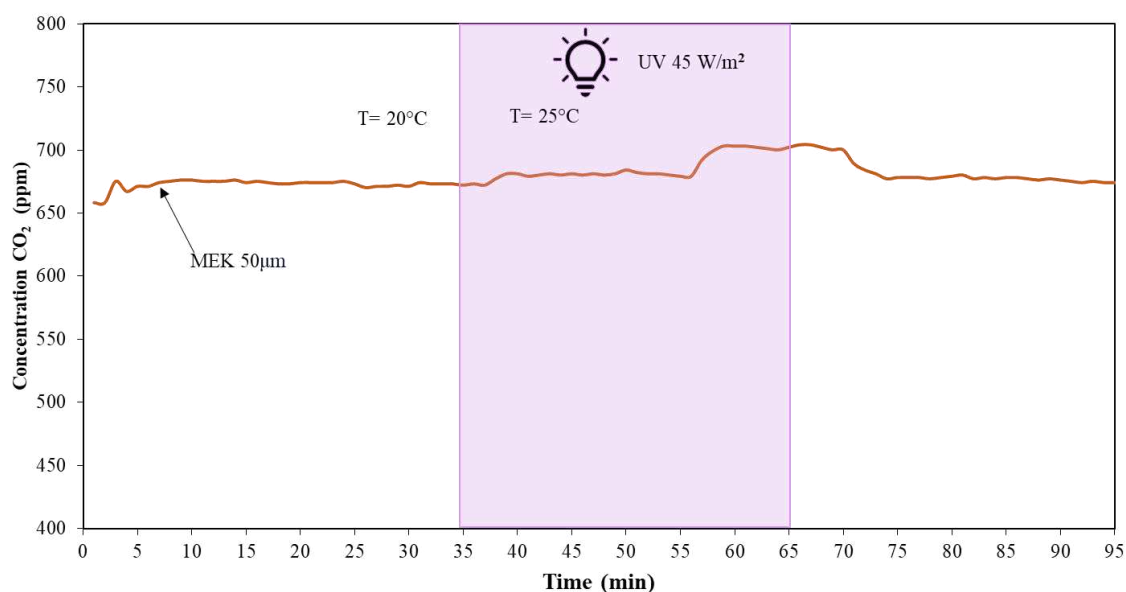
Figure 139. CO$_2$ concentration monitoring after injection of 50 µl of MEK (sample KVO_ZEO5_5).

6.6. Multifunctional finishing

6.6.1. Lab scale

6.6.1.1. Materials and methods

The finishing, labelled as UNIVPM (UNI), is an Italian Patented (No.102017000033750) hydraulic lime NHL 3.5 based mortar containing lightweight unconventional aggregates composed by a mix of adsorbent materials not commonly used in the construction sector but mainly used in air and water depuration processes. In particular the adopted unconventional aggregates are waste bottom and fly biomass ashes from biomass thermal treatment [118] (bottom ash: Dmax = 1000 µm, ρ = 1.96 g/cm3; fly ash: Dmax = 210 µm, ρ = 1.41 g/cm^3). To optimize the fresh properties, facilitate the application and avoid shrinkage cracking after the application on the substrate, 3 different commercial admixtures were added to the patented mix when applied at pilot test: i) SRA - shrinkage reducing admixtures at 0.5% on total powders mass; ii) micro cellulose at 0.7% on total powders mass and iii) super plasticizer at 0.02% on the total powders mass. The novel finish was prepared by adding water until a proper workability for the application was reached, which is about 40% of the total weight of the powders.

Based on the preliminary photocatalytic tests (presented in chapter 5), P-25 was selected and added in amount of 2% of the total dried weight to the patented finishing, according to the previous study [119]. The specimens of cylindrical shapes with diameter of 8 cm were prepared in different combinations of substrates and finishes as shown in Table 26. For comparison, 2 commercial reference finishes were selected: Limepaint (L), water-based paint currently used as a finish for the Calce Storica substrate and Argacem HP A (smoothing plaster) + Limepaint (L), currently used as a finishing package for the substrate Diathonite Deumix (D). The finishing was applied on 2 different commercial substrates: a pre-mixed mortar, Calce Storica (C) and an anti-saline plaster, Diathonite Deumix (D) by Diasen® in order to investigate if the type of substrate could affect the performance of the finishing. The commercial substates were prepared following the technical datasheet, C was prepared considering the weight ratio water: premixed of 2.6:15 for C and 6:10 for D. All the mixes, when cast, were uniformly mixed for about 6 min using a mechanical mixer. 28 days of curing at T = 20 °C and RH = 95% for the first 7 days and RH = 65% for the following 21 days were provided before the application of the UNI TiO$_2$ finishing. The finishing was applied on the substrate by spatula in 2 layers 2.5 mm thick at the time interval of 24 h. After the same curing condition described for the substrates, the depolluting properties were tested.

Table 26. List of specimens tested.

Specimen	Label
Calce Storica	C
Calce Storica + Limepaint	C+L
Calce Storica + UNI finishing	C+UNI
Calce Storica + UNI finishing + TiO$_2$	C+UNI TiO$_2$
Diathonite Deumix	D
Diathonite Deumix + Argacem HP + Limepaint	D+A+L
Diathonite Deumix + UNI finishing	D+UNI
Diathonite Deumix + UNI finishing + TiO$_2$	D+UNI TiO$_2$
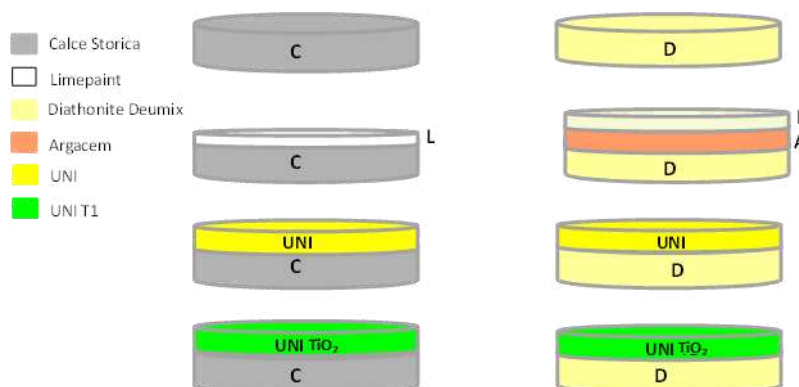
In order to evaluate depolluting properties VOCs adsorption test was performed according to procedure described below.

VOCs concentration was assessed by a gas chromatograph (Flame Ionization Detector, injector split 1:15, carrier flow 2 mL/min, capillary column, 25 m × 0.32 mm, 0.52 μm crosslinked methyl siloxane, isotherm condition 40 ∘C). Cylindrical specimens 8 cm in diameter and 0.8 cm in high were previously dried for 24 hours at T= 70 ˚C. After cooling down until constant mass, the samples were placed on the sample holder over which, on the watch glass, 50 μL of MEK (corresponding to 2402 mg/m^3) was added dropwise. Air samples were collected by a micro-syringe every 8 min and the adsorption process was monitored for 120 min.
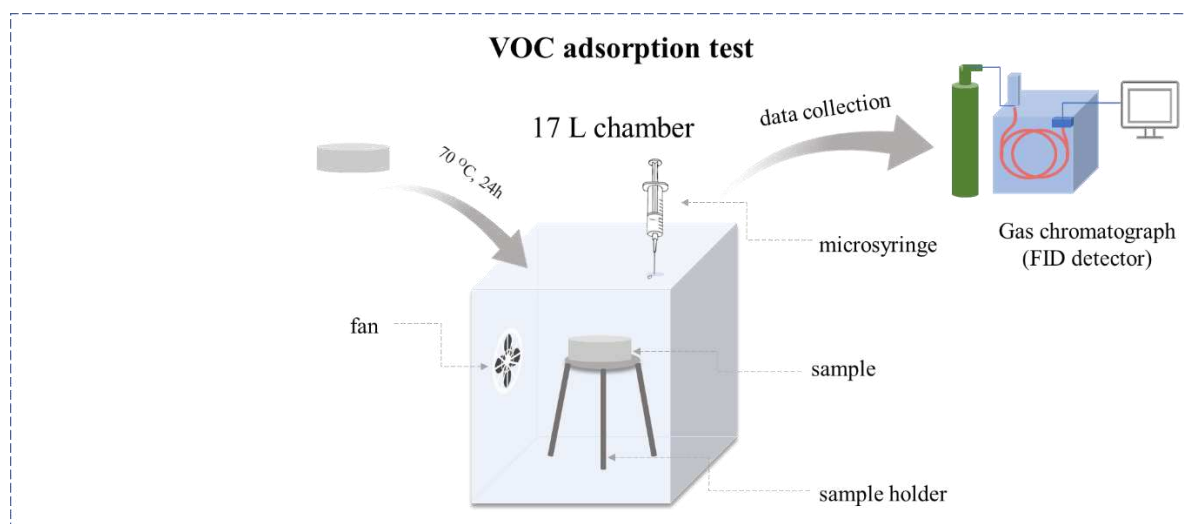
Figure 140. Experimental chamber for VOC adsorption.

Photocatalytic properties were investigated following Italian UNI standard: "*Determination of the degradation activity of nitrogen oxides in the air by photocatalytic inorganic materials*" UNI 11247. The procedure and experimental apparatus were described previously in paragraph 5.3.3. Briefly, the photocatalytic activity was tested without irradiation (dark) and under both UVA and VIS radiation and was expressed in terms of the ratio of mineralized NO over total NOx flux directed in a plug flow reactor. The NOx flux was provided by a tank at 500 ppb ± 5 NO (SAPIO S.r.l., Monza, Italy), kept constant by mixing with air at T = 25 ∘C and RH 50 ± 10% using a dilution system (Calibrator 8188, Rancon Instruments S.p.A., Milan, Italy). In the outlet flux, the concentrations of NO and NO_2 were continuously monitored using a

chemiluminescence NOx analyzer (nitrogen oxide analyzer model 8841; Monitor Labs, Englewood, CO, United States). Tested samples with the total exposed area of 64 cm^2 (cylinder with d = 8 cm and h = 0.8 cm) were positioned internally in the center of the 3L reactor. Photocatalytic activity was evaluated under visible light (Philips, 42W) with intensity equal 9 ± 1 W/m^2 and then Ultraviolet (Torcia UV halogen lamp, 400W) with measured light intensity of 20 ± 1 W/m^2. Irradiation of the sample was guaranteed until stable conditions were reached (usually 30 min).

6.6.1.2. Results and discussion

During the VOCs depolluting capacity test, the specimen was sealed inside a box, into which a known quantity of the model pollutant MEK was injected. Then, the MEK residual concentration was measured for 120 min. Figure 141 shows the results of depollution tests in terms of the percentage adsorbed MEK. The best performance is observed when UNI patented finish was applied and the % of adsorbed MEK ranged from 46 to 59% after 90 minutes of the monitoring test. The specimens with the commercial finishing, C+L and D+A+L showed lower adsorption capacity and were 19 and 21% respectively. As reported in previous studies [118], the addition of biomass ashes as conventional aggregates improves the depolluting properties. The addition, both types of TiO$_2$ did not significantly influence the depolluting capacity under dark conditions.

As expected, NO decomposed only in the presence of TiO$_2$, as shown by the NO/NO$_x$ removal results reported in Figure 142, evaluated as the percentage difference between the NOx concentration under UV and NO$_x$ concentration in dark, dived by the NO$_x$ concentration under UV. The removal of up to 6% of NO in the sample D+UNI was ascribed to photolysis of the pollutant, and to the sorption and conversion of NO into nitrous acid [73]. The abatement was detected also under VIS radiation for samples D+UNI and D+UNI+TiO$_2$ but only at a very low percentage (1%).
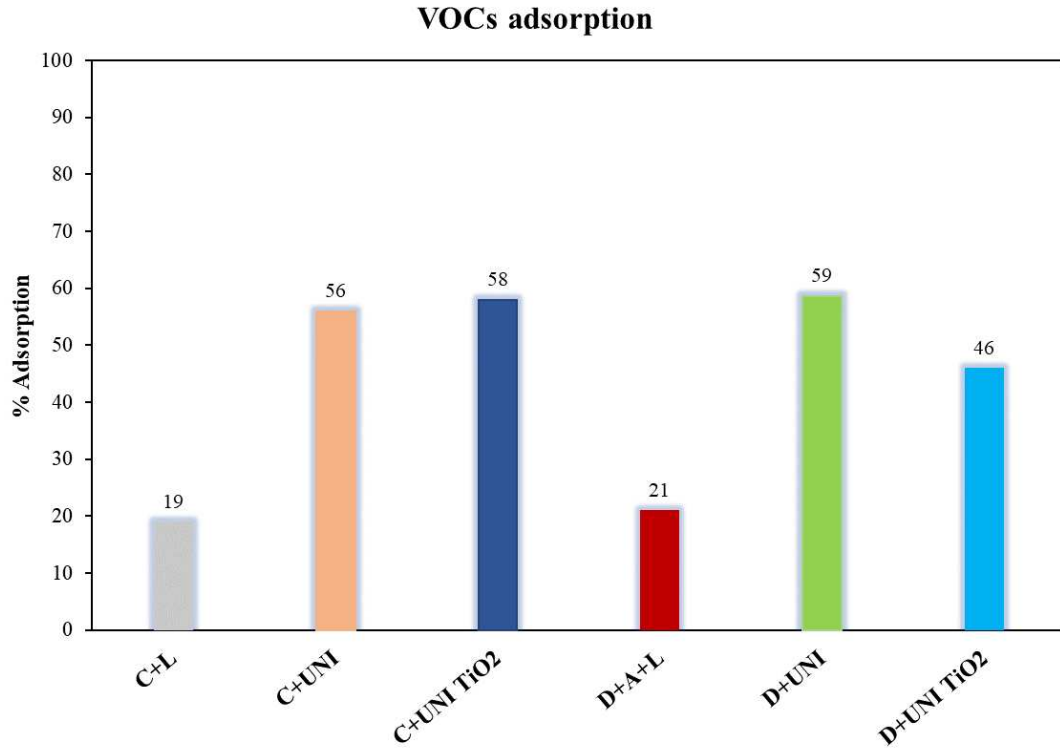
VOCs adsorption

Figure 141. VOCs adsorption test results.

NOx degradation test

■ NO (UV) ▨ NOx (UV) ■ NO (VIS) ▨ NOx (VIS)

Conditions
3 L reactor
UV 20 ± 1 W/m² (Torcia UV 400W)
VIS 9 ± 1 W/m² (Philips 42W)
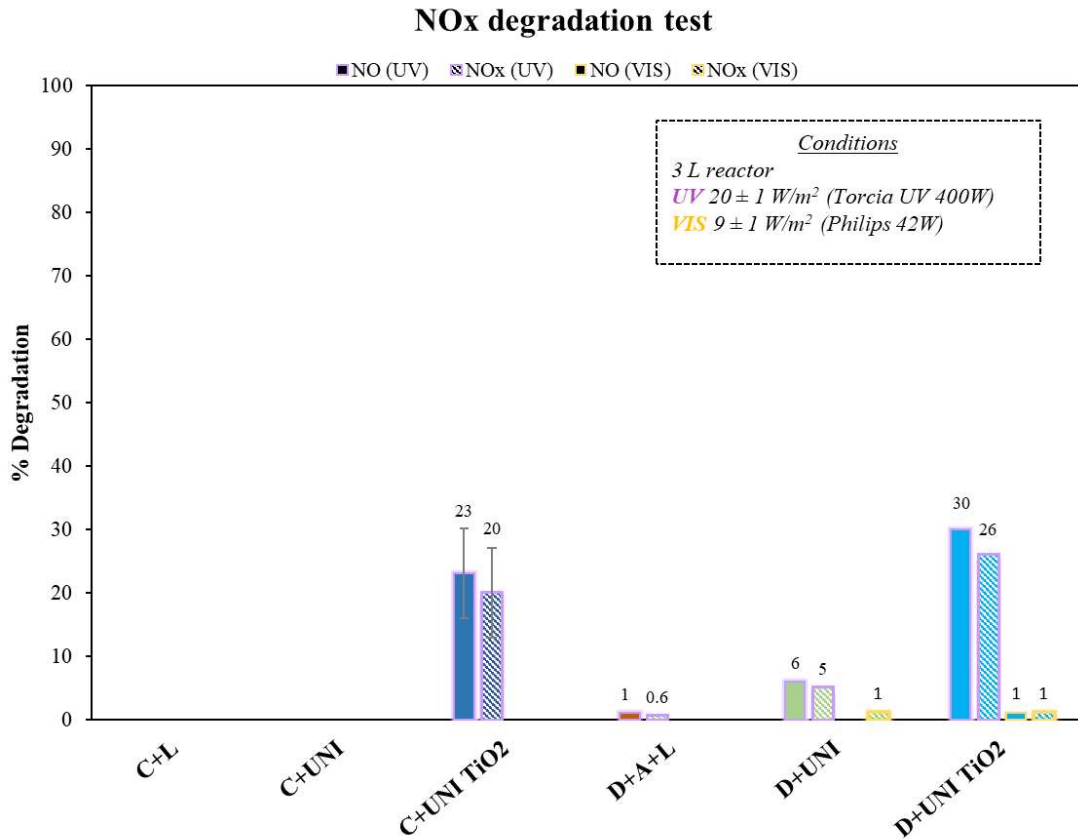
Figure 142. NOₓ degradation test results.

6.6.2. Pilot scale

6.6.2.1. Materials and methods

Calce Storica by Diasen® (C), was selected as commercial substrate for the application of both the commercial L and the patented U finish.

The tested materials have been labelled as:

- C-U for the patented mix applied on the commercial substrate.
- C-L for the commercial paint applied on the commercial substrate, as reference.

Pilot site

The area identified for the experimentation is located in Ancona, central Italy (latitude: 43.54°, longitude: 13.37°, altitude: 137 m) and is managed by the Department of Industrial Engineering and Mathematical Sciences (DIISM) of UNIVPM. The site is in an industrial zone and covers an area of approximately 5000 m^2 where structures already used in previous University projects are positioned [61] [62]. The experiment was conducted in one of the prefabricated test rooms, measuring approximately 3 x 3 x 3 m^3 characterized by an aluminum sandwich panel envelope with an internal layer of mineral wool 12 cm thick.

Figure 143. Site map. The used pilot test room is circled, Google Maps.

On the north-eastern and western sides, there is a further 10 cm thick external insulation layer of polystyrene with an aluminum finish, which gives the walls a total thickness of 22 cm. On

the southern side, the insulation layer thickness is of 12 cm and, externally, a white rendered cement board was inserted, reaching a total thickness of 15 cm.

Preparation of the pilot site: materials application and monitoring system

The construction of the internal wall subjected to the experimentation (South wall) was carried out as following: at first, the commercial substrate was applied for 2 cm on the entire wall; after, on one half of the wall the innovative U finish was applied in 2 consecutive layers, approximately 1.5 mm thick each. Specifically, TiO_2 was added only in the finish of the outermost layer. In the other half of the wall, the reference finish L was applied on a layer of fixative (D20), following the technical datasheet.

Figure 144 shows the pilot scale room during the application of the finishes, the preparation of the two test boxes, and the service area with the monitoring data acquisition system.

Figure 144. The pilot scale room: a) during the construction phase with the two different finishes applied on the wall (L on the left and U on the right), b) the two testing boxes, and c) the service area with the monitoring data acquisition system.

After the preparation of the South wall, the internal space was divided into two areas: a service area which contains the acquisition system and a test area adjacent to the southern wall. The test area is further divided into two equal boxes, each one with dimension of 1.2 x 1.2 x 2.9 m^3, separated by a plasterboard partitioning: one with the innovative finish U, labelled as box 1 (C-U), and the other with the reference commercial finish L, labelled as box 2 (C-L). For each box, a 60 x 60 cm^2 opening was realized to allow internal access, to check the irradiance

of the lamps and for maintenance purposes. During the data acquisition, the test boxes were closed with plasterboard panels and sealed with adhesive tape. A data acquisition and remote microclimatic control system was set up outside the two boxes, in the service area. The system provides the continuous data acquisition of:

(i)   VOCs concentration inside box 1 and box 2 (VOC1, VOC2),

(ii)   Air Temperature inside box 1 and box 2 (T1, T2),

(iii)   Surface Temperature of the two finishes (RTD1, RTD2),

(iv)   Air Temperature of the service area (Tser),

(v)   Relative Humidity inside box 1 and box 2 (RH1, RH2) and Relative Humidity of the service area (RHser).

Inside each box, the irradiance was measured occasionally before the beginning of the tests to assess the photocatalytic properties of the finish. In the service area, a dehumidifier to control RH values (55 ± 5%), a convector to keep a constant T (20 ± 0.5 °C) inside the boxes, a thermostat to regulate T, a probe to detect the T and RH, and a monitoring station with a computer data acquisition system working with Labview were installed as schematically shown in Figure 145. Table 27 reports the information about the sensors and instrumentation placed in the different areas of the pilot test room.
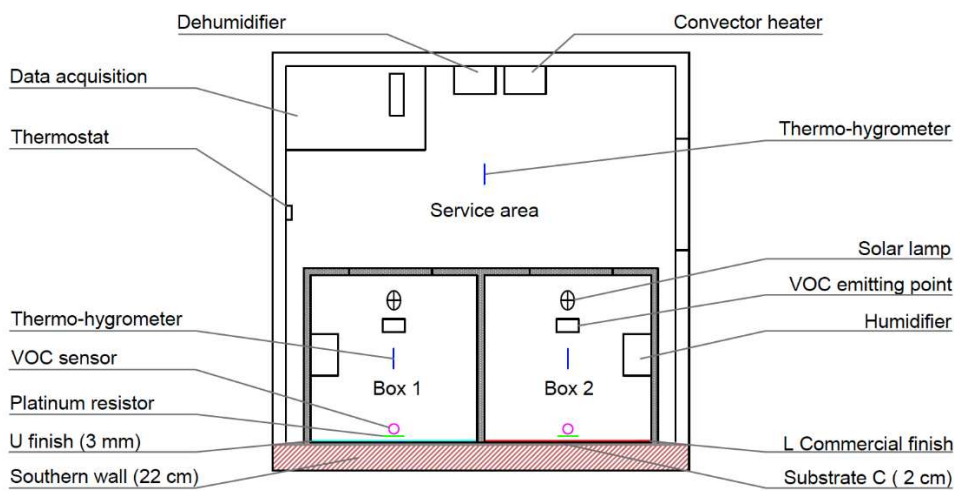
Figure 145. Top view of the experimental room.

Table 27. List of the sensors used in the experiment.

Parameter	Sensor type	Model	Range	Accuracy	Area of installation
Air temperature	Thermo-hygrometer	PCMini52, Michell	-20 °C to 80 °C	± 0.2 °C	Service area Test area
Surface temperature	Platinum resistor	PT100	-40 °C to 80 °C	± 0.05 °C	Test area
Relative humidity	Thermo-hygrometer	PCMini52, Michell	0 to 100%	<±2%	Service area Test area
VOCs concentration	Photoionization detector - PID	series 900, Aeroqual	0 to 30 ppm	±0.02 ppm +10%	Test area
Irradiance	Photo-radiometer	HD 2102.2, DeltaOhm (Probes LP471UVA, LP471RAD)	0.1 mW/m^2 to 2000 W/m^2	±1digit	Test area, only for the test of irradiance

Inside each box a humidifier (Medisana, model V-401671, 4.2 l capacity) and two different sources of radiation (lamps), namely a solar lamp (Ultravita LUX Osram, 300W) and a UV lamp (RepTech 100W), were installed. The measured irradiances were 3 and 8 W/m^2 in case of UV radiation and 18 and 30 W/m^2 in case of VIS radiation for the solar lamp and the UV lamps, respectively. When necessary, inside each box a MEK emitting point was also placed which acted as an internal source of VOCs. T and RH inside box 1 e box 2 were controlled in the service area and remotely.

The averages value between T1 (box 1) and T2 (box 2) was considered for checking the average temperature, labelled as Tm. When Tm was below 20 °C, the system turned on the convector heater to reach the fixed temperature, when Tm exceeded 20 °C, the convector switched off and the T decreased until the fixed value thanks to the split system.

A slightly different control system was set to control the RH of each box. When the average RH between RH1 and RH2, RHm, was below 30% the humidifier turned on until reaching the fixed RH value. If RH exceeded the 60% a dehumidifier turned on; it turned off when RH dropped below 60%. When RH was set to high values (75%), each test box was considered separately to evaluate how many times the humidifiers turned on for the hygroscopic buffer

assessment. Continuous monitoring data was downloaded remotely so as not to interfere with the carrying out of the experiment.

To allow a proper curing of the materials, the data acquisition of the environmental parameters of the two boxes started one month after the application of the finishes.

The effect of the two different finishes on the environmental parameters has been investigated in terms of:

• T, RH and VOCs concentration in stationary conditions, without any external perturbation of the single box conditions;

• T changes after the solar lamp switching on/off, to evaluate the indoor thermal inertia given by the finishes;

• RH changes after the humidifier switching on/off, to evaluate the indoor hygrometric inertia given by the finishes;

• VOCs concentration changes after a MEK static or spot load, to evaluate the depolluting effect by adsorption given by the finishes;

• VOCs concentration changes after the solar lamp switching on/off, to evaluate both the depolluting effect by photocatalysis and possible desorption phenomena due to the increase of T given by the finishes;

Table 28 describes the different cases monitored during the experimentation with the corresponding investigated property, adopted method and simulated conditions.

Table 28. Cases applied during the pilot tests.

Case	Investigated property	Method	Simulated conditions
1.	VOCs emitted by the finish	VOCs monitoring in stationary conditions, without external VOCs load	VOCs directly emitted by the finish itself in new or refurbished building
2.	VOCs Adsorption	VOCs monitoring after a MEK static load	Low concentration of VOCs emitted by new furniture, building materials or by household activities

3	VOCs Adsorption	VOCs monitoring after a MEK spot load	High concentration of VOCs emitted by new furniture, building materials or by household activities
4.	VOCs Photocatalytic degradation	VOCs monitoring when the UV lamp switches on/off	Maintenance of the finish depollution ability
5.	VOCs Desorption from the finish	VOCs monitoring when the UV lamp and humidifiers switch on/off	VOCs desorption from the finish due to daily/seasonal T increase or RH changes

Tests were conducted in dark conditions, and under UV/VIS radiation provided by the UV lamp, to evaluate the possible photocatalytic activity. The irradiance of UV/VIS were measured by a photo-radiometer perpendicularly to the lamp on the surface of the pilot wall and resulted equal to 8 W/m^2 and 30 W/m^2. MEK was used as a model pollutant to guarantee the same loads of VOCs into the different boxes. As reported in table above, two different cases were investigated to evaluate adsorptive properties of the finishes: static load (case number 2) - the test was carried out by placing a beaker with 10 ml of MEK, placed in the center of the floor of each box, and spot load (case number 3) - the test was carried out by injecting 50 µl of MEK inside each box with a spot load using a graduated syringe. Cases number 4 and 5 were designed to investigate the photocatalytic activity of the finishes and possible desorption phenomena.

6.6.2.2. Results and discussion

Figure 146 reports the VOCs concentration recorded for two selected weeks of the monitored period before the external MEK load (case number 1). An up to 70% higher concentration of VOCs was observed in the box with the commercial L finish compared to the one with the U finish. After this period, the VOCs concentration recorded in box with C-L reached an average daily value from 0.45 ppm to 0.30 ppm, while in the box with C-U from 0.20 ppm to 015 ppm. This can be attributed both to the lower VOCs emissions of the U-finish with respect to L finish and to the higher VOCs adsorption capabilities of the U finish compared to the commercial L one.
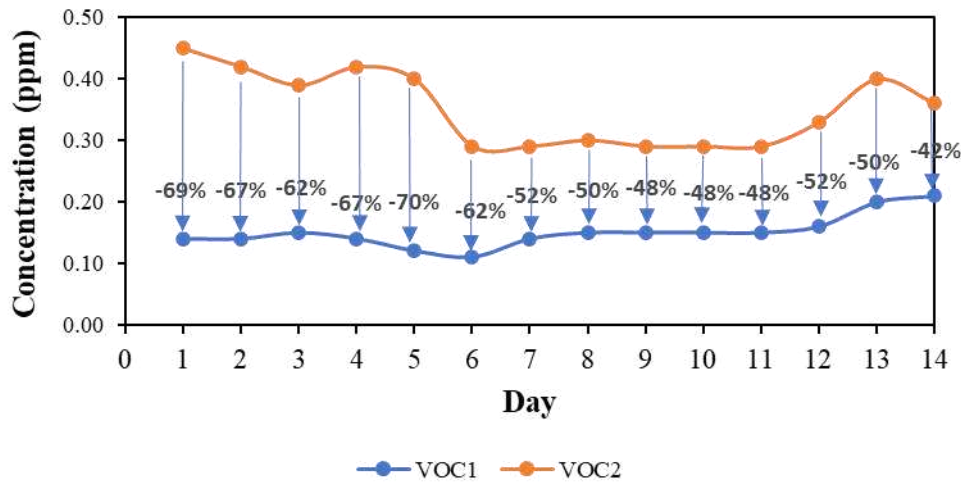
Figure 146. Initial monitoring period (14 days): initial VOCs concentration detected in box1 and box 2. The number 1 is for box 1 (C-U) and number 2 for reference box 2 (C-L).

Figure 147 reports the environmental concentration of MEK after the external loads. The graph for the static load (Figure 147a) shows that before loading, VOC values in the two boxes were approximately 0.17 ppm. As soon as the MEK load as static source was inserted into the boxes, the sensors recorded an increase in concentration, and then a steep slope followed by a stationary phase, meaning that before the initial phase the equilibrium between the MEK source and the environment was reached. However, in box 2 the MEK concentration increased up to 1.24 ppm, which in approximately 2.5 hours decreased very slowly until to stabilize around an average value of 0.39 ppm. Although the values of the slopes of the initial phase were similar (0.06 ppm/min and 0.07 ppm/min for C-L and C-U, respectively) in box 1 MEK did not reach as high values as in box 2 just after loading; in fact, the concentration rose 0.94 ppm, and it stabilized at 0.30 ppm. The MEK peak event of C-U was about 25% lower than that of C-L. This demonstrates the natural concentration decay that occurred in the two boxes and the passive adsorption property of the two materials but also the more depolluting efficacy of the innovative finish U with respect to L, since both the stabilization phase and the final concentration values were lower than the ones detected for C-L. However, another aspect that should not be underestimated is that at high stationary concentrations of VOCs, there was a difference in the VOCs values shown in Figure 147: at low concentrations, before loading, the curves coincided, at high concentrations the U finish retained up to 20% more VOCs molecules than the reference L finish. Also, high concentration of VOCs implies high noise in both VOCs

concentrations paths, more evident when C-L is applied since it was not able to adsorb as much MEK as C-U.

The spot load of 50 μl MEK (corresponding to a vapor concentration equal to 2.7 ppm) inside the boxes was followed by a peak in VOCs concentration (Figure 147b). The maximum recorded concentration was 5.77 ppm in the box 1 and 6.70 ppm in the box 2, so the peak event in C-U was around 15% lower than C-L. C-U maintained lower values of VOCs concentration compared to C-L for the entire period of monitoring. The slopes for the decreasing phase spot load were also evaluated, equal to -2.78 ppm/min and -3.10 ppm/min for C-L and C-U, respectively. This result confirms that the innovative U finish can adsorb more VOCs than a reference commercial finish even at a pilot scale.
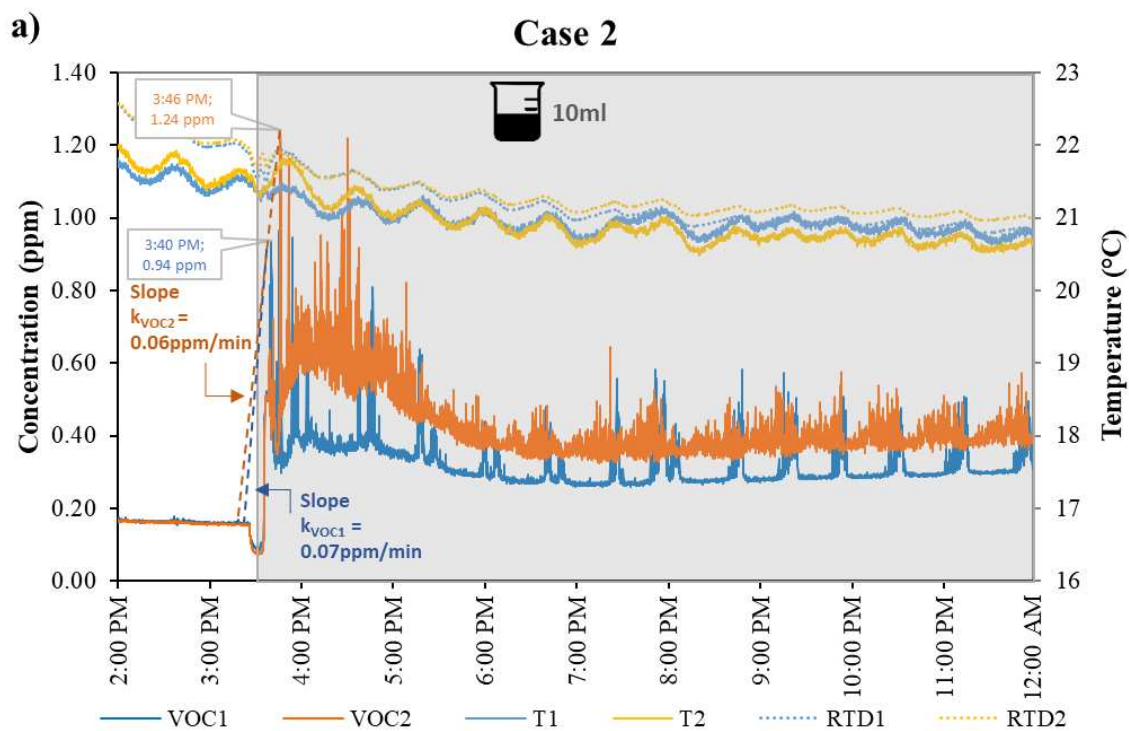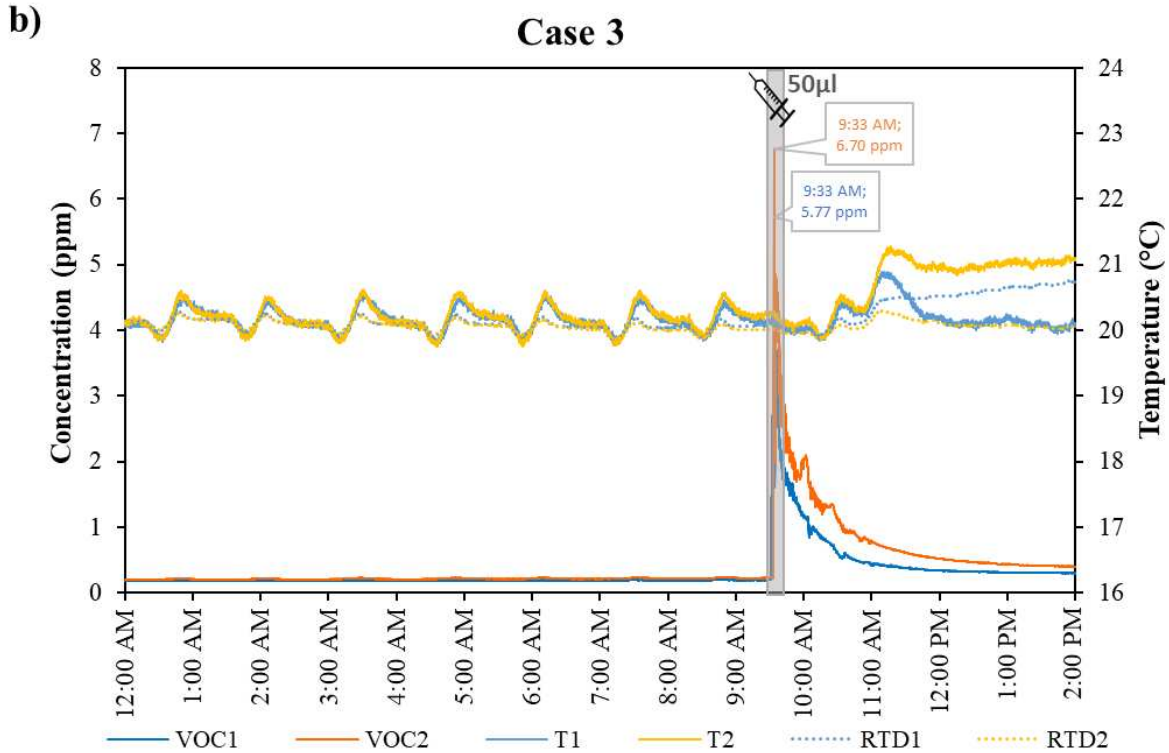
Figure 147. VOCs concentration and temperatures in the two boxes when a) static or b) spot load of MEK were provided. The number 1 is for box 1 (C-U) and number 2 for reference box 2 (C-L).

Figure 148 reports the results of the test carried out with a spot load of 100 μl of MEK (corresponding to a vapor concentration equal to 5.3 ppm) and the surface TiO_2 photocatalytic activation by means of UV lamp (100W, UV RepTech lamp), switched on after the MEK injection.

The spot load of 100 μl of MEK caused the appearance of peaks in the diagram of both boxes: 13.40 ppm and 4.98 ppm with a slope of 4.26 ppm/min and 0.52 ppm/min for C-L and C-U, respectively. 30 mins after the spot load, the 100W UV lamp was turned on for 1 h and 30 mins. During initial lighting ignition, the VOCs concentration assumed divergent trends: in box 2 the materials emitted VOCs +0.27 ppm for approximately 5 minutes, while in box 1 the C-U finish continued to adsorb the pollutants, -0.26 ppm for the same time, with a difference in concentration of 0.76 ppm between the two boxes. After 10 minutes of lighting, in box 2 the concentration started to decrease again, likely after the spot injection, due to the natural decay of MEK. The depollution kinetics of the two combined processes (adsorption and photocatalysis) is also higher in C-U (0.05 ppm/min) than in C-L (-0.05 ppm/min). This means that in case of C-L only desorption and natural decay of MEK occurred, while in C-U also a photocatalytic activity thanks to the presence of TiO_2 was present. To summarize, among the

202

two materials, the C-U system showed higher VOCs depolluting capacity. This was ascribed both to the presence of adsorbent materials [120] and to the presence of TiO_2 in the mix-design. TiO_2 was demonstrated to be able to mineralize the pollutants [121] also in a pilot scale application.
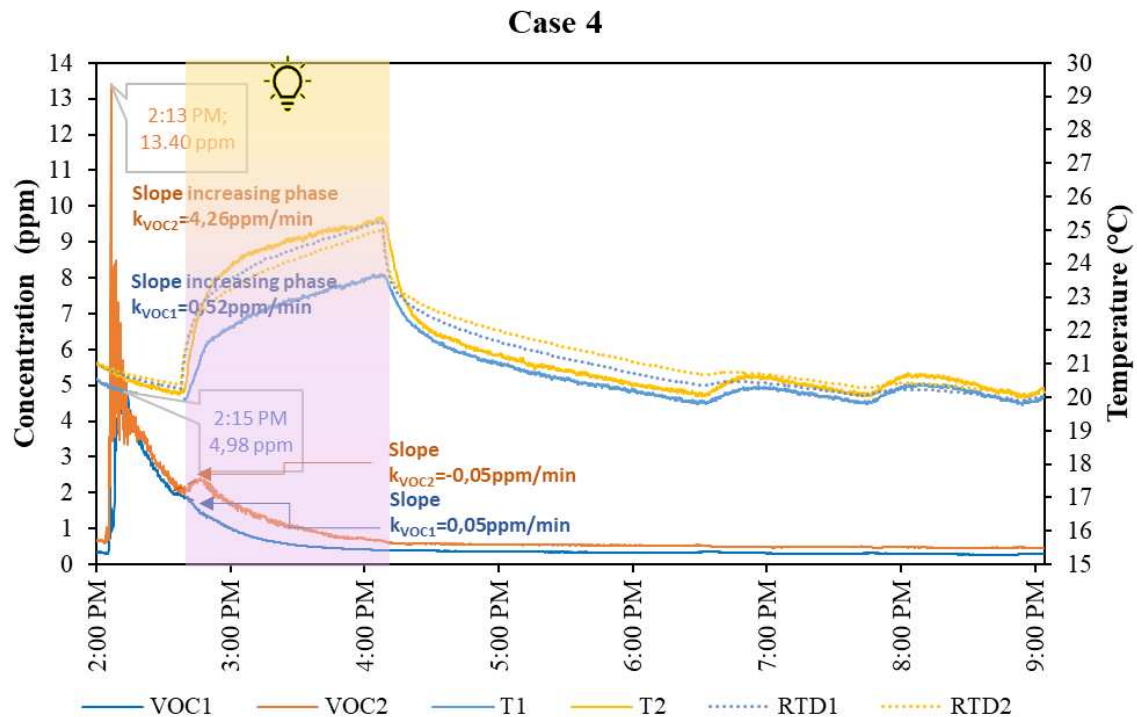
Figure 148. Spots load in the test boxes of 100 µl of MEK and comparison of the kinetics of the decrease in VOCs concentrations in the two boxes. The number 1 is for box 1 (C-U) and number 2 for reference box 2 (C-L).

Case number 5 was conducted to study the desorption properties of both finishes and the influence of T change on the adsorbed VOCs with no load and sources of VOCs added to the environment (Figure 149). As previously described (Table 29), the increase of T was provided by an irradiation (UV:3 W/m^2 and vis:18 W/m^2) with a solar lamp (300W Ultravita LUX, Osram) for 1 h, rising T from 20 °C to 28 °C. As expected, the increase in T increased VOCs concentration inside box 1 and box 2 of 13% (from 0.27 ppm to 0.31 ppm) and 21% (from 0.43 ppm to 0.53 ppm) respectively, after one hour of irradiation; with the C-L finish the increase was up to double that of C-U finish. Moreover, after turning off the lamp, in box 2 where the commercial finish was applied, VOCs concentration took 3 hours to return to a steady state value, 0.45 ppm instead of the initial 0.43 ppm. On the other hand, in box 1, VOCs concentration took only 1 hour to return to a steady state value, 0.27 ppm instead of the initial

0.29 ppm. As regards the VOCs concentration, in general, data showed an increase in VOCs release under higher temperature confirming the results obtained by [122].
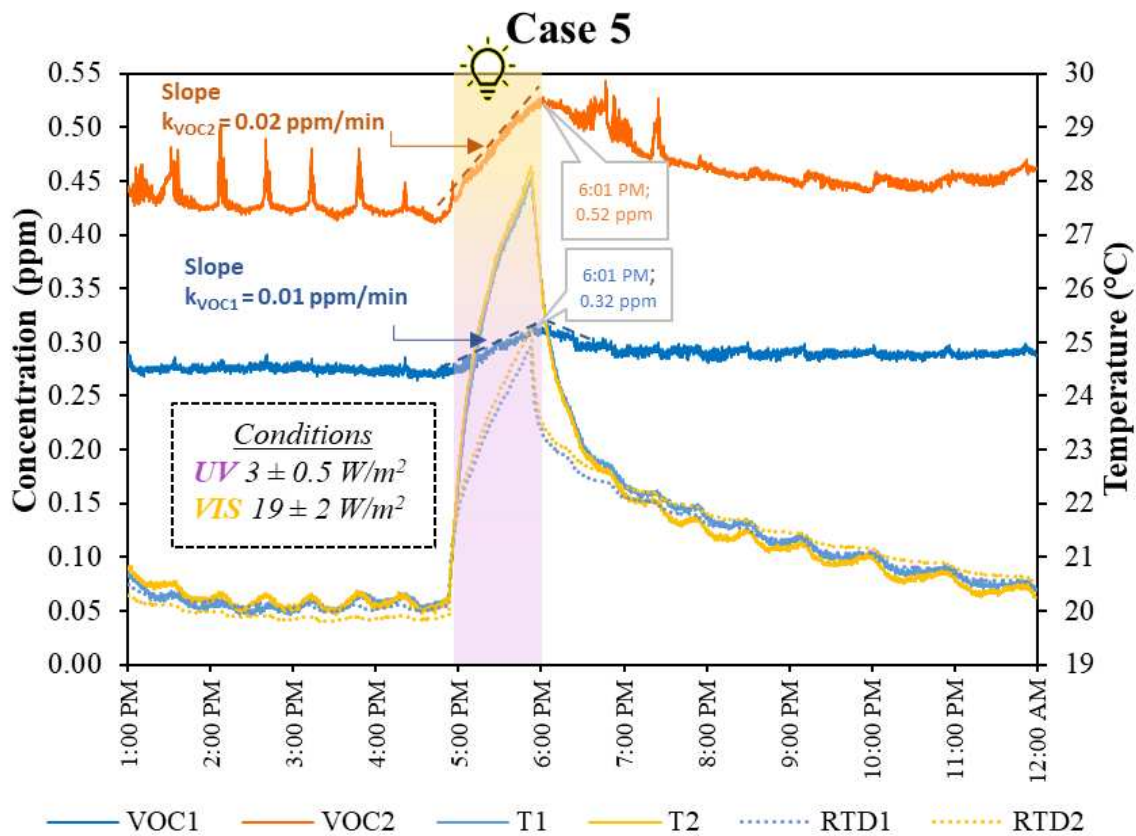
Figure 149. Increase of VOCs concentration due to T increase by irradiation. The number 1 is for box 1 (C-U) and number 2 for reference box 2 (C-L).

In case 6 (Figure 150), also the correlations between RH and VOCs concentration in the boxes was studied. Few days after the MEK spot loads test, RH of the boxes was set at 75% for 8 h to check the influence of RH on the VOCs desorption. When RH started to increase, also VOCs concentration increased; in both boxes initially the increase of both parameters was gradual than at RH = 70% with peaks. Subsequently, when RH was set at 30%, the VOCs concentrations in the two boxes decreased, demonstrating the desorption of MEK from the superficial open porosity (active sites) of both finishes occurring when a rise in RH occurred [123], [124]. However, in C-L box 2, the VOCs concentration initially increased faster than in box 1, probably because MEK, adsorbed only superficially, was easily removed by water. The small amount of MEK adsorbed by C-L quick ended; the VOCs concentration remained quite stable, and it decreased very slow for natural decay. In case of C-U box 1, the VOCs concentration reached the maximum when RH arrived around 70%. At this moment, the

concentration on VOCs in box 1 became higher than in box 2, because water by saturating the porosity of the unconventional aggregates, removed the high amount of MEK adsorbed during the load tests, due to the desorption process occurred in presence of high RH values. The two spikes on VOCs concentration in box1 and the high noise in VOCs concentrations trend for both C-U and C-L could be ascribed to a possible interference between the water drops generated by the humidifier and the VOCs sensor due to the small volume of analysis. In any case, this interference did not hide the evidence of VOCs desorption discussed above, demonstrating that also environmental parameters such as T and RH modify the response of finishes in terms of adsorption/absorption of airborne pollutants.
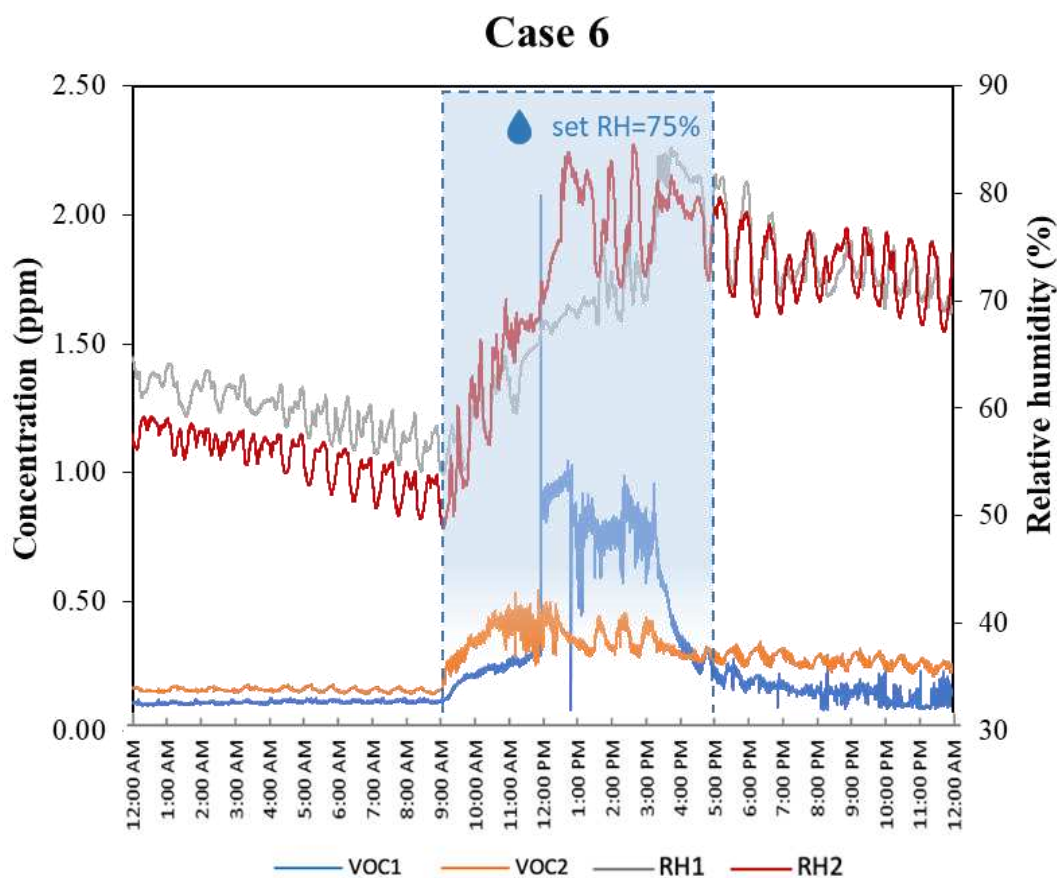
Figure 150. Concentration during the increase of RH. The number 1 is for box 1 (C-U) and number 2 for reference box 2 (C-L).

6.6.2.3 Conclusions

The present work is aimed at verifying the efficacy of an innovative finish material for indoor applications in terms of depolluting abilities in both laboratory and pilot scale tests. To this aim, the innovative finish was compared to a commercial one for the same application applied

on the same substrate. In particular, the tests were conducted to evaluate the ability of the two finishes to passively improve indoor comfort and health in terms of temperature and moisture buffering capacity and Volatile Organic Compounds adsorption.

From the laboratory and pilot scale results, the following main conclusions can be drawn:

- The VOCs concentration is influenced both by T and Relative Humidity. The increase of these parameters causes VOCs desorption, but the innovative finish is more influenced by RH whereas the commercial one by T. Increase of T causes VOCs desorption only from the most external surface, and at the tested temperature of 25 °C, it does not cause the release from the active sites of the unconventional aggregates. On the contrary, at a RH of 70% water molecules remove VOCs from the internal porosity of the adsorbent aggregates of the new finish. For this reason, the application of the new finish in indoor environment with high RH value and high RH variations, should be carefully studied.

- Among the two finishes, the innovative one showed a higher VOCs depolluting capacity. This was ascribed both to VOCs adsorption by unconventional aggregates, and to photooxidation by TiO_2. The latter was able to mineralize the pollutants, also in pilot scale applications if activated by UV light. It would be interesting to evaluate such types of process to maintain the finish functionality over time during the service life of the building in which the innovative U finish is applied to optimize IAQ.

Publications

Some of the topics present in this thesis have been published in international journal papers, national and international congresses/conferences.

List of the journal papers:

- ❑ Development of activated carbons derived from wastes: coffee grounds and olive stones as potential porous materials for air depollution.
  Natalia Czerwinska, Chiara Giosue, Ines Matos, Simona Sabattini, Maria Letizia Ruello, Maria Bernardo

  https://doi.org/10.1016/j.scitotenv.2024.169898

- ❑ New waste-derived TiO_2 nanoparticles as a potential photocatalytic additive for lime based indoor finishing.
  Qaisar Maqbool, Natalia Czerwinska, Chiara Giouse, Simona Sabbatini, Maria Letizia Ruello, Francesca Tittarelli

  https://doi.org/10.1016/j.jclepro.2022.133853

- ❑ A novel hierarchically-porous diamondized polyacrylonitrile sponge-like electrodes for acetaminophen electrochemical detection
  Mattia Pierpaoli, Pawel Jakobczak, Bartlomiej Dec, Chiara Giosue, Natalia Czerwinska, Aneta Lewkowicz, Maria Letizia Ruello, Robert Bogdanowicz

  https://doi.org/10.1016/j.electacta.2022.141083

- ❑ Characterization and Filtration Efficiency of Sustainable PLA Fibers Obtained via a Hybrid 3D-Printed/Electrospinning Technique
  Mattia Pierpaoli, Chiara Giosue, Natalia Czerwinska, Michał Rycewicz, Aleksandra Wieloszyńska, Robert Bogdanowicz, Maria Letizia Ruello

  https://doi.org/10.3390/ma14226766

References

[1] WHO (2018). https://www.who.int/news/item/02-05-2018-9-out-of-10-people-worldwide-breathe-polluted-air-but-more-countries-are-taking-action (accessed March 14, 2024).

[2] WHO (2010), Guidelines for indoor air quality: selected pollutants.

[3] WHO, Global Air Quality Guidelines, (2021). https://iris.who.int/bitstream/handle/10665/345329/9789240034228-eng.pdf (accessed May 4, 2024).

[4] ANSES, (2018). https://www.anses.fr/fr/system/files/Tableau_VGAI_Juillet2018EN.pdf (accessed May 4, 2024).

[5] O. US EPA, Why Indoor Air Quality is Important to Schools, (2015). https://www.epa.gov/iaq-schools/why-indoor-air-quality-important-schools (accessed May 3, 2024).

[6] W.H.O.R.O. for Europe, Indoor Air Quality: Organic Pollutants : Report on a WHO Meeting, Berlin (West), 23-27 August 1987, World Health Organization, Regional Office for Europe, 1989.

[7] S. Rovelli, A. Cattaneo, A. Fazio, A. Spinazzè, F. Borghi, D. Campagnolo, C. Dossi, D.M. Cavallo, VOCs Measurements in Residential Buildings: Quantification via Thermal Desorption and Assessment of Indoor Concentrations in a Case-Study, Atmosphere 10 (2019) 57. https://doi.org/10.3390/atmos10020057.

[8] C. Gubb, T. Blanusa, A. Griffiths, C. Pfrang, Potted plants can remove the pollutant nitrogen dioxide indoors, Air Qual Atmos Health 15 (2022) 479–490. https://doi.org/10.1007/s11869-022-01171-6.

[9] S. Vilčekova, Indoor Nitrogen Oxides, in: Advanced Air Pollution, IntechOpen, 2011. https://doi.org/10.5772/16819.

[10] A. Dėdelė, A. Miškinytė, Seasonal variation of indoor and outdoor air quality of nitrogen dioxide in homes with gas and electric stoves, Environmental Science and Pollution Research 23 (2016). https://doi.org/10.1007/s11356-016-6978-5.

[11] 40 CFR Appendix J to Part 50 - Appendix J to Part 50—Reference Method for the Determination of Particulate Matter as PM10 in the Atmosphere, LII / Legal Information Institute (n.d.). https://www.law.cornell.edu/cfr/text/40/appendix-J_to_part_50 (accessed February 20, 2024).

[12] Q. Liu, Y.J. Son, L. Li, N. Wood, A.M. Senerat, J. Pantelic, Healthy home interventions: Distribution of PM2.5 emitted during cooking in residential settings, Building and Environment 207 (2022) 108448. https://doi.org/10.1016/j.buildenv.2021.108448.

[13] R. Tang, C. Pfrang, Indoor particulate matter (PM) from cooking in UK students' studio flats and associated intervention strategies: evaluation of cooking methods, PM concentrations and personal exposures using low-cost sensors, Environmental Science: Atmospheres 3 (2023) 537–551. https://doi.org/10.1039/D2EA00171C.

[14] S.W. See, R. Balasubramanian, Risk assessment of exposure to indoor aerosols associated with Chinese cooking, Environmental Research 102 (2006) 197–204. https://doi.org/10.1016/j.envres.2005.12.013.

[15] I. Alameddine, K. Gebrael, F. Hanna, M. El-Fadel, Quantifying indoor PM2.5 levels and its sources in schools: What role does location, chalk use, and socioeconomic equity play ?, Atmospheric Pollution Research 13 (2022) 101375. https://doi.org/10.1016/j.apr.2022.101375.

[16] P. Kumar, Mohd.A. Kausar, A.B. Singh, R. Singh, Biological contaminants in the indoor air environment and their impacts on human health, Air Qual Atmos Health 14 (2021) 1723–1736. https://doi.org/10.1007/s11869-021-00978-z.

[17] O. US EPA, What are biological pollutants, how do they affect indoor air quality?, (2019). https://www.epa.gov/indoor-air-quality-iaq/what-are-biological-pollutants-how-do-they-affect-indoor-air-quality (accessed February 29, 2024).

[18] L. Schibuola, C. Tambani, High energy efficiency ventilation to limit COVID-19 contagion in school environments, Energy and Buildings 240 (2021) 110882. https://doi.org/10.1016/j.enbuild.2021.110882.

[19] M.M. Andamon, P. Rajagopalan, J. Woo, Evaluation of ventilation in Australian school classrooms using long-term indoor CO2 concentration measurements, Building and Environment 237 (2023) 110313. https://doi.org/10.1016/j.buildenv.2023.110313.

[20] Food waste and food waste prevention - estimates, (n.d.). https://ec.europa.eu/eurostat/statistics-explained/index.php?title=Food_waste_and_food_waste_prevention_-_estimates (accessed February 6, 2024).

[21] Food Waste - European Commission, (n.d.). https://food.ec.europa.eu/safety/food-waste_en (accessed February 6, 2024).

[22] olive-oil-dashboard_en.pdf, (n.d.). https://agriculture.ec.europa.eu/system/files/2023-07/olive-oil-dashboard_en.pdf (accessed August 18, 2023).

[23] Textiles and the environment: the role of design in Europe's circular economy — European Environment Agency, (n.d.). https://www.eea.europa.eu/publications/textiles-and-the-environment-the (accessed February 6, 2024).

[24] L.F. Ballesteros, J.A. Teixeira, S.I. Mussatto, Chemical, Functional, and Structural Properties of Spent Coffee Grounds and Coffee Silverskin, Food Bioprocess Technol 7 (2014) 3493–3503. https://doi.org/10.1007/s11947-014-1349-z.

[25] S. Valvez, A. Maceiras, P. Santos, P.N.B. Reis, Olive Stones as Filler for Polymer-Based Composites: A Review, Materials 14 (2021) 845. https://doi.org/10.3390/ma14040845.

[26] Marta Prześniak-Welenc (0000-0002-7640-2677) - ORCID, (n.d.). https://orcid.org/0000-0002-7640-2677 (accessed February 28, 2024).

[27] Małgorzata Nadolska (0000-0001-5998-2975), ORCID (n.d.). https://orcid.org/0000-0001-5998-2975 (accessed February 28, 2024).

[28] M. Nadolska, M. Szkoda, K. Trzciński, P. Niedziałkowski, J. Ryl, A. Mielewczyk-Gryń, K. Górnicka, M. Prześniak-Welenc, Insight into Potassium Vanadates as Visible-Light-Driven Photocatalysts: Synthesis of V(IV)-Rich Nano/Microstructures for the Photodegradation of Methylene Blue, Inorg. Chem. 61 (2022) 9433–9444. https://doi.org/10.1021/acs.inorgchem.2c00136.

[29] J.S. Noh, J.A. Schwarz, Estimation of the point of zero charge of simple oxides by mass titration, Journal of Colloid and Interface Science 130 (1989) 157–164. https://doi.org/10.1016/0021-9797(89)90086-6.

[30] A. Gaitán, W. Gacitúa, Morphological and Mechanical Characterization of Electrospun Polylactic Acid and Microcrystalline Cellulose, BioResources 13 (2018) 3659–3673. https://doi.org/10.15376/biores.13.2.3659-3673.

[31] V.H. Sangeetha, T.O. Varghese, S.K. Nayak, Isolation and characterisation of nanofibrillated cellulose from waste cotton: effects on thermo-mechanical properties of polylactic acid/MA-g-SEBS blends, Iran Polym J 28 (2019) 673–683. https://doi.org/10.1007/s13726-019-00733-3.

[32] D.B. Purchas, K. Sutherland, CHAPTER 3 - Non-woven Fabric Media, in: D.B. Purchas, K. Sutherland (Eds.), Handbook of Filter Media (Second Edition), Elsevier Science, Amsterdam, 2002: pp. 81–116. https://doi.org/10.1016/B978-185617375-9/50004-3.

[33] J. Xue, T. Wu, Y. Dai, Y. Xia, Electrospinning and Electrospun Nanofibers: Methods, Materials, and Applications, Chem Rev 119 (2019) 5298–5415. https://doi.org/10.1021/acs.chemrev.8b00593.

[34] T.-N. Lam, C.-H. Wu, S.-H. Huang, W.-C. Ko, Y.-L. Huang, C.-Y. Ma, C.-C. Wang, E.-W. Huang, Multi-Scale Microstructure Investigation for a PM2.5 Air-Filter Efficiency Study of Non-Woven Polypropylene, Quantum Beam Science 3 (2019) 20. https://doi.org/10.3390/qubs3040020.

[35] Adv Funct Materials - 2020 - Dai - An Advanced Dual-Function MnO2-Fabric Air Filter Combining Catalytic Oxidation of Formaldehyde, (2020). https://doi.org/10.1002/adfm.202001488

[36] D.-Q. Chang, C.-Y. Tien, C.-Y. Peng, M. Tang, S.-C. Chen, Development of composite filters with high efficiency, low pressure drop, and high holding capacity PM2.5 filtration, Separation and Purification Technology 212 (2019) 699–708. https://doi.org/10.1016/j.seppur.2018.11.068.

[37] C. Zou, Y. Shi, X. Qian, Characterization of glass fiber felt and its performance as an air filtration media, Journal of Industrial Textiles 51 (2022) 1186S-1206S. https://doi.org/10.1177/1528083720961410.

[38] M. Tang, Y. Liang, J. Hu, The Impact of Fiber Dispersion on Filtration and Tensile Properties of Glass Fiber Filter Paper, Journal of Engineered Fibers and Fabrics 11 (2016) 155892501601100. https://doi.org/10.1177/155892501601100401.

[39] Michael Jacob Ioelovich, Microcellulose Vs Nanocellulose – A Review, World J. Adv. Eng. Tech. Sci. 5 (2022) 001–015. https://doi.org/10.30574/wjaets.2022.5.2.0037.

[40] C.P. Teng, M.Y. Tan, J.P.W. Toh, Q.F. Lim, X. Wang, D. Ponsford, E.M.J. Lin, W. Thitsartarn, S.Y. Tee, Advances in Cellulose-Based Composites for Energy Applications, Materials 16 (2023) 3856. https://doi.org/10.3390/ma16103856.

[41] B. Nurhadi, A. Angeline, N. Sukri, N. Masruchin, H.R. Arifin, R.A. Saputra, Characteristics of microcrystalline cellulose from nata de coco: Hydrochloric acid versus maleic acid hydrolysis, Journal of Applied Polymer Science 139 (2022) 51576. https://doi.org/10.1002/app.51576.

[42] R.M. Rasal, A.V. Janorkar, D.E. Hirt, Poly(lactic acid) modifications, Progress in Polymer Science 35 (2010) 338–356. https://doi.org/10.1016/j.progpolymsci.2009.12.003.

[43] H. Fong, I. Chun, D.H. Reneker, Beaded nanofibers formed during electrospinning, Polymer 40 (1999) 4585–4592. https://doi.org/10.1016/S0032-3861(99)00068-3.

[44] M. Pierpaoli, C. Giosuè, N. Czerwinska, M. Rycewicz, A. Wieloszynska, R. Bogdanowicz, M. Ruello, Characterization and Filtration Efficiency of Sustainable PLA Fibers Obtained via a Hybrid 3D-Printed/Electrospinning Technique, Materials 14 (2021) 6766. https://doi.org/10.3390/ma14226766.

[45] L.F.O. Silva, D. Pinto, A. Neckel, G.L. Dotto, M.L.S. Oliveira, The impact of air pollution on the rate of degradation of the fortress of Florianópolis Island, Brazil, Chemosphere 251 (2020) 126838. https://doi.org/10.1016/j.chemosphere.2020.126838.

[46] M. Oliveira, B. Tutikian, C. Milanés Batista, L. Silva, Atmospheric contaminations and bad conservation effects in Roman mosaics and mortars of Italica, Journal of Cleaner Production 248 (2020) 119250. https://doi.org/10.1016/j.jclepro.2019.119250.

[47] L.F.O. Silva, D. Pinto, A. Neckel, M.L.S. Oliveira, An analysis of vehicular exhaust derived nanoparticles and historical Belgium fortress building interfaces, Geoscience Frontiers 11 (2020) 2053–2060. https://doi.org/10.1016/j.gsf.2020.07.003.

[48] T. Grøntoft, S. López-Aparicio, M. Scharff, M. Ryhl-Svendsen, G. Andrade, M. Obarzanowski, D. Thickett, Impact Loads of Air Pollutants on Paintings: Performance Evaluation by Modeling For Microclimate Frames, Journal of the American Institute for Conservation 50 (2011) 105–122. https://doi.org/10.1179/019713611804480953.

[49] T. Grøntoft, O. Marincas, Indoor air pollution impact on cultural heritage in an urban and a rural location in Romania: the National military museum in Bucharest and the Tismana monastery in Gorj County, Heritage Science 6 (2018) 73. https://doi.org/10.1186/s40494-018-0238-6.

[50] M. Lapuerta, J.J. Hernández, A. Pazo, J. López, Gasification and co-gasification of biomass wastes: Effect of the biomass origin and the gasifier operating conditions, Fuel Processing Technology 89 (2008) 828–837. https://doi.org/10.1016/j.fuproc.2008.02.001.

[51] M. Sevilla, N. Díez, A.B. Fuertes, Toward more sustainable chemical activation strategies for the production of porous carbons, (n.d.).

[52] D.R. Lobato-Peralta, A. Ayala-Cortés, A. Longoria, D.E. Pacheco-Catalán, P.U. Okoye, H.I. Villafán-Vidales, C.A. Arancibia-Bulnes, A.K. Cuentas-Gallegos, Activated carbons obtained by environmentally friendly activation using solar energy for their use in neutral electrolyte supercapacitors, Journal of Energy Storage 52 (2022) 104888. https://doi.org/10.1016/j.est.2022.104888.

[53] D. Adinata, W.M.A. Wan Daud, M.K. Aroua, Preparation and characterization of activated carbon from palm shell by chemical activation with K2CO3, Bioresource Technology 98 (2007) 145–149. https://doi.org/10.1016/j.biortech.2005.11.006.

[54] A. Mestre, C. Freire, J. Pires, A. Carvalho, M. Pinto, High performance microspherical activated carbons for methane storage and landfill gas or biogas upgrade, Journal of Materials Chemistry A 2 (2014) 15337. https://doi.org/10.1039/C4TA0342J.

[55] A.S. Mestre, F. Hesse, C. Freire, C.O. Ania, A.P. Carvalho, Chemically activated high grade nanoporous carbons from low density renewable biomass (Agave sisalana) for the removal of pharmaceuticals, Journal of Colloid and Interface Science 536 (2019) 681–693. https://doi.org/10.1016/j.jcis.2018.10.081.

[56] G. Singh, I.Y. Kim, K.S. Lakhi, P. Srivastava, R. Naidu, A. Vinu, Single step synthesis of activated bio-carbons with a high surface area and their excellent CO_2 adsorption capacity, Carbon 116 (2017) 448–455. https://doi.org/10.1016/j.carbon.2017.02.015.

[57] K.K. Kishibayev, J. Serafin, R.R. Tokpayev, T.N. Khavaza, A.A. Atchabarova, D.A. Abduakhytova, Z.T. Ibraimov, J. Sreńscek-Nazzal, Physical and chemical properties of activated carbon synthesized from plant wastes and shungite for CO_2 capture, Journal of Environmental Chemical Engineering 9 (2021) 106798. https://doi.org/10.1016/j.jece.2021.106798.

[58] J. Serafin, B. Dziejarski, J. Sreńscek-Nazzal, An innovative and environmentally friendly bioorganic synthesis of activated carbon based on olive stones and its potential application for CO_2 capture, Sustainable Materials and Technologies 38 (2023) e00717. https://doi.org/10.1016/j.susmat.2023.e00717.

[59] A. Bedoui, S. Souissi-Najar, S.S. Idris, N.A. Rahman, A. Ouederni, Thermal behaviour of impregnated olive stones with phosphoric acid via TGA-MS, Comptes Rendus. Chimie 24 (2021) 149–162. https://doi.org/10.5802/crchim.118.

[60] J. Hayashi, T. Horikawa, I. Takeda, K. Muroyama, F. Nasir Ani, Preparing activated carbon from various nutshells by chemical activation with K_2CO_3, Carbon 40 (2002) 2381–2386. https://doi.org/10.1016/S0008-6223(02)00118-5.

[61] G. Singh, A. Maria Ruban, X. Geng, A. Vinu, Recognizing the potential of K-salts, apart from KOH, for generating porous carbons using chemical activation, Chemical Engineering Journal 451 (2023) 139045. https://doi.org/10.1016/j.cej.2022.139045.

[62] S. Wang, Y.-R. Lee, Y. Won, H. Kim, S.-E. Jeong, B. Wook Hwang, A. Ra Cho, J.-Y. Kim, Y. Cheol Park, H. Nam, D.-H. Lee, H. Kim, S.-H. Jo, Development of high-performance adsorbent using KOH-impregnated rice husk-based activated carbon for indoor CO_2 adsorption, Chemical Engineering Journal 437 (2022) 135378. https://doi.org/10.1016/j.cej.2022.135378.

[63] M.-J. Kim, Simple synthesis of spent coffee ground-based microporous carbons using K_2CO_3 as an activation agent and their application to CO_2 capture, Chemical Engineering Journal (2020) 11.

[64] M.A.E.-S. El-Hashemy, N.F. Alotaibi, Purification of benzene-laden air by static adsorption of benzene onto activated carbon prepared from Diplotaxis acris biomass, Biomass Conv. Bioref. 13 (2023) 1763–1777. https://doi.org/10.1007/s13399-021-01462-5.

[65] T. Takada, R. Tanaka, R. Ono, Removal of Volatile Toluene Using K_2CO_3-Activated Carbon Adsorbents Prepared from Buckwheat Hull, Pollutants 2 (2022) 12–20. https://doi.org/10.3390/pollutants2010002.

[66] J. Li, X. Ma, H. Wu, L. Yang, Adsorption of Low-Concentration VOCs on Modified Activated Carbons in a Humid Atmosphere, Energy Fuels 35 (2021) 5090–5100. https://doi.org/10.1021/acs.energyfuels.0c03971.

[67] A. Anfruns, M.J. Martin, M.A. Montes-Morán, Removal of odourous VOCs using sludge-based adsorbents, Chemical Engineering Journal 166 (2011) 1022–1031. https://doi.org/10.1016/j.cej.2010.11.095.

[68] E. Batur, S. Kutluay, Dynamic adsorption behavior of benzene, toluene, and xylene VOCs in single- and multi-component systems by activated carbon derived from defatted black cumin (Nigella sativa L.) biowaste, Journal of Environmental Chemical Engineering 10 (2022) 107565. https://doi.org/10.1016/j.jece.2022.107565.

[69] X. Shen, Record-high capture of volatile benzene and toluene enabled by activator implant-optimized banana peel-derived engineering carbonaceous adsorbents, Environment International (2020) 11.

[70] Y. Diao, W.P. Walawender, L.T. Fan, Activated carbons prepared from phosphoric acid activation of grain sorghum, Bioresource Technology 81 (2002) 45–52. https://doi.org/10.1016/S0960-8524(01)00100-6.

[71] S. Palmieri, M. Pierpaoli, L. Riderelli, S. Qi, M.L. Ruello, Preparation and Characterization of an Electrospun PLA-Cyclodextrins Composite for Simultaneous High-Efficiency PM and VOC Removal, J. Compos. Sci. 4 (2020) 79. https://doi.org/10.3390/jcs4020079.

[72] Q. Maqbool, N. Czerwinska, C. Giosue, S. Sabbatini, M.L. Ruello, F. Tittarelli, New waste-derived TiO2 nanoparticles as a potential photocatalytic additive for lime based indoor finishings, Journal of Cleaner Production 373 (2022) 133853. https://doi.org/10.1016/j.jclepro.2022.133853.

[73] C. Giosuè, M. Pierpaoli, C. di Perna, B. Citterio, G. Mangiaterra, M.L. Ruello, F. Tittarelli, Properties of an innovative multi-functional finish for the improvement of indoor air quality, Building and Environment 233 (2023) 110091. https://doi.org/10.1016/j.buildenv.2023.110091.

[74] P. Sangines de Carcer, M. Domínguez, F. Sánchez, G. San Miguel, Slow pyrolysis of olive stones in a rotary kiln: Chemical and energy characterization of solid, gas, and condensable products, Journal of Renewable and Sustainable Energy 7 (2015). https://doi.org/10.1063/1.4923442.

[75] L. Hongqiang, Q. Yongshui, J. Xu, Microwave-Assisted Conversion of Lignin, in: 2014: pp. 61–82. https://doi.org/10.1007/978-94-017-9612-5_4.

[76] M.H. Park, Y.S. Yun, S.Y. Cho, N.R. Kim, H.-J. Jin, Waste coffee grounds-derived nanoporous carbon nanosheets for supercapacitors, Carbon Letters 19 (2016) 66–71. https://doi.org/10.5714/CL.2016.19.066.

[77] H. Laksaci, A. Khelifi, B. Belhamdi, M. Trari, Valorization of coffee grounds into activated carbon using physic—chemical activation by KOH/CO 2, Journal of Environmental Chemical Engineering 5 (2017) 5061–5066. https://doi.org/10.1016/j.jece.2017.09.036.

[78] K.L. Foster, R.G. Fuerman, J. Economy, S.M. Larson, M.J. Rood, Adsorption characteristics of trace volatile organic compounds in gas streams onto activated carbon fibers, Chem. Mater. 4 (1992) 1068–1073. https://doi.org/10.1021/cm00023a026.

[79] R. Hazzaa, M. Hussein, Adsorption of cationic dye from aqueous solution onto activated carbon prepared from olive stones, Environmental Technology & Innovation 4 (2015) 36–51. https://doi.org/10.1016/j.eti.2015.04.002.

[80] A. Gundogdu, C. Duran, H.B. Senturk, M. Soylak, M. Imamoglu, Y. Onal, Physicochemical characteristics of a novel activated carbon produced from tea industry waste, Journal of Analytical and Applied Pyrolysis 104 (2013) 249–259. https://doi.org/10.1016/j.jaap.2013.07.008.

[81] L. Zhu, N. Zhao, L. Tong, Y. Lv, Structural and adsorption characteristics of potassium carbonate activated biochar, RSC Adv. 8 (2018) 21012–21019. https://doi.org/10.1039/C8RA03335H.

[82] X. Li, L. Zhang, Z. Yang, P. Wang, Y. Yan, J. Ran, Adsorption materials for volatile organic compounds (VOCs) and the key factors for VOCs adsorption process: A review, Separation and Purification Technology 235 (2020) 116213. https://doi.org/10.1016/j.seppur.2019.116213.

[83] D.R. Vardon, B.R. Moser, W. Zheng, K. Witkin, R.L. Evangelista, T.J. Strathmann, K. Rajagopalan, B.K. Sharma, Complete Utilization of Spent Coffee Grounds To Produce Biodiesel, Bio-Oil, and Biochar, ACS Sustainable Chem. Eng. 1 (2013) 1286–1294. https://doi.org/10.1021/sc400145w.

[84] M. Thommes, K. Kaneko, A.V. Neimark, J.P. Olivier, F. Rodriguez-Reinoso, J. Rouquerol, K.S.W. Sing, Physisorption of gases, with special reference to the evaluation of surface area and pore size distribution (IUPAC Technical Report), Pure and Applied Chemistry 87 (2015) 1051–1069. https://doi.org/10.1515/pac-2014-1117.

[85] J. Lykiema, K.S.W. Sing, J. Haber, M. Kerker, E. Wolfram, J.H. Block, N.V. Churaev, D.H. Everett, R.S. Hansen, R.A.W. Haul, J.W. Hightower, R.J. Hunter, Prepared for publication by the Subcommittee on Reporting Gas Adsorption Data Consisting of K. S. W. SING (UK, Chairman); D. H. EVERETT (UK); R. A. W. HAUL (FRG); L. MOSCOU (Netherlands); R. A. PIEROTTI (USA); J. ROUQUEROL (France); T. SIEMIENIEWSKA (Poland), (1984).

[86] M.M. Talakesh, M. Sadeghi, M.P. Chenar, A. Khosravi, Gas separation properties of poly(ethylene glycol)/poly(tetramethylene glycol) based polyurethane membranes, Journal of Membrane Science 415–416 (2012) 469–477. https://doi.org/10.1016/j.memsci.2012.05.033.

[87] A. Mukhtar, N. Mellon, S. Saqib, S. Lee, M. Bustam, Extension of BET Theory to CO2 Adsorption Isotherms for Ultra-Microporosity of Covalent Organic Polymer (SN Applied Sciences), SN Applied Sciences (2020). https://doi.org/10.1007/s42452-020-2968-9.

[88] X.-Y. Liu, M. Huang, H.-L. Ma, Z. Zhang, J.-M. Gao, Y.-L. Zhu, X. Han, X. Guo, Preparation of a Carbon-Based Solid Acid Catalyst by Sulfonating Activated Carbon in a Chemical Reduction Process, Molecules (Basel, Switzerland) 15 (2010) 7188–96. https://doi.org/10.3390/molecules15107188.

[89] A.B. Pérez Marín, M.I. Aguilar, V.F. Meseguer, J.F. Ortuño, J. Sáez, M. Lloréns, Biosorption of chromium (III) by orange (Citrus cinensis) waste: Batch and continuous studies, Chemical Engineering Journal 155 (2009) 199–206. https://doi.org/10.1016/j.cej.2009.07.034.

[90] X. Wei, S. Wu, P. Liu, S. Huang, X. Li, J. Yang, Y. Wu, Characterization of physicochemical properties of activated carbons prepared from penicillin mycelial residues and its adsorption properties for VOCs, Journal of Environmental Chemical Engineering 11 (2023) 109733. https://doi.org/10.1016/j.jece.2023.109733.

[91] M. Benallou Benzekri, N. Benderdouche, B. Bestani, N. Douara, L. Duclaux, Valorization of olive stones into a granular activated carbon for the removal of Methylene blue in batch and fixed bed modes, Jmes 9 (2018) 272–284. https://doi.org/10.26872/jmes.2018.9.1.31.

[92] M.J. Saad, C. Chia, S. Zakaria, M.S. Sajab, S. Misran, M.H. Bin Abdul Rahman, S.X. CHIN, Physical and Chemical Properties of the Rice Straw Activated Carbon Produced from Carbonization and KOH Activation Processes, Sains Malaysiana 48 (2019) 385–391. https://doi.org/10.17576/jsm-2019-4802-16.

[93] OSHA, CARBON DIOXIDE. https://www.osha.gov/chemicaldata/183 (accessed July 7, 2023).

[94] OSHA, 2-BUTANONE (METHYL ETHYL KETONE; MEK). https://www.osha.gov/chemicaldata/680 (accessed July 7, 2023).

[95] OSHA, TOLUENE. https://www.osha.gov/chemicaldata/89 (accessed July 7, 2023).

[96] ACGIH, CARBON DIOXIDE, ACGIH (2022). https://www.acgih.org/carbon-dioxide/ (accessed August 26, 2023).

[97] ACGIH, METHYL ETHYL KETONE, ACGIH (2022). https://www.acgih.org/methyl-ethyl-ketone-2/ (accessed August 26, 2023).

[98] ACGIH, TOLUENE, ACGIH (2022). https://www.acgih.org/toluene/ (accessed August 26, 2023).

[99] T. La Rocca, E. Carretier, D. Dhaler, E. Louradour, T. Truong, P. MOULIN, Purification of Pharmaceutical Solvents by Pervaporation through Hybrid Silica Membranes, Membranes 9 (2019). https://doi.org/10.3390/membranes9070076.

[100] L. Zhu, D. Shen, K.H. Luo, A critical review on VOCs adsorption by different porous materials: Species, mechanisms and modification methods, Journal of Hazardous Materials 389 (2020) 122102. https://doi.org/10.1016/j.jhazmat.2020.122102.

[101] N. Le-Minh, E.C. Sivret, A. Shammay, R.M. Stuetz, Factors affecting the adsorption of gaseous environmental odors by activated carbon: A critical review, Critical Reviews in Environmental Science and Technology 48 (2018) 341–375. https://doi.org/10.1080/10643389.2018.1460984.

[102] I.K. Shah, P. Pre, B.J. Alappat, Effect of thermal regeneration of spent activated carbon on volatile organic compound adsorption performances, Journal of the Taiwan Institute of Chemical Engineers 45 (2014) 1733–1738. https://doi.org/10.1016/j.jtice.2014.01.006.

[103] X. Zhang, B. Gao, A.E. Creamer, C. Cao, Y. Li, Adsorption of VOCs onto engineered carbon materials: A review, Journal of Hazardous Materials 338 (2017) 102–123. https://doi.org/10.1016/j.jhazmat.2017.05.013.

[104] I.I. Salame, T.J. Bandosz, Study of Water Adsorption on Activated Carbons with Different Degrees of Surface Oxidation, Journal of Colloid and Interface Science 210 (1999) 367–374. https://doi.org/10.1006/jcis.1998.5918.

[105] Contents Vol. 163, DWT 163 (2019) v–vii. https://doi.org/10.5004/dwt.2019.24804.

[106] X. Zhao, X. Zeng, Y. Qin, X. Li, T. Zhu, X. Tang, An experimental and theoretical study of the adsorption removal of toluene and chlorobenzene on coconut shell derived carbon, Chemosphere 206 (2018) 285–292. https://doi.org/10.1016/j.chemosphere.2018.04.126.

[107] B. Lei, H. Xie, S. Chen, B. Liu, G. Zhou, Control of pore structure and surface chemistry of activated carbon derived from waste Zanthoxylum bungeanum branches for toluene removal in air, Environ Sci Pollut Res 27 (2020) 27072–27092. https://doi.org/10.1007/s11356-020-09115-2.

[108]   A. Khazraei Vizhemehr, Predicting the Performance of Activated Carbon Filters at Low Concentrations Using Accelerated Test Data. https://core.ac.uk/download/pdf/211517627.pdf (accessed August 20, 2023).

[109]   T.-R. Kuo, H.-W. Huang, C. Kongvarhodom, M. Saukani, S. Yougbaré, H.-M. Chen, L.-Y. Lin, Efficiently catalyzing photo-oxidation of water by surface engineering of bismuth vanadate with nickel molybdenum oxide coverages, International Journal of Hydrogen Energy 51 (2024) 613–622. https://doi.org/10.1016/j.ijhydene.2023.10.147.

[110]   H. Sun, P. Qin, Z. Wu, C. Liao, J. Guo, S. Luo, Y. Chai, Visible light-driven photocatalytic degradation of organic pollutants by a novel Ag3VO4/Ag2CO3 p–n heterojunction photocatalyst: Mechanistic insight and degradation pathways, Journal of Alloys and Compounds 834 (2020) 155211. https://doi.org/10.1016/j.jallcom.2020.155211.

[111] S. Gatto, Photocatalytic activity assessment of micro-sized TiO2 used as powders and as starting material for porcelain gres tiles production https://air.unimi.it/retrieve/handle/2434/243448/328834/phd_unimi_R09615.pdf (accessed February 28, 2024).

[112]   G. Marcì, E. García-López, G. Mele, L. Palmisano, G. Dyrda, R. Słota, Comparison of the photocatalytic degradation of 2-propanol in gas–solid and liquid–solid systems by using TiO2–LnPc2 hybrid powders, Catalysis Today 143 (2009) 203–210. https://doi.org/10.1016/j.cattod.2008.12.029.

[113]   Z. Rao, G. Lu, L. Chen, A. Mahmood, G. Shi, Z. Tang, X. Xie, J. Sun, Photocatalytic oxidation mechanism of Gas-Phase VOCs: Unveiling the role of holes, •OH and •O2−, Chemical Engineering Journal 430 (2022) 132766. https://doi.org/10.1016/j.cej.2021.132766.

[114]   Z. Shayegan, F. Haghighat, C.-S. Lee, Carbon-doped TiO2 film to enhance visible and UV light photocatalytic degradation of indoor environment volatile organic compounds, Journal of Environmental Chemical Engineering 8 (2020) 104162. https://doi.org/10.1016/j.jece.2020.104162.

[115]   M.J. Soberman, S. Tabe, R.R. Farnood, Adsorption of organic micropollutants onto electrospun nanofiber membranes functionalized with activated carbon, Carbon Trends 5 (2021) 100081. https://doi.org/10.1016/j.cartre.2021.100081.

[116]   Z. Ding, X. Hu, P.L. Yue, G.Q. Lu, P.F. Greenfield, Synthesis of anatase TiO2 supported on porous solids by chemical vapor deposition, Catalysis Today 68 (2001) 173–182. https://doi.org/10.1016/S0920-5861(01)00298-X.

[117]   R. Orlando, A. Afshari, P. Fojan, Cellulose acetate-TiO 2 and activated carbon electrospun composite fibre membranes for toluene removal, Journal of Industrial Textiles 53 (2023) 152808372211502. https://doi.org/10.1177/15280837221150200.

[118]   C. Giosuè, A. Mobili, G. Toscano, M.L. Ruello, F. Tittarelli, Effect of Biomass Waste Materials as Unconventional Aggregates in Multifunctional Mortars for Indoor Application, Procedia Engineering 161 (2016) 655–659. https://doi.org/10.1016/j.proeng.2016.08.724.

[119]   C. Giosuè, M. Pierpaoli, A. Mobili, M.L. Ruello, F. Tittarelli, Multifunctional Lightweight Mortars for Indoor Applications to Improve Comfort and Health of Occupants: Thermal Properties and Photocatalytic Efficiency, Front. Mater. 7 (2020) 255. https://doi.org/10.3389/fmats.2020.00255.

[120]   X. Zhou, Y. Liu, C. Song, X. Wang, F. Wang, J. Liu, Modelling and testing of VOC source suppression effect of building materials modified with adsorbents, Building and Environment 154 (2019) 122–131. https://doi.org/10.1016/j.buildenv.2019.03.003.

[121]   Nanomaterials | Free Full-Text | A Review on Catalytic Nanomaterials for Volatile Organic Compounds VOC Removal and Their Applications for Healthy Buildings, Nanomaterials 9(6), 910 (2019). https://doi.org/10.3390/nano9060910

[122]   J. Xiong, P. Zhang, S. Huang, Y. Zhang, Comprehensive influence of environmental factors on the emission rate of formaldehyde and VOCs in building materials: Correlation development and exposure assessment, Environmental Research 151 (2016) 734–741. https://doi.org/10.1016/j.envres.2016.09.003.

[123]   C. Jung, N.S.A. Mahmoud, N. Alqassimi, Identifying the relationship between VOCs emission and temperature/humidity changes in new apartments in the hot desert climate, Front. Built Environ. 8 (2022). https://doi.org/10.3389/fbuil.2022.1018395.

[124]   P. Markowicz, L. Larsson, Influence of relative humidity on VOC concentrations in indoor air, Environ Sci Pollut Res 22 (2015) 5772–5779. https://doi.org/10.1007/s11356-014-3678-x.
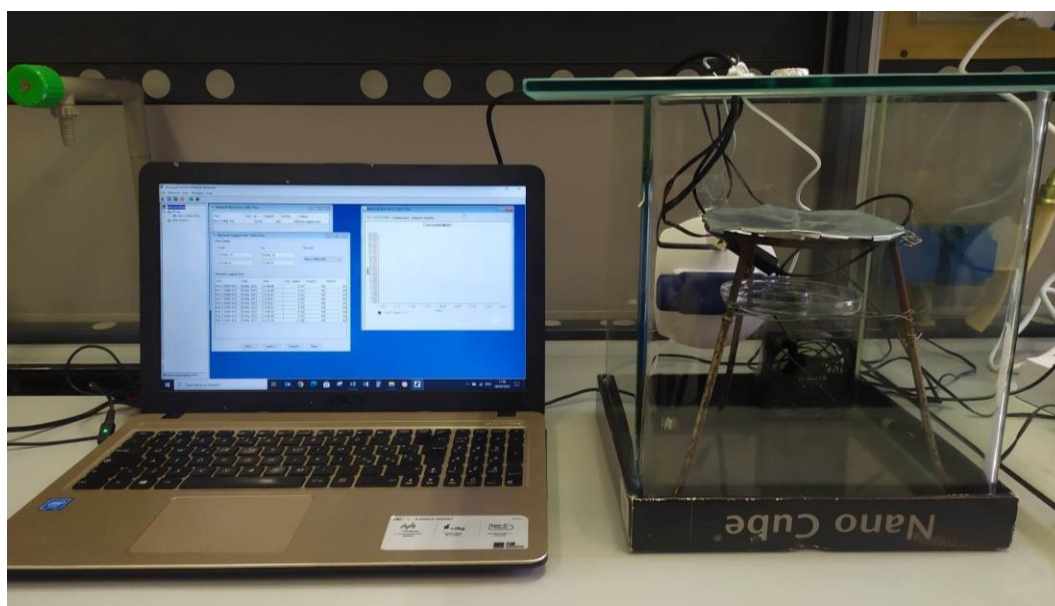
Appendix

Appendix Figure 4.1. VOCs adsorption set-up.

Appendix Table 4.1. Elemental analysis of raw samples and after pyrolysis and activation.

	ELEMENTAL ANALYSIS (WT%)							ATOMIC O/C RATIO
SAMPLE	**C**	**O**	**Mg**	**K**	**S**	**Ca**	**P**	
CG	57.41	41.22	<1	0.54	<1	0.22	<1	0.54
OS	58.53	39.46	-	0.54	<1	1.25	-	0.51
AC-K_2CO_3-CG	83.42	12.80	<1	1.64	-	0.66	-	0.09
AC-K_2CO_3-OS	88.89	10.53	<1	0.06	-	0.22	-	0.09
AC-CO_2-OS	85.08	9.90	<1	2.87	-	0.80	<1	0.08
AC-CO_2(2H)-CG	86.50	8.92	<1	2.30	-	0.95	<1	0.09
AC-CO_2(1H)-CG	88.74	10.60	<1	0.37	-	0.26	<1	0.08
B-(2H)-CG	80.63	10.70	<1	0.11	-	6.38	<1	0.12
B-(15')-CG	87.07	9.08	<1	2.38	-	1.13	<1	0.09
AC COM	82.11	9.85	<1	3.00	<1	2.52	-	0.10

Appendix Table 4.2. Total volume, volume of pores >0.50nm and volume of pores >0.57nm of produced carbons.

Sample	[a]V_{total}	$V_{pores > 0.50}$ [cm^3/g]	%	$V_{pores > 0.57}$ [cm^3/g]	%
AC-K$_2$CO$_3$-CG	0.53	0.44	83	0.39	74
AC-K$_2$CO$_3$-OS	0.22	0.11	49	0.08	35
AC-CO$_2$-OS	0.21	0.11	55	0.08	44
AC-CO$_2$(2h)-CG	0.18	0.09	50	0.07	37
AC-CO$_2$(1h)-CG	0.16	0.07	43	0.05	31
B-(2h)-CG	0.09	0.05	54	0.04	42
B-(15')-CG	0.07	0.05	66	0.04	53

[a] Determined through the DFT method